

University of Southampton Research Repository ePrints Soton

Copyright © and Moral Rights for this thesis are retained by the author and/or other copyright owners. A copy can be downloaded for personal non-commercial research or study, without prior permission or charge. This thesis cannot be reproduced or quoted extensively from without first obtaining permission in writing from the copyright holder/s. The content must not be changed in any way or sold commercially in any format or medium without the formal permission of the copyright holders.

When referring to this work, full bibliographic details including the author, title, awarding institution and date of the thesis must be given e.g.

AUTHOR (year of submission) "Full thesis title", University of Southampton, name of the University School or Department, PhD Thesis, pagination

UNIVERSITY OF SOUTHAMPTON

Pulsed Laser Deposition of Chalcogenide Glass Materials
for Potential Waveguide Laser Applications

By Paul Edmund Rivers

Doctor of Philosophy

FACULTY OF ENGINEERING & APPLIED SCIENCE

ELECTRONICS & COMPUTER SCIENCE

July 2000

UNIVERSITY OF SOUTHAMPTON

ABSTRACT

FACULTY OF ENGINEERING & APPLIED SCIENCE

ELECTRONICS & COMPUTER SCIENCE

Doctor of Philosophy

Pulsed Laser Deposition of Chalcogenide Glass Materials for
Potential Waveguide Laser Applications

By Paul Edmund Rivers

There are many applications for small scale, solid state lasers in the near infrared, where conversely there are very few such devices. A lasing device in a rare earth doped gallium-lanthanum-sulphide thin film is attractive due to emission at wavelengths in the 2 to 5 μm region where many gasses and liquids have fundamental vibrations and overtones and so are detectable. This region also covers the 3 to 5 μm atmospheric 'windows'. Some examples of such detection is presented in this thesis.

Using Pulsed Laser Deposition, a relatively new deposition technique, we are able to grow thin films of the chalcogenide glass; gallium-lanthanum-sulphide, gallium-sodium-sulphide and variations of oxysulphides, on a variety of substrates. EXAFS measurements have shown that some of the elements in the glass structure change their bonding arrangement when grown at different energy density producing 'wrong bonds'. This points to the origin of the increased absorption and shift of the optical bandgap which is seen in the materials. It is this tail absorption which ultimately prevented the production of an actual solid state, rare earth laser device.

These amorphous semiconductors have a transmission range from the visible through to the mid infrared part of the spectrum. Chalcogenides can be photomodified, i.e. they have an ability to change refractive index when illuminated with photons whose energies lie in the optical bandgap of the material. This process can be reversible or irreversible depending on post deposition treatment and so gives them potential applications such as optical memory, holographic recording media, lithographically written waveguide structures and potentially laser mediums. For such uses a detailed knowledge of the chalcogenide materials optical parameters is needed.

A novel technique for the optical characterisation of the thin films has been developed which is able to measure differences in refractive index to an accuracy of 8.5×10^{-5} . We are able to map refractive index changes across an entire surface and more uniquely whilst they are occurring during, and after, photomodification or heating.

I would like to dedicate this thesis and all of the work involved to my parents, Derek and Angela. My sense of personal achievement is their sense of pride and relief.

Contents

Acknowledgement	XII
-----------------------	-----

Part 1: Pulsed Laser Deposition for Potential Infrared Waveguide Devices

1. Introduction to Lasers	2
1.1 The Beginning of the Laser	3
1.2 The Rare Earths	4
1.3 The need for Infrared Optical Materials	5
1.3.1 The Infrared	5
1.3.2 Temperature Sensing	6
1.3.3 Applications of 2-5 μm Lasers	6
1.4 Low Phonon Energy Hosts	8
2. Chalcogenide Glasses	11
2.1 Introduction	12
2.2 Other Attributes of Chalcogenide Glasses	13
2.3 Chalcogenide Glass Systems	14
2.3.1 Common Properties	14
2.3.2 Sulphide Glasses	15
2.3.3 Selenide Glasses	16
2.3.4 Telluride Glasses	17
2.3.5 Adding Oxides to the Melt	17
2.3.6 Halides	18
2.4 Doping Chalcogenides	19
2.5 Photoinduced Effects	20
2.5.1 Photomodification	20
2.5.2 Reversible and Irreversible Changes	21
2.5.3 Photoinduced Effects Seen To-date	24

3. Pulsed Laser Ablation	28
3.1 Optical Thin Films and Waveguide Fabrication Techniques	29
3.2 The Beginning of Laser Ablation	31
3.2.1 The Introduction	31
3.2.2 Ablation Without Growth	34
3.3 Laser Deposition	34
3.3.1 Laser-Matter Interaction	34
3.3.2 Plume Dynamics and Background Gasses	37
3.3.3 Non-Laser Induced Ablation	39
3.3.4 Deposition Analysis Techniques	40
3.3.5 Other Considerations	41
3.4 Particulates	42
3.4.1 The Problem of Particulates	42
3.4.2 Reducing and Removing Particulates	44
3.5 The Design of a New Ablation Chamber	46
3.5.1 Vacuum Technology	46
3.5.2 System Design	47
3.5.3 Internal Features	47
3.5.4 Summary of Final Design	50
3.6 Large Scale or Commercial PLD	51
 4. Gallium Sulphide Based Glasses	 53
4.1 Production of the Glass Targets	54
4.1.1 Methods of Synthesis of Chalcogenide Glasses	54
4.1.2 Glass Target Manufacture	54
4.1.3 Quality of Final Material	55
4.1.4 Early Research with GLS	56
4.2 EXAFS Analysis	57
4.2.1 Introduction	57
4.2.2 Synchrotron Radiation	57
4.2.3 X-ray Absorption Fine Structure	58
4.2.4 Experimental Procedure	59
4.2.5 Data Analysis	61
4.2.6 Results and Discussion	63

4.2.7	Summary of EXAFS Results	71
4.3	Different Components and Impurities	71
4.3.1	Components Used to Make Our Glasses	71
4.3.2	Loss Mechanisms in Infrared Optical Materials	73
4.3.3	Intrinsic Absorption Mechanisms	74
4.3.4	Extrinsic Loss Measurements	75
4.4	Absorption and Fluorescence	77
4.5	Conclusion	79
5.	Determination and Optimisation of Optical Parameters and Thin Film Uniformity	81
5.1	Current Techniques for Film Parameter Measurement	82
5.2	Fitting Model: Basic Optics and Equation Derivations	83
5.2.1	Normal and Anomalous Dispersion	83
5.2.2	Reflection and Transmission From a Single Surface	86
5.2.3	Transmission Through a Thin Film Layer	87
5.3	Refractive Index and Thickness	89
5.3.1	Fitting the Optical Thickness	89
5.3.2	Absorption Coefficient of GLS	96
5.4	Thin Film Uniformity	99
5.4.1	Thickness Profiling	99
5.4.2	Improved Film Uniformity	101
5.5	Conclusions	108
6.	Measurements of Photomodification	110
6.1	Introduction	111
6.2	Differential Reflectance Technique	112
6.2.1	Theory	112
6.2.2	Experimental Arrangement	117
6.2.3	Calibration	118
6.2.4	Summary	123
6.3	Photomodification of Thin Films	124
6.3.1	Measurements of Refractive Index Changes	124
6.3.2	Ageing of Chalcogenide Thin Films	129

6.3.3 Monitoring the Photothermal Parameter, <i>In-situ</i>	132
6.3.4 Other Chalcogenide Thin Films	132
6.4 Fast Photomodification Effect	133
6.5 Bulk Photomodification	136
6.5.1 Change in Refractive Index	136
6.5.2 Measurements at Longer Wavelengths	138
6.6 Photoinduced Gratings	140
6.6.1 Introduction to Gratings	140
6.6.2 Stabilised Interferometer	141
6.6.3 Mapping Photomodified Gratings	150
6.7 Conclusions	154

Part 2: Practical Example of Sensing Using Infrared Lasers

7. Remote Surface Moisture Detection	158
7.1 Design Brief	159
7.2 Schematic Design	160
7.2.1 Basic Components	160
7.2.2 First Analogue System	161
7.2.3 Progression to Digital Measurement System	162
7.3 The Next Generation System	163
7.3.1 Principles of Operation	163
7.3.2 Model of System Response	166
7.4 Results and Conclusion	168
7.4.1 The Experimental Materials	168
7.4.2 Methodology and Results	169
7.4.3 Analysis of Data	184
7.4.4 Future Requirements and Considerations	185
7.4.5 Conclusions	186
8. Conclusion and Future Work	189
8.1 Conclusions	190
8.2 Future Considerations	193
List of Publications and Conferences	195
References	i

List of Figures

Figure 1·1	Black body spectral emittance curves against temperature. Reproduced from Savage.	7
Figure 1·2	Nonradiative relaxation rates of RE in different hosts. Reproduced from Digonnet.	9
Figure 2·1	Infrared transmission cut-off for some oxide and chalcogenide glasses at ~ 2 mm thick.	13
Figure 2·2	(a) Possible E - q diagram for energy levels in chalcogenide material, (b) Example of As_2S_3 transmission limit when annealed and illuminated at 514·5 nm.	23
Figure 3·1	Schematic of the basic principle for Pulsed Laser Deposition.	33
Figure 3·2	Schematic of pumping system for Pulsed Laser Deposition Chamber.	46
Figure 3·3	Pictures of the components and their individual function for the substrate holder in the Pulsed Laser Deposition Chamber.	48
Figure 3·4	Schematic of substrate mounting and extraction using load lock arrangement for Pulsed Laser Deposition Chamber.	49
Figure 3·5	Schematic of the target holder, nicknamed the 'wobble device' which was used to continually alter the direction of the plume and so create a painting effect, before and after rotation, (a) and (b) respectively.	50
Figure 4·1	The extent of the glass forming region of Ga_2S_3 with other rare earths. (\leftrightarrow , *) homogeneous glass formed; (+) glass with crystals.	56
Figure 4·2	A typical XAFS spectrum for; (a) the gallium K-edge and (b) its respective Fourier transform function using the experimental data and the theoretical fit.	62
Figure 4·3	A typical example of a k^3 - weighted EXAFS curve for the GLS thin film (prepared at 3 J cm^{-2} energy density) at the Ga K-edge together with the corresponding Fourier transform. ... - experimental results and — is the best fits to the data.	64
Figure 4·4	A typical example of a k^3 - weighted EXAFS curve for the GLS thin film (prepared at 3 J cm^{-2} energy density) at the S K-edge together with the corresponding Fourier transform. ... - experimental results and — is the best fits to the data.	65
Figure 4·5	A typical example of a k^3 - weighted EXAFS curve for the GLS thin film (prepared at 3 J cm^{-2} energy density) at the La L_{III} - edge together with the corresponding Fourier transform. ... - experimental results and — is the best fits to the data.	66
Figure 4·6	(a) The partial co-ordination numbers obtained from EXAFS data as functions of the energy density in GLS thin film samples. (b) Total Ga and S co-ordinations as functions of the energy density. The solid lines are drawn as a guide to the eye.	68
Figure 4·7	First-shell bond distances for GLS thin film samples prepared at various ablation energy densities. \circ - r_{La-S} , \bullet - r_{Ga-S} , \diamond - r_{S-Ga} .	69
Figure 4·8	The energy density dependence of the mean square deviation in inter-atomic distances, σ^2 , obtained from the EXAFS data for GLS samples. \circ - σ^2_{La-S} , \bullet - σ^2_{Ga-S} , \diamond - σ^2_{S-Ga} .	70
Figure 4·9	Thin films of differing percentages of Ga to La, starting at pure Ga to pure La, on both CaF_2 and BK7 glass pieces.	72
Figure 4·10	Transmission through 1 mm thick glass pieces of both GLS (—) and GNS (—) to compare optical transparency.	75
Figure 4·11	Reflection from thin films of La_2S_3 in a background of O_2 (—), Ga_2S_3 in a background of O_2 (—), La_2O_3 (—) and Ga_2O_3 (—) all grown by pulsed laser ablation with an energy density of $4·0 \text{ J cm}^{-2}$ and Target-Substrate separation of 80 mm.	76
Figure 4·12	Experimental set-up used to record the fluorescence spectra of a Nd^{3+} doped GLS thin film pumped at 488 nm and recorded on an FTIR spectrophotometer.	78

Figure 5-1	The reflectivity from a surface with different refractive index in air. Showing relative intensity of reflected radiation polarisation parallel to plane of incidence, \mathcal{R}_p (—) and perpendicular to the plane of incidence (—) \mathcal{R}_s (Absorption of the material as assumed to be zero).	87
Figure 5-2	Following the schematic of a ray tracing diagram to show the path that the reflected and transmitted components of a laser beam incident on a thin film - substrate combination.	88
Figure 5-3	Two examples of GLS thin films on BK7 glass substrates showing the actual FTIR spectra (—) and the computer 'fit' (—) using the total transmission equation model (Equation 5-12) to find refractive index and film thickness.	90
Figure 5-4	Two examples of GLS thin films on BK7 glass substrates whose thicknesses are measured to compare with the values fitted to the optical transmission as detailed above and shown in Figure 5-3.	91
Figure 5-5	An example of the variation of GLS thin film refractive index with wavenumber, for the thick sample shown in Figure 5-3.	92
Figure 5-6	Graphical representation of the data in Table 5-3. (•) oxygen and (◊) argon gas data points with the respective coloured best fit line as a guide to the eye.	95
Figure 5-7	GLS film thickness changes rapidly as the parallelism of the target and substrate is removed and the angle between them becomes more obtuse. The films were grown in a background of 10^{-5} mbar of O_2 and 0° refers to a parallel target and substrate orientation.	96
Figure 5-8	(a) Transmission and reflectivity with wavelength for GLS thin film sample, (b) Absorption coefficient spectra deduced from T and R for GLS films prepared at different energy density.	97
Figure 5-9	A typical transmission spectra through a thin GLS film (—), after saturated photomodification (—) and after annealing at 400°C for three hours (—).	99
Figure 5-10	(a) The experimental arrangement used to produce the thickness profile of a thin film layer, (b) a plot of the interference fringes and (c) the averaged data (.....) and the film thickness change (—).	100
Figure 5-11	The electronic waveforms required to drive the laser pulses which work with the 'wobble' target holder to paint the plume and ultimately produce more uniform films across the substrate surface.	102
Figure 5-12	(a) Data from Figure 5-10(c) with the averaged data (.....) and the film thickness change (—) repeated for comparison with, (b) the thin film, only 10% thickness, with optimum width:deviation ratio of 37:25 (see highlight in Table 5-6(b)). The respective thickness changes are indicated for the 55-89 mm uniformity width detailed in the Table.	108
Figure 6-1	The differentials of $\frac{\partial \mathcal{R}_s}{\partial \theta_1}$ and $\frac{\partial \mathcal{R}_p}{\partial \theta_1}$ when n_2 is 1.5 (—), 2.5 (— — —) and 3.5 (· · · · ·).	113
Figure 6-2	'Optimum' polarisation angle as a function of angle of incidence with respect to p plane. The graph is plotted for media of refractive index, n_2 ; 1.5, 2.5, 3.0, 3.5 and 4.0 in air.	113
Figure 6-3	The ratio of the partial differential $\frac{\partial \mathcal{R}_p}{\partial n_2}$ before and after orientation at the angles calculated for Figure 6-2, with values for n_2 at 1.5, 2.5, 3.0, 3.5 and 4.0.	114
Figure 6-4	Reflectivity of a $0.151\ \mu\text{m}$ thin film over a range of refractive indices on a BK7 glass substrate ($n_3=1.51$) at incidence angle: (a) 15° (—), (b) 60° (— — —) and (c) a GLS film ($n_2=2.76$) on an imaginary theoretical substrate (....) for p polarised light.	116
Figure 6-5	The optical layout as a dithered light beam is reflected from a surface, onto a single detector.	117
Figure 6-6	Differential reflectance signal as a photomodified sample of GLS travels through the path of a dithered, polarised laser beam for each respective region of translation.	119
Figure 6-7	Differential reflectance signal from a GLS thin film being photomodified in-situ. One of the dithered spots is positioned in the area being modified whilst the other is in an adjacent area. As the refractive index changes the plot shows both the magnitude and direction of this change.	123
Figure 6-8	GLS photomodified with the various single lines of an Argon ion laser. Over a 30 minute period the same power of each line achieves a different magnitude of refractive index change.	128
Figure 6-9	GLS photomodified with the 458 nm line of an Argon ion laser at differing output power and constant beam diameter, until saturation is reached.	129

Figure 6-10	GLS refractive index as the structure self-relaxes over a two year period. The refractive index is measured on a monthly basis using the fitting technique detailed in Section 5.3.1, refractive index is quoted at one micron.	131
Figure 6-11	GNS photomodified with the various single lines of an Argon ion laser. Over a 6 minute period the same power of each line achieves a different magnitude of refractive index change.	133
Figure 6-12	Comparison of the reflectivity change during in-situ photomodification and the intensity of the argon beam which passes through the GLS sample as it induces the structural change. Transmission can be seen to fall and rise again as the process progresses.	134
Figure 6-13	Comparison of the initial increase in GLS refractive index during in-situ photomodification and the required laser power. Also shown is the best fit line to these data points.	135
Figure 6-14	Comparison of the changes in refractive index from just before the laser is turned off, then 5 and 10 minutes after turn off. This is a bulk sample of GLS and hence has the characteristic increase in refractive index.	137
Figure 6-15	Change in refractive index during photomodification at various Argon Ion laser lines all at same power density on a bulk GLS sample.	137
Figure 6-16	Change in refractive index at various wavelengths during photomodification by an Argon Ion laser in a bulk GLS sample.	139
Figure 6-17	Basic principle of an interferometer used to write gratings into samples of GLS.	142
Figure 6-18	The correct choice of resistor shows how the control signal can move one arm of the interferometer is sensitive to fringe translation.	143
Figure 6-19	The principle of fringe magnification used in our interferometer.	144
Figure 6-20	The experimental arrangement to stabilise the interference fringes used in our interferometer for the potential production of diffraction gratings.	146
Figure 6-21	Fringe detection signal (—) is in phase with the reference mirror driver signal (—).	148
Figure 6-22	Fringes drift approximately 90° out of phase with the reference mirror driver signal (—).	148
Figure 6-23	Fringes drift 180° out of phase with the reference mirror driver signal (—).	148
Figure 6-24	The full system layout combining sample holder and active stabilisation, showing schematic layout of components.	150
Figure 6-25	Grating profile written on the surface of a GLS thin film after different photomodification time periods. The measurement technique can only measure the difference in refractive index so all traces appear to start at 0% and must be viewed relative to each other rather than absolute.	152
Figure 6-26	Grating profile written on the surface of a GLS thin film whilst being stabilised using the technique detailed in this section, and with stabilisation turned off for comparison.	152
Figure 6-27	Intensity profile of a recombined laser beam (—) which if moved across the surface of a photomodifiable thin film by an amount shown (···) as two extreme positions, will cause a resultant photomodified profile normalised and shown here (—). Theoretical intensity for the onset of photomodification is shown to stress this point (— —).	153
Figure 6-28	Grating profile written on the surface of a GLS thin film after photomodification and after being left for 21 months. The measurement technique can only measure the difference in refractive index so traces appear to start at 0% and must be viewed relative to each other rather than absolute.	153
Figure 7-1	The absorption spectra of water used to identify the characteristic fingerprint of the molecules. The dotted markers are at 1.29 µm and 1.47 µm wavelength, referred to in the text.	159
Figure 7-2	A schematic of the logic circuit and respective switch locations to select the amplifier operation of the digital moisture measurement system.	164
Figure 7-3	Schematic of the amplifier stages showing the logic link between them on the digital moisture measurement system.	165

Figure 7-4	(a) The theoretical gain required to reach the target voltage for various amplifier gain clocking speeds, (b) the output voltage after amplification. Four speeds are chosen to show how the output is affected by the amplifier clock rate.	167
Figure 7-5	The results of moisture measurements for a full size red house brick. (a) FTIR reflection spectra after: (—) 'wet', (—) after 2 hours, (—) after 5½ hours, (—) after 13½ hours, (—) after 24 hours, (—) 'dry', (b) The reflection spectra values at 1.3 µm wet (—) and dry (---), at 1.4 µm wet (—) and dry (---), and the difference between them when wet (—) and completely dry, original as new, weight (---), (c) A small scanned area of sample, 'wet' and 'dry' including the average colour for the region in terms of its Red, Green and Blue constituents, (d) frequency of sound emitted as a measure of 'dampness' from a 2 probe "Draper" damp detector, (e) 'dampness' ratio from prototype laser damp detector, (f) Weight of sample as it dries with time (—) and completely dry, original as new, weight (---), (g) The Red, Green and Blue colour values for all sample scans over test period, see (c) above.	171
Figure 7-6	The results of moisture measurements for a square yellow paving slab. (a) FTIR reflection spectra after: (—) 'wet', (—) after 2 hours, (—) after 5½ hours, (—) after 13½ hours, (—) after 24 hours, (—) 'dry', (b) The reflection spectra values at 1.3 µm wet (—) and dry (---), at 1.4 µm wet (—) and dry (---), and the difference between them when wet (—) and completely dry, original as new, weight (---), (c) A small scanned area of sample, 'wet' and 'dry' including the average colour for the region in terms of its Red, Green and Blue constituents, (d) frequency of sound emitted as a measure of 'dampness' from a 2 probe "Draper" damp detector, (e) 'dampness' ratio from prototype laser damp detector, (f) Weight of sample as it dries with time (—) and completely dry, original as new, weight (---), (g) The Red, Green and Blue colour values for all sample scans over test period, see (c) above.	172
Figure 7-7	The results of moisture measurements for 10 mm thick medium density chipboard. (a) FTIR reflection spectra after: (—) 'wet', (—) after 2 hours, (—) after 5½ hours, (—) after 13½ hours, (—) after 24 hours, (—) 'dry', (b) The reflection spectra values at 1.3 µm wet (—) and dry (---), at 1.4 µm wet (—) and dry (---), and the difference between them when wet (—) and completely dry, original as new, weight (---), (c) A small scanned area of sample, 'wet' and 'dry' including the average colour for the region in terms of its Red, Green and Blue constituents, (d) frequency of sound emitted as a measure of 'dampness' from a 2 probe "Draper" damp detector, (e) 'dampness' ratio from prototype laser damp detector, (f) Weight of sample as it dries with time (—) and completely dry, original as new, weight (---), (g) The Red, Green and Blue colour values for all sample scans over test period, see (c) above.	173
Figure 7-8	The results of moisture measurements for an interior dark grey carpet tile. (a) FTIR reflection spectra after: (—) 'wet', (—) after 2 hours, (—) after 5½ hours, (—) after 13½ hours, (—) after 24 hours, (—) 'dry', (b) The reflection spectra values at 1.3 µm wet (—) and dry (---), at 1.4 µm wet (—) and dry (---), and the difference between them when wet (—) and completely dry, original as new, weight (---), (c) A small scanned area of sample, 'wet' and 'dry' including the average colour for the region in terms of its Red, Green and Blue constituents, (d) frequency of sound emitted as a measure of 'dampness' from a 2 probe "Draper" damp detector, (e) 'dampness' ratio from prototype laser damp detector, (f) Weight of sample as it dries with time (—) and completely dry, original as new, weight (---), (g) The Red, Green and Blue colour values for all sample scans over test period, see (c) above.	174
Figure 7-9	The results of moisture measurements for 6 mm thick plywood. (a) FTIR reflection spectra after: (—) 'wet', (—) after 2 hours, (—) after 5½ hours, (—) after 13½ hours, (—) after 24 hours, (—) 'dry', (b) The reflection spectra values at 1.3 µm wet (—) and dry (---), at 1.4 µm wet (—) and dry (---), and the difference between them when wet (—) and completely dry, original as new, weight (---), (c) A small scanned area of sample, 'wet' and 'dry' including the average colour for the region in terms of its Red, Green and Blue constituents, (d) frequency of sound emitted as a measure of 'dampness' from a 2 probe "Draper" damp detector, (e) 'dampness' ratio from prototype laser damp detector, (f) Weight of sample as it dries with time (—) and completely dry, original as new, weight (---), (g) The Red, Green and Blue colour values for all sample scans over test period, see (c) above.	175
Figure 7-10	The results of moisture measurements for 10 mm thick plasterboard. (a) FTIR reflection spectra after: (—) 'wet', (—) after 2 hours, (—) after 5½ hours, (—) after 13½ hours, (—) after 24 hours, (—) 'dry', (b) The reflection spectra values at 1.3 µm wet (—) and dry (---), at 1.4 µm wet (—) and dry (---), and the difference between them when wet (—) and completely dry, original as new, weight (---), (c) A small scanned area of sample, 'wet' and 'dry' including the average colour for the region in terms of its Red, Green and Blue constituents, (d) frequency of sound emitted as a measure of 'dampness' from a 2 probe "Draper" damp detector, (e) 'dampness' ratio from prototype laser damp detector, (f) Weight of sample as it dries with time (—) and completely dry, original as new, weight (---), (g) The Red, Green and Blue colour values for all sample scans over test period, see (c) above.	176

Figure 7·11	The reflection spectra values at 1·3 μm wet (—) and dry (---), at 1·4 μm wet (—) and dry (---), and the difference between them when wet (—) and the completely dry, original as new, weight (---).	177
Figure 7·12	Frequency of sound emitted as a measure of 'dampness' from a standard, traditional 2 probe "Draper" damp detector.	178
Figure 7·13	'Dampness' ratio from prototype laser damp detector.	179
Figure 7·14	Weight of sample as it dries with time (—) and completely dry, original as new, weight (---).	180
Figure 7·15	The Red, Green and Blue colour values for all sample surface scans over the entire test period, see example pictures in Table 7·I. The dotted lines show original 'dry' colours respectively.	181
Figure 7·16	'Dampness' ratio from prototype laser damp detector, (—) brick, (—) paving slab, (—) chipboard, (—) carpet tile, (—) Plywood and (—) plasterboard.	182
Figure 7·17	'Dampness' ratio from prototype laser damp detector, (—) brick, (—) paving slab, (—) chipboard, (—) carpet tile, (—) Plywood and (—) plasterboard. 20 divisions have been marked along ordinate to show accuracy of a 20 bar light emitting diode array as output signal. (a) clay based, (b) woods and (c) synthetic materials.	183

List of Tables

Table 1·1	The Lanthanide elements with their respective atomic number.	4
Table 1·2	Target lasing wavelengths for a selection of rare earth ions with a potential gas sensing application.	7
Table 2·1	Radiative Lifetimes and Laser Cross Sections of various Nd ³⁺ rare earth doped glasses.	19
Table 3·1	Energy-beam vaporisation methods for thin film growth.	39
Table 3·2	Methods used to reduce the undesirable particulate material inherent in PLD.	45
Table 4·1	Comparisons of the two beamline stations at the CLRC Laboratory at Daresbury, used for GLS analysis.	60
Table 4·2	Growth rates and thicknesses of thin films of La ₂ S ₃ , Ga ₂ S ₃ , La ₂ O ₃ and Ga ₂ O ₃ , to ensure that all samples are of equal thickness. All grown at 5 J cm ⁻² and 20 Hz.	76
Table 4·3	List of identified absorption peaks found in thin films of ❶ La ₂ S ₃ , ❷ Ga ₂ S ₃ , ❸ La ₂ O ₃ and ❹ Ga ₂ O ₃ . Second half of the table groups similar bondings.	77
Table 5·1	Physical thickness and refractive index of GLS thin films grown at increasing laser energy density.	92
Table 5·2	GLS thin films grown at increasing pulse repetition rate (constant fluence), in vacuum and for comparison in different background pressures of oxygen. The results show changes in physical thickness and refractive index.	93
Table 5·3	Physical thickness and refractive index of GLS thin films grown in vacuum and, for comparison, in different background pressures of oxygen and argon gases at constant fluence.	94
Table 5·4	The optical band gap for the thin films grown by pulsed laser ablation at different energy densities.	98
Table 5·5	Parameters which are believed to effect the thin film grown uniformity, showing the respective change in values which can be easily achieved, to experimentally find the optimum set of conditions for thin film production.	103
Table 5·6	GLS thin films grown with the various deposition parameters shown in Table 5·5 and rearrangement for providing improved uniformity presented schematically in Figure 5·II.	105
Table 6·1	The characteristics of the materials used for calibration.	121
Table 6·2	PSD output signals for the calibration and test sample interfaces.	121
Table 6·3	GLS thin films grown at increasing energy density, increase in physical thickness with a complementary decrease in refractive index.	125
Table 6·4	GLS thin films grown, some in vacuum and for comparison, some in different background pressures of both oxygen and argon gases. The results show changes in physical thickness and refractive index (samples grown at an energy density of 3·5 J cm ⁻²).	126
Table 6·5	Decrease in refractive index and time taken to reach this saturation for a GLS thin film photomodified at various argon ion laser wavelengths (all at 46 mW).	128
Table 6·6	GLS thin films, refractive index (Δn) and thickness changes due to heating and room light over a two year period. ● cold, ● hot, ● dark and ○ light.	131
Table 7·1	Characteristics of the six materials used to evaluate the feasibility of damp measurement using infrared surface reflections.	168

Acknowledgement

There are so many people that I need to thank for their help and support throughout this work that I feel a complete list would almost need a separate volume. Some deserve nevertheless to be singled out in a vastly edited list:

I wish to thank EPSRC for financial support at the start of this project. They were just one of many other people and organisations that contributed through gifts and employment: J Sainsbury Plc, Protimeter Plc (Fil Dadachanji), Southampton University, Southampton City Council, Lloyds TSB, my parents and Professor Harvey Rutt.

I must thank my parents and brother for their endless love, support and understanding. I promised that one day it would all be over, they just didn't expect it to be such a hard slog. Harvey (my supervisor throughout) guided me as much as he could. I am glad that he had the patience and felt that it was worth the effort. For all that he has done, I will always be grateful.

Thank you Susan (Barrow) for being part of my life from the beginning of this work. Some of the credit for this has to go to you and I hope that my influence on your life means just as much to you. I wish you every happiness and all my love.

Vikkie (Hall), my best friend, played her part perfectly, through initially getting me here in the first place and then being there as often as she could. I hope that I was as useful to you during your thesis as you were to me during my attempt. Unfortunately for you, the rest of my life will need you around just as much!

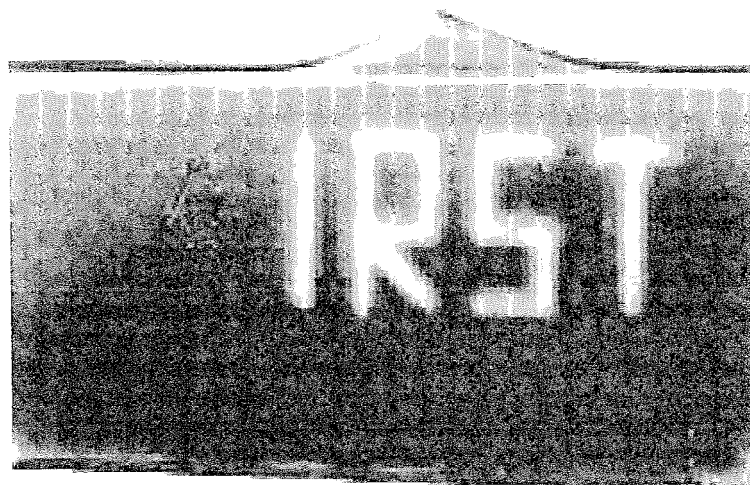
Who better to push me along and keep me moving than the people going through the same challenges. The ones whom understood everything that we were all going through. Colin Mansfield (Dr), Peter Fairley (Dr) and Julian Sarkies (Dr). Well done to you all.

Finally, thank you to David Pointer who not only created Point Source Ltd, but saw potential in a commercially inexperienced me, to give me a chance to further develop and prove myself. This was a priceless opportunity for me and I will always be grateful. This introduced me to Al-Dav (Alan Davis) and Grifter (Leighton Griffiths) who distracted me enough to insist that I joined them on so many nights out. That in itself was an education!

Thanks again to all of you. Now I will try to repay you.

Part 1

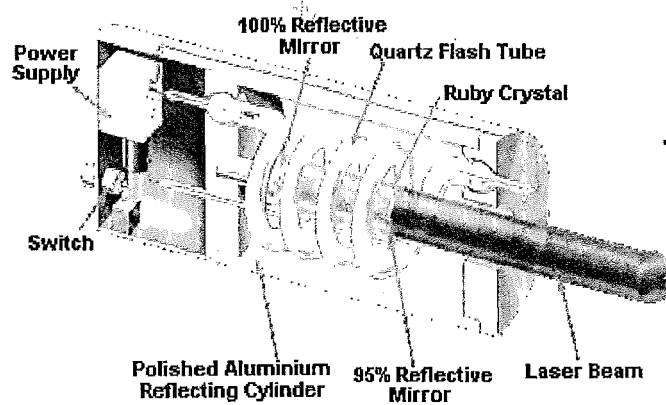
Pulsed Laser Deposition for Potential Infrared Waveguide Devices



A thin film of Gallium-Sodium-Sulphide (GNS) with the Infrared Science & Technology groups initials 'written' by photomodification using an Argon ion laser

1

Introduction to Lasers



Major components of the first Ruby laser.

1-1

The Beginning of the Laser

1-2

The Rare Earths

1-3

The need for Infrared Optical Materials

1-4

Low Phonon Energy Hosts

1.1 The Beginning of the Laser

In 1917 Einstein predicted stimulated emission using thermodynamic arguments based on Planck's explanation of the standard continuous spectrum emitted at a definite temperature by an opaque object ("black body"), accepting the idea of photons, but not involving any hypothesis about the electronic structure.

A laser is a device that amplifies optical radiation by stimulated emission to create coherent, monochromatic light. The present day understanding was first suggested by Townes^[1] and demonstrated by his research group for microwave radiation^[2] originally given the acronym maser. Six years later Maiman showed that it could also work with optical radiation (694.3 nm) using ruby as the gain medium^[3, 4] and another year on this was halved (usually referred to by its reciprocal: frequency doubled) into the ultraviolet^[5] making it the first non-linear optical experiment. At about the same time, the first fibre laser was demonstrated^[6]. Ever since these discoveries, other materials and wavelengths have been researched, making it a very active and still developing technology.

A laser consists of an optical material containing, usually, laser active ions inside a resonator, which simplistically consists of two appropriate reflectors. The medium is pumped: optically for most glass and crystal lasers, although there are numerous other methods depending on the laser material in use (e.g. electrical field, electrons or ions, radio/microwave and chemical). When the laser medium is excited, spontaneous radiation is emitted, which is amplified by causing stimulated emission. In the resonator discrete wavelengths of the radiation form standing waves, the different profiles in which these standing waves oscillate in a particular resonator are called modes. The optical resonator provides feedback for many of the modes but stimulated emission amplifies a few, meaning that a considerable amount of energy is put into the selected modes. This concentration of energy results in the characteristically great coherence of laser radiation.

The advantages of diode pumped solid state lasers were recognised by Newman^[7] shortly after the demonstration of the first diode laser. In 1964 Keyes *et al.*^[8] demonstrated the first diode pumped solid state laser, $\text{U}^{3+}:\text{CaF}_2$ pumped by five GaAs diode lasers and this method was extended to Nd:YAG in 1971 by Ostermayer^[9]. The promise of efficient, high average power, diode pumped solid state lasers began to be realised when Scifres *et al.*^[10] in 1978 produced the first linear multi-stripe diode array. This opened the door to compact solid state laser systems and partly explains the explosion in new laser materials based on rare earth ions.

From drilling micron sized holes^[11] to accurate alignment for boring tunnels under the English channel, from entertainment to detecting antique forgeries^[12] the research groups of

the mid 50's and early 60's could not have imagined how diverse our application and need for lasers would become.

1.2 The Rare Earths

By definition the rare earths are the sesquioxides M_2O_3 , where M represents the seventeen elements now known to have the atomic numbers 21, 39 and from 57 to 71. The individual metallic elements have been readily available, since about 1950, and are themselves often loosely referred to as "rare earths". Most of them belong to the group classed as the Lanthanides (Table 1.1), from lanthanum to lutetium in the Periodic Table, they are rather similar to the transition metals in that an "inner" sub-shell (4f) is being filled after an "outer" sub-shell (6s). The "rare earths" are not especially rare; of the average crust 120 ppm are lanthanides and 0.15 percent of the Earth's crust consists of the elements with Z above 30. It is mainly for historical reasons that scandium is called a rare earth, since Nilson (1879) found it in erbium-ytterbium concentrates. The trivalent ionisation state is the most stable for the rare earth ions, it is formed by the removal of two outer 6s and one inner 4f electron.

57	58	59	60	61	62	63	64	65	66	67	68	69	70	71
La	Ce	Pr	Nd	Pm	Sm	Eu	Gd	Tb	Dy	Ho	Er	Tm	Yb	Lu

Table 1.1. The Lanthanide elements with their respective atomic number.

Rare earth ions (RE) have a long history of optical and magnetic applications. They can be easily incorporated into many glasses; so these systems represent in principle an interesting area of research. It was noticed quite early that in glasses, as might be expected, the most prominent feature of the RE crystal spectra, the extreme sharpness of the optical lines, vanishes. Therefore, RE ions in glasses were not studied for some time. When it was later realised that RE's in glasses could be used as laser materials, a number of investigations into their spectra and fluorescence properties were undertaken^[13, 14]. In general, the spectral lines are found to be broad compared to crystals and therefore not practical for a study of glass properties; however, the transition rates and lifetimes are also similar to those found in crystalline hosts.

Fluorescence measurements have been made on all of the rare earth trivalent ions with the potential for laser action, Ce^{3+} , Pr^{3+} , Nd^{3+} , Pm^{3+} , Sm^{3+} , Eu^{3+} , Gd^{3+} , Tb^{3+} , Dy^{3+} , Ho^{3+} , Er^{3+} , Tm^{3+} , Yb^{3+} and Lu^{3+} ^[15-25]. Trivalent rare earth ions in hosts have a number of features which

make them attractive for use in lasers; the most important of which are their narrow absorption (and emission) lines. The main drawback of trivalent rare earth ions is that they have small absorption cross sections, that is, they absorb only in narrow lines. The problem has been alleviated since the introduction of the diode laser, we now have narrow wavelength pump sources to suit the ions.

A pump wavelength can be absorbed by the ground state of an atom. This excited atom can now decay to an intermediate state by the emission of either a photon or phonon. Then finally another emission occurs returning the atom to its original ground state. Such a process in a laser medium is called a "three level" laser. Some RE doped laser mediums can be made to act as a "four level" system: this is the term given to laser materials which can be pumped to an excited state, in turn decaying rapidly to a metastable state. The lasing transition proceeds from this metastable state to yet another, lower, excited state. Finally the atom returns to its ground state by a rapid, usually nonradiative, decay. The advantage of a four level system is that an atom in its ground state is unable to absorb the emitted photons from other excited atoms directly, hence not reabsorbing the photons emitted by neighbouring ions. It is also easier to create a population inversion when there is low lower level (electron) population.

1.3 The need for Infrared Optical Materials

1.3.1 The Infrared

The infrared is split into the three regions for which there is no general agreement on the names of the various subsections: The near infrared (NIR) follows on from the visible, starting at 0.75 μm . The longer wavelength limit is taken as 3 μm , with detectors for the longer wavelengths of this region being different to those used in the visible. Most of the other technology is similar in that ordinary glass is transparent and thermal emission is negligible.

From 3 μm the mid infrared region begins (MIR) and most physicists and chemists consider it to continue to between 20 and 50 μm . It contains the characteristic vibrational spectrum of many molecules so is sometimes called the 'fingerprint' region (most commonly defined as 2.5 to 25 μm).

Logically the final region, up to 1 mm, is known as far infrared (FIR) beyond which millimetre waves and microwave waveguide technologies take over. Thermal emission at room temperature is dominant in the mid- and far-IR, peaking at 10 μm . There are few transparent materials, water vapour and carbon dioxide in the atmosphere absorb and poor,

usually cryogenic detectors are needed. Combined with the lack of tuneable sources this is a difficult region to operate within.

1.3.2 Temperature Sensing

It is fortunate that the two most common gases in the atmosphere, nitrogen and oxygen are homonuclear diatomic molecules and possess neither a permanent nor an induced dipole moment, hence they do not exhibit infrared active molecular vibrations which would result in the absorption of infrared radiation. In the initial region of the infrared spectrum from 0.75 μm to 14.0 μm the absorptions of the minor atmospheric constituents, water vapour and carbon dioxide result in three main 'windows' in the atmosphere, one from 0.75 μm to 2.5 μm , another from 3.0 μm to 5.0 μm and a third from 7.5 μm to 14.0 μm . From the black body spectral emittance curves shown in Figure 1.1 it is clear that to detect relatively hot objects the 3.0 μm to 5.0 μm window is most suitable and to detect objects at room temperature the 7.5 μm to 14.0 μm window is most suitable. There is a major interest in thermal surveillance systems at present and these practical uses of infrared radiation are concerned with wavelengths up to about 12.0 μm . In order to focus this infrared radiation onto detection systems, windows, lenses and telescopes are required made from materials exhibiting adequate transmission in this wavelength region. Generally the requirements for infrared transmitting materials are set primarily by the black body curve and secondarily by the atmospheric transmission range, the detectors and by the signal levels and bandwidth requirements of particular systems.

1.3.3 Applications of 2 - 5 μm Lasers

The xenon-helium laser operates between 2.6 to 4 μm , CO laser around 5 and 6 μm and the chemical lasers based on DF, HF and HBr all have transitions in the second window. The only solid state commercially available laser to operate close to this range (2.94 μm) is the Er:YAG pulsed laser. Water absorbs this erbium line far better than the 10.6 μm (CO₂) line presently more common in medical applications. Changing to the erbium system would leave a thinner damaged layer between healthy tissue and the area removed by surgery. Here the water absorption is so strong that it could also be used to cut bone (so would include dentistry). The military require eye-safe laser range finders and target designators for training exercises between 1.4 μm , where dangers of retinal damage drop and 2.2 μm where the eye becomes sensitive to corneal burns^[26]. There is a lack of compact, CW solid state lasers which can operate effectively within the above region and this has sparked research into materials suitable as laser mediums for practical systems.

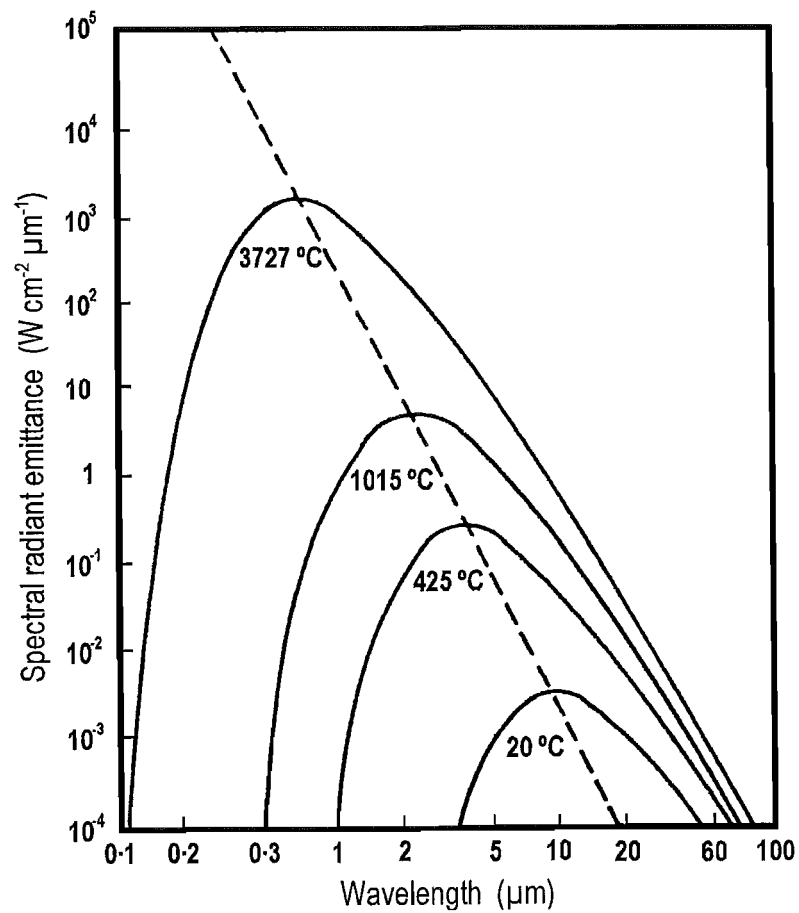


Figure 1.1. Black body spectral emittance curves against temperature. Reproduced from Savage [27].

Wavelength achievable (μm)	Source	Compound detectable	Target wavelength (μm)
3.3 → 3.5	praseodymium	hydrocarbons nitric oxide	3.39 3.44
3.6 → 3.8	erbium	hydrogen sulphide	3.73 → 3.83
3.8 → 4.0	holmium	nitric oxide sulphur dioxide	3.81 3.68 → 4.0
4.1 → 4.5	dysprosium	carbon dioxide	4.26
4.8 → 5.0	praseodymium	carbon monoxide	4.67

Table 1.2. Target lasing wavelengths for a selection of rare earth ions with a potential gas sensing application.

New laser sources operating at specific wavelengths in the 3 to 5 μm region can easily identify trace amounts of toxic or undesirable gases. By measuring the amount of light absorbed when a laser beam travels through a sample we can quantify the amounts of such gases present in a given volume. The 3.9 μm emission from Ho^{3+} is an ideal wavelength for atmospheric transmission. Diode pumped rare earth doped waveguide lasers would offer compact and efficient alternatives to either relatively weak, or very complex MIR sources currently available, such as thermal emitters, gas lasers, or semiconductor lasers.

1.4 Low Phonon Energy Hosts

Materials with phonon energies less than $\sim 500 \text{ cm}^{-1}$ are classed as “low phonon energy” materials. An excited atom will relax with the loss of some energy either radiatively (photon emitted) or nonradiatively (phonons produced). Transitions with energies above the “phonon energy” of the material are statistically more likely to relax with a mechanical loss to the surrounding atoms, as lattice vibrations (heat). In crystalline materials these vibrations are well defined, the quantised phonons characterise the phonon spectrum of the material. In contrast, there is a spread of values in amorphous systems due to the lack of ordered structure. In both cases the largest phonon value present is referred to as the “phonon energy” of the material. If phonon emission is the preferential relaxational route for a material intended to be used as a laser host, photon emission will be drastically reduced and hence is detrimental. By moving to materials with lower phonon energies, the probability of nonradiative relaxation can be decreased, improving the potential for lasing action.

The phonons in an amorphous material are quantised excitations of a known energy and the interaction with the constituent atoms will be similar to those in a crystal. If the electronic states are closely spaced, rapid transitions will occur between them, involving only one or two phonons, leading to the rapid thermal population of energy levels above the ground state or excited state for energies of a few kT (where k is the Boltzmann's constant and T is absolute temperature). The gaps between energy levels are in general considerably larger than kT and require several phonons to bridge them in order to conserve energy. The extent to which an excited state is depopulated by phonon emission governs the efficiency of luminescent processes originating from that state.

The analysis of multiphonon processes^[28] requires high order perturbation theory and since the decay rate decreases rapidly as the order (number of phonons) of the process increases, the highest energy phonons of the host material give the largest contribution to the process. Hence, nonradiative rates are lower in materials which only support low energy phonon

modes. The rate is found to be almost insensitive to both rare earth ion and the electronic state involved^[29].

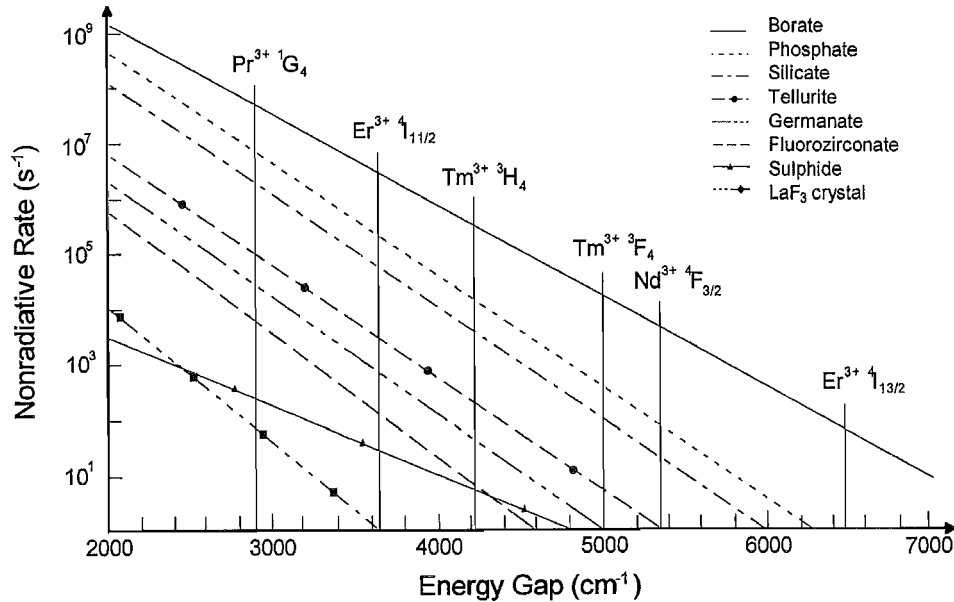


Figure 1-2. Nonradiative relaxation rates of RE in different hosts. Reproduced from Dignonet [28]. {Original in colour}

The probability of an excited state decaying nonradiatively by multiphonon emission decreases exponentially with the increasing energy of the transition. The nonradiative emission rate, ω_{nr} , of a particular transition is found to obey the expression^[30],

$$\omega_{nr} = C[n(T) + 1]^p e^{-\alpha \Delta E} \quad \dots \quad (1.1)$$

where C and α are host dependent parameters, p is the number of photons required to bridge the gap, ΔE (i.e. the order of the process) and $n(T)$ is the Bose-Einstein equation, giving the number of phonon modes of energy $\hbar\omega$ at temperature T :

$$n(T) = \frac{1}{\exp\left(\frac{\hbar\omega}{kT}\right) - 1} \quad \dots \quad (1.2)$$

Therefore the depopulation rate increases at higher temperatures. Figure 1-2 shows the nonradiative relaxation rate across a range of $4f$ energy gaps at room temperature, for hosts with different maximum phonon energies. Oxide containing hosts exhibit the highest nonradiative rates due to their strong covalent bonds, giving rise to higher phonon energies. Halide containing hosts are mainly ionic with much weaker bonds and thus have lower

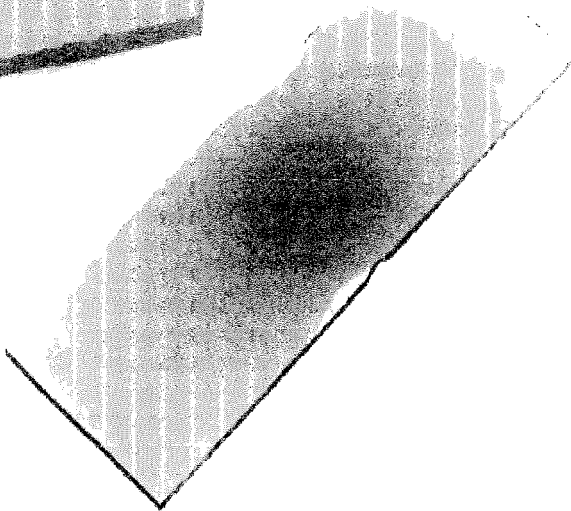
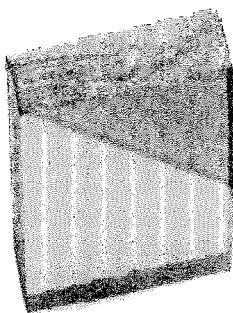
phonon energies. A rough approximation that is often used to judge the phonon energy E_p , or the infrared cut-off E_c of the host is,

$$E_p = \frac{E_c}{3} \dots\dots\dots (1.3)$$

This arises as significant infrared absorptions exist due to overtones of the fundamental absorption, however these become progressively weaker and beyond the third overtone are extremely small. This is one of the advantages of using $\text{Ga}_2\text{S}_3\text{-La}_2\text{S}_3$ (GLS) glasses as a laser host, it is classed as a low phonon energy material with transmission up to around $8\text{ }\mu\text{m}$ giving a phonon energy of around 420 cm^{-1} and because of the lanthanum content, can easily be doped with other rare earth trivalent ions. Rare earth chalcogenide glasses in general, can have phonon energies of as low as 200 cm^{-1} . If we compare this to the maximum phonon energy of about 1010 cm^{-1} in silicate glass, we may expect the nonradiative relaxation in the chalcogenide glasses to be much lower than in silicate glass and emission from levels, which usually relax nonradiatively in the oxide glass, will be observed in the chalcogenides.

2

Chalcogenide Glasses



2-1

Introduction

2-2

Other Attributes of Chalcogenide Glasses

2-3

Chalcogenide Glass Systems

2-4

Doping Chalcogenides

2-5

Photoinduced Effects

A typical sample of bulk GaLaS and a thin film deposited by Pulsed Laser Deposition onto a glass microscope slide.

2.1 Introduction

Glasses have been made for over 4000 years and for most of that time the vitreous state was considered to be prerogative of oxygen based compounds. Even in the late 1800's when vitreous selenium, arsenic sulphide and selenide were discovered^[31], glasses based on these materials still did not attract investigators' attention. From the 1950's, with the requirement for IR optics, it became necessary to produce new IR transparent materials, so investigations began looking at these materials again, both pure and with additions of other chalcogenides^[32-35]. In 1957 the American "Servo Corporation" began to advertise vitreous As_2S_3 as a commercial material: servofrax^[36]. Historically, the term 'glass' has been applied to materials exhibiting a meta-stable state, whereas the term 'amorphous' only designates a state characterised by an atomic arrangement which lacks long range order.

Although many optical crystals are known, glasses are the principal material used in the majority of optical systems. The technology of manufacture is comparatively easy, they are lower in cost and can be produced in larger quantities. Most importantly glasses can be produced with a broad variety of compositions and consequently of optical properties.

Silicates, borates and phosphates are only transparent in the near infrared range, with glasses based on germanium dioxide transmitting into the mid infrared, up to 6 μm . This is the transparency limit for the oxygen containing glasses because the third overtone of the vibrational frequency of oxygen bonds with any other element in the periodic table approximates this value.

The absorption edge for glasses in the infrared is determined by the frequency of vibration of cation-anion bonds. Because of the disordered structure of glasses, this frequency cannot be calculated with any accuracy. However, an estimate can be made from the relationship for two bodies of given masses m_1 and m_2 , vibrating with an elastic restoring force of given force constant, k , which is an indication of bond strength:

$$\nu = \frac{1}{2\pi} \sqrt{\frac{k(m_1+m_2)}{m_1m_2}} \dots\dots\dots (2.1)$$

The fundamental absorption frequency of a diatomic molecule consisting of two point masses can thus be calculated. When this diatomic molecule is placed within a glass structure, the influence of all the other constituents in the structure perturb the calculated frequency. Bond strengths and bond lengths vary depending on the glass constitution. However, a very rough approximation of influence of network-forming constituents on the infrared absorption edge can be made from field strength, Z/r^2 , where Z is ionic charge and

r is the crystal ionic radius. In devising glasses that transmit in the infrared, the general rule is that anions and cations with lower field strengths will move the optical transmittance of the material to longer wavelengths. Unfortunately, lower field strengths and weaker chemical bonding also limit the available compositions that form glasses. Physical and chemical properties also become poorer with weaker bonding.

Chalcogenides are compounds whose anions belong to group VI of the Period Table i.e. oxygen, sulphur, selenium, tellurium and polonium. In vitreous systems, the term chalcogenide is routinely used to distinguish sulphide, selenide and telluride glasses from the oxide glasses. Polonium has no stable isotopes so is omitted from the chalcogenide classification. Figure 2.1 shows the transmission characteristics of some oxide and non-oxide glasses [37]. In contrast to the oxides, chalcogenide glasses clearly display long wavelength transmission characteristics, a property of low phonon energy materials.

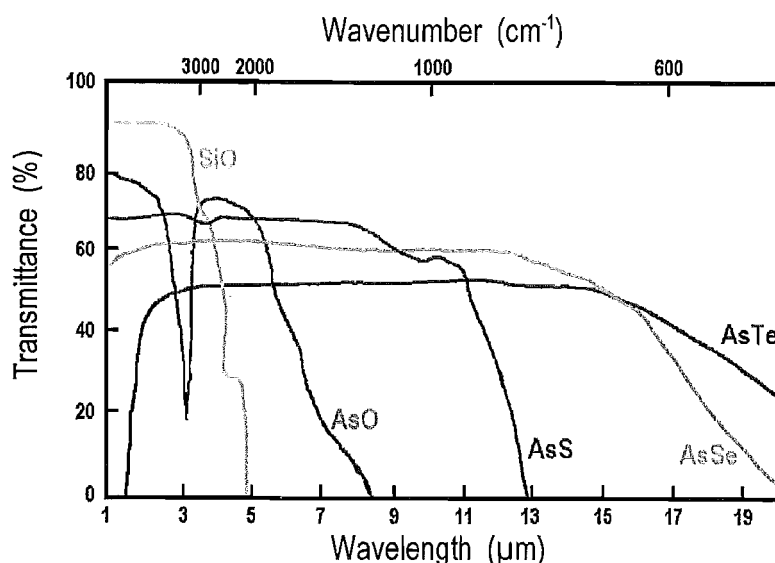


Figure 2.1. Infrared transmission cut-off for some oxide and chalcogenide glasses at ~ 2 mm thick [38]. {Original in colour}

Glasses based on fluorine compounds with heavy metals have been studied in recent years, but their high crystallisation tendency poses problems for industrial manufacturing. Thus, along side ZBLAN, chalcogenide glasses still represent the only true commercial vitreous material transparent in the mid infrared range.

2.2 Other Attributes of Chalcogenide Glasses

Modulation methods based on the acousto-optical effect involve the change of the refractive index of a substance under the influence of mechanical stresses [39, 40]. Such materials have

uses as acoustically controlled modulators and deflectors for example. The effect occurs when an ultrasonic wave is passed through a material, causing variations in refractive index to give an effective acoustic diffraction grating within the glass.

The thermo-optical effect in chalcogenides relates to an index change due to heating and because of this it is the slowest response of the optically induced effects. It has also been used to measure the thickness of thin films^[41]. In chalcogenide materials a photoinduced effect, photo-modification, also exists using photons to produce index changes. This will be discussed further in Section 2.5 and chapters 5 and 6 in much more detail.

In 1956 semiconductor properties were first discovered in a chalcogenide glass during research into the system $\text{Ti}_2\text{Sb}_2\text{Se}_4$ ^[42]. Chalcogenide glasses can be either p- or n-type semiconductors depending on composition^[43], most are p-type and according to Sadeek and Fadel, their electrical conductivity's are usually insensitive to added impurities^[44].

Lanthanum based chalcogenide glasses are mainly covalently bonded materials with room temperature resistivities between 10^8 and $10^{11} \Omega \text{ cm}$ ^[45]. There also exists a time dependent electric relaxational processes and it has been shown that current flow in As_2S_3 samples (at fixed voltage) decreases with time to a constant residual current^[46]. The phenomenon is named "high-voltage polarisation" and is probably due to a movement, redistribution and capture of electrical charges inside or in the electrode regions. After the external electrical field is switched off, a reverse depolarisation current appears and decreases slowly to zero. The electronic properties of the glasses arise from changes in the electrical conductivity, at a specific voltage, some chalcogenide glasses have been seen to undergo structural change and the glasses "switch" to a higher conduction state. This change in conduction can be several orders of magnitude and is useful in switching circuit devices^[47]. If the structural change is irreversible, crystallisation would occur causing memory switching. These off and on states of memory switching were demonstrated on the Ge-As-Se system^[48]. This shows the potential of these materials when combined with photomodification and its mask-less lithography.

2.3 Chalcogenide Glass Systems

2.3.1 Common Properties

The first goal in devising a useful composition is to form a stable glass and then find the best combination of infrared transmission and other key properties^[49, 50]. The advantage of chalcogenide glasses is that they have the best IR transmission of any vitreous system that can be formed into large pieces. It is possible to modify the structure and refractive index of

the glasses just by illuminating them with the correct laser wavelength and power density (see section 2.5).

The disadvantages of chalcogenide glasses are: Difficulty of manufacture; oxygen contamination is a serious problem because it is very difficult to eliminate and it seriously damages IR transmission. Poor visible transmission; sulphide glasses are usually dark red, selenides and tellurides are opaque. Poor physical properties; expansion coefficients are very high, therefore thermal shock resistance is also poor. Mechanical hardness is low. They sag at relatively low temperatures compared to oxide glasses. Finally they have poor chemical properties; for example arsenic trisulphide dissolves above pH6, shows appreciable swelling below pH6 and is hygroscopic^[38].

Most of the early work on amorphous chalcogenide materials, concentrated on the arsenic and germanium based sulphide and selenide glass compositions. However all these have low devitrification temperatures so that manufacture of the glass by quenching is difficult. Ga-La-S is easier to prepare because it is more thermally stable with a transition temperature, T_g , of typically $\approx 600\text{ }^{\circ}\text{C}$ ($50\text{ }^{\circ}\text{C}$ above the crystallisation temperature, T_c)^[51]. Also it does not suffer from toxicity risks, a factor associated with the more popular chalcogenide material, As_2S_3 .

2.3.2 Sulphide Glasses

These materials are thermally stable with high melting points and are mechanically strong with moderate expansion coefficients (compared to the other chalcogenides). The rare earth sulphides (La to Er) are not glass formers but form reasonably stable glasses when mixed with other glass-forming sulphides such as gallium, germanium and arsenic sulphides^[51]. Glasses containing several rare earth sulphides with gallium sulphide and aluminium sulphide are known to exist. While most of these glasses are stable with high glass transition and crystallisation temperatures, the glasses based on aluminium sulphide are hygroscopic. The gallium-sulphide based glasses transmit very well into the infrared with a transmission cut-off at $\sim 10\text{ }\mu\text{m}$ ^[52].

Gallium sulphide by itself is not an easy glass former. However, additions of Ga_2S_3 to other sulphide compounds results in glasses quite easily^[51]. Extensive experiments carried out by French researchers^[50-53] have shown that Ga_2S_3 forms glasses with a majority of sulphides from the lanthanide series with the exception of thulium, ytterbium and lutetium. In the case of europium (Eu), two glass forming regions have been reported with the monosulphide of europium. Lanthanum sulphide, La_2S_3 shows the largest glass forming region.

Al_2S_3 glasses can be formed with most of the rare earth sulphides with the exception of europium and terbium and the glass forming domain is again largest for La_2S_3 . The glass forming region has been reported to extend from 63 \Rightarrow 82 mol% Al_2S_3 [30]. These glasses transmit partially in the visible and into the infrared exhibiting a transmission cut-off at around 6 μm . They show good thermal stability with glass transition temperature of 540 \Rightarrow 560 $^\circ\text{C}$ and crystallisation temperatures of 660 \Rightarrow 680 $^\circ\text{C}$ for compositions corresponding to 88 \Rightarrow 75 mol% Al_2S_3 , respectively. Since the glasses are not chemically stable, their use is limited.

Glasses in the system Ge-La-S have been synthesised by mixing GeS_2 with La_2S_3 . The glass forming domain for these materials extend from 60 \Rightarrow 100 mol% GeS_2 . Their colour varies from ruby red to brown, with compositions richer in GeS_2 tending to be dark brown. In the late eighties calcium lanthanum sulphide (CaLa_2S_4) materials were developed [45, 54] having similar properties to zinc sulphide (ZnS), for example, transmission to 11.5 μm is slightly better than the 10 μm of the zinc sulphide.

Arsenic trisulphide, As_2S_3 , is the best known of the sulphide glasses. It is one of the most thoroughly investigated chalcogenide glass compositions and is a highly stable glass former. I will return to this material through many comparisons with my work in the following sections and chapters. Other sulphide examples include: Ge-P-S [55], As-Ge-S [56], Ge-Ga-S [57], Ge-Bi-S [43], and Sb-S [58].

2.3.3 Selenide Glasses

Selenium and its compounds in thin film form have been used in the photocopying industry and this glass must be regarded as the most important chalcogenide in terms of current commercial exploitation. However, because of its poor general physical properties it was found unsuitable for many bulk optical applications. It is particularly important that the thermal and mechanical properties are improved without degradation of the infrared cut-off limit.

Selenide glasses transmit further into the infrared, have higher refractive indices, densities and have lower thermal expansions, than the sulphides for analogous compositions. The systems in which most research has been concentrated are Ge-Sb-Se [27] and As-Ge-Se [59]. Of all the chalcogenide glasses, selenide systems provide glasses with the a good combination of IR transmission, formability and acceptable (not ideal) physical and chemical properties. Other researched examples include Si-Sb-Se [60], Ge-Bi-Se [44], P-Ge-Se [61] and Pb-Cd-Se [62].

2.3.4 Telluride Glasses

While telluride glasses have best IR transmission range (out to $\sim 20\text{ }\mu\text{m}$ ^[63]) their stability and formability are poorer than for the sulphides and selenides. The largest glass-forming region has been found in the Si-As-Te^[60] system, but silicon is difficult to incorporate into the melts because of its high melting point, making the glass difficult to produce and homogenise. Impurities mean that there are two absorption bands at 10 and 14 μm that impair the infrared transmission. While the Ge-As-Te glass-forming area is smaller, these glasses do have the IR transmission predicted for the tellurides. Of the chalcogenide glasses, the tellurides are least effected by oxide impurity due to limited solubility of oxide in telluride melts. Other examples include Hg-Cd-Te^[64], Ge-Bi-Te^[44], Ge-S-Se-Te^[65] and Cd-Te^[66].

2.3.5 Adding Oxides to the Melt

Of all glass systems, silicate glasses have, by far, the largest compositional area, providing very stable glasses with good physical and chemical properties. Unfortunately the IR absorption edge extends only to between 4 and 5 μm , being limited by the first overtone of the fundamental Si-O-Si stretching vibration at 9.1 μm (1100 cm^{-1}).

An interesting feature of Ga_2S_3 is that its glass formation behaviour is not limited to other sulphides, but is also observed with some oxides. From this point of view, glasses have been formed with lanthanum sulphide, oxysulphide and oxide. Of the two ternary systems La_2O_3 - La_2S_3 - Ga_2S_3 and La_2O_3 - Ga_2S_3 - Ga_2O_3 , a glass region is not observed in the latter and we may conclude that a relatively high proportion of sulphur is necessary for the formation of gallium rare earth glasses^[51]. With rare earth oxysulphides and oxides no glasses are obtained after neodymium sulphide addition.

An extended region of glass formation has been observed in the gallium-lanthanum-oxysulphide (La_2S_3 - La_2O_3 - Ga_2S_3) system, towards the lanthanum rich area. The system comprising $\text{La}_2\text{O}_2\text{S}$ and Ga_2S_3 has been investigated with regard to glass formation by Flahaut *et al.*^[51], they can be obtained in the composition range roughly extending from 60 \Rightarrow 80 mol%, Ga_2S_3 . Glass forming domains have been shown to exist for glasses containing oxysulphides of Ce, Pr and Nd^[51]. The glasses are typically obtained by quenching, following the conventional technique described in section 5.2. For lanthanum oxysulphide - gallium sulphide glasses^[67] it is not possible to heat the samples at such high temperatures because the partial reaction of the sulphide and oxide causes the evolution of sulphur dioxide, which causes the sealed ampoule to explode, an open ampoule would require a sophisticated extraction system to remove the toxic gasses being emitted and would effect stoichiometry of the melt. The highest, stable temperature of the molten mixture is about

1100 °C. For lanthanum oxide - gallium sulphide glasses, the same difficulty is present with similar consequences.

The glasses show much better chemical stability and are more resistant to atmospheric moisture attack compared to the corresponding sulphides. They also exhibit reasonably good thermal stability, similar to the gallium sulphide based rare earth glasses and show glass transition temperatures around 600 °C which shows a decreasing trend with increasing Ga₂S₃ content.

Even a very small quantity of oxygen in the GLS mix would be highly detrimental to the properties of the glass that we would like to use, mainly the infrared transmission range and the low phonon energy. Because laser ablation can use pure chalcogenides as the target material and can be performed in very high vacuum, oxygen can be avoided. Producing a glass outside of this environment makes it far more difficult to avoid oxygen from entering the mix.

2.3.6 Halides

To insert the elements of the VII group - namely, fluorine, iodine, bromine and chlorine - into chalcogenide glasses, should retain good transparency in the infrared, high chemical stability and high refractive index. These atoms are similar in size to the chalcogenide group. Such combination of halogen containing glasses' provides new material properties and possible applications of chalcogenide materials. Since both halides and chalcogenides are transparent in the infrared region, it is of interest to know if mixtures of these glasses are also IR-transmitting.

The investigation of chalcahalides began in the 1960's with the system As-S-I. Pearson and his colleagues were the first to demonstrate that the addition of iodine reduces the softening temperature^[68]. Lin and Ho studied the compositional influence upon chemical resistance of such glasses and established that iodine reduces it^[69]. The glasses do not suffer attack from moisture and acid solutions, but like other chalcogenide glasses, they are dissolved by alkalis.

Chalcahalide glasses are becoming an important class of materials for optoelectronic applications because of their high transparency in the mid IR-region up to ~ 10 µm. While the bonds in chalcogenide glasses are predominantly covalent, in halides they are mainly ionic. In practice, combination of glasses containing both chalcogen and halogen elements can improve some of the weaknesses associated with the individual materials. On the one hand chalcogenide glasses have relatively high refractive indexes but halide glasses exhibit relatively poor chemical durability and low glass transition temperature. Examples include

As-Te-I^[70], Ge-S-I^[71] and La-Ga-S-Cl-Cs^[72, 73]. Unfortunately, the technical applications for most of them have been limited due to having poorer thermal properties than the individual chalcogenides and halides.

2.4 Doping Chalcogenides

Radiative and nonradiative transition probabilities of the rare earth ions in various host media have raised great interest^[14]. The electronic levels of Er³⁺ are well established and is the most suitable ion for study of the multiphonon relaxation in oxide glasses^[74]. In such glasses the multiphonon transition rates of the RE are independent of the coupling between a given oxide glass and rare earth ion^[14], but dependent exponentially on the phonons bridging the emitting and next lower level. Because of their low phonon energy and high refractive index, the RE doped chalcogenide glasses form a new type of fluorescent material^[75]. It has been found that Er is not so readily incorporated in the As₂S₃ network as in the case of some other chalcogenide glasses^[76, 77], since it contains residual Er₂S₃ crystallites. A high solubility of RE ion is not required for a glass to support a lasing ion (typically 0.1→1%), but dispersion of the ions in the glass matrix is necessary to reduce cross-quenching. In addition to the optical properties, glasses containing rare earths tend to be more refractory than their counterparts that do not contain rare earths. The increase can have positive advantages in the chalcogenide system where small difference between glass transition temperature (T_g) and the crystallisation temperature (T_c) can inhibit the practical workability of the glass.

Glass	Wavelength (nm)	Stimulated emission cross section (pm ²)	Radiative lifetime (μs)
Oxides			
Silicate	1057 - 1088	0.9 - 3.6	170 - 1090
Phosphate	1052 - 1057	2.0 - 4.8	280 - 530
Borate	1054 - 1062	2.1 - 3.2	270 - 450
Halides			
Fluoroberyllate	1046 - 1050	1.6 - 4.0	460 - 1030
Fluorozirconate	1049	2.9 - 3.0	430 - 450
Chlorine	1062 - 1064	6.0 - 6.3	180 - 220
Oxyhalides			
Fluorophosphate	1049 - 1056	2.2 - 4.3	310 - 570
Chlorophosphate	1055	5.2 - 5.4	290 - 300
Rare earth chalcogenides			
GaS-LaS	1075 - 1077	7.9	100
AlS-LaS	1075 - 1077	8.2	100
Rare earth oxysulphides			
GdOS-GaS	1075	4.2	92

Table 2.1. Radiative Lifetimes and Laser Cross Sections of various Nd³⁺ rare earth doped glasses^[78].

The nonradiative relaxation rate in the chalcogenide glasses is much lower than in silicate glass^[13]. This phenomenon was studied with Er^{3+} in the As_2S_3 chalcogenide glass^[76, 77] and in lanthanum glasses doped with Nd^{3+} ^[76, 79], Er^{3+} ^[77, 36] and Ho^{3+} ^[59, 75]. Some of the lanthanum sites are easily filled by another rare earth ion dopant since they are closely related in physical size and properties.

Some of the fluorescent properties of glasses doped with Nd^{3+} are shown in Table 2.1 for comparison. The stimulated emission cross-sections and radiative life times at wavelengths around 1077 nm are given for two chalcogenide glasses alongside values for other oxide, oxysulphide, oxyhalides and halides. The cross-sections are larger and the radiative lifetimes smaller than those reported for the oxide, oxyhalides and halide glasses. These properties, therefore, make these rare earth glasses doped with Nd^{3+} good candidates for laser application^[78]. In conclusion, fluorescence in rare earth chalcogenide glasses has very interesting features: the fluorescence of rare earth ions are of higher intensity than in oxide glasses and additional wavelength peaks appear. These facts are promising for other rare earth ions. Nd is not the most desired RE ion for chalcogenide glasses as shown earlier in Table 1.2. The 1.06 μm transition works well in YAG and Vanadate for example, however laser hosts based on doped chalcogenide glasses have the prospect of expanding this performance to longer wavelengths in glasses doped with Nd^{3+} and other trivalent rare earth ions are of greater interest.

Table 1.2 showed examples of a need for longer wavelength lasers in the 3.3 to 5.0 μm region. The requirements of such a host medium is the longer infrared transmission, a low nonradiative rate and a high refractive index, the latter making waveguide devices easier to produce. The additional ability to photomodify makes GLS a good contender. The lanthanum content means that the material is ready to incorporate rare earth ions.

2.5 Photoinduced Effects

2.5.1 Photomodification

Various photoinduced phenomena such as photosynthesis in plants chlorophyl and photographic processes in inorganic and organic materials are well known. Understanding of the mechanisms is of considerable scientific importance and in recent years growing optoelectronic industries for optical mass memories have stimulating related researches in photo-responsive glass materials. Such materials could be used to fabricate waveguide devices using for example photomodified gratings and defined light guides to produce DFB lasers. This would allow structures to be directly written into thin film layers on an appropriate substrate without the need for a mask or implantation, meaning that very high resolution could be achieved to create high definition devices on a large scale.

Since the discovery of photoinduced phenomena^[80] there appear to be two mechanisms responsible for the changes induced by exposure to absorbed light; thermal and optical. Changes in mechanical, particularly rheological, properties can also be induced by absorption of bandgap light, for example the surface roughness can decrease on irradiation. The main effect is a parallel shift of the absorption spectrum with respect to the wavelength^[81]. Measuring the optical properties at a wavelength above and close to the bandgap, a parallel shift towards lower wavelength (higher energy) will give rise to a decrease of absorption coefficient and, through the Kramers-Kronig relations, a decrease in the refractive index. This shift in the absorption edge is referred to as photobleaching. If the shift moves towards lower energy then the material photodarkens. Chalcogenide systems also have potential as photo-resists for micro-lithography in the fabrication of integrated circuits, since some of the effects can be stimulated by X-rays and electron beams, as well as light and very high resolution can be achieved. The wavelengths of light required to induce photomodification are in the optical bandgap region of the material, hence the power density that is required to penetrate into the material to cause the photoinduced changes needs to be large otherwise only surface effects will take place and so requires that thin films be used. However, if thin films are used it is impossible to measure variations of light transmission before and after photomodification in the weak optical absorption region.

The amorphous structure is stabilised during annealing and high temperature deposition process. This happens due to the reduction of dangling bonds through a thermally activated atomic rearrangement process. Thin films are known to relax over a period of time, this is known as the 'ageing process' and any change in the stoichiometry or a major change in the nature of chemical bonding is unlikely. Any changes in refractive index as a function of ageing time and temperature results from a structural relaxation. This will be reported for our GLS films in Chapter 6. There are implications from this; as the structure relaxes, photomodified regions are changing refractive index with time, potentially destroying devices.

2.5.2 Reversible and Irreversible Changes

Photomodification effects have been divided into two categories: Those where the original state of structure and optical properties are recoverable, in which case the changes can be removed by annealing to the glass-transition temperature, T_g , whereupon the changes can be reintroduced. The second category are the irreversible changes, which invariably occur in samples which are structurally unstable^[82].

If a 'freshly deposited' (virgin) film is illuminated, photomodification is generally irreversible as a subsequent annealing of films at T_g only partially restores their initial optical

transmission. However, the second and all following photo exposure-annealing cycles are completely reversible. The virgin state of the film cannot be reproduced by any illumination or heating. In some materials photoexpansion and thermal contraction are induced, indicating that some atomic rearrangement occurs upon heating and illumination and the change in optical transmission may be the result of such atomic rearrangement. However, As_2O_3 crystallites are found on the film surface after light irradiation indicating that either significant surface heating or photo-chemistry occurs during bandgap illumination in air.

Although a number of models to explain photostructural changes have been advanced during the past fifteen years, its exact mechanism is still the subject of much debate. No scheme has been proposed to tie all the related phenomena together. Conventional models that have been presented so far suggest a transition between two sites in an adiabatic potential diagram which assumes the existence of a double-well potential and a barrier between two minima^[83]. The presumed potentials are variously attributed to self-trapped excitons and 'wrong' bonds^[84]. It has been suggested^[85] that the structural change induced by light consists of minor bond rearrangements involving the chalcogen atoms relaxing between the minima of these double-well potentials.

In amorphous chalcogenide semiconductors, the electron-lattice interaction is so strong due to the structural randomness and low co-ordination character of the chalcogen atoms, that electron motions are necessarily accompanied by lattice distortion. Such dynamics can be written down explicitly by using energy/configuration (E/q) diagrams.

Tanaka^[86] demonstrated that features of the reversible and dynamic photodarkening could be considered qualitatively with an assumption of the existence of a defect, which is represented by an E/q diagram as shown in Figure 2-2(a). The diagram has an excited electronic state Z of a single well and a ground state consisting of double wells X and Y and the minimum of Z is located above the well Y . (Such models of single and double wells have already been used to clarify the electronic properties in ionic^[87] and ferroelectric^[88] crystals). When a sample is in the dark, the defects are in X or Y configurations and the site densities N_X and N_Y are modified by illumination and heat treatment. For instance, if the sample is illuminated with bandgap light at a particular temperature, transitions $X \rightleftharpoons Z \rightarrow Y$, $X \leftarrow Z \rightleftharpoons Y$ and $X \rightleftharpoons Y$ take place. If the sample is heat-treated in the dark, only the last transitions $X \rightleftharpoons Y$ are induced. Probabilities of the occurrence of these transitions depend upon the temperature as well as the photon energy and intensity of the illumination.

Figure 2-2(b) shows a typical result of reversible photodarkening measured at 80 K^[83]. The curve "annealed" is the optical absorption edge of the film annealed at 450 K, just below the

glass-transition temperature and then slowly cooled to 80 K. The curve "illuminated" indicates the absorption edge of this film illuminated at 80 K. If the illuminated specimen is annealed again and the transmittance measured, then the results are identical to that for the "annealed" case. With further illumination, the absorption edge shifts to "illuminated". Note that the change in the transmittance is a nearly parallel shift of the absorption edge and the magnitude is around 0.15 eV. A similar experiment can be performed at 20 K and it is found that the edge shift is approximately the same, ~ 0.16 eV, this shift is retained even if the specimen is warmed to 80 K.

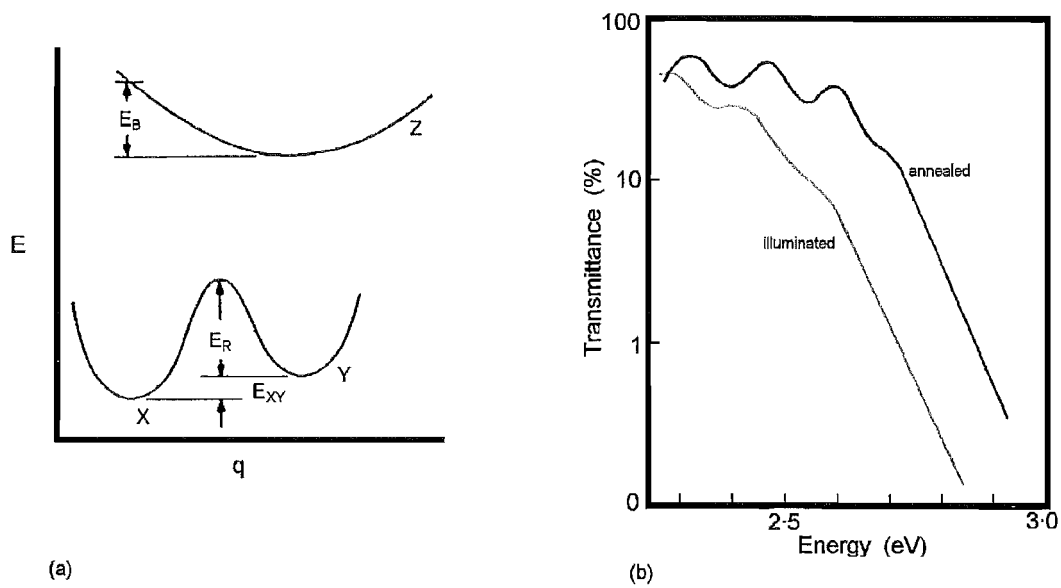


Figure 2.2. (a) Possible $E - q$ diagram for energy levels in chalcogenide material, (b) Example of As_2S_3 transmission limit when annealed and illuminated at 514.5 nm. {Original in colour}

The configuration of the defects in these annealed and illuminated states can be assessed by means of the SDW model (see, Figure 2.2(a)). Annealing at 450 K makes the process of surmounting the barrier E_R possible and the transitions $X \rightleftharpoons Y$ are induced. Since the X configuration is lower than the Y configuration by E_{XY} , the process $X \leftarrow Y$ becomes more and more dominant as the specimen is cooled. Finally, when the temperature is decreased to 80 K, it is supposed that almost all of the defects have the X configuration. In contrast, under bandgap illumination at 80 K, it is considered that only the transition $X \rightarrow Z \rightarrow Y$ is induced and as a result the defects have the Y configuration; the reasons for the latter being: first, the fact that the film illuminated at 20 K does not change its edge characteristics after being warmed to 80 K, suggesting that the barrier height $E_R/k \gg 80$ K (k is Boltzmann's constant) and the transitions $X \rightleftharpoons Y$ are negligible at 80 K. Secondly, equal magnitudes of

the photodarkening at 20 and 80 K imply that $E_R/k \gg 80$ K and the transition $X \leftarrow Z \leftarrow Y$ cannot be induced by the bandgap illumination at 80 K^[86]. Therefore, almost all of the defects have a Y configuration after the bandgap illumination at 80 K.

When the sample is slowly cooled down to room temperature, the distribution between the configurations X and Y are approximately given by:

$$N_Y/N_X \simeq \exp(-E_{XY}/kT) \dots\dots\dots (2.2)$$

where $T \simeq 300$ K. In contrast, if the sample is rapidly quenched, then the distribution under the heat treatment, which is determined by Equation 2.2 with $T \simeq 473$ K, can be frozen in. This frozen-in state has more defects of Y configuration and as a result the film becomes darkened.

2.5.3 Photoinduced Effects Seen To-date

A wide variety of light-induced changes has been observed in amorphous chalcogenide semiconductors, ranging from relatively subtle effects involving minor atomic rearrangements and manifested mainly by shifts in the optical absorption edge (i.e. photodarkening and photobleaching), to more substantial atomic and molecular reconfigurations which cause a variety of physical and chemical changes (e.g. photo-polymerisation, photo-crystallisation, photo-enhanced dissolution of metals etc.). These effects are of interest because of the information they provide on metastable structural states in amorphous solids and because they are mostly unique to the amorphous state. Listed here is a summary of those effects which have been identified to date.

Photoinduced bleaching or darkening: To briefly recap, photoinduced reversible changes in local atomic structure are subtle effects which are induced by light of photon energy close to that of the optical bandgap, E_g , of the chalcogenide glass. They are manifested mainly by small red-shifts in the optical absorption edge (photodarkening)^[89] or a photoinduced blue-shift in the absorption edge is termed photobleaching. Both can be accompanied by small changes in the radial distribution function and by barely discernible changes in volume (contraction or expansion). Changing the proportions of the constituent materials can switch a material from being one that photodarkens to one which photobleaches and vice versa^[90]. In chalcogenide materials, photodarkening appears to be the preferred effect for the majority of materials. However for GLS thin films, it will be shown that there is a decrease in refractive index through photomodification.

Photo-decomposition, is the light-induced dissociation of a compound into its constituents. It is frequent in amorphous As-S and As-Se compositions and illumination of photon energy greater than E_g is necessary. Absorption of a photon of energy greater than E_g causes a dissociation of the arsenic-chalcogen bond, and this is followed by thermal diffusion of the arsenic to form arsenic clusters, which are highly absorbing^[86]. Photo-decomposition causes small but detectable changes in X-ray diffraction and vibrational spectra. Provided the energy and intensity of illumination are not too great the photo-decomposition is reversible on annealing at T_g . Another associated phenomenon is increased solubility in alkaline solution by photo-irradiation, known as the photochemical effect^[91].

Photo-crystallisation, of amorphous layers can be induced optically^[92]. The opposite phase change from the crystalline to the amorphous state below the melting point of the corresponding crystals is rather surprising and has not been observed frequently. It was mostly observed in intermetallic compounds^[93]. Optically induced athermal amorphisation^[94] was also recently described in $\text{As}_{50}\text{Se}_{50}$ crystalline chalcogenide films^[92], the crystals can also be amorphised thermally. Photoinduced crystallisation^[95] and 're-amorphisation' has been studied in thin films of As-Te-Ge compositions^[96]. 'Re-amorphisation' requires that the temperature of the film first be raised to the melting point of the crystals and this can be achieved with a laser pulse. Strictly, therefore, this is an irreversible process.

Photoinduced morphological changes, is a term used to denote effects usually described in the literature as 'photo-volumetric changes' or 'photocontraction', since the phenomenon has its origin in changes in the macroscopic structure of chalcogenide thin-films, that is in their morphology. Changes in morphology have been observed in thin films of Ge-Se^[61] compositions which grow on the substrate in a columnar structure. On illumination, particularly with UV light, the films contract in volume. The magnitude of the change depends to some extent on composition but mainly on the angle of incidence at which the vapour-deposited film is grown. Prolonged exposures produce greater contractions, the deepest ones of them being over 20% of the film thickness^[97] has been observed in 80° incidence growth angle^[98]. Continuous increase in the photocontraction is observed with increasing obliqueness. It should be noted that no thickness change is observed in normal incidence (0°) deposited films. The magnitude of the photocontraction effect has been found to depend on the Ge content in the alloy films. Volume changes were seen in GLS thin films but were due to growth conditions and not photomodification as referred to in this section.

Surface contraction of the same order has been observed in amorphous Se-Ge films^[98] and Te-Se-I films^[99]. Another effect seen in As_2S_3 thin films is thickness increases of up to 5% with exposure to sub-band-gap light^[100]. The expanded volume remain stable after illumination is terminated, whereas the deformation can be recovered with annealing at the glass-transition temperature; it has been used to produce 'micro-lenses'^[101].

Photo-dissolution of metals: To observe the photo-dissolution/photo-doping effect requires the use of a thick amorphous chalcogenide film on (or beneath) a deposited thin metallic layer, typically 0.01-0.05 μm in thickness. Illumination from either the chalcogenide or metallic side with light above or below E_g for the chalcogenide causes the metal to dissolve rapidly into the amorphous film and migrate through it with very pronounced vertical edges^[102], with negligible lateral movement in most cases. For silver dissolution, it is generally reported that the concentration profile for the dissolved atoms is step-like, which implies that the phenomenon is not a straightforward diffusive process.

Experiments were conducted to see if silver could be used to dope tracks for waveguide devices in thin GLS films, by increasing the refractive index slightly. The silver was evaporated onto a substrate prior to the GLS thin film being grown. When the thin film layer had been added, experiments were conducted to see if the silver layer on the underside of the film would diffuse into the GLS layer and hence, cause an increase in the refractive index within the region of illumination. No refractive index change could be seen using the power densities for illumination that were available during this work.

It is probable, that the effect occurs in most amorphous chalcogenides. Silver and copper are used most frequently as the dissolving metal^[49], but gold also dissolves and it is likely that other metals such as indium and thallium would be susceptible to photo-dissolution. In the case of silver, for example, silver halides, silver nitrate, silver selenide and potassium silver selenide have been used successfully. It is often sufficient simply to dip the chalcogenide into a solution of a silver compound to produce the coating. Photo-dissolution also occurs in chalcogenides deposited on bulk substrates, for example Ag_2S ^[103].

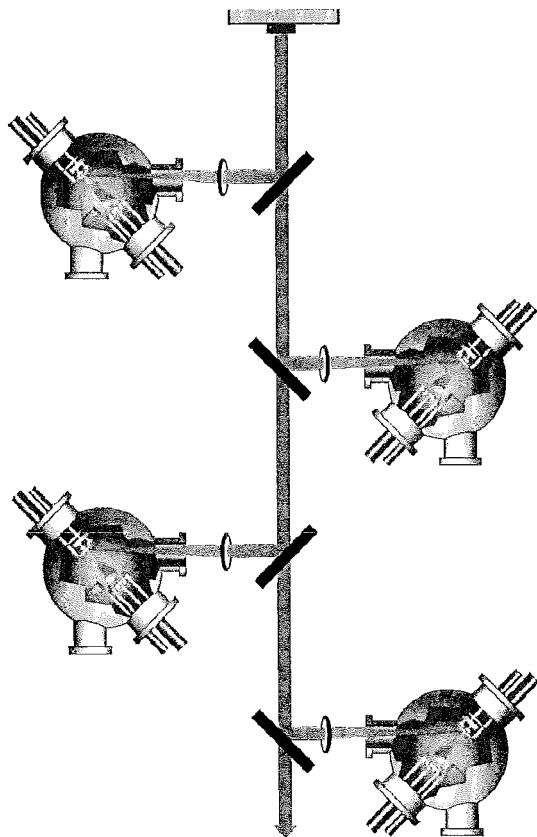
Other effects in specific cases: Another local structural change has been proposed to account for the appearance of optical anisotropy in certain chalcogenides when illuminated with plane-polarised light^[104]. This phenomenon, which has been termed the 'vectorial effect', is believed to involve the reorientation of small anisotropic structural units already present in the amorphous material. The principal axes of these units are initially randomly oriented but under illumination with plane-polarised light the units are forced to reorient themselves in such a way that the axes become aligned with some preferred direction defined by the plane of polarisation. The induced anisotropy can be erased by unpolarised or circularly polarised light.

Photo-vaporisation has been studied mainly in amorphous As_2S_3 thin-films. It is strictly a photo-oxidation reaction followed by thermal evaporation of the volatile oxidation products^[105].

Whilst this is an extensive list of photomodification parameters, usually only a selection are seen in any one material. Changing the constituent elements can reduce or eliminate one photomodification property and induce a new one. Photobleaching, photodarkening and photo-chemical changes are seen in GLS glasses.

3

Pulsed Laser Ablation



One pulsed laser source can be employed to ablate target materials in many individual chambers simultaneously if necessary.

3-1

Optical Thin Films and Waveguide Fabrication Techniques

3-2

The Beginning of Laser Ablation

3-3

Laser Deposition

3-4

Particulates

3-5

The Design of a New Ablation Chamber

3-6

Large Scale or Commercial PLD

3.1 Optical Thin Films and Waveguide Fabrication Techniques

Thin film growth techniques can be categorised into equilibrium and non-equilibrium processes according to the ways in which the source materials are vaporised or become gaseous. An equilibrium process is typified by thermal evaporation including the conventional resistive heating, e-beam evaporation and molecular beam epitaxy (MBE). Non equilibrium processes include sputtering and similar forms such as ion beam deposition. In comparison with these techniques, thin-film deposition by laser ablation does not fall cleanly into either category. Depending on laser conditions, the ablation process can be either thermal, non-thermal, or a mixture of the two.

Recently, chalcogenide amorphous films have become used in phase-change-erasable optical storage technology. These films have ordinarily been prepared by two methods, vacuum vaporisation and vacuum sputtering. RF sputtering makes it easier to control the thickness and chemical composition of thin films and these thin films are more dense than those made by evaporation. A selection of techniques for the fabrication of thin films or waveguide layers are briefly detailed below. Many of them have been used to produce chalcogenide thin films.

Dip coating and spin coating, have both used to deposit thin films usually of polymer materials, such as photoresist, onto a substrate. In spin coating, polymer materials are dissolved and one drop is put on the substrate. The thin film is formed by rapidly spinning the substrate. With dip coating, a thin film is formed by dipping the substrate in solution and then lifting it. CdS is a chalcogenide that has been developed by sol-gel synthesis^[106]. The very high temperatures required in an environment free from oxygen make this technique impractical for the growth of GLS thin films.

Thermal Evaporation: Thin films are produced by depositing a material vaporised in a vacuum chamber, usually below 10^{-5} Torr, on a substrate. For low boiling point materials the resistor heating technique is used and electron beam heating is used for high boiling point materials. Whilst the method is suitable for the deposition of amorphous materials or metals it is not ideal for more complex, multicomponent materials whose constituent parts can have very different boiling points which cause preferential evaporation rates leaving the thin film with a different composition to that of its parent target. Although it is more often used for crystalline materials, binary chalcogenide thin films have been successfully grown by evaporation, for example, GeS_2 ^[107], As_2S_3 ^[108] and As_2Se_3 ^[109]. These materials are all binary compounds, the extreme difference in vapour pressure of the components, make this route inapplicable to our materials.

Film thickness depends on the separation between vaporising source and substrate. Larger distances produce better thin film uniformity but has a lower deposition rate. Common to many growth processes, the substrate can be heated to improve surface mobility for the incoming species, particularly during crystal film growth.

Sputtering: Inert, nonactive gases such as Ar, Ne and Kr can be made into a plasma whose positive ions collide with a target plate (with several kV applied), particles are kicked out as a result of this impact and deposit on a substrate. This technique is used for high melting point materials which can not be evaporated thermally. The majority of films grown by sputtering are either in the amorphous or polycrystalline phase, although some results have suggested that epitaxial layers can also be deposited.

The plasma produced is not always well confined and comes into contact with the walls of the chamber, contributing to contaminants in the film. In the sputtering method described, the gases do not react with target materials during sputtering. Reactive sputtering can be achieved with an appropriate (background) gas to deposit thin films of its chemical compound with a target material by chemical reaction, O_2 being a good example. Chalcogenides have been successfully grown using RF sputtering for example, Ge-Sb-Te^[110]. Sputtering would probably be a feasible route to thin GLS films due to the similarities which exist with laser ablation.

Chemical Vapour Deposition (CVD): The CVD method causes the chemical reaction of gases and vapours to deposit them on a substrate. A disadvantage of CVD is that it is difficult to change materials so that deposition chambers are usually dedicated to only one material. Diffusion layers could be formed between the substrate and thin film as often high substrate temperatures are required. For example, thin films of Ga_2S_3 have been produced in both amorphous and crystalline forms using this technique^[111] and thin film layers of Pb-Se-Te^[112]. Whilst work with Ga_2S_3 have shown that this component can be grown by this technique, the lack of volatile lanthanide precursors makes this a nonviable technique for GLS.

Molecular Beam Epitaxy (MBE): Gives precise control of film thickness by using molecular beams generated in effusion cells. An MBE chamber uses very high vacuum and is able to grow monolayers of a material. Numerous effusion cells producing different molecular beams are within the chamber, producing single or combined multilayer samples on a substrate.

This sophisticated technique has been applied for the growth of optical materials^[113]. It does suffer from high capital costs, depositions are slow and the chamber is not quickly modifiable

to grow many different materials. Chalcogenides have been grown as thin film layers using this technique, for example Pb-S, Pb-Eu-Se and Pb-Sn-Se^[111]. It would be possible to grow GLS thin films this way, but low growth rates and huge capital costs do not favour this route.

Ion Implantation: By implanting 20 to 300 keV accelerated ions into a substrate, lattice disorder takes place, resulting in a change of refractive index layer. This method has the advantage that it is able to control the ion dose distribution with good accuracy. As an example, by implanting hydrogen ions into a As₂S₃ substrate, once annealed, can produce good quality thin film layers^[114].

Flame Hydrolysis: The FHD technique allows thick layers of high silica glass to be deposited on to planar substrates^[115]. The metal chlorides of the species required are hydrolysed in an oxyhydrogen flame to produce the metal oxide. The resulting oxide is produced in the form of a low density soot, which is deposited on the a planar substrate held on a rotating turntable. The soot is consolidated into a uniform glass film by sintering. The B₂O₃ : GeO₂ : SiO₂ glass composition has been shown to have a photosensitive response and could allow potential integration of rare earth doped lasers with photosensitive writable mirrors. Rare earth ions can be incorporated into the glass film; the rare earth oxide is dissolved in water and the resulting solution nebulised to produce an aerosol. This aerosol is fed directly to an oxygen rich flame, where the rare earth is directly incorporated into the film.

Pulsed Laser Ablation: This technique was chosen for its complete versatility. If the GLS films were to be doped with rare earth sulphides, it is much easier to mix the starting powders into their required starting quantities and ablate the target than have separate constituent components. The method of multiple targets allows growth to be achieved either from the individual binary compounds or the stoichiometric melt. The target can be powders or a glass and so material proportions which do not form a glass through standard quenching techniques, could be investigated with pulsed laser ablation. The aim of this work was to look at some of these possibilities as well as the GLS waveguide device potential.

3.2 The Beginning of Laser Ablation

3.2.1 The Introduction

Research involving laser-material interactions began in the 1960s setting the stage for many aspects of laser ablation. Brech and Cross^[116] collected and spectrally dispersed the emitted light from ruby laser ablated metals. Linlor^[117] made measurements of the energy of ejected

ions by time-of flight determinations. This work, along with that of Honig and Woolston^[118], was the first example of laser mass spectrometry. Muray^[119] was the first of many to investigate laser photoemission of electrons. The study of ablation plumes by photography was initiated by Ready^[120] in 1963. Other important papers appearing in 1963 were by Rosan *et al.*^[121] for the first ablation studies of biological material and Howe^[122] who used rotationally and vibrationally resolved molecular emission bands to measure temperatures of ablation plumes. Berkowitz and Chupka^[123] were the first to observe particulates in an ablation plume.

Basov and Krokhin^[124] made the first suggestion of laser fusion and as higher power lasers were used, vacuum ultraviolet^[125] and X-ray emissions^[126] were detected in ablation pulses. Higher power also led to the observation of multiply charged ions^[127] and to two-^[128] and three-photon^[129] photoemission. Finally, of great importance in terms of modern applications of ablation, the first laser deposition of a thin film was demonstrated by Smith and Turner^[130] in 1965. Unfortunately these early films were of poor quality and the technique could not compete with other established techniques. It was a further twenty years before laser produced films were competitive.

During the 1970s and early 1980s the understanding and development of laser desorption and ablation processes were incremental and steady. The availability of new, brighter lasers with shorter pulse lengths, combined with a broader wavelength capability led to the application of ablation studies to ever more types of materials. However, the principal use of laser ablation continued to be in emission and mass spectrometry for chemical analysis.

In the late 1980s the situation changed dramatically, Zaitsev-Zotov *et al.*^[131] first produced superconducting thin films by laser ablation in 1983 but the technique went virtually unnoticed until Venkatesan and co-workers^[132, 133] demonstrated in 1987 the growth of the newly discovered high-temperature superconductors by laser ablation of bulk Y-Ba-Cu material followed by annealing in air or oxygen. The stoichiometry of the thin films was virtually identical to that of the bulk. The ablation technique offered several advantages of simplicity, versatility, and experimental ease over traditional methods of sputtering or coevaporation. Over the past decade there has been an order of magnitude increase in laser ablation research¹.

The diversity of this technique is reflected in the fact that it does not have a common name and acronym. Names such as: laser assisted sputtering^[62], Laser Assisted Deposition and Annealing (LADA)^[134, 64], Pulsed Laser Evaporation (PLE)^[132], Laser Molecular Beam Epitaxy (LMBE)^[135], Laser-Induced Flash Evaporation (LIFE)^[136, 137], Laser Ablation Deposition

¹ A search of the Bath Information and Data Service (BIDS) for the word 'ablation' generates 277 hits for 1988, this increases to 2637 hits for the single year 1998, showing a ten fold increase of the publication rate in as many years.

(LAD)^[138], Laser pulse vapour deposition^[139], Laser-induced evaporation^[86, 131], Laser sputtering deposition^[140] and Pulsed laser irradiation^[141], Pulsed laser ablation^[142, 143] and Pulsed Laser Deposition^[144-146] have so far been used, the latter, being adopted as standard over the past few years.

The basic experimental design is similar to any other physical vapour deposition processes, the major difference being the evaporation technique. In laser deposition, the power is supplied by a laser located outside of the vacuum chamber. This reduces the requirements of the vacuum chamber size. The principal is shown diagrammatically in Figure 3-1.

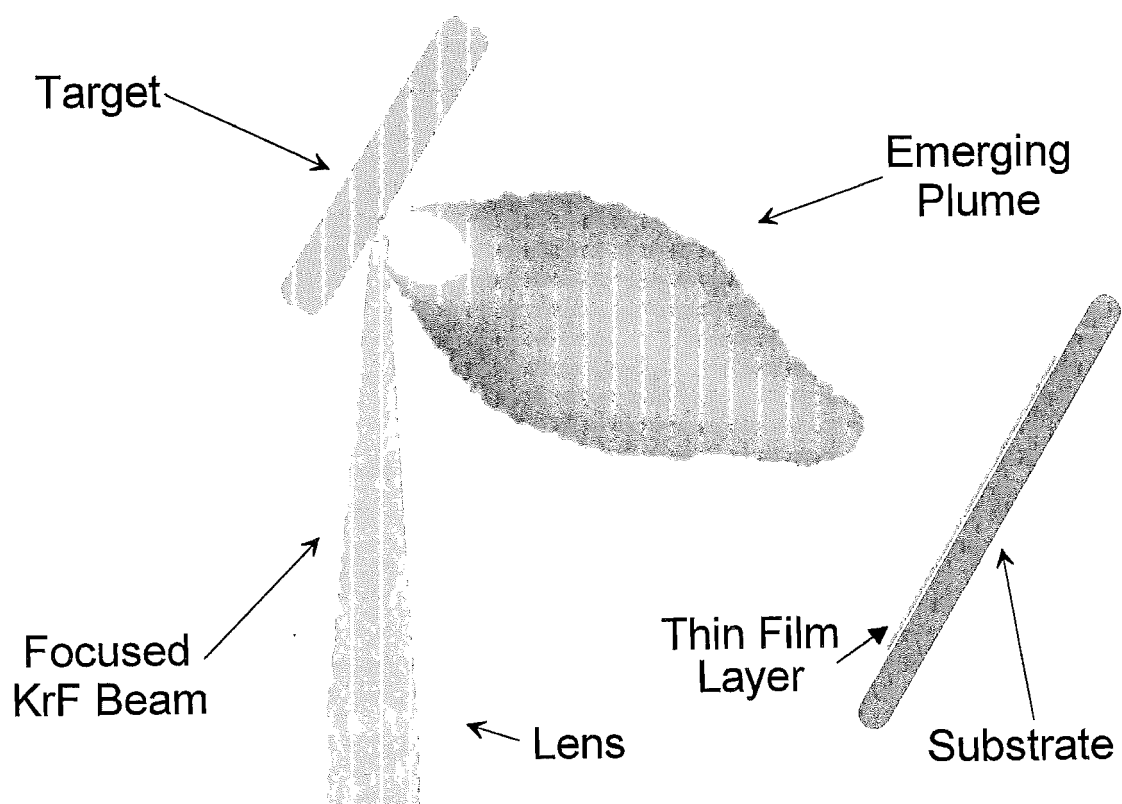


Figure 3-1. Schematic of the basic principle for Pulsed Laser Deposition.
{Original in colour}

Congruent evaporation is undoubtedly one of the most significant advantages in laser ablation. The stoichiometry of a multi-component source can be preserved during thin film growth if the thermal cycle (heating and cooling of a region on the target) is short in comparison with the segregation time of the individual components. This condition can be achieved not only by pulsed laser but also by CW laser with a fast scanning rate.

The current increasing use of PLD is due to rapidly developing interest in the use of thin film materials for many applications (magnetics, microelectronics, optics) coupled with the need for a technique which is easily adaptable to materials with widely different properties.

Although the underlying ablation process is complex, PLD is conceptually and experimentally simple. It has become the natural choice for preparing high temperature superconductor films^[132]. Its increasing use in the preparation of many other classes of films (metals^[147], X-ray mirrors^[148], semiconductors^[90] diamond-like carbon^[139]) also bears witness to its advantages and versatility and along with traditional substrate heating techniques, the substrates can also be heated using CO₂ laser, avoiding problems associated with the poor thermal contact between heater and substrate. The targets can be made compositionally rich in a particular element if a thin film appears to lose stoichiometry as is occasionally seen^[149].

3.2.2 Ablation Without Thin Film Growth

Particularly spectacular has been the growth of laser-based medical procedures which started in the late 1980s^[26]. Laser based ophthalmology is now widely available and laser reshaping of soft tissue of the throat for the treatment of sleep apnoea and control of snoring is an established technique. Laser ablation is a useful tool in the dermatology field for the removal of birthmarks or tattoos and most recently for cosmetic smoothing of wrinkled skin. Dental applications are being studied as well^[150]. In 1965, Schawlow proposed and demonstrated the first 'laser eraser'^[151]. The different absorbencies of the paper and ink allowed the laser to selectively remove typewriter print without damaging the underlying paper. With the evolving sophistication of laser ablation, 35 years later we have a tool for graffiti removal^[152, 153], for art restoration^[154] and cleaning^[155], lasers are even used to cut and carve wood without carbonisation^[156].

Nd:glass and ruby lasers were used for a major portion of the pioneering work. CO₂ and Nd:YAG laser offer excellent long term stability and long operating lifetime, while the excimer lasers offer short wavelength photons for ablating metals. Like the excimer, TEA CO₂ also has a high energy content at a few joules per pulse however, its main drawback is the long output wavelength which requires special transmissive optical materials compatible with ultra-high vacuum equipment. The choice of laser is usually dependent on the wavelength. The material being removed must absorb the incident radiation and the higher the absorption coefficient at the laser wavelength the lower the fluence (energy density) which is needed to instigate material removal.

3.3 Laser Deposition

3.3.1 Laser-Matter Interaction

While laser ablation is simple conceptually and experimentally, the physics are complicated, given that they involve laser solid interactions at the target, plasma formation off the target,

vapour/plasma plume transport toward the deposition substrate with its associated hydrodynamics and atomic physics, as well as plume-solid interactions at the deposition substrate. Laser induced desorption and ablation result from the conversion of an initial electronic or vibrational photoexcitation into kinetic energy of nuclear motion, leading to the ejection of atoms, ions, molecules and clusters from a surface.

The nature of laser-solid interaction depends on many factors such as power density, pulse duration, wavelength, and the thermodynamic and optical properties of the solid. In principle, any laser which is strongly absorbed and having sufficient output power, can be used to induce evaporation. The ejected particles contain a mixture of ions, electrons, hyperthermal neutral atoms and molecules, neutral species in their electronically excited states, UV photons, and even soft X-rays. The evaporation is basically a thermal process with the temperature of the plasma plume reaching 2×10^4 K^[122] and pressures of up to 10^7 atmospheres can be reached on the target surface^[167].

For film growth, the "ablation" regime is defined as the laser energy density range for which congruent transfer of material is obtained. The reason for this definition is that the process of pulsed emission of atoms/ions/molecules from a surface actually involves two successive energy density thresholds, E_1 and E_2 . The first (lowest) threshold is that for the onset of laser etching, accompanied by particle emission. This pulsed atomic/molecular emission process is highly nonlinear in laser fluence and also may be highly selective for a particular chemical species^[158]. The second threshold is for simultaneous stoichiometric transfer of all chemical species from target to substrate; for a multi-element target material, this occurs only at higher E_2 . For example, for GLS the KrF (248 nm) etching threshold is near 1 J cm^{-2} , but film deposition is not obtained until 2.5 J cm^{-2} , (data presented later in Table 5.1).

The reason for the two different thresholds is that atomic/molecular emission at low E_d results either from pulsed heating or from selective desorption from particular near-surface sites (e.g. defects, cracks, impurities). At low energy E_1 , variations in melting points and vapour pressures among the constituent elements of a target will result in noncongruent transfer. The stoichiometric transfer regime is reached only when the pulse energy is sufficiently high to form a laser-generated plasma; congruent transfer and the ablation regime for thin film growth. Consequently desorption studies at low laser fluence usually are not directly relevant to film growth in the useful ablation regime.

The onset of stoichiometric deposition coincides with the threshold fluence for formation of a dense laser generated plasma just above the target surface^[159]. The plasma's formation and expansion is self sustaining throughout the laser pulse, being continuously fed material removed from the target by absorbing incident laser energy. Visible light emission from the

plasma is continuously present during this period^[159]. Consequently the very bright emission from near the target surface is a useful indicator of the onset of the plasma hence laser target interaction that preserves stoichiometry in film deposition. When comparing long and short pulses, longer pulses eventually do not increase the ablation rate, this behaviour is consistent with self regulating ablation rate controlled by plasma shielding of the target^[160].

When using a low power density laser source, the material to be evaporated must be opaque, having a large absorption coefficient^[161]. For transparent materials, compressed tablets of fine powders were often used as targets to enhance absorption by increasing the surface area and localising heat more efficiently due to the low thermal conductivity^[137, 162].

During CW laser-induced evaporation, the volume of material being heated is large compared to when using a pulsed laser. The thermal cycle is also much longer when the beam is rastered. Therefore, CW laser evaporation is similar to a conventional e-beam evaporation process in many ways and a “warm-up” period is needed before evaporation begins. Again due to differing vapour pressures of the constituent components of GLS, CW thin film growth is not suitable for this glass material.

The thermal evolution of the irradiated target is dictated by the balance between the absorption of the laser light and the dissipation of the thermal energy in the target surface according to the heat flow equation. To give an idea of the heating and cooling rates involved in the process, consider the heat flow in the target surface as the laser pulse impinges upon it. The energy absorbed during the time τ of laser irradiation is confined to a surface layer of approximate thickness $d = (4D\tau)^{1/2}$, where D is the thermal diffusivity. For nanosecond irradiation of metals this is about 1 μm . The fact that a single laser pulse is capable of inducing melting, i.e. heating the surface to a temperature of the order of some 10^3 K, reveals that extremely high heating rates of up to 10^{12} K s⁻¹ and thermal gradients as high as 10^9 K m⁻¹ are achieved. The associated heat flow $\kappa \nabla T$ of 10^{11} W m⁻¹ leads to subsequent rapid cooling at rates of the order of $D \nabla T / d = 10^{10}$ K s⁻¹ and solidification may proceed at several tens of meters per second. Non-equilibrium processes, which are governed by reaction kinetics rather than thermodynamics, are likely to occur under such extreme conditions.

Evaporants can be classified into six categories according to their chemical states either as individual atoms or combinations, forming molecules. They are neutrals, ions, electronically excited species, electrons and photons, and macroscopic particles^[163] (this sixth set will be dealt with in Section 3.4). Such a diversity is unmatched by any other deposition technique.

Neutrals: These dominant species are induced by low and intermediate power density laser radiations. More than 95% of the matter in an expanding laser-induced plume is neutral^[163].

Ions: As the power density of the radiation increases, so does the fraction of the ions in the evaporation plume. Atomic and molecular ions produced by laser evaporation are positively charged ^[164]. They are formed either by direct laser-solid surface interaction, or by indirect processes such as radiation heating of the plasma, plasma-solid surface interaction and processes involving direct electronic transitions in the solid. The ions are mostly in atomic form, but dimeric and polymeric positive ions are also present.

Electronically Excited Species: Luminescence from excited electronic states of neutral or ionic species is often observed in PLD ^[165]. Excitation has well-defined laser power level thresholds ^[166]. Luminescence from the excited species in vacuum has been observed in targets of metals, semiconductors, chalcogenides and non-metallic surfaces. Bhat and co-workers ^[166] detected optical emission from InSb induced by PLD. The emission spectrum was resolved and identified to result from the luminescence of excited In and Sb atoms, showing that the colour of the glow is dependent on the chemical constituents of the target.

Electrons and soft X-ray emission: Although electrons are inevitably a major constituent of the plasma, particularly at high ablation energy, the studies on their properties are very sparse. Hoing ^[167] investigated the emission of electrons from Ta and Ge targets.

3.3.2 Plume Dynamics and Background Gases

The absence of heating elements allows the introduction of various gases into the vacuum chamber without burning out heaters. Therefore, laser ablation is an ideal technique for reactive deposition. Such gases, if added, will be incorporated into the plume or the growing film surface. The plume cooling in a processing gas is a natural consequence of collisions between fast components at the expanding front of the plasma and the background atoms which cool the plasma and can slow its progress. Background gases are virtually always introduced to the vacuum chamber when an elemental or molecular component is to be incorporated into the depositing thin film layer. Oxygen is by far the most popular background gas ^[165, 168], however nitrogen ^[169, 170], N₂O ^[171] and OCS ^[172] are other examples. Water has also been used as a background medium ^[173].

Experimental observations have shown marked differences between plume expansion in vacuum and in the presence of a background gas. Ablation into ambient gases results in shock waves and expansion fronts propagating through the background gases. Camera images of plume development have revealed two different emissive components in the plume ^[173]. The first and fastest one, whose expansion takes place at a velocity of about 10^4 m s^{-1} , shows the development of a shock wave in its front, resulting from the interaction between the species released from the target and the background gas. A gas can slow this component to values of about $3 \times 10^3 \text{ m s}^{-1}$. The second and slowest component expands at

a constant velocity of $5 \times 10^2 \text{ m s}^{-1}$ and is constituted by hot particulates leaving the target. Hence, there is an energetic component that propagates at vacuum speed (as if the gases were not present) and another that is can be significantly slowed down, depending on the pressure of the background gas.

Papakonstantinou *et al.* found that the photon emission intensity from a plume depends on the oxygen pressure, P_{O_2} , and the distance from the target^[174]. Generally, it decreased with distance and increased with P_{O_2} . The emission from this process increases with oxygen because the background gas acts to confine the plasma to a smaller volume close to the target, facilitating increased collisional photon emission rates of all plasma species. Chemi-luminescence may well begin to increase photon emission as the oxygen pressure increases and the molecules combine with the plume matter. The emission also decreases with distance because the expanding plume cools and collisions become less frequent in the expanding gas.

These workers continued to show that, at distances less than 5 mm from the target, the effective velocity of the plasma species was not influenced significantly by the presence of oxygen up to 0.5 mbar. However, a much more pronounced influence was observed at large distances, as increasing oxygen pressure resulted in the evolution of much broader and slower temporal profiles with intense emission. The overall optical plasma emission clearly demonstrated how increasing the oxygen pressure confines the plasma, slows its expansion and enhances the emission, particularly at its expanding front.

It is concluded that the role of oxygen pressure is not only to supply the oxygen constituent in the film but also to slow down the highly energetic species which otherwise will cause damage to the film deposited. However, if the pressure is too high, the velocities of the atoms and ions will become too slow and there will be little surface activation^[174]. At high pressure (0.5 mbar) the plume is restricted to short distances and non-luminous thermalised species reach the substrate.

Unlike vacuum PLD, the interaction of the laser produced plasma flux with the gas changes the dynamics, chemistry and energy spectrum of the plasma species. Flux parameters critical for film growth change drastically with distance from the target^[175, 176]. At a specific distance, characteristic to the material, the flux loses its unidirectional velocity, scatters and thermalises. It has been experimentally discovered that this distance provides the optimum conditions for film growth.

The molecular weight of the ambient gas is found to markedly affect the expansion dynamics of the spherical plume in much the same way as the ambient pressure^[177]. Plume splitting is of great interest because the fast component may damage the growing film or

otherwise affect its microstructure. Also, clustering of film constituents in the gas phase or on the surface presents difficulties of non-uniformity and localised different structures.

For GLS to maintain its infrared transmission range, oxygen must not be incorporated into the thin films. This could be either by having a poor vacuum or from background gas added after initial pump down. However other gases could be investigated to monitor various film parameters grown under different conditions. N_2 and Ar could be used for plume control properties for possible interest. Sulphur containing gases have safety issues associated with them. H_2S is a possibility but might introduce hydrogen into the thin films which like the oxygen is undesirable. H-S bonds have various absorption bands in the 2 to 4 μm region^[178, 179].

3.3.3 Non-Laser Induced Ablation

Energy input by non-thermal means is a powerful and widely used process tool in thin film deposition. Energy may be directed into any of the three process steps: to vaporise the source material, to activate it during transport, or to modify film structure during deposition. The energy may be delivered by electrons, photons, or ions. Table 3.1 compares the energy-beam technologies that are used for vaporisation. The key feature to note is that in each of the first four processes listed, the electrons, ions, and photons, respectively, are directed at the source material in a narrow beam of at most a few millimetres diameter, whereas in "sputtering," the 'ion beam' used covers a much broader area. The use of narrow beams leads to intense heating of the source material at the point of impact, so that the vaporisation mechanism is thermal even though the energy input is non-thermal. Conversely, sputtering involves direct momentum transfer from bombarding ions to the surface atoms of relatively cool source material.

Technology	Typical Beam Species (eV)	Mechanism	Beam Diameter	Operating pressure (Pa)	Particulate problem
Electron beam	10 000	Thermal	5 mm	$<10^{-2}$	Small
Cathodic arc	20	Thermal	10 μm	<10	Large
Anodic arc	20	Thermal	5 mm	<10	Small
Pulsed laser	4 - 7	Thermal	5 mm	$<10^2$	Large
Ion-beam sputtering	1 000	Momentum transfer	10 cm	$10^{-3} - 10^{-2}$	None
Glow-discharge sputtering	500	Momentum transfer	20 cm	$10^{-2} - 10^{-1}$	Negligible <20 Pa

Table 3.1. Energy-beam vaporisation methods for thin film growth.

There are several advantages to using energy beams for vaporisation rather than directly heating sources. One is that any material can be vaporised, no matter how refractory in the narrow beam processes, because of the very high energy density and surface temperature which can be achieved. In sputtering, it is because the bombarding ions have energies far exceeding the chemical-bond strengths, which are a few eV. In all of these cases, one can (and must!) avoid energy input to the materials of the structures which enclose the target. This is not possible with conventionally heated sources. Energy directional control is often claimed to result in a higher-purity evaporant; however, conventional sources can be extremely clean, as evidenced by the impressive achievements of molecular-beam epitaxy. The ability to vaporise any material is an important advantage of pulsed laser deposition plus the depth of source material removed is only tens of nanometres, which results in stoichiometric (congruent) vaporisation of multi-element materials. This does not guarantee a stoichiometric deposit, because the sticking coefficients of the vapour species can differ. The size of the glass target that we manufactured means that only the narrow energy beams are possible contenders as an alternative to the excimer laser in our work.

3.3.4 Deposition Analysis Techniques

Laser evaporation carried out in vacuum is compatible with other UHV-based techniques. All of the in-situ analytical tools used by MBE can be applied here without any modifications. Deposition flux is the vapour flux arriving at the substrate times the sticking coefficient and there are several approaches to deposition flux monitoring, principally: (1) mass deposition on a vibrating quartz crystal in the vicinity to the substrate, (2) change in optical reflection intensity, or phase in the case of ellipsometry, from the film itself with increasing thickness^[180] and (3) periodicity in the reflection high-energy electron diffraction (RHEED) signal from epitaxial films^[181]. All of the techniques are extremely sensitive, with monolayer resolution being achievable in some. It is important to keep in mind that none of these actually measure film thickness, it must be calculated by knowing or assuming a film property, namely for the above cases, (1) density, (2) index of refraction and (3) monomolecular layer (monolayer) thickness.

The quartz crystal mass-deposition monitor is one of the most widely used diagnostic instruments in thin film technology. A quartz crystal generates an oscillating voltage across itself when vibrating at its resonant frequency, as the deposition flux coats one side of the crystal, this mass loading causes the resonant frequency to decrease, monitoring this frequency provides indirect film thickness measurements. A quartz crystal was added to our deposition chamber in the latter stages of the project.

The optical techniques of deposition flux monitoring have several advantages: they are applied directly to the depositing film, yet they involve too low an energy density to perturb

the deposition process and they can be used in high pressure or plasma environments. On the other hand, their interpretation requires considerable knowledge of the optical properties of the film and substrate, finally the film must also have some transparency. The matter being deposited from an ablated plume does perturb the surface reflected energy beam momentarily ^[137] because of the high density cloud and refractive indices depend on temperature. This would be an issue in high repetition rate pulsed laser ablation.

Optical thickness measurements were made at 655 nm using a collimated diode laser and a silicon detector both placed inside the deposition chamber. In principle the arrangement did work and hence could be used to monitor film thickness if multiple films were to be produced whose thicknesses needed to be the same.

Real time growth rate measurement is desirable for accurate control of layer thickness in device fabrication. The structural information provided by RHEED to monitor surface quality has proven to be very useful for in situ monitoring, its pattern gives information about atomic arrangement of the film surface and the growth rate which can be accurately resolved from the oscillation period of the RHEED specular beam intensity, intermittently in a gas or continuously in vacuum. Because GLS is amorphous, RHEED is not a suitable thickness measuring technique. Crystalline films could take advantage of this.

3.3.5 Other Considerations

During thin-film deposition, some evaporants will inevitably condense on the vacuum window and attenuate the laser beam passing through it. The condensation of evaporants could gradually slow down the deposition rate and limit the film thickness. Whilst in our case the windows were coated over a period of time, rendering viewing ports unusable, the excimer laser would clean the inner area of the window through which the pulses passed into the chamber. This prevented degradation of performance in our system.

The experimental set-up is very flexible. Multiple sources can be evaporated simultaneously by splitting and focusing the laser beam onto separate sources or by exposing individual targets to the laser beam sequentially. Other beam processing techniques such as substrate surface cleaning and *in-situ* annealing can also be adapted easily by using the appropriate optics to direct the laser onto the substrate either before (substrate cleaning) or during (*in-situ* laser annealing) thin film deposition.

A separate target can be used to grow each layer, with a multi-target "carousel" for rapid target exchange. Growth is inherently 'digital' because each layer's thickness can be controlled precisely simply by calibrating the deposition rate per laser pulse and counting the

pulses. By choosing a low deposition rate, it is possible to control film growth near the atomic layer level. Typically an average GLS layer would grow for 25 minutes at 20 Hz pulse rate, producing a thickness of 300 nm. From this it can be seen that the effective deposition rate is 0.1 Å per pulse.

3.4 Particulates

3.4.1 The Problem of Particulates

Parameters such as the photon energy and density incident on the target, the surface contamination, as well as the nature of the environment present during ablation strongly affect the kinetics and nature of the species emitted from the target and subsequently influence the film stoichiometry and physical quality. Also important are the laser pulse width, repetition rate and the thermodynamic properties of the target material.

Microscopic particles (droplets) from the target, first discovered in 1964^[123], are common in laser ablation. The presence of these 'particulates' can severely deteriorate the film quality and morphology and is a disadvantage of this deposition technology. Particulates are usually spherical or disk shaped with smooth surfaces, indicating condensation from molten globules. The presence of particulates has been reported for many materials^[182] and range from a few tens of microns to sub-micron dimensions. Their velocity is size-dependent through an inverse linear relationship determined by Lubben and co-workers^[182]. For a 1 µm size particle, the velocity is approximately 10⁴ cm s⁻¹.

The particulates can arise in three ways: They are either droplets of the liquid phase carried off by the plume momentum from the surface of the target, they are formed by condensation of the vapour as it expands into the vacuum or they are fragments of material ejected due to the shock-wave which travels through the target^[183]. The problem of particulate debris is not exclusive to laser ablation and the thin films prepared by electron beam evaporation and sputtering also show the presence of large numbers of particulates on the surface. Although easily reduced to a certain density, particulate elimination has not been achieved with conventional PLD, only with some special variations^[184, 185] (see Section 3.4.2). Two kinds of particulates in laser deposited films have been reported. Droplets which usually have rounded shapes and the same composition as the film matrix^[182, 186] and others that have a composition different to the film matrix^[186].

One significant problem is texturing of the target by the incident laser beam due to the laser impinging at a non-normal incidence angle to the target. As the target is irradiated the shadowing effect amplifies surface features, which results in the formation of cones. Cone

formation leads to three problems: a drop in the deposition rate with time, an increase in the incidence of particle formation on the films and a shift in the angle of the emitted evaporant toward the laser by as much as 20 degrees^[187]. Since the composition and the film thickness is optimum at the peak of the emitted plume, a shift of the plume direction is a serious problem for the production of high quality thin films.

A polished target will have a flat surface at the start of a deposition run, as the deposition continues, the laser etches a trench in the rotating target surface. The evolution of this trench alters the laser spot shape and fluence, as well as modifying the angular distribution of the ejected mass species as a function of time. The density of particulates is reduced for the first few films deposited using a newly polished target.

After removal of the top layer from a fresh target by PLD, the surface becomes rough with the formation of micro-cracks, pits, craters, and loosely attached particles. These features are mechanically weak and disintegrate under the thermal shock induced by subsequent laser pulses. Consequently surface 'nodules' are susceptible to ejection from the target by subsequent laser pulses, ultimately forming micron-sized particulates. A small contribution may occur due to the rapid expansion of trapped gas bubbles beneath the surface during laser induced heating.

The true splashing effect and plume formation, as described by Ready^[120], can only occur if the transfer of laser energy into heat occurs at a faster rate than is needed to evaporate a mass volume. The theory assumes superheating of a subsurface layer before the surface itself has reached the vapour phase.

Since the particulates are solidified from molten droplets expelled from the target, cooling rate is the major parameter that controls the microstructure of the particulates. At the present time there is still scarcely any available theory or experiment pertinent to the cooling process of the laser ablated liquid droplets. Crude estimates on the cooling rate obtained by two different methods are presented here. When the ablation experiment is done in vacuum, cooling is predominantly radiation. The cooling rate can be expressed as:

$$\frac{dT}{dt} = \left(\frac{6}{d\rho C_p} \right) \varepsilon \sigma (T^4 - T_0^4) \dots\dots\dots (3.1)$$

where d is the particulate diameter, ρ is the material density, C_p is the heat capacity of the material, ε is the radiant emissivity, σ is the Stefan-Boltzmann constant, T is the temperature of the particulate and T_0 is the ambient temperature. This formula is adapted from a more general formula applicable to "conventional" powder fabrication process^[188]. Considering a micron-sized La molten droplet ablated into an ambient background at room

temperature and assuming the physical properties of the molten state are similar to those of its solid state counterpart, namely, $\rho = 5.96 \text{ g cm}^{-3}$, $C_p = 0.195 \text{ J g}^{-1} \text{ K}^{-1}$, $\varepsilon = 0.254$ and typical $T \sim T_m = 920 \text{ K}$ ^[189], the cooling rate $\frac{dT}{dt}$ is of the order of $5.2 \times 10^4 \text{ K s}^{-1}$.

It should finally be pointed out that particulates are not always undesirable. In the process 'pulsed laser vaporisation controlled condensation', particulates are produced using a cold screen and the ablation of a target material^[190] and can have novel electric, optic, magnetic, photochemical and catalytic properties, depending on their composition.

3.4.2 Reducing and Removing Particulates

Particulates between 0.1 and 10 μm in size and the production of high energy species which enhance film quality are often coupled phenomena. To take advantage of the higher energy species for better thin-film quality, the splashing of microscopic particulates must be reduced. Table 3.2 provides a summary list of the methods which have been reported in the literature. Some of these tabulated methods could be incorporated into our system with relative ease and little, if any expense; these are referred to below. Many of the other techniques which are listed as successful for reducing or removing particulates could be tried with further investment of specialist equipment.

Laser fluence on the target has the most significant influence on the particulate size and density. The simplest approach is to reduce the laser power density, at the same time, the benefit of having the high energy species, which can improve the thin-film quality, is sacrificed^[191, 143].

A change in wavelength of the excimer laser would be possible. Currently the laser is filled with a krypton and fluorine mix to operate at 248 nm, it would be possible to switch to an argon and fluorine mix, reducing the wavelength to 193 nm to look at film deposition at a higher photon energy^[186, 192]. The target could be spun at a much higher rate^[193]. The problem with this remains overheating of the motor itself since conduction into the chamber is minimal and convection is not possible in vacuum.

The surface of the target could be polished after a small number of film growth runs. This would drastically reduce the number of films that could be produced in a given time due to the extra labour involved but would provide a smooth target surface at regular intervals^[194, 195]. Small substrates could be orientated end-on so that both sides are slowly coated simultaneously^[184]. It will however be shown that the angle which the substrate makes relative to the plume direction can affect the film thickness. Changing the target to substrate distance might find a more optimum separation to reduce the particulate density

Technique	Comments	Reference
Charged Substrate	A negative potential applied to the substrate repels charged particulate matter.	[83]
Laser fluence	There is an optimum fluence for a given material which produces minimum number of particulates.	[191] [143]
Twin targets	Two targets orientated so that their lines of normal incidence cross. If a laser pulse is split so as to ablate both targets simultaneously, the intersection produces a high pressure zone redirecting the lighter species towards the substrate surface.	[196]
Hot screen	A heated screen reflects the plume matter, additionally heating the particulates, so reducing their cooling rate.	[197]
Laser wavelength	Choice of wavelength for the ablating laser can reduce the number of particulates, the absorption coefficient of the target is critical to particulate generation.	[186] [192]
Twin laser ablation	Two pulses are separated by a short delay, the first ablates the target and the second parallel to the target surface (delayed slightly) heats the plume.	[198]
Spinning target	If the target spins at high speed, the tangential momentum of the ablated matter will divert larger particulate matter away from the substrate centre.	[193]
Chamber pressure	A lower quality vacuum or a background gas in the chamber increases particulate size due to increased number of molecular collisions and combinations.	[199]
Surface quality	Rough target surfaces, have out growths from previous pulses has increased particulate matter when compared to recently polished surfaces.	[194] [195]
Substrate orientation	A substrate which is end on, i.e. forms the normal to the target surface, has both sides coated simultaneously with a reduction in particulates.	[184]
Target-substrate distance	An optimum separation of the target and substrate reduce particulate density. Too close and the thin film is not stoichiometric and conversely the plume cools and condenses into larger particulates.	[200] [201]
Gas jets	Nozzles eject high speed gases into the plume after a pre-set delay, collisions can be capable of momentum transfer to the larger particulates due to increased diameter.	[202]
Liquid or heated target	Heating the target material into its liquid state has been shown to reduce the particulate density of the deposited thin films.	[203] [204]
Mechanical filter	Spinning discs or rotating vines are used to capture material travelling less than a predefined speed. Based on the principle that particulates are slower than the initial plume components.	[205] [206]
Gas directioning	Using an atomic gas to redirection lighter plume components towards substrate. The heavy particulates are unaffected. Continuous flow at slower speeds than the gas jets approach above.	[207]
Thermal conductivity	Addition of elements which improve the thermal conductivity of the target has been shown to reduce the formation of particulate production, e.g. addition of Ag.	[208]
Pulse length	The duration of the ablating pulse changes the particulate density, CW laser evaporation often has a lower particulate density as longer pulses heat the developing plasma plume further. Linked to laser fluence value.	[160] [168]
Beam homogeneity	Excimer and CO ₂ gas lasers have low quality beam homogeneity. The intensity variation across the beam profile can increase particulate density.	[209]
Symmetrically centred beam	Symmetric positioning of the beam over the target centre automatically reverses the direction of the laser beam with respect to the target, avoiding shadowing effects and reducing surface texturing.	[210]

Table 3.2. Methods used to reduce the undesirable particulate material inherent in PLD.

which has been successful for a number of other researchers [200, 201]. Some of these ideas will be shown in Section 5.3 and 5.4 when looking at the optical properties of the thin film deposition parameters.

3.5 The Design of a New Vacuum Chamber

3.5.1 Vacuum Technology

Vacuum pumps have an optimum pressure range over which they operate, this does not always start at atmospheric pressure and so requiring a 'roughing' pump to first reduce the pressure to one which is safe to start pumping via the second device. This creates a sequential link of pumps, each pumping the chamber to lower pressures than the preceding one. Rotary pumps are most commonly used as roughing pumps to reduce gas pressure before connection to either one or more of the following: Molecular drag, Turbo-molecular and cryosorption (trapping type pump). It should also be noted that some gases present special pumping problems. H_2 and He have high molecular speeds because of their low mass. This limits their compression in molecular-drag, turbo-molecular or oil-diffusion pumps, all of which use supersonic velocity of the pumping medium to push molecules along.

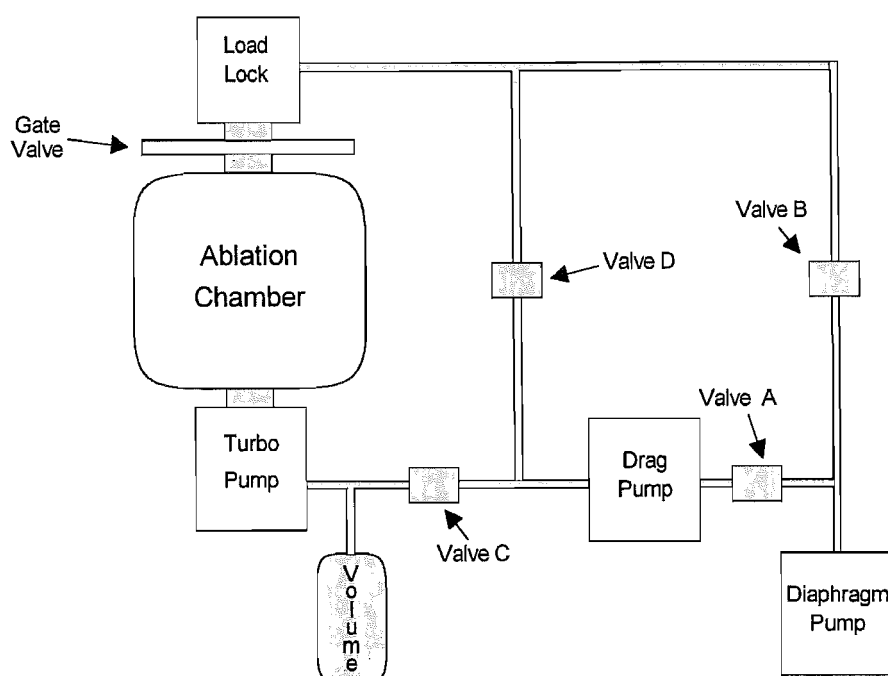


Figure 3.2. Schematic of pumping system for Pulsed Laser Deposition Chamber. {Original in colour}

The materials used in the deposition chamber must be chosen carefully to minimise contamination. Pumping down from atmospheric pressure can stir up dust and particles from

previous depositions, throwing them onto the substrate. Regular chamber cleaning is required for high quality samples to be repeatedly produced.

3.5.2 System Design

The main stainless steel chamber has a diameter of 50 cm and a volume of 59 litres. Three vacuum pumps were used to reduce the pressure to 1×10^{-7} mbar, all being oil free to help reduce contamination. The chain starts with the a diaphragm pump used to reduce the initial chamber pressure to 10 mbar, this precedes a molecular-drag pump capable of reducing the pressure to 1×10^{-2} mbar before the final stage is achieved via a turbo-molecular pump. The finished system takes five hours to pump down to operating pressure and because of this a 'load-lock' arrangement is used. Having a volume of around an eighth that of the chamber we can reload with a new substrate and return to growth pressure within an hour.

To reduce the duplication of pumps the load-lock is roughed using the first two main system pumps via an arrangement of valves, before the gate valve is opened. A schematic of the arrangement is shown in Figure 3-2. During deposition, the valves labelled B and D are closed. To change a substrate after deposition the gate valve is closed and the load lock opened. Once reloaded valve A is closed and B opened to rough the load lock. When the pressure has reduced to 10 mbar valve B is closed and A reopened. By following the same procedure with valves C and D the load lock pressure is quickly reduced to 1×10^{-2} mbar and upon restoring the valves to their operating positions, the gate valve can be opened again. This increases the chamber pressure to around 10^{-3} mbar, but only takes in the region of twenty minutes to recover. A two litre volume has been added between valve C and the turbo pump. This acts as an enclosed volume for the exhaust gases whilst this valve is closed during load lock pump downs.

We designed the resulting chamber to have many ports strategically placed around the walls and one viewing port on the lid. Some ports are for electrical feed-throughs, pressure gauges, some for possible interferometric film measurements and three with ultraviolet windows for a range of excimer laser input angles.

3.5.3 Internal Features

A versatile substrate holder was designed so as to take advantage of the proposed substrate lowering facility to move new, clean substrate materials from the load lock to the chamber, mechanically. The substrates are lowered into the chamber on a 700 mm stainless steel pipe, the lower end of which is at the top of the load lock during the substrate change. Figure 3-3 shows the substrate holder. The four main sections are made from alternating stainless steel

and aluminium so to prevent seizure of the dovetail joints during substrate heating. The arrangement allows for angular changes i.e. the target and substrate not necessarily parallel, target-substrate separation (± 40 mm), plume centre alignment (± 10 mm) and substrates of various shapes and sizes to be accommodated ($60 \text{ cm}^2 \text{ max.}$).

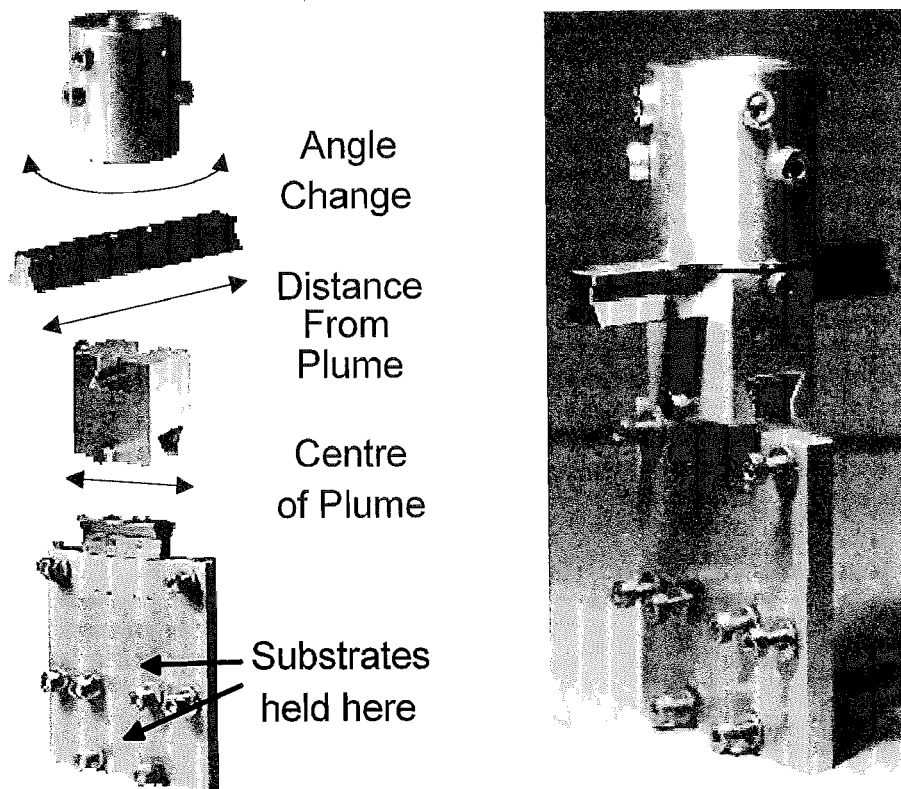


Figure 3-3. Pictures of the components and their individual function for the substrate holder in the Pulsed Laser Deposition Chamber. {Original in colour}

A coil of vacuum compatible heater wire is fastened to the back of the substrate holder which is capable of heating the substrates to in excess of 600°C . The pipe over which the cup at the top of the substrate holder fits can be filled with liquid nitrogen increasing the range of temperatures available to us, down to -124°C . Early work with thin films of GLS showed that growth at room temperature shifted the visible cut-off to shorter wavelengths when compared with films grown at 150°C . This introduced the need to cool the substrate further to examine this trend.

Figure 3-4 is a schematic of the above arrangement with the load lock position shown for the two states. In the lower position the substrate is mechanically oscillated vertically by ± 13 mm to improve film uniformity in one dimension. Uniformity is improved in the second dimension by means of a "wobble device". Shown in Figure 3-5, the target holder spins off axis which achieves two objectives, firstly the spinning target prevents hole drilling by the incident excimer

laser and since the ejected plume is always perpendicular to the target surface, this constant angular change scans the plume in a horizontal direction.

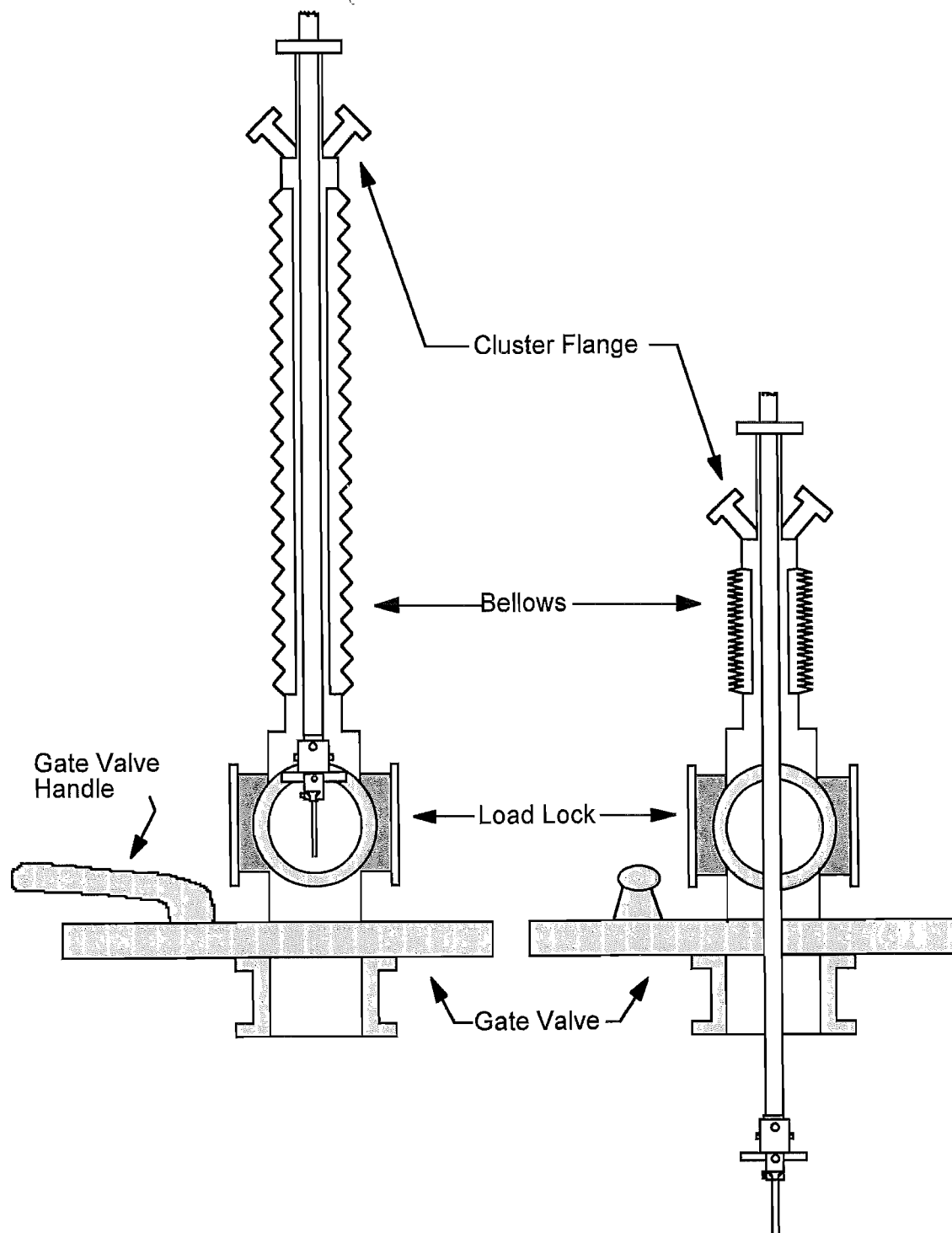


Figure 3.4. Schematic of substrate mounting and extraction using load lock arrangement for Pulsed Laser Deposition Chamber. {Original in colour}

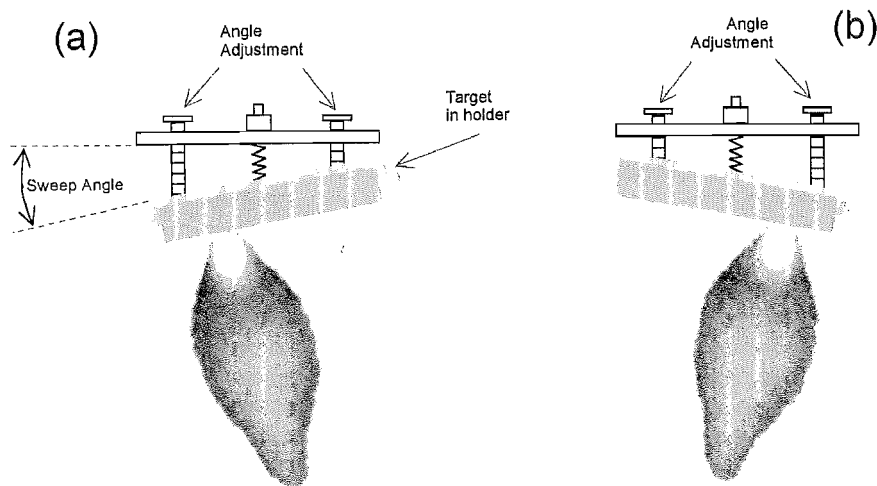


Figure 3.5. Schematic of the target holder, nicknamed the 'wobble device' which was used to continually alter the direction of the plume and so create a painting effect, before and after rotation, (a) and (b) respectively. {Original in colour}

3.5.4 Summary of the Final Design

The ablation chamber has been designed to allow access to the substrate holder without returning the main chambers pressure to atmospheric. This was achieved by mounting a *gate-valve* on the lid of the chamber and below a *load-lock*, allowing the substrates to be taken out of the chamber whilst only having to increase the load-lock pressure to open the system. The arrangement also prevents air and other contaminants, particularly water vapour, from entering the main chamber each time a substrate is changed. The main chamber only has to be opened to replace worn out targets or change type. With a bellow construction above this load-lock it was possible to mechanically raise and lower the substrate holder between the load-lock and chamber below, all at around 1×10^{-7} mbar. Prior to insertion into the chamber load lock, the substrates were cleaned and degreased.

The substrate holder is attached via a dovetail joint to a stainless steel cup. In turn this cup fits, snugly over the end of a 700 mm stainless tube. Any temperature between -124 and 600 °C can be selected, for substrates up to 60 cm² which in turn can be moved in three dimensional space relative to the target. During deposition, the target was rotated azimuthally while the laser beam was directed off axis to provide a uniform circular erosion pattern. With the mechanical oscillation in the vertical plane and the "wobble device" controlling the horizontal oscillations, uniform films are routinely produced by our system.

Laser irradiation was provided by a rare-gas halide pulsed-excimer laser operated with KrF (248 nm, or 5 eV, photons) and a pulse duration of ≈ 20 ns. The beam was focused through

a spherical lens with a 20 cm focal length, passed through a fused quartz window in the growth chamber allowing the incident laser flux was varied from 2 to 16 Jcm⁻² by changing the beam area on the surface of the target. The ablated plume of material is ejected perpendicular to the target surface and deposited onto the substrate, positioned either parallel or at some oblique angle to the target at a distance of $\approx 4 \rightarrow 12$ cm.

3.6 Large Scale or Commercial PLD

Over the past decade Pulsed Laser Deposition (PLD) has become a routine laboratory tool with which to grow a wide variety of complex chemical compounds. A recent review of the literature has shown that this process can be used to grow uniform films over substrates up to 200 mm (8 inch) diameter in size with growth rates compatible with competing physical vapour deposition techniques [212, 213]. One of the drawbacks confronting laser-deposition is that there is little infrastructure or standardisation to support either laboratory or production process equipment. PLD has drawn on the infrastructure which presently exists for the semiconductor and electro-optics industry for tools such as vacuum gauging, mass flow controllers and vacuum pumps. However, for production-oriented applications, this laser driven process will require other types of monitors and controls which are presently unavailable from the semiconductor industry. Areas which need to be addressed before PLD becomes more than a research tool include keeping the chamber's entrance window clean from film deposits, monitoring and controlling On-Target Laser Fluence (OTLF), measuring and controlling film deposition rate and issues relating to target size and target resurfacing. With the right types of monitors and control systems in place the PLD process could be completely automated in such a way as to yield highly uniform and reproducible film growth properties.

As the PLD process is scaled up to large substrate sizes the diameter of the ablation target will need to be increased. Typically the focused laser beam is rastered across a complete target radius in order to achieve a high degree of film uniformity across the opposing substrate [212, 213]. Increases in the target diameter will produce changes in the focused spot size and therefore in the OTLF as the laser beam is rastered from the centre of the target to the target edge.

As the substrate size increases so does the amount of material that needs to be deposited, thus 156 times more material is needed to cover a 125 mm diameter substrate compared to that of a 10 mm diameter sample. This has significant impact on the laser requirements, target size as well as deposition chamber design. Possible ways to scale up the substrate size are:

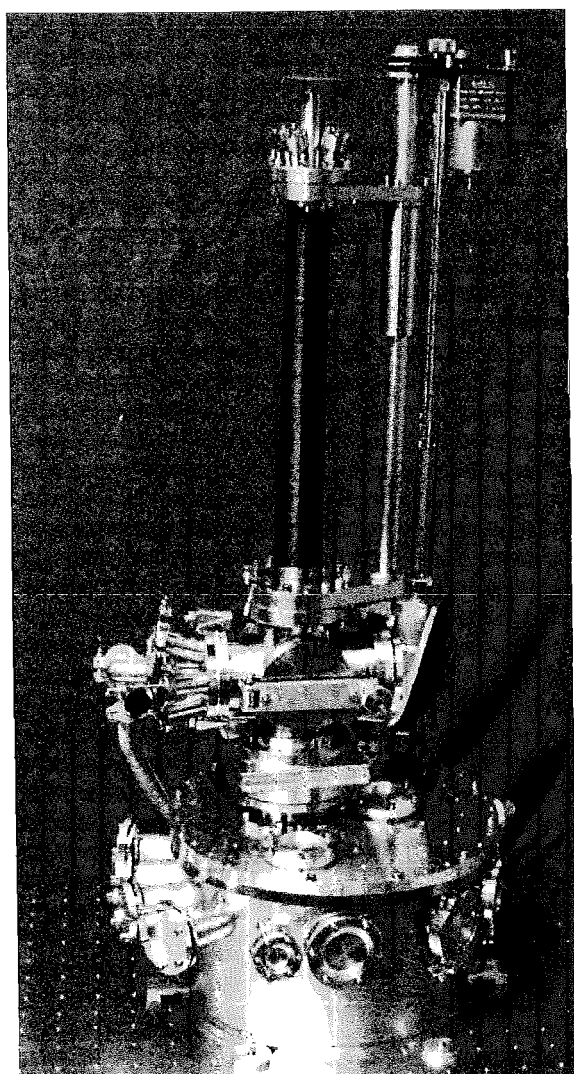
Off-axis PLD: The simplest scale-up approach is called "off-axis" PLD^[188]. In this case a focused stationary laser beam is directed at the outer edge of a small rotating target at an angle of 45° with respect to the target normal. The location of the ablation plume is offset by a fixed distance, from the axis of a rotating substrate. However, care has to be taken to prevent the plume direction change as a groove is slowly cut into a rotating target with stationary laser^[214].

Laser-beam rastering: Growing large-area films by PLD utilises a rastered laser beam^[215]. The focused laser beam is first reflected off a mirror and projected onto a large diameter rotating ablation target. The laser beam can be rastered with a variable velocity back and forth across the entire target diameter if desired. By allowing the beam to dwell longer at larger radii the centre of the plume is directed at the outer edge of the rotating substrate which greatly improves the films uniformity.

Laser ablation has been very successful mainly in the production of high temperature superconductors. Most of its success to date has been with films which contain or are grown in a background gas of oxygen. As more elaborate arrangements develop this will become a standard manufacturing technology, to produce high quality commercial thin films. Further work is needed to reduce particulate matter so that other materials can be produced with similar results.

4

Gallium Sulphide Based Glasses



Chamber used for Pulsed Laser Deposition during this research project.

4.1

Production of the Glass Targets

4.2

EXAFS Analysis

4.3

Components and Impurities

4.4

Absorption and Fluorescence

4.5

Conclusion

4.1 Production of the Glass Targets

4.1.1 Methods for Synthesis of Chalcogenide Glasses

The production technology of chalcogenide glasses differs from that of oxides, mainly due to the necessity of removing from the glass melt traces of oxygen and hydrogen, present mainly as oxides of various elements (extrinsic and intrinsic), hydroxides containing OH-groups, sorbed molecular moisture, etc. Also intolerable are carbon and carbon compound impurities. Chalcogenide glasses with high transparency must not contain these impurities. There two principal methods of synthesis:

- 1) Synthesis in a flow of inert gases or other oxygen-free gaseous substances (in practice nitrogen).
- 2) Synthesis in evacuated vessels or in the atmosphere of inherent vapours.

The first method generally involves mixing the dry starting powders in a crucible and heating the mixture at the required temperature, for the necessary duration. An advantage of having an open crucible is that it is possible to mix/stir the molten glass during this initial processing stage. However a disadvantage is that sulphur and selenium vapours can escape. In the case of arsenic based materials being used arsenic oxide could easily form in these conditions. Together these examples show that there are complicated safety procedures to instigate.

This drawback is removed by the second method. The starting powders still need to be mixed, initially in an inert gas to prevent oxygen, water vapour or other contaminants entering the mixture before it is sealed in the required, gas or vacuum conditions.

4.1.2 Glass Targets Manufacture

High purity powders of Ga_2S_3 and La_2S_3 were supplied by Merck, UK and combined in a glovebox containing dry nitrogen. For GLS targets, the powders are thoroughly mixed, unless otherwise stated, with 70% molar mass of gallium sulphide and 30% molar mass of lanthanum sulphide. When targets are doped some of the La_2S_3 is substituted by a trisulphide of the required rare earth, usually 1–3% molar mass of the total. Approximately 10 g of thoroughly mixed powder is transferred to a vitreous carbon crucible, pre placed in a silica ampoule. The carbon is required to prevent the glass melt from reacting with the silica ampoule walls. This reaction devitrifies the melt. The ampoule is evacuated, sealed and placed in a furnace at 1200 °C for 2 hours to melt the powders. To prevent crystallisation the liquid is quenched in room temperature water, resulting in a 10 mm thick glass disk. The edges of the finished target showed signs of bubbling where the sides were in contact with the crucible walls, but these however affected only the first one millimetre of material. Finally one surface is polished to give a clean, smooth finish which will face the laser pulses

when transferred to the chamber. This methodology is standard for the production of similar materials with appropriate variations on temperature, time and quenching methods.

The above procedure is almost identical for the production of the other glass materials. Sodium sulphide has to be stored in a sealed blackened container as even small amounts of UV change the starting powders from white to a lilac/pale purple colour.

Smaller disks are also made from a percentage of the original powder, following the above procedure. These are ~ 12 mm in diameter and 5 mm thick. They are used as bulk samples for measurements which are taken to compare with the deposited films. The target holder in our chamber is designed to hold glass targets with a diameter of 39.0 ± 0.5 mm. The holder has been carefully designed to provide a surface to radiate the absorbed power load and minimise conduction to the in-vacuum stepper motor. The rotor of this motor is poorly cooled owing to the absence of convection and gas conduction in vacuum, and very poor thermal conduction via the bearings. Hence thermal load on the rotor via the shaft must be minimised. This is achieved by having a large surface area on the target holder with minimal contact on the rotor shaft itself.

4.1.3 Quality of the Final Material

The principal property of optical glass, which sets it apart from glasses of other applications, is its high homogeneity. Optical glass must have a homogeneous composition, i.e., it should not contain inclusions (threadlike or laminated) with a refractive index different from that of the major glass melt, so-called striae. There must also not be long range chemical heterogeneities, which cause continuous changes of the refraction index in the glass volume. It must also be free of heterogeneities arising from irregularities of a physical character, namely, double refraction, caused by mechanical stresses. Apart from high homogeneity, optical glass must have a maximum transparency in the required wavelength interval. Whilst most of these properties are not required in our targets, they are in our bulk samples when optical measurements need to be made.

The absence of the crystalline phase and other defects in oxide and some chalcogenide glasses is easily seen with the naked eye during examination in transmitted light or under a microscope. Whilst GLS is an exception, chalcogenide glasses are as a rule opaque for radiation with wavelengths less than 580 nm, i.e. they transmit only in the red/orange part of the visible spectrum range. The presence in the glass volume of different defects, such as bubbles or dark inclusions, deriving from unmelted powders or contamination, changes the physical properties. However the principal defect is usually partial crystallisation. It is worth pointing out that chalcogenide glasses which are opaque in visible light, require viewing with

an infrared microscope or lengthy X-ray structural analysis to check their optical quality. Acoustic surface waves have also been used to look for surface cracks^[215].

Gallium-lanthanum sulphide glasses are transparent and are yellow coloured; the intensity of the colour decreasing with increasing oxygen content on substitution of either La_2O_3 or Ga_2O_3 for one of its sulphide analogues. Fortunately, all of the glasses used in this work had partial transmission in the visible region which makes it possible to inspect the quality of the material by eye. Small bubbles appeared on many of the target materials which were easily removed by polishing the material on one surface. Whilst not essential when being used as an ablation target, due to congruent evaporation, at least one high quality piece is needed for bulk optical measurements, with both surfaces being polished and parallel.

4.1.4 Early Research with GLS

The gallium-lanthanum sulphide glasses were originally reported by Lozac'h *et al.*^[216] and the extent of the glass-formation domain has been discussed by Flahaut *et al.*^[51]. The rare earth sulphides (La-Er) are not glass formers but form reasonably stable glasses when mixed with other chalcogenide glass-forming sulphides. Glasses containing rare earth sulphides with gallium sulphide are stable with high glass transition and crystallisation temperatures (with a large separation between the two). The gallium sulphide-based glasses transmit very well into the infrared with a transmission cut-off at 10 μm .

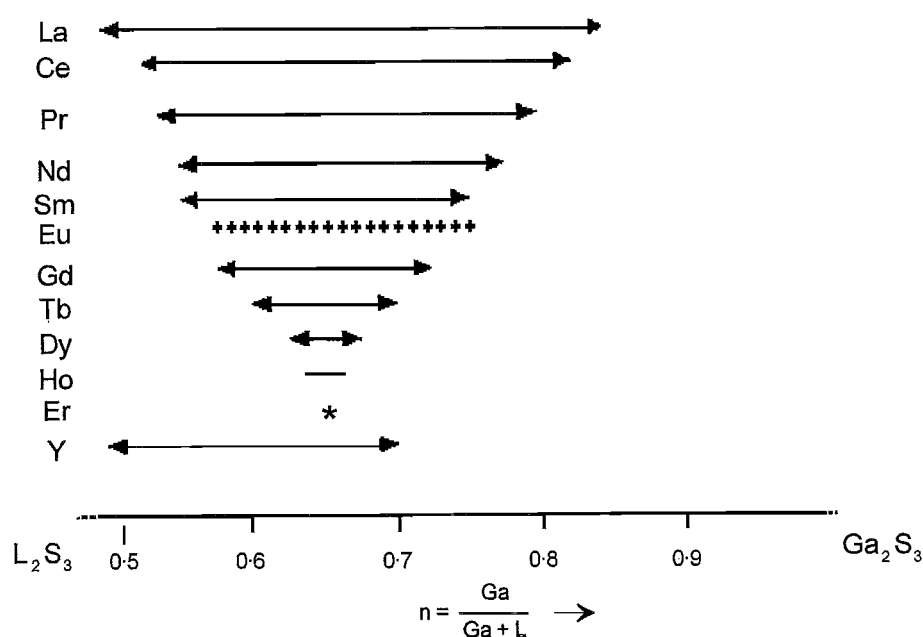


Figure 4.1. The extent of the glass forming region of Ga_2S_3 with other rare earths. (\leftrightarrow , *) homogeneous glass formed; (+) glass with crystals.

Figure 4.1 shows the extent of the homogeneous glass forming region for all the rare-earths. Lanthanum glasses have the most extended domain of composition and are formed with compositions from $n = 0.50$ to $n = 0.85$ when quenched from $1200\text{ }^{\circ}\text{C}$ ($n = \text{Ga}/\text{Ga}+\text{La}$). Moreover, lanthanum glasses constitute a very convenient matrix for fluorescent materials like other rare-earth sulphides, due to ion size and valency equivalence that makes substitution easy^[51-53, 58, 75].

The gallium lanthanum sulphide glasses have a high transition temperature (about $600\text{ }^{\circ}\text{C}$) which slowly decreases with increasing proportions of gallium sulphide. The crystallisation temperature is more rapidly decreasing, from about $680\text{ }^{\circ}\text{C}$ for $\text{La}_2\text{S}_3\cdot\text{Ga}_2\text{S}_3$ glass to about $600\text{ }^{\circ}\text{C}$ for $\text{La}_2\text{S}_3\cdot 6\text{Ga}_2\text{S}_3$ glass. So, from the thermal point of view, these glasses have a good stability at room temperature and they can conveniently be annealed at $500\text{--}550\text{ }^{\circ}\text{C}$.

4.2 EXAFS Analysis

4.2.1 Introduction

Whilst a crystal lattice is well defined and has an ordered structure, amorphous materials do not. Atomic arrangement for glass materials is more complicated as they have both local structure and long range structure which are very different. One technique for looking at the atomic arrangement of materials is EXAFS, although this technique requires a synchrotron radiation source and hence is expensive. The following subsections discuss the merits and limitations of EXAFS and show the results that were obtained during three visits to the CLRC synchrotron facility at Daresbury.

4.2.2 Synchrotron Radiation

A synchrotron accelerates charged particles, such as electrons, to speeds close to that of light. A series of magnets is used to bend the path of the electrons into a circular shape. As they pass these 'bending' magnets, the path of the electrons is deflected and they emit intense beams of light, known as synchrotron radiation. Discovered in 1947^[217], the first facility became available in Washington in 1961^[10]. A Synchrotron Radiation Source (SRS) is usually a three stage machine, comprising a linear accelerator (an 'electron gun'), a booster synchrotron and a storage ring. Electrons are fired from the linear accelerator into the booster synchrotron, where they are accelerated to almost the speed of light before being injected into a storage ring. Here the electrons travel in a vacuum inside a tube around the circumference of a ring and remain stored in orbit producing synchrotron radiation. This radiation is produced at each of the bending magnets and covers part of the electromagnetic spectrum, from infrared through gamma-rays. This light can be fed to a number of experimental areas, where researchers select the proportion of the spectrum that

they need and use it to perform experiments. It is used to investigate the structure and properties of all forms of matter.

Whilst there are presently around 30 synchrotron facilities throughout the world today, only the Central Laboratory for the Research Councils (CLRC) exists in the UK. The present facility is a 2 GeV source, 96 m radius storage ring. There are 40 stations along the various beamlines all simultaneously using the source which lasts approximately 20 hours between 'beam dumps'.

4.2.3 X-ray Absorption Fine Structure

In the XUV region (Extended Ultra Violet, which encompasses wavelengths down to 7 nm^[218]), for example, much insight has been gained on the band structure of pure and mixed solids by observing the properties of ejected photoelectrons using the well defined polarisation characteristics and continuous spectral nature of synchrotron radiation. The XAFS (X-ray Absorption Fine Structure) region yields details of the local order around a spectroscopic centre (absorbing species) such as a metal atom. Thus irrespective of the sample state, detailed information has been gained on diverse materials such as metallo-proteins, surfaces and glasses. There is a close interplay between XAFS and crystallography. Indeed, XAFS is a special case of diffraction, where the modulations in the absorption spectrum are observed due to the diffraction of the photoexcited electron from the neighbouring atoms. In this way, the XAFS technique encompasses features of diffraction and spectroscopy.

X-rays can be absorbed by atoms in molecules. Generally, the proportion of X-rays absorbed (the absorption coefficient) will decrease as their energy increases, approximately as $1/E^3$. At certain values of energy, specific to each element, a sudden increase in the amount of energy absorbed is observed. This sudden rise in the absorption at the edge occurs when an incident X-ray photon has just sufficient energy to cause transition of an electron from the 1S state of some element (first edge, K) in the sample to an unfilled state of predominantly p-character (i.e. angular momentum $l=1$). In the near edge region, called XANES (X-ray Absorption Near Edge Structure) transitions may occur to unfilled bound states or nearly-bound states (resonance's). Well above the absorption edge, in the EXAFS (Extended X-ray Absorption Fine Structure) region, transitions are to a continuum of states. Edges due to transitions from the less deeply bound levels (e.g. 2S, 2P_{1/2}, 2P_{3/2}, 3S... which are designated L_I, L_{II}, L_{III}, M_I... edges) also occur at lower X-ray energies. These contribute a smooth background absorption to the K-edge spectrum. The L-edges are themselves suitable for measuring XAFS, particularly for higher atomic number elements for which the K-edge energies maybe experimentally difficult to reach.

Consider the wave nature of the ejected photoelectron and regarding the atoms as point scatterers a simple picture can be imagined in which the backscattered waves interfere with the forward wave to produce constructive and destructive interference. The phase of the back scattered wave at the central atom will change with the energy of the incoming photon. This leads to the oscillatory nature of the interference effect. Since backscattering amplitude and phase are dependent on the type of atom doing the backscattering and the distance it is from the central atom, information regarding the co-ordination environment of the absorbing atom can be obtained by analysing the EXAFS data.

EXAFS spectroscopy differs from diffraction X-ray techniques as it is sensitive only to short-range order and can be applied equally well to crystalline or amorphous solids, liquids and gases. As EXAFS is element-specific, the presence of impurities which either do not contain the absorber, or are far from the absorber, will not cause interference.

Once analysed the EXAFS data can provide information as to: how many, what type of atom and at what distance from a specific atom site it is located. These covalent bonded distances can be measured very accurately ($\pm 0.02 \text{ \AA}$). Other than the need for a synchrotron radiation source, structural information requires a high concentration of atom sites and probes a radius of 4-5 \AA from them. Co-ordination numbers and atom-type determinations are inaccurate. The data analysis is only straightforward for elements with atomic numbers greater than or equal to 20 (Ca).

It has become clear in recent years that there is no fundamental distinction between the physics of EXAFS and XANES; the distinction is only one of complexity of the spectra. For example, effects such as multiple scattering and energy dependence of the central atom absorption are more important in the XANES region. Modern theories are capable of modelling the entire spectral range within the context of multiple scattering theory. For this reason EXAFS and XANES are now referred to jointly under the more general term 'XAFS'.

4.2.4 Experimental Procedure

Typically a synchrotron radiation source is divided into 'beamlines' to allow many experiments to run concurrently. Our experimental results were produced during time spent on stations 3.4 and 7.1 at CLRC in Daresbury. Table 4.1 shows the basic parameters of the two beamlines for comparison.

The simplest XAFS experiments are done in transmission mode. X-rays are produced at a desired energy band of approximately 1 eV bandwidth and selected by diffraction in a silicon double crystal monochromator. Only those X-ray photons that are of the correct wavelength, will be reflected from the first crystal: The parallel second crystal is used as a mirror to

restore the beam to its original direction. The monochromatic X-rays then pass through the sample, which should absorb approximately 50%-90% of the incident X-rays. The incident and transmitted X-ray fluxes are monitored with gas ionisation chambers, containing an argon-helium mixture. This was the arrangement on Station 7.1 where absorption spectra for the gallium K and lanthanum L_{III} edges were recorded.

Property	Station 3.4	Station 7.1
Energy Range (keV)	0.8 to 3.5	4.0 to 10
Double Crystal Monochromator	Beryl 0.8-1.56 YB ₆₆ 1.07-2.00 Quartz 1.50-1.83 InSb(III) 1.68-4.00 Ge(III) 1.93-4.00	Si(III)
(with energy range, keV)		
Beam size (mm)	3 Ø	10 × 0.8
Detector	Ammeter, for current flow	Standard ion chambers, 20% Ar : 80% He
Substrates for thin films	Copper (for conduction)	Mylar (for X-ray transmission)

Table 4.1. Comparisons of the two beamline stations at the CLRC Laboratory at Daresbury, used for GLS analysis.

Films for this station were deposited on Mylar substrates. Mylar (aluminised polyester film) absorbs very little of the X-ray range in the region of gallium and lanthanum absorption edges. Typical XAFS data acquisition times on this station were 30 mins, with each sample being repeated three times for each edge. The three spectra were averaged after manual removal of the occasional obvious 'glitch'.

The sulphur K edge data were obtained on station 3.4 (SOXAFS: Soft XAFS), which has a chromium plated mirror to focus the beam at the sample. The mirror also has a high energy reflectivity cut-off at about 3.5 keV so that harmonic contamination of the monochromatic beam is minimal. The energy of the X-ray beam was defined using, an InSb(111) double crystal monochromator. Samples are placed in an evacuated chamber (10^{-6} mbar), since soft X-rays are appreciably attenuated in air. The electron drain current method was used to measure the absorption coefficient, $\mu(E)$ ^[219]. This method requires conducting samples; hence, the thin-film samples were deposited onto copper substrates for these experiments. Bulk glass samples are of high resistivity and the drain current method proved impractical. Measurements were made using powdered glass (30%) diluted in graphite and pressed into pellets and hence allowing the use of the drain current technique. Data collection from this

station typically took 45 minutes per scan. As with station 7.1 collection of at least three sets were taken and averaged.

4.2.5 Data Analysis

There are five variables which are fit to the EXAFS data. These are: The Debye-Waller factor (σ) which takes account of thermal vibrations and static disorder at a distance r_j away; r_j is the inter-atomic distance between the neighbouring atoms; E_{edge} is the minimum energy required to eject an electron out of a particular atomic state, known as threshold energy; The number of neighbouring atoms (N); and the mean free path of the incident or ejected electron, λ .

The traditional method of data analysis involves a sequence of steps: correction for instrumental effects such as detector dead time losses and resolution; spectrum averaging and removal of monochromator 'glitches'; normalisation of the spectrum to unit edge step to compensate for variations in sample thickness or concentration; selection of the energy threshold E_0 and interpolation to k -space; subtraction of smooth background (typically using cubic spline functions) to generate the EXAFS intensity $\chi(k)$; fourier transformation and filtering to produce single shell amplitude and phase; determination of model parameters using the 'ratio method' of nonlinear least squares fitting of data using empirical or theoretical standards.

A suite of programs are available at the Daresbury Laboratory, notably EXCALIB, EXBACK and EXCURV92^[220] to fulfil the above requirements. The EXCALIB program was used for summation of multiple data sets and calibration of their edges and absorption intensities. Pre- and post-edge backgrounds were removed by fitting low order (1-3) polynomials to the appropriate regions of the experimental spectra using the program EXBACK. The normalised EXAFS function $\chi(E)$, was first converted into $\chi(k)$ using

$$\frac{\hbar^2 k^2}{2m} = [E - E_{edge}] + E_0 \quad \dots\dots\dots (4.1)$$

Where E is the incident photon energy, E_{edge} is the appropriate threshold energy and E_0 is the energy offset, being the difference between the energy of a $k = 0$ photoelectron and the lowest unoccupied energy level. $\chi(k)$ is then multiplied by k^3 in order to compensate for the diminishing amplitudes of the experimental spectrum at high k -values^[220]. In order to obtain structural information, the program EXCURV92 was used to make a comparison of the least-squares fitting of the k^3 - weighted experimental spectrum to the theoretical spectrum

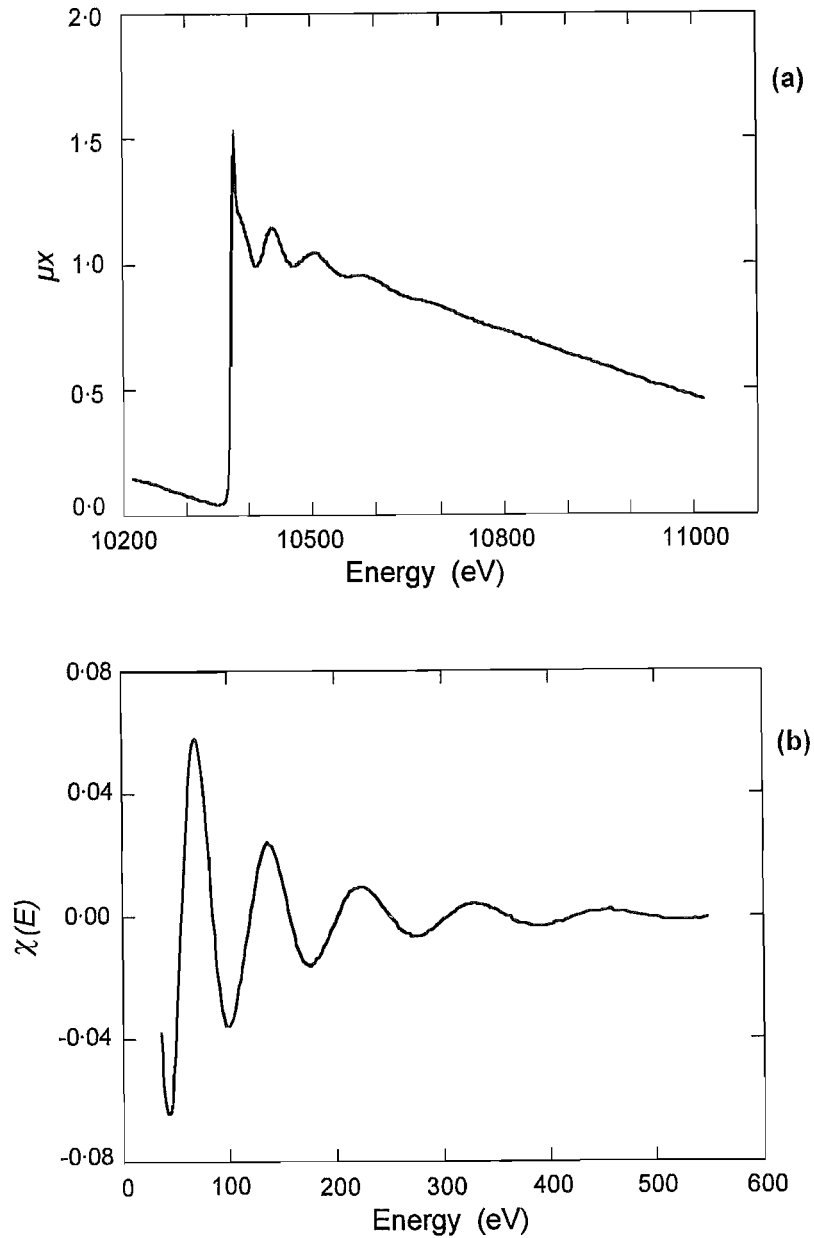


Figure 4-2. A typical XAFS spectrum for; (a) the gallium K-edge and (b) its respective Fourier transform function using the experimental data and the theoretical fit. {Original in colour}

which was calculated using the rapid curved wave theory^[221, 222]. The basic formula describing the theoretical EXAFS spectra for K edges is^[223]:

$$\chi(k) = -\frac{A(k)}{k} \sum_j \frac{N_j}{r_j^2} |f_j(k, \pi)| \exp(-2\sigma_j^2 k^2) \exp\left(\frac{-2r_j}{\lambda}\right) \sin(2kr_j + 2\delta(k) + \psi_j(k)) \quad (4.2)$$

where k is the momentum of the photoelectron, N_j is the number of atoms at a distance r_j each with a back-scattering amplitude $f_j(k, \pi)$. $A(k)$ is a correction factor for absorption events that

do not result in EXAFS, such as multi-electron excitations. λ is the elastic mean free path of the photoelectron (only elastically scattered electrons can interfere). It is this factor which restricts the range of contributions to $\chi(k)$. The exponential term is a Debye-Waller factor in which σ_j^2 is the mean square variation in the inter-atomic distance between emitting and scattering atoms. This accounts for both thermal motion and static disorder. The term δ is the phase shift produced by the passage of the photoelectron through the emitting atom potential and ϕ is the phase of the back-scattered wave.

Structural information was obtained by multi-parameter fitting of the experimental data to the EXAFS function in k -space. The parameters fitted were bond length (r_j), co-ordination number (N_j) and mean square variation in bond length (σ^2). The amplitude reduction factor ($A(k)$), which takes account of events such as shake-up and shake-off process at the central atom^[223], is obtained from EXAFS data for a crystalline $\text{Mn}_6\text{Ga}_2\text{Mn}_2\text{S}_{14}$ sample taken during the same experimental shifts as our glass samples. This factor was varied on the standard sample to obtain a most likely value for each atom type; its magnitude was fixed at this 'best' result thereafter. The useful energy range of the spectra extended to 500 - 600 eV for gallium and sulphur, and 400 eV for lanthanum above the edge and Gaussian windows were used in the Fourier transformations. The result of a Fourier transform is a series of peaks, corresponding to each shell of atoms contributing to the EXAFS. Figure 4-2 shows an example of the k -edge data as seen during (a) initial acquisition and (b) its resulting Fourier transform.

4.2.6 Results and Discussion

4.2.6.1 The Data

The compositions of the samples were determined by a DS 130 scanning electron microscope (SEM) to which an energy-dispersive X-ray analyser (EDAX) was attached. No significant variations in composition were found between different areas of the same samples, showing that the GLS films were compositionally homogeneous, at least down to a scale of $5 \times 5 \mu\text{m}$ (the area probed by the EDAX measurements). Transmission electron microscope measurements yielded electron diffraction patterns consisting only of a few diffuse rings, indicating that the ablated GLS films were amorphous. The samples were grown with 9000 pulses (10 Hz) from a $70\text{Ga}_2\text{S}_3:30\text{La}_2\text{S}_3$ target and substrate located parallel at 80 mm away in vacuum. The energy density used to grow the thin films were 3.0, 3.5, 4.0, 5.0 and 6.0 J cm^{-2} .

Figures 4-3, 4-4 and 4-5 give examples of the background-subtracted EXAFS function $\chi(k)$, weighted by k^3 , and their associated Fourier transforms. As always with EXCURV92 output^[220], the Fourier transforms are phase-corrected so that the peaks appear at the true inter-atomic

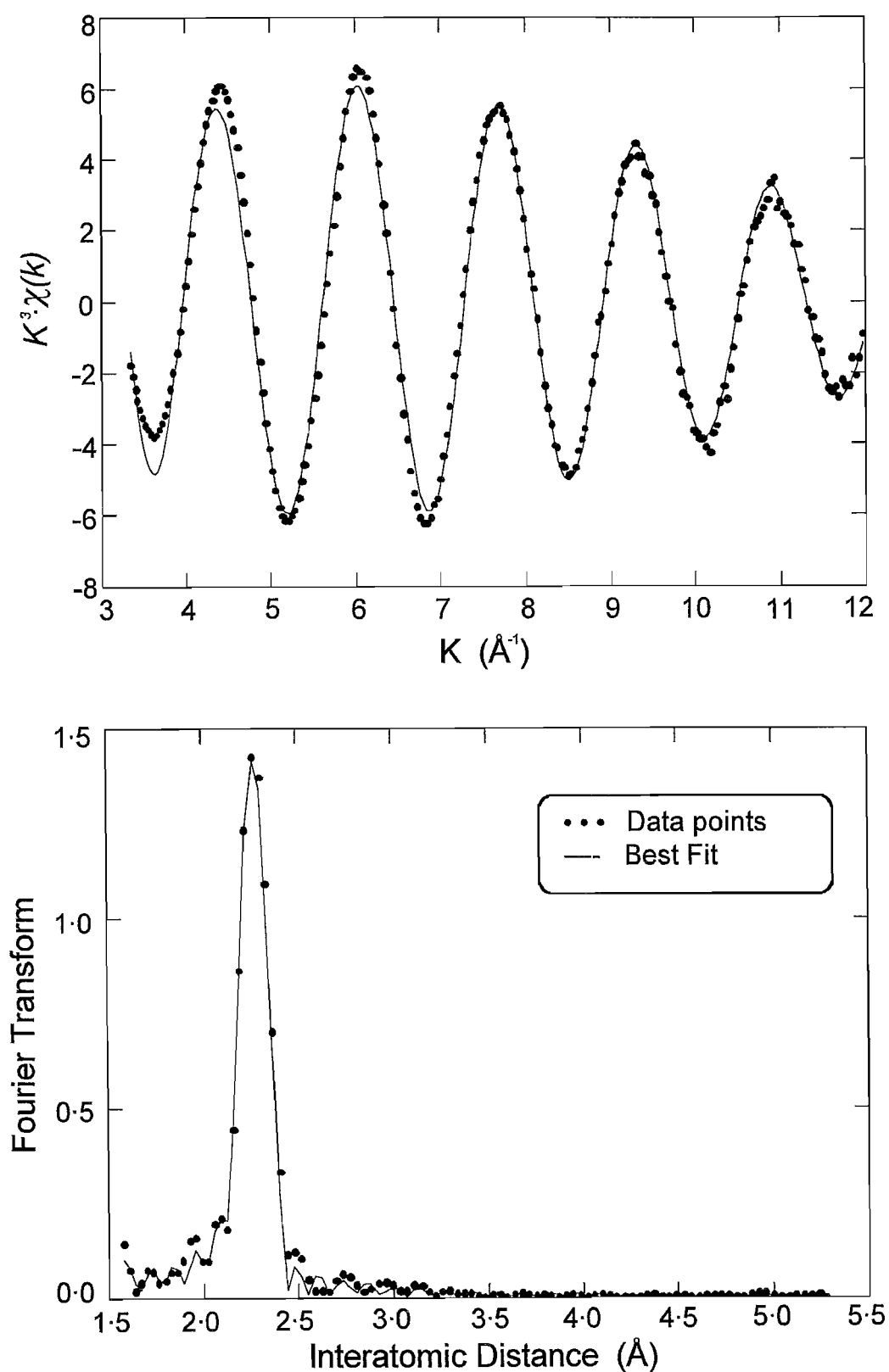


Figure 4.3. A typical example of a k^3 - weighted EXAFS curve for the GLS thin film (prepared at 3 J cm^{-2} energy density) at the Ga K-edge together with the corresponding Fourier transform. ••• - experimental results and — is the best fits to the data. {Original in colour}

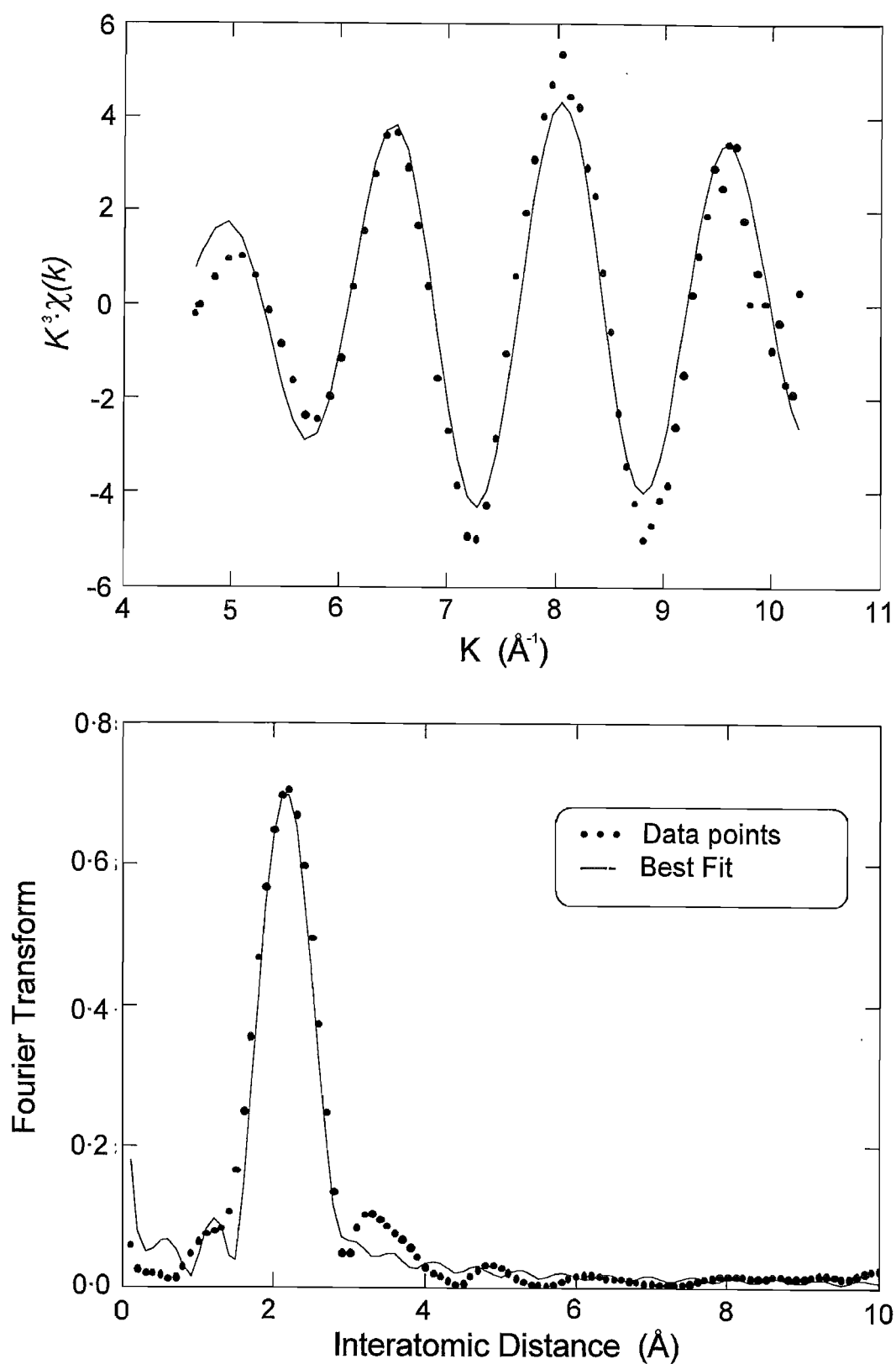


Figure 4.4. A typical example of a k^3 - weighted EXAFS curve for the GLS thin film (prepared at 3 J cm^{-2} energy density) at the S K-edge together with the corresponding Fourier transform. $\bullet\bullet\bullet$ - experimental results and — is the best fits to the data. {Original in colour}

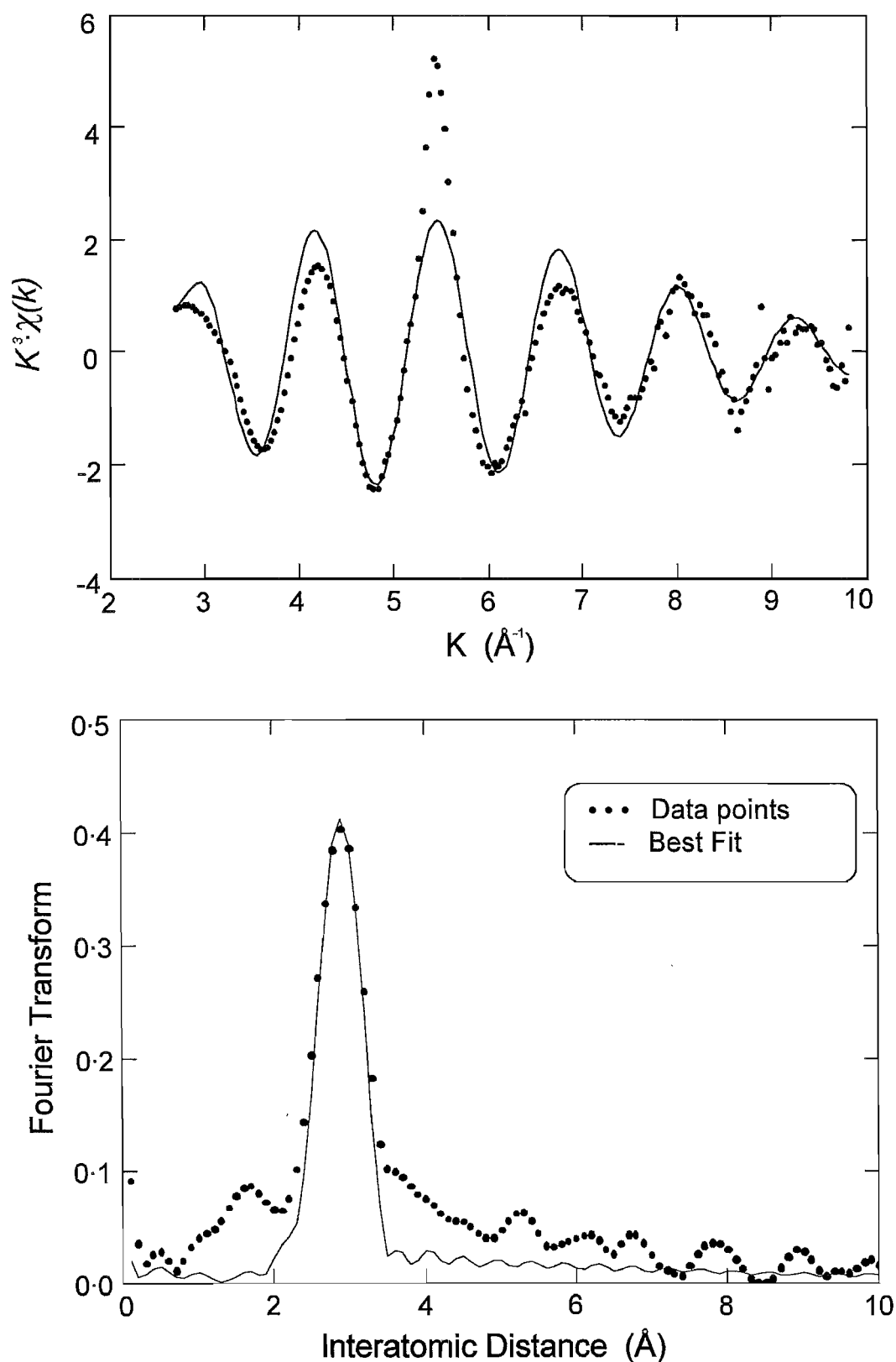


Figure 4.5. A typical example of a k^3 - weighted EXAFS curve for the GLS thin film (prepared at 3 J cm^{-2} energy density) at the La L_{III} -edge together with the corresponding Fourier transform. $\bullet\bullet\bullet$ - experimental results and — is the best fits to the data. {Original in colour}

distances. In most cases described here, the noise level was sufficiently low to allow data out to $k = 10 - 12 \text{ \AA}^{-1}$ to be used. Gallium K edge spectra (Figure 4-3) were typically excellent with very good fitting to the observed spectra. Sulphur K edge data (Figure 4-4) were also generally good, but slightly inferior to the gallium edge data in signal to noise and quality of fit. Typical lanthanum L_{III} edge data are shown in Figure 4-5. The relatively short data range for the La L_{III} edge spectra was unavoidable as the La L_{II} edge lies only about 400 eV above the L_{III} edge. The EXAFS spectra obtained from the La L_{III} edge measurements each show an additional peak between $5-7 \text{ \AA}^{-1}$ due to double excitations involving the 2p and 4d electrons^[224]. However, in spite of this we were still able to analyse the La L_{III} edge data. The La edge EXAFS spectra (typical example shown in Figure 4-5) have a remarkably constant phase and a slowly decreasing amplitude with increasing energy density, suggesting that the La environment is constant.

The data are unusual in that they include EXAFS data derived from all three elements present, allowing a detailed picture of the glass structure to be derived, and internal consistency checks. The EXAFS results, for bulk GLS, are in good agreements (within experimental error) with that found by Benazeth *et al.*^[225]. However the earlier data was much more limited as it only provided data from the Ga and S atom environments.

4.2.6.2 Co-ordination Numbers

Figures 4-6(a) and 4-6(b) show that the gallium and sulphur, and lanthanum partial co-ordinations, as well as the total co-ordination number for both gallium, N_{Ga-T} , and sulphur, N_{S-T} , as functions of the thin film deposition energy density. The dotted horizontal lines in this figure and subsequent figures correspond to the values in the bulk glass sample. It can be seen that for the ablated films the partial co-ordination number of Ga, N_{Ga-S} , and S, N_{S-Ga} , decreases with increasing energy density. This behaviour may be interpreted as the breakage of Ga-S bonds and the formation of homonuclear bonds ('wrong bonds'), i.e. Ga-Ga and S-S. This view is clearly supported by the associated increase in the Ga-Ga, N_{Ga-Ga} , and S-S, N_{S-S} , co-ordination numbers. It should be noted that, within the error limits indicated, the total gallium co-ordination N_{Ga-T} (obtained by summing the partial Ga co-ordinations) is approximately 4.0 throughout the energy density range studied. The fourfold total co-ordination of gallium in GLS samples, together with twofold sulphur, implies that the bonding is covalent, obeying Mott's 8N co-ordination rule^[226]. By means of EXAFS measurements on GaAs flash-evaporated samples, Theye *et al.*^[227] and Del Cueto *et al.*^[228] did detect Ga-Ga bonds at distance of $2.46 \pm 0.03 \text{ \AA}$ ^[227] and 2.45 \AA ^[228].

It is also clear from Figure 4-6(a) that lanthanum (N_{La-S}) was always approximately eight-coordinated by sulphur, indicating that there is no observable change in the local

environment of the La atoms. The EXAFS experiments could not detect any La-La bonds in any of our samples. Attempts to fit La-La bonds at 3.1 Å (the first nearest neighbour distance in

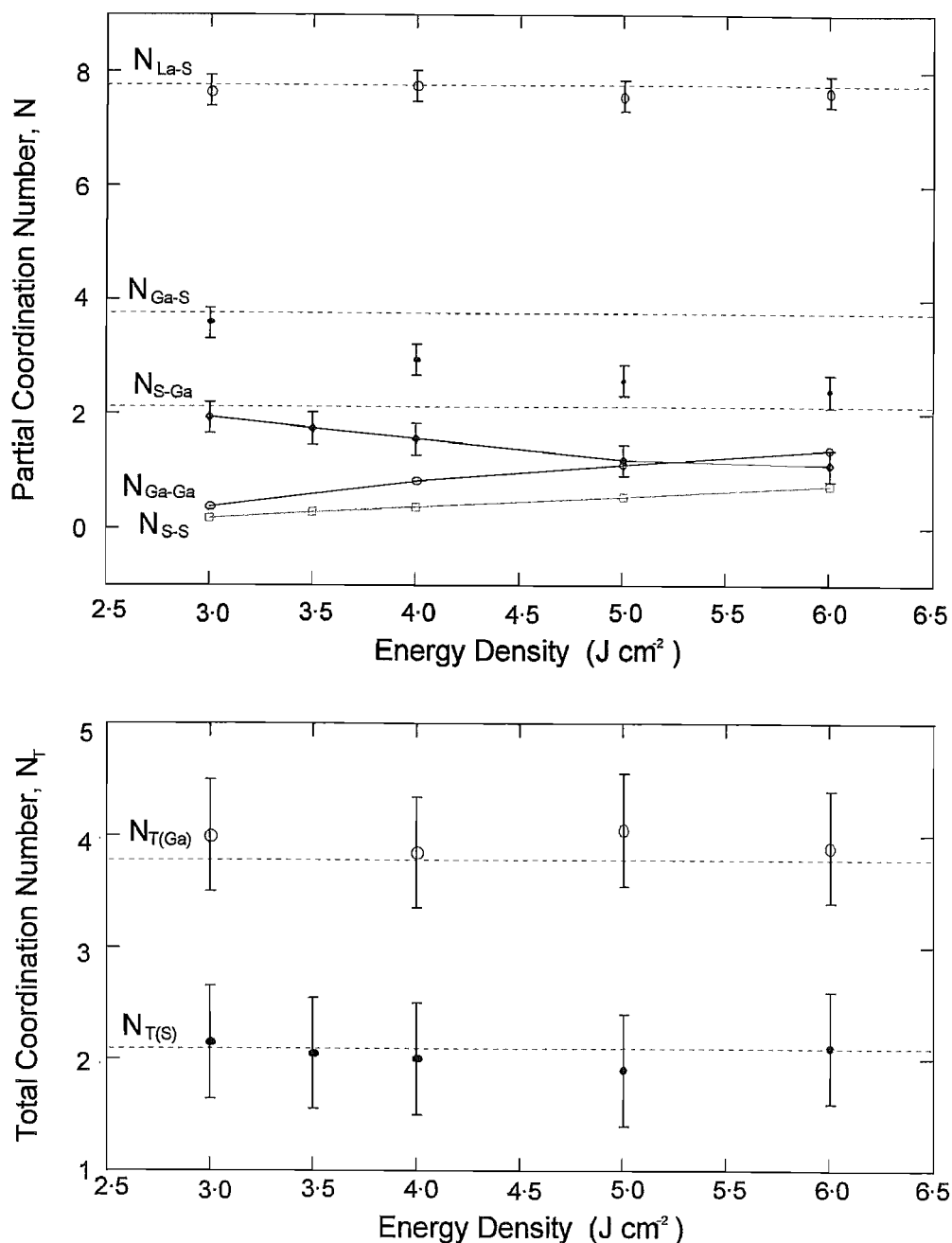


Figure 4.6. (a) The partial co-ordination numbers obtained from EXAFS data as functions of the energy density in GLS thin film samples. (b) Total Ga and S co-ordinations as functions of the energy density. The solid lines are drawn as a guide to the eye. {Original in colour}

metallic La) or at distances around 3.4 Å (twice the covalent radius of La) did not produce significant improvements to the fits. This could reflect a very large spread in the bond length of any La-La bonds, or more probably a low level of La-La bonds. Our results show that gallium is always four-fold co-ordinated in the GLS network. Both Ga-Ga and S-S bonds occur in GLS thin-film samples but the lanthanum atoms remain co-ordinated by sulphur alone.

4.2.6.3 Bond Lengths

The fitted values for the various bond lengths are plotted as a function of thin film deposition energy density in Figure 4.7. r_{Ga-S} denotes the Ga-S interatomic distance fitted from Ga edge EXAFS data while r_{S-Ga} represents the same bond length but deduced from S edge measurements; r_{La-S} is the La-S bond length measured from La L_{III} edge. Inspection of the figure reveals that there is clearly consistency, within experimental error, between the experimental values for r_{Ga-S} and r_{S-Ga} . All of the bond lengths determined by our analysis were found to be independent of deposition energy density and within their uncertainties essentially the same as those found in the bulk glass. This shows that the mean bond length is unaffected by the type of bonds surrounding each atom. The lengths of the Ga-Ga and S-S bonds, as determined from our EXAFS analysis, were found to be 2.8 ± 0.02 Å and 1.9 ± 0.02 Å respectively. The values reported for the Ga-Ga bond length are 2.76 Å in amorphous Ga^[229] and 2.48 Å for dimers in crystalline orthorhombic Ga^[230]. The close similarity of our measured bond lengths to those of stoichiometric materials strongly suggest that the covalent bonds are well defined and unchanging entities in thin-film samples.

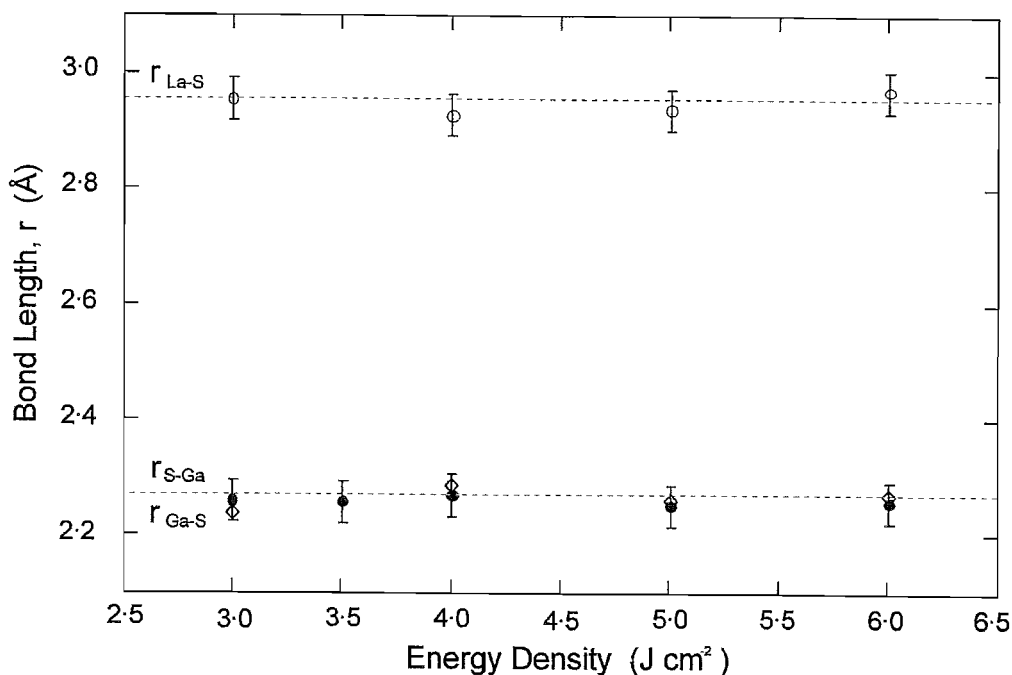


Figure 4.7. First-shell bond distances for GLS thin film samples prepared at various ablation energy densities, ○ - r_{La-S} , ● - r_{Ga-S} , ◇ - r_{S-Ga} . {Original in colour}

4.2.6.4 Debye-Waller Factors

The Debye-Waller factors, Figure 4.8, for Ga-S bonds determined from Ga and S edge data are clearly consistent with one another at all energy densities within experimental error. This is

expected since they both show the spread of the same bond length, namely Ga-S bond, and thus provide a consistency check on the fitted values. The values of σ^2_{Ga-S} and σ^2_{S-Ga} increase with increasing energy density, indicating an increase in the configurational (static) disorder of the bond length. This result is also consistent with optical data, where the Urbach parameter (disorder parameter) is seen to increase with increasing deposition energy density, see Section 5.3.2. For an amorphous structure, the Debye-Waller factor determined experimentally has contributions from both thermal and static disorder $\sigma^2_{(exp)} = \sigma^2_{thermal(cryst.)} + \sigma^2_{static}$. In the crystalline state, the above equation becomes $\sigma^2_{(exp)} = \sigma^2_{thermal(cryst.)}$ which allows as to estimate the static disorder of the amorphous materials. From our EXAFS analysis on the standard (crystalline) sample, the Debye-Waller factor for Ga-S was found to be $54 \times 10^{-4} \text{ \AA}^2$. By comparing this value with observed samples values (Figure 4.8) we can conclude that there is a considerable static disorder in the Ga-S bond length in our samples. It is also clear from the data presented in Figure 4.7 that there is no significant change in Debye-Waller factor for La-S bonds, σ^2_{La-S} , with energy density, which within experimental error are the same as that found in bulk glass. This suggests that the configurational disorder in the local environment of the La

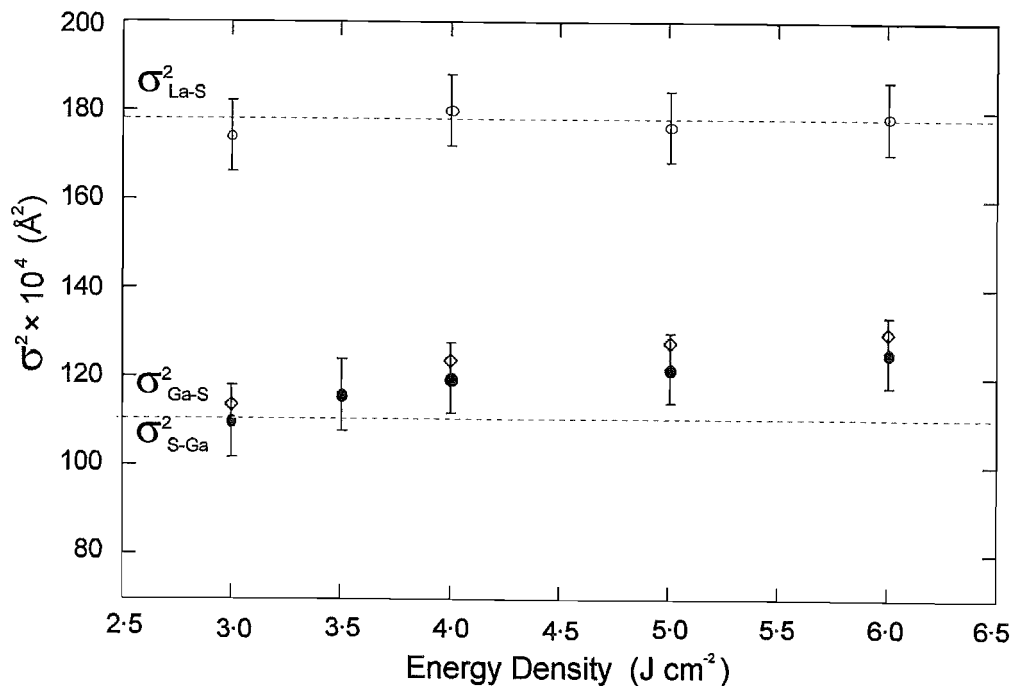


Figure 4.8. The energy density dependence of the mean square deviation in inter-atomic distances, σ^2 , obtained from the EXAFS data for GLS samples.

○ - σ^2_{La-S} , ● - σ^2_{Ga-S} , ◇ - σ^2_{S-Ga} , {Original in colour}

atoms is much the same across the energy density range studied and is consistent with the constant co-ordination number of La-S bond lengths described previously. The room temperature thermal contribution to σ^2 for the La-S bond is equal to $150 \times 10^{-4} \text{ \AA}^2$ (the value for the crystalline sample). Therefore, there is very little static disorder in the La-S bond length in

our samples. The Debye-Waller factors for Ga-Ga and S-S bonds in our thin film samples remain low ($90 \times 10^{-4} \text{ \AA}^2$ and $70 \times 10^{-4} \text{ \AA}^2$ respectively) at all deposition energy densities, indicating that bond length disorder for these bonds type is low. To my knowledge, there is no data available in the literature for comparison.

4.2.7 Summary of EXAFS Results

The EXAFS results clearly indicate that the deterioration in the properties of the films produce a high density of Ga-Ga and S-S 'wrong bonds', whilst the La co-ordination remains identical to that of the bulk glass to within experimental error. Although at low energy density the level of 'wrong bonds' falls below the EXAFS detection limit, the overall trend strongly suggest that significant densities of these defects remain even in the films prepared at low deposition energy density. It is also clear that this chalcogenide system is very much more difficult to ablate as a low-defect-density film than the extremely wide range of oxide based materials which have been successfully ablated^[231].

The results for thin film samples indicate that there is a significant change in the local environment of the Ga atoms as the deposition energy density is increased and the structure appears to be chemically disordered with Ga-Ga bonds favoured due to their lower configuration energy. Optical data are consistent with this (see Section 5.3.2). The bond lengths were found to be independent of the energy density and were the same as those found for bulk glass. Although the nearest neighbour is well defined, there is a considerable bond-angle variation, hence a wide variation in second neighbour distance.

The Debye-Waller factors for Ga-S determined from both the Ga and S edges were consistent with each other and vary appreciably with deposition energy. There is considerable static disorder in the Ga-S bond length, but little in the length of the La-S bond.

4.3 Different Components and Impurities

4.3.1 Components Used to Make Our Glasses

The backbone of the work undertaken throughout the course of my research was based on the gallium-lanthanum-sulphide components for starting materials. The initial and standard mix of $7\text{Ga}_2\text{S}_3:3\text{La}_2\text{S}_3$ was replaced by $3\text{Ga}_2\text{S}_3:7\text{La}_2\text{S}_3$ once the EXAFS results had shown that there was a general loss of bonding to sulphur and that the Ga atoms were forming 'wrong bonds' with each other. It can be seen from Figure 4.1 that this is outside of the glass forming region which ends at 50%. This reversed percentage material produced a target

that appeared as a chocolate brown disk of firm sponge like ceramic material with lots of voids. Whilst this is not an optical glass, the extremely high quenching rates achieved during laser ablation made it possible to produce an amorphous thin film from the target. Figure 4-9 shows the resultant thin films produced by pulsed laser deposition from pure Ga_2S_3 , pure La_2S_3 and the above two amorphous mixes. All of these films are amorphous as determined by X-ray analysis. Surface resistivity measurements showed that the La_2S_3 thin film has a value of around $1 \text{ k}\Omega \text{ cm}^{-1}$. For the other samples this was greater than $10 \text{ M}\Omega \text{ cm}^{-1}$, indicating they are non-metallic (Lanthanum based chalcogenide materials typically have resistivity values of $10^8 - 10^{11} \Omega \text{ cm}^{-1}$ [46]). It can also be seen from Figure 4-9 that higher lanthanum concentrations have a detrimental effect on the optical transmission of the films.

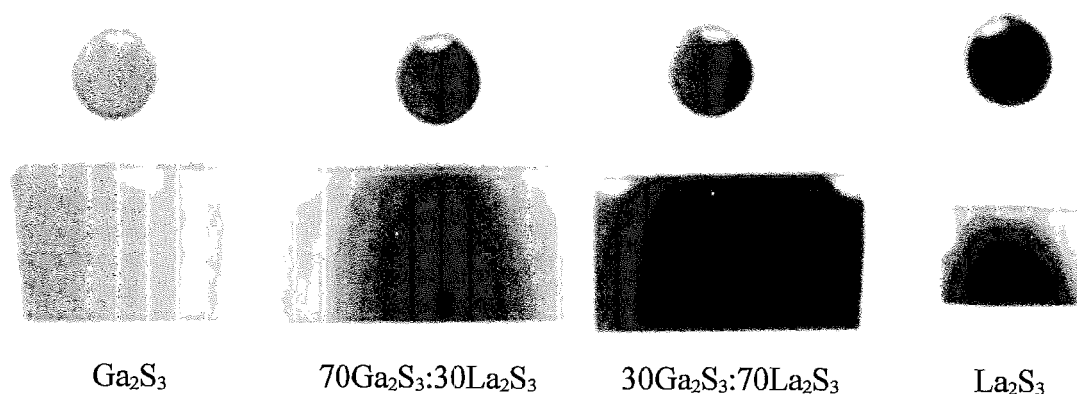


Figure 4-9. Thin films of differing percentages of Ga to La, starting at pure Ga to pure La, on both CaF_2 and BK7 glass pieces. {Original in colour}

Whilst it had been shown that the thin films were not stoichiometric and that both Ga-Ga and S-S bonds increased in the thin film structure, the pure Ga_2S_3 film does not appear to adopt the more brown colour which was reminiscent of the La containing films. The pure Ga_2S_3 target was later ablated at the highest energy density which showed the most detrimental effects in terms of the EXAFS detectable values for the Ga and S properties. For GS films we found that the optical band gap had negligible difference (2.41 eV and 2.35 eV) for thin films grown at low and high ablation energy density (3.0 J cm^{-2} and 5.0 J cm^{-2} respectively, see Section 5.3.2). This suggests that whilst the structure of the material is not the same, there is virtually no difference in optical transmission due to the Ga-Ga or Ga-S bonding. The visual evidence in Figure 4-9 and the EXAFS results show that there is a very high possibility that an undetectable level of La-La bonds creates high optical absorption. One final point that should be noted in regard to this postulate is that thin films of lanthanum-oxide do not show this film darkening which is seen in the sulphide equivalents. This suggests that if the La is bonded to oxygen atoms, it finds it more difficult to form La-La bonds in the final laser ablation grown thin film. The much higher La-O bond energy (5.85 eV) as compared to La-S (4.60 eV) is probably the root cause of the difference [232].

This observation led to a change in the general direction of the project. Work which was being conducted within the ORC (Optoelectronics Research Centre, here at Southampton University) with GLS fibres had found that the purity of the La-S starting powder was not adequate for the production of long, low loss fibres and impurities were causing unacceptably high losses. At the same time a literature search^[233, 234] showed that research had begun with a new material based on mixtures of $7\text{Ga}_2\text{S}_3:3\text{Na}_2\text{S}$, which were being produced as optical fibre for further investigation.

A GNS target is produced in exactly the same way as GLS, but with a lower melting point of $900\text{ }^\circ\text{C}$ ^[233]. Optical glasses can be formed in the range of 76 - 58% Ga_2S_3 ^[235] and are paler yellow than their GLS counterparts. Our laser ablation results have shown that GNS has typically a 50% lower ablation threshold (1.5 J cm^{-2} , see Table 5.1) than that of GLS. The material shows much improved losses and a very large change in refractive index when photomodified, which would potentially make it a possible thin film waveguide candidate. It has also been shown it can easily be doped with rare earth ions and fluorescence measurements have been made (Nd^{3+} ^[236] and Pr^{3+} ^[233] are examples) and because of the ease by which these ions incorporate, the GNS tertiary system has been produced with proportions of La_2S_3 added^[237]. However, GNS is hygroscopic which is very detrimental to uncapped thin film layers.

4.3.2 Loss Mechanisms in Infrared Optical Materials

In chalcogenides the short wavelength cut-off frequency is determined by electronic transitions across the bandgap while the long wavelength cut-off results from lattice absorptions due to the vibrational modes of the atoms or ions of the solids. When electromagnetic radiation is incident upon a material some radiation is reflected and some maybe scattered at the surface of the solid and/or in the bulk. The bulk scatter can arise from defects, inclusions or perturbations in the refractive index, particularly in a complex solid consisting of several atoms of different elements of the mix as with chalcogenide glasses. The mechanisms which give rise to bulk absorption may be classified as intrinsic or extrinsic ones. The intrinsic absorption mechanisms are those which result in electronic and vibrational structural absorptions in vitreous material of specific chemical composition. Extrinsic mechanisms are those associated with impurity atoms and molecules and deviations from stoichiometry. The intrinsic mechanisms define the region of transparency to electromagnetic radiation in a solid and the ultimate transmission achievable within this region, while the extrinsic mechanisms generally determine the percentage of the theoretical level of transparency achievable in practice within this region.

The intrinsic bands can be identified on the grounds that they must be observed in the spectra of glasses of the given compositions, independently of the purity of the initial

materials and changes in the synthesis regime. Their intensity in a glass of given composition must remain practically constant across many samples prepared under different conditions or starting material batches. If any of the bands are absent in the spectrum of at least one specimen, the loss is extrinsic.

4.3.3 Intrinsic Absorption Mechanisms

The total intrinsic optical loss in an optical glass in its low loss region is due to three factors and the corresponding attenuation coefficient α can be approximated by:

$$\alpha = A \exp\left(\frac{-a}{\lambda}\right) + B\lambda^{-4} + C \exp\left(\frac{e}{\lambda}\right) \dots\dots\dots (4.3)$$

The first term is associated with multiphonon absorption mechanisms and is dependent on the IR edge. The second term represents Rayleigh scattering and is due to electronic absorption fluctuations on a microscopic scale. At long wavelengths, λ , this term is negligible. The third term, the Urbach tail, is related to the bandgap absorption and describes the limitation of transmission in the visible part of the spectrum.

In order to transmit infrared radiation a solid must be an insulator or a semiconductor exhibiting an energy gap E_g (i.e. the energy to excite bound electrons to a conduction band). It is the bandgap that sets the transmission limit at the short wavelength end of the spectrum of a solid. This short wavelength cut-off is given by the relationship shown in equation 4.4, where h is Planck's constant and c the velocity of light:

$$\lambda_c = \frac{hc}{E_g} \dots\dots\dots (4.4)$$

The low frequency tail of this short wavelength cut-off extends slightly into the transparent region of the solid. This is known as the Urbach tail^[238] and as shown in equation 4.3, it can be rewritten in the form:

$$\beta \propto e^{c\omega/kT} \dots\dots\dots (4.5)$$

where ω is the frequency, k being Boltzmann's constant, T is absolute temperature and β represents the absorption coefficient.

An explanation of this exponential tail in the visible inter-band edge has been recently put forward. It is known that the random structure in glasses gives rise to varying local electric

fields on a microscopic scale. Theoretical work by Tauc^[239] provides evidence that such local microfields cause intrinsic absorption in chemically pure materials in what is normally the transparent region below the fundamental inter band absorption edge. The mechanism is due to local field induced broadening of exciton levels which are created at optical absorption energies close to but below the inter-band edge.

The long wavelength cut-off in a solid is set by lattice absorptions which in a solid is usually set by an overtone of the fundamental lattice absorption. In the case of multi-element chalcogenide glasses equation 2.1 can be used to provide general rules as to the likely long wavelength transmission limit, as discussed in section 2.1. A sufficiently wide spectral window exists between these two limits, where these materials are usefully transparent. Figure 4.10 shows the both the long and short wavelength cut-off for a 1 mm thick sample of GLS and GNS for comparison. The samples are each polished on both sides to the same optical quality. The Figure also suggests that whilst the glasses have good infrared transmission, there could be absorption problems if a short wavelength pump laser is to be used in a waveguide laser device using these materials as host.

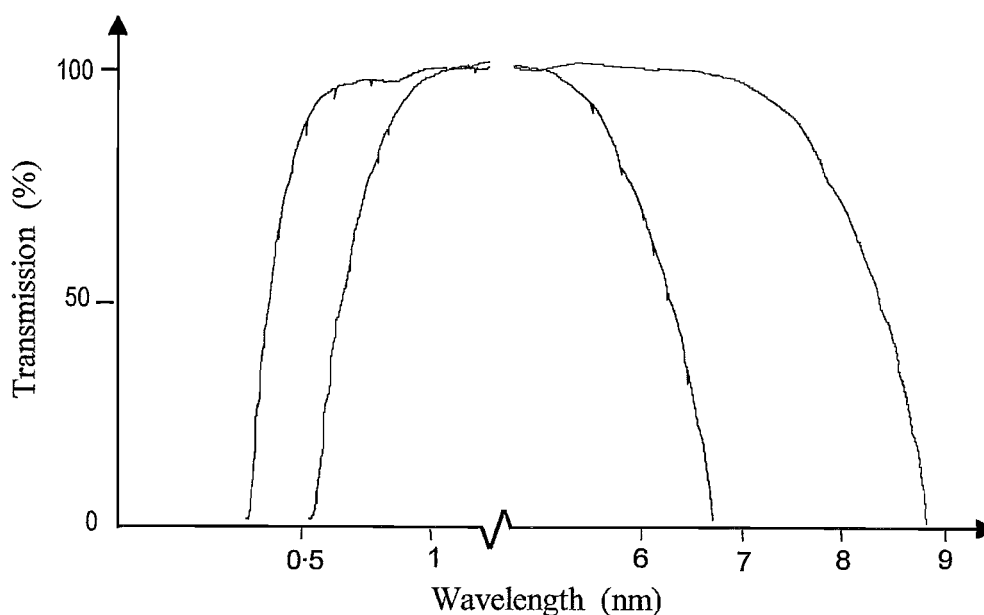


Figure 4.10. Transmission through 1 mm thick glass pieces of both GLS (—) and GNS (---) to compare optical transparency. {Original in colour}

4.3.4 Extrinsic Loss Mechanisms

Extrinsic loss mechanisms determine the transparency achievable in a glass in practice within the available window region. These mechanisms are scatter and absorption arising from the optical quality of the material and impurity absorption. For instance OH, hydrocarbons and oxygen in chalcogenide glasses give rise to unacceptable absorptions at specific wavelengths and inadequately homogenised glass can give rise to unacceptable

scatter in the near and middle infrared. The extrinsic loss mechanisms are specific to a particular glass or family of glasses and the method of synthesis gives an appreciation of the problem of extrinsic loss be obtained.

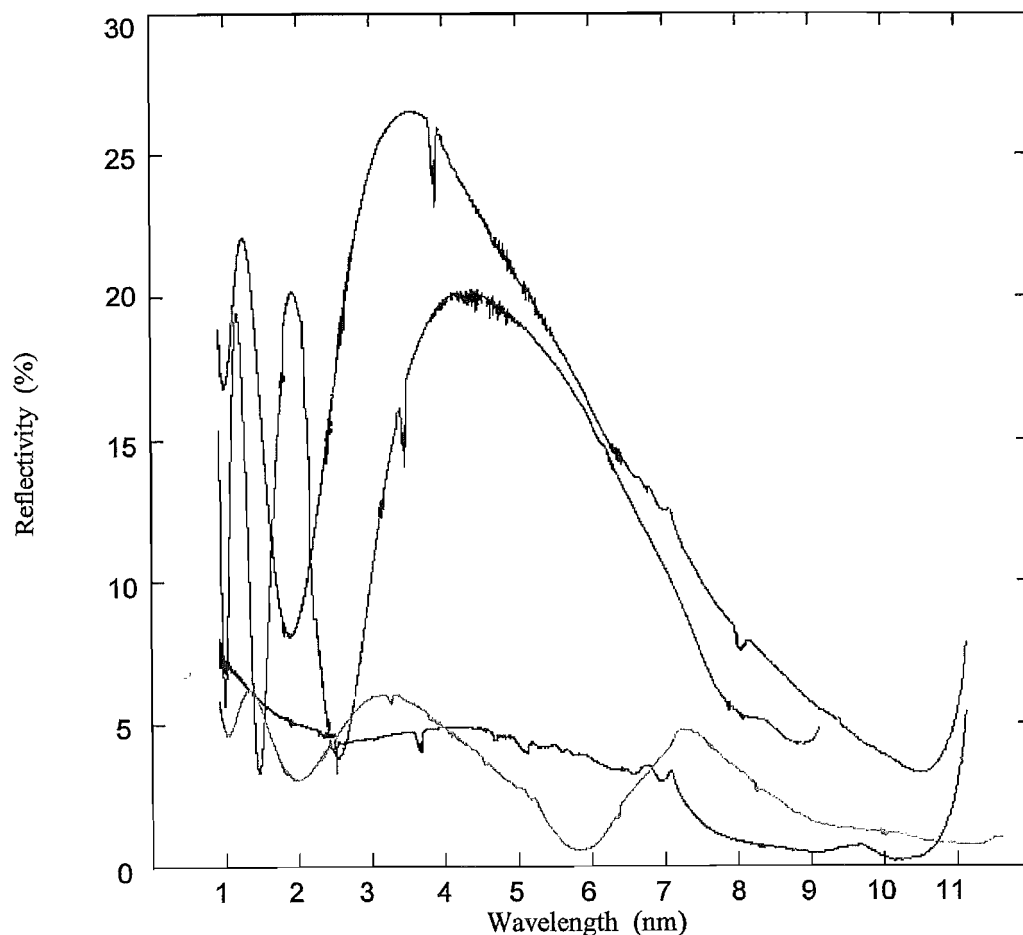


Figure 4.11. Reflection from thin films of La_2S_3 in a background of O_2 (—), Ga_2S_3 in a background of O_2 (---), La_2O_3 (— · —) and Ga_2O_3 (····) all grown by pulsed laser ablation with an energy density of 4.0 J cm^{-2} and Target-Substrate separation 80 mm. {Original in colour}

Material	Growth Rate (\AA)	Final Thickness (nm)
Ga_2S_3	0.122	308
La_2S_3	0.119	291
Ga_2O_3	0.101	317
La_2O_3	0.096	301

Table 4.2. Growth rates and thicknesses of thin films of La_2S_3 , Ga_2S_3 , La_2O_3 and Ga_2O_3 , to ensure that all samples are of equal thickness. All grown at 5 J cm^{-2} and 20 Hz.

Position (μm)	Cause	Reference	Contained in sample:
1.44	O-H	[178]	
1.92	O-H	[178]	❶ ❷ ❸ ❹
2.05	S-H	[178]	
2.29	O-H	[178]	❶ ❷ ❸ ❹
2.54	S-H	[178]	❷
2.74	O-H	[240]	❸
2.76-2.84	H ₂ O	[241, 178, 179, 118]	
2.90-2.92	O-H	[178, 242, 179]	
3.11	S-H	[178]	❶
3.69	S-H	[178]	❶ ❷
3.94	S-H	[243]	❶ ❷
4.03	S-H	[178, 179]	❶ ❷
4.57	O-H	[178]	❶ ❷ ❸ ❹
6.27	O-H	[118]	❶ ❷ ❸ ❹
7.78	S-S	[33]	❶ ❷
10.8	S-S	[33]	
11.9	S-S	[33]	

Cause	Position (μm)	Reference
H ₂ O	2.76-2.84	[241, 179]
	1.44	[178, 118]
	1.92	[178]
	2.29	[178]
O-H	2.74	[240]
	2.90-2.92	[178, 242, 179]
	4.57	[178]
	6.27	[118]
	2.05	[178]
	2.54	[178]
S-H	3.11	[178]
	3.69	[178]
	3.94	[243]
	4.03	[178, 179]
	7.78	[33]
S-S	10.8	[33]
	11.9	[33]

Table 4-3. List of identified absorption peaks found in thin films of ❶ La₂S₃, ❷ Ga₂S₃, ❸ La₂O₃ and ❹ Ga₂O₃. Second half of the table groups similar bondings.

Thin films of La₂S₃, Ga₂S₃ (these first two samples were ablated in a background of oxygen gas), La₂O₃ and Ga₂O₃ (ablated in vacuum) were produced for comparative purposes, to examine if the oxygen incorporates to produce the same film when ablated with the O atoms as part of the compound and when O₂ molecules are introduced to the plume as a gas and hence via collisions. Figure 4-11 shows an overlay of the above results. It should be noted that the films were grown for different times (after an initial run to determine growth rate) to achieve the same thickness in all cases for a better visual comparison of the data, Table 4-2 details the variations. The identified absorption peaks are referred to in Table 4-3 with their respective literature references. Water absorption appears in some of the spectra due to water in the atmosphere whilst the reflection measurements were being made.

4-4 Absorption and Fluorescence

The lanthanum content of the GLS glass material is easily substitutable with another lanthanide element, in the trivalent form. This allows the GLS host material to be used as a laser gain medium. A number of doped glass samples have been produced and reported extensively in the literature, i.e. so far Er³⁺ [244, 245], Pr³⁺ [246, 247], Nd³⁺ [248, 249], Dy³⁺ [250], Tb³⁺ [251],

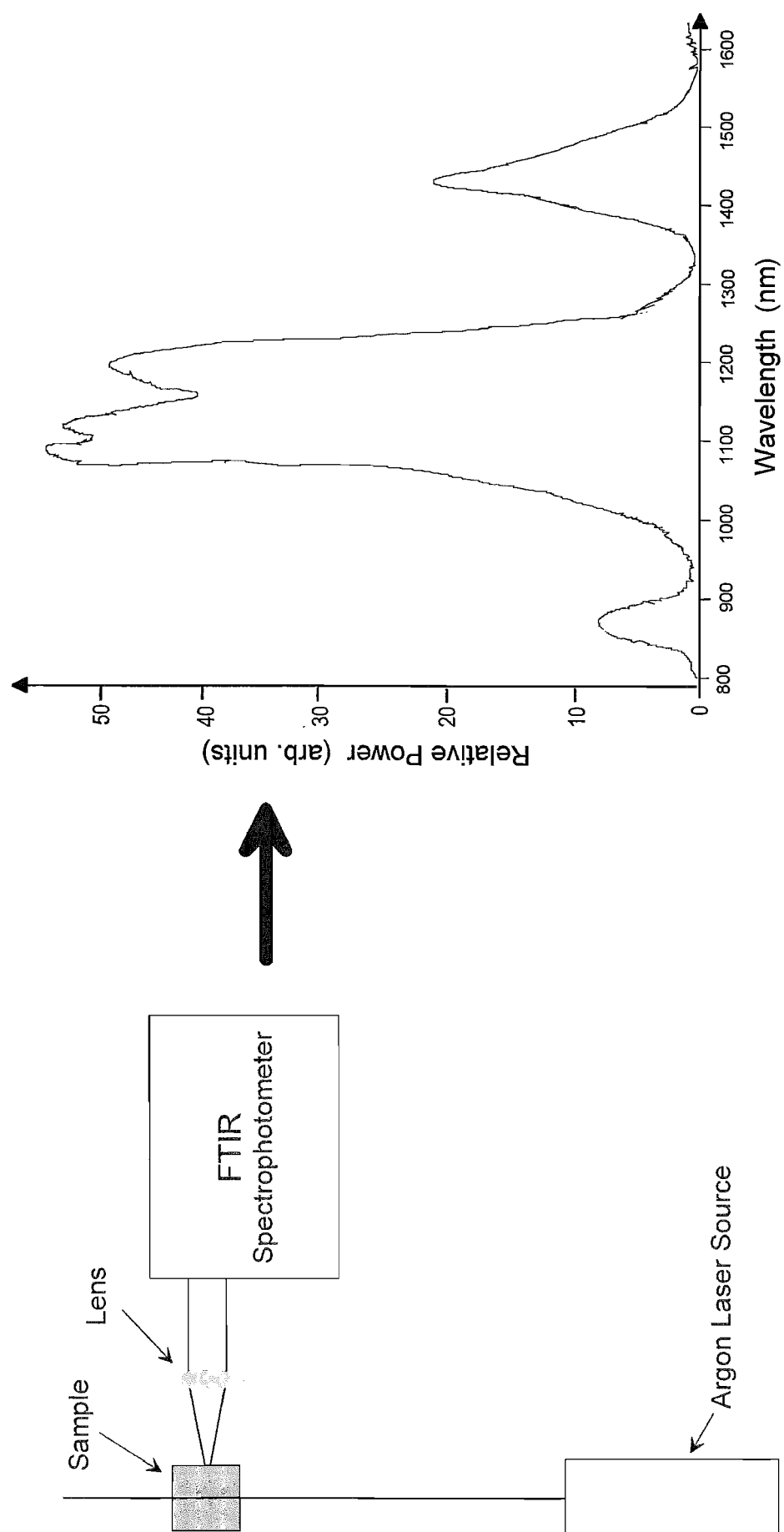


Figure 4.12. Experimental set-up used to record the fluorescence spectra of a Nd^{3+} doped GLS thin film pumped at 488 nm and recorded on an FTIR spectrophotometer. {Original in colour}

Ho³⁺ [251]. The glass forming region seen in Figure 4-1 and the similarity in atomic size of the lanthanide range indicates that all of the rare earth should incorporate into GLS. We needed to ensure that the rare earth ion is transferred from a bulk target and into a thin film which has been grown by laser ablation.

Fluorescence measurements can be made via the FTIR in the region 0.7 to 1.8 μm . Emission can be directed into the external port of the spectrophotometer and the data recorded as a background reference. The resulting spectrum is not a true representation of the emission due to the wavelength dependent throughput of the instrument. A 'standard lamp' is then used to calibrate the FTIR data. Figure 4-13 shows a schematic of the experimental arrangement for measuring fluorescence spectra and the normalised results which are achieved.

The thin film doped with 1 mol% Nd³⁺ is illuminated with a pump source at 488 nm (single line from Ar⁺ laser) and any surface emitted light forms the external source of the FTIR. The results show that the thin films contain the Nd³⁺ rare earth and have the potential to become channel or slab waveguide lasers. This does not provide a potentially new lasing wavelength, as many hosts achieve 1.08 μm radiation and lase here, but it does show that the ion is incorporated into the thin film layer. Nd³⁺ doped GLS has already been shown to lase as a bulk sample and a fibre laser by other researchers in the Optoelectronics Research Centre here at Southampton [252, 253]. The main peak shown in Figure 4-13 from the thin film fluorescence spectrum is at the correct wavelength region for Nd³⁺ incorporated in the bulk piece of doped GLS (see Table 2-1).

4.5 Conclusion

Chalcogenide glasses must have all traces of oxygen and hydrogen removed from the glass melt, to reduce intrinsic absorption bands. The optical absorption of GLS makes the glasses appear yellow coloured; the intensity of the colour decreasing with increasing oxygen content. Laser ablation is required as a growth technique due to congruent evaporation. Results showed that there is no detectable difference in the absorption of the thin films of Ga or La sulphides and oxides, if the initial material contains the oxygen as one of its constituents or the chamber is back-filled with O₂. This is believed to be due to the higher bond energy of oxygen than sulphur and this being the favoured recombination in the plume or on the film surface.

Atomic scale structure changes in GLS bulk glass and PLD thin films have been studied by the X-ray absorption fine structure technique. EXAFS spectra have been recorded at the S and Ga K-edges and the La L_{III}-edge for thin films grown at different energy density. This

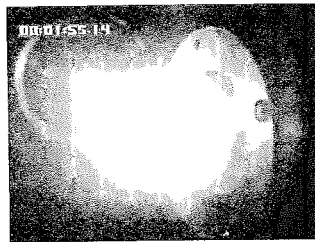
allowed us to construct a picture of the local structure in the bulk glass and thin films. The lanthanum environment is constant into which other rare earths could be substituted, suggesting low inhomogeneous broadening. The high “wrong bonding” which has been found demonstrates the structural origin of the absorption problems which we have found in the shift of the Urbach tail (presented and discussed in Section 5.3.2). The photomodification results (Section 6.3.1) show that the films grown at higher energy density have a larger refractive index change when illuminated with an Argon ion laser. Since photomodification is believed to involve bond breaking and small scale restructuring, films grown at a higher energy density are less structurally relaxed, which indicates why this happens. Visual evidence and the EXAFS results show that there is a very high possibility that the undetectable La-La bonds (due to low sensitivity of the EXAFS technique) create high optical absorption.

The La-La bonding observation lead to a change in the general direction of the project, producing a GNS target in an attempt to remove the La content of the glasses without removing the ability to incorporate rare earth trivalent sulphides. A selection of doped glass targets were produced and the bulk and thin film absorption spectra were produced on the FTIR. The results show that the thin films contain the respective trivalent rare earth ions and have the potential to become channel for slab waveguide lasers. The long wavelengths transmission shows the suitability of GLS for mid-infrared operating devices that can be operated with pump sources above the visible radiation region. The next chapter looks in more depth at the optical properties of these materials and shows how they changed due to different laser ablation growth parameters. More specifically the set of films grown with increasing energy density and analysed by EXAFS will be investigated further.

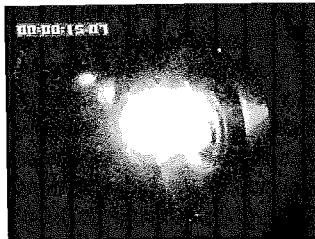
5

Determination and Optimisation of Optical Parameters and Thin Film Uniformity

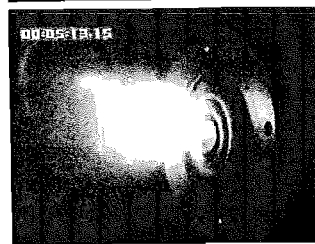
Vacuum



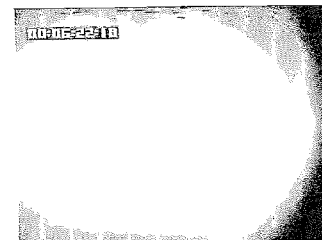
Nitrogen



Argon



Oxygen



5.1

Current Techniques for Film Parameter Measurement

5.2

Fitting Model: Basic Optics and Equation Derivation

5.3

Refractive Index and Thickness

5.4

Thin Film Uniformity

5.5

Conclusions

Visible emission from ablation plumes in different background gasses at equal pressure and in vacuum.

5.1 Current Techniques for Film Parameter Measurement

Characterisation of a thin film includes determination of its optical constants; the refractive index, n , absorption coefficient, α and the film thickness, t . For effective characterisation of any thin film, its optical constants should be determined over a range of wavelengths, λ . The $n(\lambda)$ spectra can then be correlated to film properties, such as chemical composition or transmission range.

Optical methods are used in thin film technology for *in-situ* characterisation of the growing films. Amongst these methods ellipsometry^[254-256], reflectance-difference techniques^[257, 258] and laser interferometry^[259-262] have so far gained the greatest attention. In all these methods the knowledge of the basic optical constants of the characterised material at the growth temperature plays an important role. This is especially true when one intends to continually evaluate instantaneous absolute values of the determined quantities, e.g. growth temperature, growth rate or surface morphology of the film.

A well known method to determine refractive indices of films in the infrared region is the measurement of the absolute reflectance of the film-substrate combination at a maximum or minimum value of the reflectance - wavelength curve. A second method often used in conjunction with the above technique is the measurement of the physical thickness of the layer, followed by the derivation of the film refractive index from the wavelengths of reflectance or transmittance extrema.

The non-destructive techniques for measuring the thickness of a transparent film make use of the interference phenomenon between the radiation reflected from the film-air interface and that from the film-substrate interface, e.g. CARIS (constant angle reflection interference spectroscopy)^[263] and VAMFO (variable angle monochromatic fringe observation)^[264] are commonly used. CARIS determines the film thickness spectroscopically by measuring the reflection from the sample film at a fixed angle. In VAMFO interference fringes are formed by varying the angle of incidence. In both techniques the film thickness and refractive index cannot be determined simultaneously without an iterative algorithm to compare the theoretical calculation with the experimental data. Laser based techniques tend to find refractive index values, n , at a specific wavelength, whilst n is truly a function of wavelength and is often given a real value in a region where the index change is negligible with respect to wavelength.

Various, angles of incidence for 'polarisation independent reflectance matching' (PIRM)^[265] provides a technique for the simultaneous measurement of thickness and refractive index of

transparent thin films on any substrate. It is simple and accurate, but requires that the thickness of the sample film be greater than $\lambda/4$ and that part of the substrate has an uncoated area. The thickness limitation is also common to CARIS and VAMFO.

Ellipsometry is an accurate technique for measurement of both the refractive index and thickness of a thin film. This method is more useful for extremely thin films than the above mentioned methods, but for thick films the order of thickness periodicity has to be known to obtain the exact value. This limitation is overcome by multiangle of incidence (MAI) ellipsometry, but it needs more complicated apparatus and more involved data analysis than the relatively simple methods previously described. Infrared ellipsometry is very rare and so not a viable, practical assessment technique for our work.

The FTIR Spectrophotometer can be used to provide transmission or reflection intensity spectra with respect to wavelength. Such data is 'fit' to an algorithm which is based on an optical parameter model to match the data and the best fit parameters for the sample under investigation. The more parameters which are known, the more accurate the resulting optical or physical constants.

The transmission / reflection data could be recorded over a large infrared wavelength range (beyond the transmission of the materials under investigation), but the method chosen to assess the optical parameters in our samples was based on modelling the transmission and reflection of the thin film layer on a bulk substrate and comparing the FTIR transmission spectra to the appropriate algorithm. This allowed the refractive index to be found as a function of wavelength which is more practical for assessing the suitability of waveguide devices which require detailed knowledge of very small index changes.

5.2 Fitting model: Basic Optics and Equation Derivations

5.2.1 Normal and Anomalous Dispersion

The complex index of refraction, $N = n - ik$, describes intrinsic optical properties of a material, where n is the refractive index and k the extinction coefficient. Both n and k are functions of the wavelength of light, λ , i.e., $n = n(\lambda)$ and $k = k(\lambda)$. For pure crystalline materials $n(\lambda)$ and $k(\lambda)$ are characteristic of the chemical structure of the crystal. On the other hand, for amorphous materials, $n(\lambda)$ and $k(\lambda)$ are not easily predicted, so they depend on processing conditions. If processing conditions for thin film deposition vary,

microstructure and composition of the film can vary. Any changes in microstructure or composition will generate changes in $n(\lambda)$ and $k(\lambda)$. However, the $n(\lambda)$ and $k(\lambda)$ values cannot be measured directly. In order to determine the $n(\lambda)$ and $k(\lambda)$ spectra of any material, i.e., in order to characterise any material, observable quantities such as reflectance, $R(\lambda)$, or transmittance, $T(\lambda)$, are measured, from which intrinsic material quantities such as $n(\lambda)$ and $k(\lambda)$ are determined.

For a thin film on a substrate, reflectance, $R(\lambda)$, depends on thickness of the film, optical constants of the film, optical constants of the substrate, surface roughness of the film and substrate, the angle of incidence and polarisation. For a multi-layer structure, reflectance depends on the thickness, n and k values of each layer and all of the other properties already listed.

n and k can also be described as functions of photon energy, becoming $n(E)$ and $k(E)$ respectively. The principle of causality^[266] leads to a fundamental relation between the real, $n(E)$ and imaginary, $k(E)$, parts of $N(E)$, the Kramers-Kronig relation. This relation dictates that if the equation for k as a function of E is known, then $n(E)$ is determinable by a Hilbert Transform of $k(E)$. The complex index of refraction, $N = n - ik$, is related to the complex dielectric function, $\varepsilon = \varepsilon_1 - i\varepsilon_2$, via $\varepsilon = N^2$. Thus, $\varepsilon_1 = n^2 - k^2$ and $\varepsilon_2 = 2nk$. In the limit $E \rightarrow 0$ ($\lambda \rightarrow \infty$), $\varepsilon \rightarrow \varepsilon_0$, where ε_0 represents the electrically measured dielectric constant of the medium; thus, an important correlation exists between optical and electronic properties of materials. $n(E)$ is determined empirically by fitting data to various model equations. In 1836^[267] Cauchy showed that in a region of *normal dispersion*, i.e. regions of low absorption with relatively small refractive index variations with respect to wavelength, that the change in refractive index, n , with wavelength can be represented by an expression of the form:

$$n = A + \frac{B}{\lambda^2} + \frac{C}{\lambda^4} \dots\dots\dots (5.1)$$

where A , B and C are constants characteristic of the medium and λ is the vacuum wavelength. Alternatively, Sellmeier-type equations are also commonly used or equations involving a sum of Sellmeier terms, all valid for a limited range of energies (see Equation 5.4 for example). The particular equation applied to a given material is determined by the quality of the resulting fit it gives to measured data. The average error between the actual data and the theoretical curve is used to judge which refractive index form has the closest match.

Whilst this is not true of all absorption regions throughout the transmission spectrum, insulating and semiconductor materials have, in general, two broad ranges of absorption as a function of frequency, known as *anomalous dispersion* regions. The lower frequency range, associated with lattice vibrational absorption bands, occur in the far-infrared. Higher frequency bands usually occur at or above optical frequencies and are associated with electronic transitions between the valence and conduction bands. Between these two bands there is normally a region in which the imaginary part, $\epsilon_2(\omega)$, of a complex dielectric response function, $\epsilon(\omega)$, is low causing the optical properties of the material to be dominated by the real part, $\epsilon_1(\omega)$. If $\epsilon_2(\omega)$ can be represented as a sum of peaks at frequencies ω_i and the optical region frequency ω is far from these peaks, then from the Kramers-Kronig relation^[269] the real part of the response function, $\epsilon_1(\omega)$ can be derived as:

$$\epsilon_1(\omega) - 1 = \sum_i \frac{S_i \omega_i^2}{\omega_i^2 - \omega^2} \dots\dots\dots (5.2)$$

In which S_i is a dimensionless oscillator strength. Converting to the vacuum wavelength form (using $\lambda = 2\pi c/\omega$), this equation becomes the Sellmeier dispersion formula for the material:

$$\epsilon_1(\lambda) = 1 + \sum_i \frac{S_i \lambda^2}{\lambda^2 - \lambda_i^2} \dots\dots\dots (5.3)$$

The number of terms, i , required to satisfactorily define the dispersion between the absorption peaks depends on the material; however three terms are usually enough, two for electronic oscillators and one representing lattice vibrations.

Sellmeier equation:

$$n^2 = 1 + \frac{S_1 \lambda^2}{\lambda^2 - \lambda_1^2} + \frac{S_2 \lambda^2}{\lambda^2 - \lambda_2^2} + \frac{S_3 \lambda^2}{\lambda^2 - \lambda_3^2} \dots\dots\dots (5.4)$$

Herzberger published his dispersion formula in 1958^[269] and modified it slightly in 1959^[270]. He concentrated his efforts on the electronic effects as these were nearer to the visible region than the infrared asymptotic behaviour. This makes his formula useful for visible and near infrared refractive indices. In the following equation $A \rightarrow E$ are constants for a given material and λ_0^2 is substituted by $0.028 \mu\text{m}^2$ being, the square of, the average position of the ultraviolet asymptote in most materials. In its final form Herzberger's dispersion formula differs from Sellmeier's formula in that the latter relates n^2 as opposed to n with λ^2 , both have infinite numbers of terms and are usually approximated to the first three (as with equation 5.4) when used:

Herzberger equation:

$$n = A + BL + CL^2 + D\lambda^2 + E\lambda^4 \dots\dots\dots (5-5)$$

Where $L = \sqrt{\lambda^2 - 0.028}$ and is the same for most materials.

In all cases, once the absorbing region is encountered, it is no longer possible to consider only the real part of the complex dielectric response function $\varepsilon(\omega)$. Both formulae are used extensively in publications since their introduction to define the refractive index of a material at constant temperature. Cauchy's formula has since been expanded to include dispersion due to temperature changes^[267] with respect to wavelength; still however, over ranges away from the anomalous dispersion regions. All three versions of the various formula for the refractive index were fitted to transmission data for GLS samples. Values of $n(\lambda)$ based on the Sellmeier formula produced the least deviation compared to the actual data and hence was used throughout the investigations in this work in preference to the other two alternatives.

5.2.2 Reflection and Transmission from a Single Surface

The refractive index of a material is the ratio of the sine of the angle of incidence and the sine of the angle of refraction. If both media at an interface are non-absorbing to the incident radiation, it can be seen from the previous section that this ratio will be real and conversely complex if either media absorbs the beam. An incident light ray is represented by two orthogonal, incoherent, equal amplitude polarisation components (Transverse Electric component, TE and Transverse Magnetic component, TM). At a boundary or interface of two differing index media, such an incident beam is partially reflected and transmitted with proportions based on the well known Fresnel formulae^[271] for the intensity of light:

For a TE wave:

$$\mathfrak{R}_S = \left| \frac{N_1 \cdot \cos \theta_1 - N_2 \cdot \cos \theta_2}{N_1 \cdot \cos \theta_1 + N_2 \cdot \cos \theta_2} \right|^2 \dots\dots\dots (5-6)$$

$$\mathfrak{T}_S = \left| \frac{2 \cdot N_1 \cdot \cos \theta_1}{N_1 \cdot \cos \theta_1 + N_2 \cdot \cos \theta_2} \right|^2 \cdot \left(\frac{N_1 \cdot \cos \theta_1}{N_2 \cdot \cos \theta_2} \right) \dots\dots\dots (5-7)$$

For a TM wave:

$$\mathfrak{R}_P = \left| \frac{N_2 \cdot \cos \theta_1 - N_1 \cdot \cos \theta_2}{N_2 \cdot \cos \theta_1 + N_1 \cdot \cos \theta_2} \right|^2 \dots\dots\dots (5-8)$$

$$\mathfrak{T}_P = \left| \frac{2 \cdot N_2 \cdot \cos \theta_1}{N_2 \cdot \cos \theta_1 + N_1 \cdot \cos \theta_2} \right|^2 \cdot \left(\frac{N_1 \cdot \cos \theta_1}{N_2 \cdot \cos \theta_2} \right) \dots\dots\dots (5-9)$$

In these equations N_1 and N_2 are the refractive indices of the first and second media and θ_1 and θ_2 are the angles of incidence and refraction respectively. Whilst the resulting s and p reflectivity curves are well known, they are reproduced in Figure 5.1 for reference. \mathcal{R}_s (\perp) increases monotonically with θ_1 , whilst \mathcal{R}_p (\parallel) initially decreases, reaching zero at the Brewster angle (θ_B) before rapidly increasing. It can be seen from Figure 5.1 that as the refractive index of the substrate material, n_2 , is increased \mathcal{R}_s , \mathcal{R}_p and θ_B all increase. The total reflectivity, \mathcal{R} , is the combination of these polarisation components such that: $\mathcal{R} = \mathcal{R}_s \cdot \cos^2 \phi + \mathcal{R}_p \cdot \sin^2 \phi$, where ϕ is the polarisation angle. A similar, inverted, profile follows for the two transmission components, \mathcal{T}_s and \mathcal{T}_p .

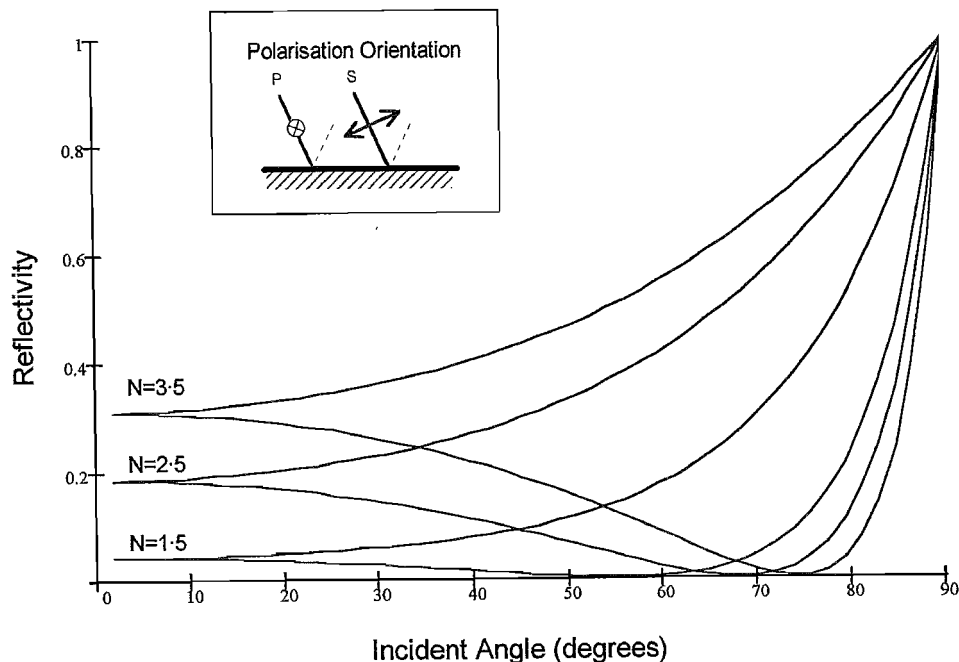


Figure 5.1. The reflectivity from a surface with different refractive index in air. Showing relative intensity of reflected radiation polarised parallel to plane of incidence, \mathcal{R}_p (—) and perpendicular to the plane of incidence (---) \mathcal{R}_s (Absorption of the material is assumed to be zero). {Original in colour}

5.2.3 Transmission Through a Thin Film Layer

Light incident upon a surface will undergo a change in phase and direction at the boundary of differing refractive index. Some of this light is reflected and some refracted. The refracted component travels through the medium until it impinges on another boundary, where as before some is reflected. This will also emerge from the initial upper surface

causing interference with the previously reflected component. The optical path difference dictates the resultant signal intensity.

Transmission through a thin film layer on a substrate requires that the incident radiation cross three boundaries: the air-film interface, film-substrate and substrate-air. At normal incidence the transmission equations for \mathfrak{T}_s and \mathfrak{T}_p (equations 5.7 and 5.9 respectively) are equal and the equations are very much simplified when $\cos \theta_i$ is substituted by 1 at normal incidence.

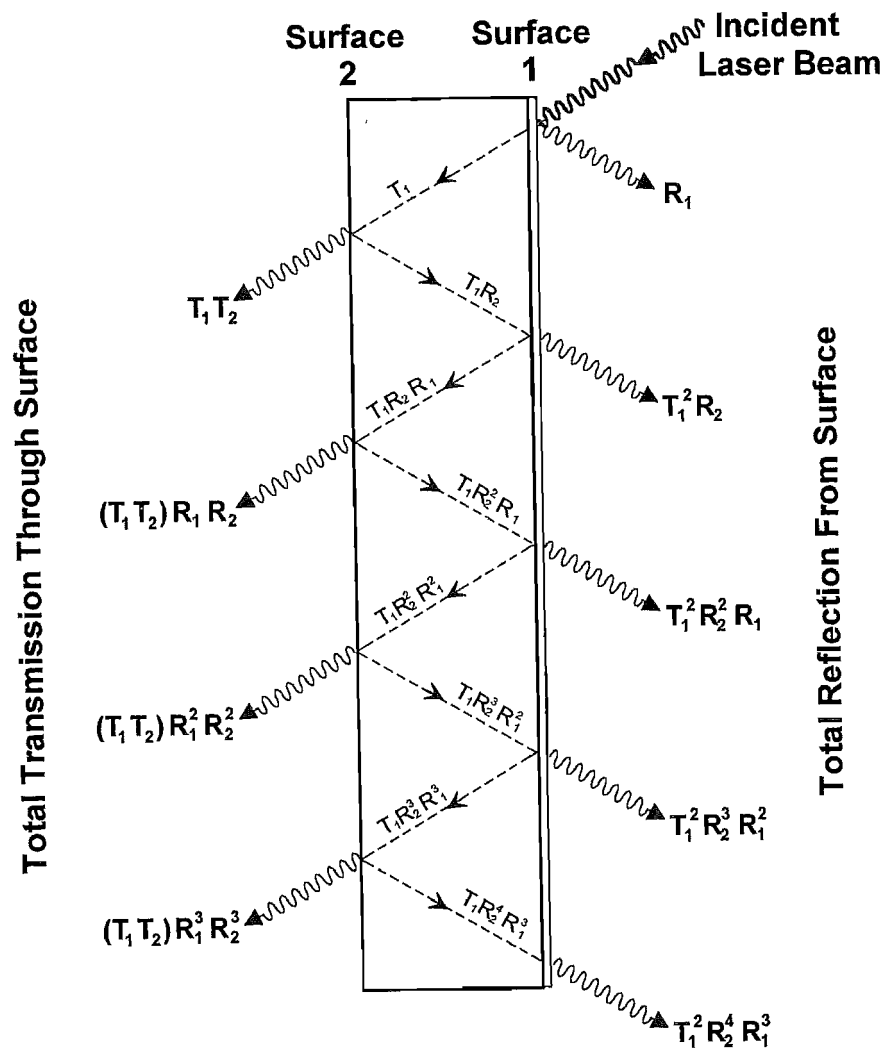


Figure 5.2. Following the schematic of a ray tracing diagram to show the path that the reflected and transmitted components of a laser beam incident on a thin film - substrate combination. {Original in colour}

For a thin film layer on a substrate material two surfaces have to be combined, at normal incidence and the refractive index for air being 1, it can be shown that^[271]:

$$\mathfrak{T}_{S \text{ or } P} = \left| \frac{\left(\frac{2}{1+N_1} \right) \cdot \left(\frac{2 \cdot N_1}{N_1+N_2} \right) \cdot A}{1 + \left(\frac{1-N_1}{1+N_1} \right) \cdot \left(\frac{N_1-N_2}{N_1+N_2} \right) \cdot A} \right|^2 \cdot N_2 \quad \dots\dots\dots (5.10)$$

where N_1 is the refractive index of the film and N_2 , that of the substrate; A is a term which takes into account the phase difference between the transversing wave and the two surfaces of the thin film material, given by:

$$A = e^{i \cdot \frac{4\pi}{\lambda} \cdot N_1 \cdot h} \quad \dots\dots\dots (5.11)$$

where h is the thickness of the film. If incident radiation passes through the thin film and transparent substrate combination. Figure 5.2 shows a schematic of the path of both the reflected and transmitted individual contributions to the total transmission through the combined sample.

The total transmission, \mathfrak{T}_T , is the sum of all these components which when simplified as a geometrical progression and summed to infinity is: first term/(1-common difference). If surface 1 (the thin film side) is represented by Equation 5.10, TS_1 , and surface 2 (back surface of substrate), TS_2 , is obtained from Equation 5.7 with the substitution for normal incidence radiation and air being beyond the back interface, the sum of transmissions becomes:

$$\mathfrak{T}_T = \frac{TS_1 \cdot TS_2}{1 - RS_2 \cdot RS_1} \quad \dots\dots\dots (5.12)$$

Here RS_2 and RS_1 are the surface reflections for the respective sides as shown in the figure. This theoretical representation of the transmission of light through a transparent substrate with a thin film layer is used to deduce the optical thickness of the thin film itself from the experimental data in the following sections and chapters.

5.3 Refractive Index and Thickness

5.3.1 Fitting the Optical Thickness

Representing a thin film layer on a substrate and the respective refractive indices with Sellmeier equations, allows the transmission to be modelled in the near infrared region. The substrate optical constants are available from the literature (CaF_2 [272], ZnSe [273, 274], ZnS [273, 275] and Si [276] were used in the project). The transmitted intensity of light through this combination for calcium fluoride can be represented by Equation 5.12, so as to include the

multiple reflections which also occur between the thin film and the back surface of the substrate.

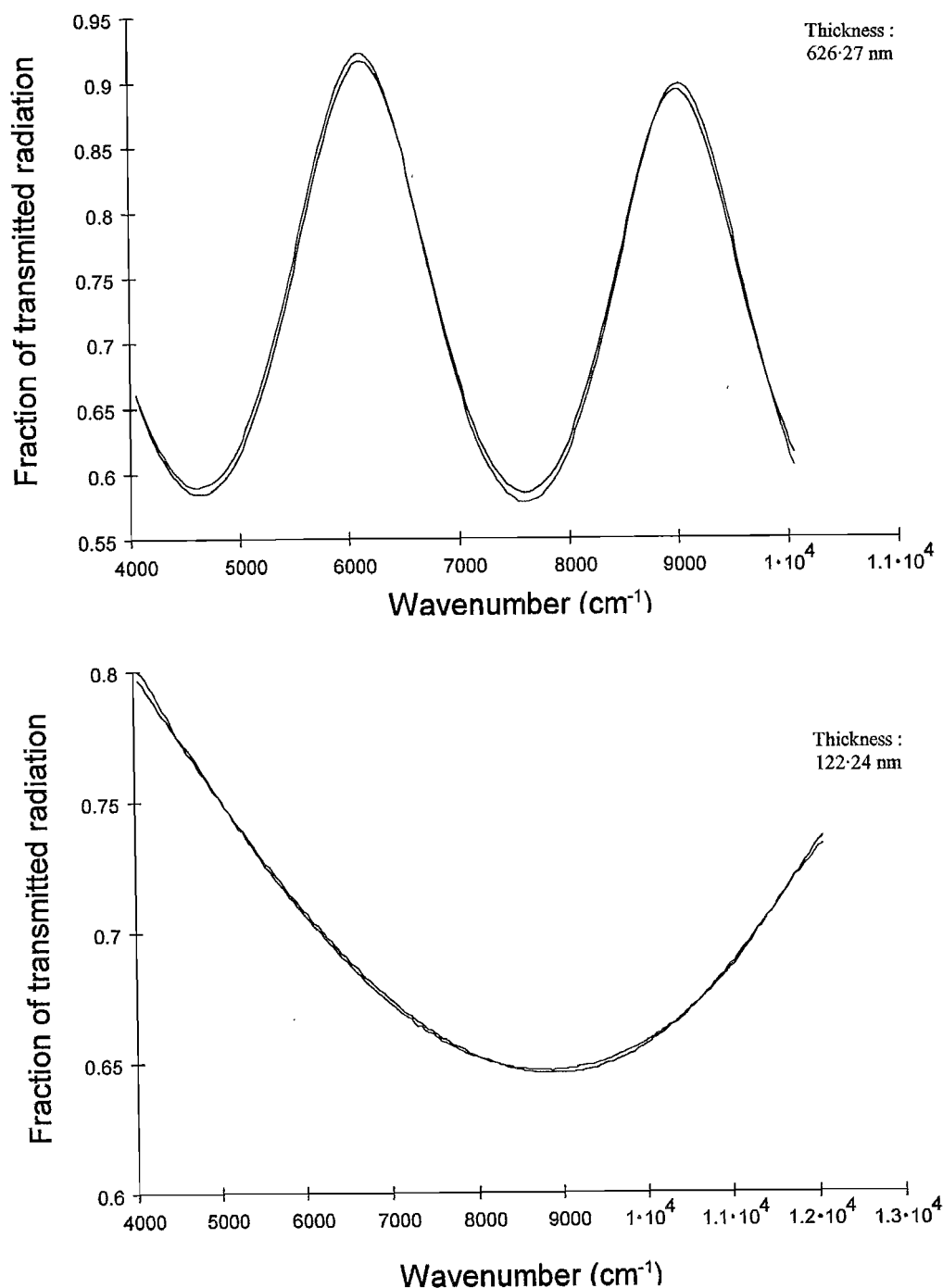


Figure 5.3. Two examples of GLS thin films on BK7 glass substrates showing the actual FTIR spectra (—) and the computer 'fit' (---) using the total transmission equation model (Equation 5.12) to find refractive index and film thickness. {Original in colour}

Data from the FTIR spectrophotometer can be compared to show the deviation between the actual data and the models theoretical data. The refractive index and thickness of the thin

film can be resolved using an iterative algorithm based on the Levenberg-Marquardt ^[277→279] method. When the sum of squares error between the modelled data and the experimental data are minimised, the refractive index as a function of wavelength and film thickness of the sample are deduced.

Figures 5-3 shows two examples of such a model representation. The red and blue lines sometimes do not completely match accurately at the maxima and minima, this is thought to be because of the necessity of a 3 mm aperture during data collection and a slight variation in the thin film thickness over the aperture. The refractive index and virtually all of the thickness information for the samples in this project are found using this technique. All of the samples which were additionally measured mechanically using a Talysurf to confirm their thickness were the same as the data fit to within the error of the instrument and the data error, confirming the accuracy of this analysis model. Figure 5-4 shows, by means of an example, the two thin films shown in the previous figure for comparison of the two thickness measuring techniques. Figure 5-5 shows how the refractive index of the thickest GLS sample shown in Figure 5-3 varies with near infrared wavelength.

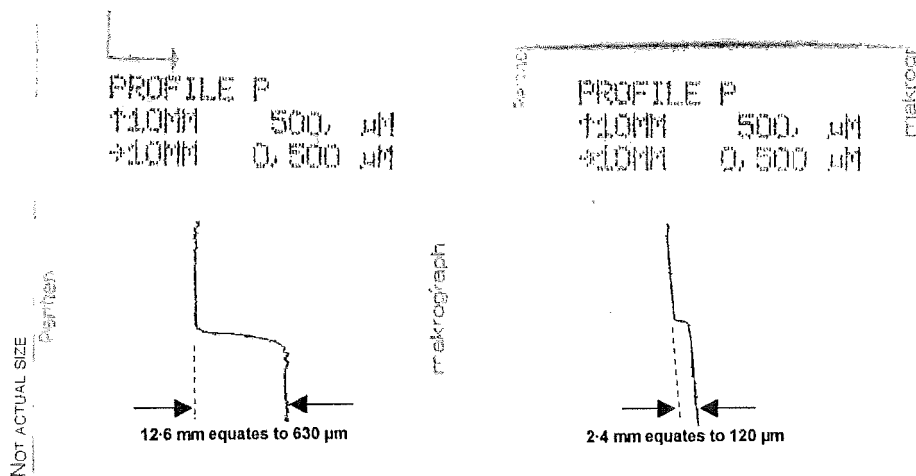


Figure 5-4. Two examples of GLS thin films on BK7 glass substrates whose thicknesses are measured to compare with the values fitted to the optical transmission as detailed above and shown in Figure 5-3. {Original in colour}

Most of the GLS films were grown as part of a set, mainly to vary one or more of the deposition parameters. Table 5-1 presents the data for a set of films grown with the same number of pulses and at the same pulse repetition rate with a variation from 2.0 to 6.0 J cm⁻² energy density range. No film was detected as a result of the ablation run at the lowest energy density, hence the threshold value for the ablation of GLS is 2.5 J cm⁻². Whilst it is logical to assume that greater energy densities will ablate more material to produce thicker films for the same number of pulses, it is obvious from the data that the refractive index of the films decreases. If this is considered along with the EXAFS results from the previous chapter (Section 4-2-6 and 4-2-7), the conclusion is that an increased number of S-S and

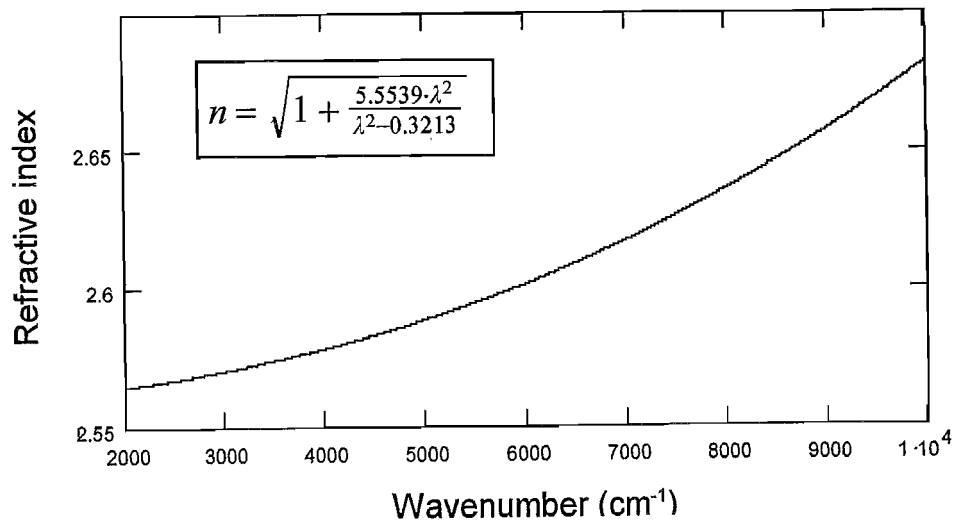


Figure 5.5. An example of the variation of GLS thin film refractive index with wavenumber, for the thick sample shown in Figure 5.3. {Original in colour}

Energy (Jcm ⁻²)	Fitted Thickness after 9,000 Pulses (nm)	Refractive Index at 633 nm
2.0	no film	N/A
2.5	122.41	3.31
3.0	347.43	3.17
3.5	626.27	2.91
4.0	734.36	3.02
4.5	868.07	3.05
5.0	940.46	2.83
5.5	970.84	2.72
6.0	992.56	2.54

Table 5.1. Physical thickness and refractive index of GLS thin films grown at increasing laser energy density.

Ga-Ga 'wrong' bonds, amongst other things, changes the refractive index of the film. Visually the film becomes a darker brown with increasing energy density and although this could be related to the increased thickness, it is probably due to a reduced thin film density as a likely result of increasing disorder. This darker brown appearance would then be a result of an increase in the Urbach absorption edge. These films will be reintroduced in the next chapter during further analysis. However at this point, it is worth mentioning that

increased film thickness is also accompanied by the increased size and density of particulate matter which results in inferior optical properties.

Background Oxygen Pressure (mbar)	Rep. Rate of Ablating Laser (Hz)	Fitted Thickness after 9,000 Pulses (nm)	Refractive Index at 633 nm
Vacuum	2.5	269.41	3.35
	5	274.34	3.21
	10	273.72	3.22
	20	260.97	3.29
	40	265.21	3.24
5×10^{-4} (MFP = 126.6 mm)	2.5	243.10	3.02
	5	246.19	2.96
	10	240.75	2.89
	20	236.01	2.93
	40	232.23	2.89
1×10^{-2} (MFP = 6.33 mm)	2.5	220.42	2.52
	5	213.75	2.42
	10	190.62	2.29
	20	171.22	2.22
	40	159.53	2.08

Table 5.2. GLS thin films grown at increasing pulse repetition rate (constant fluence) in vacuum and for comparison in different background pressures of oxygen. The results show changes in physical thickness and refractive index.

A second example of parameter fitting is presented in Table 5.2; here the aim is to see how the thin films optical properties change when the energy density remains constant and the films are produced by being grown with the same number of excimer laser pulses. The table also shows similar data for two different background oxygen pressures. The mean free path (MFP) of the oxygen molecules is noted in the table; at one value (126.6 mm) ~ 50 % of the plume travelling the 80 mm from target to substrate should statistically meet with an oxygen molecule en-route. The resultant thin film is 10% thinner and has an equally reduced magnitude (10%) of refractive index than the equivalent thin films grown in vacuum. For this oxygen pressure and the vacuum deposition, the film thickness does not decrease much as the repetition rate of the excimer laser is increased. When the mean free path is much lower than the distance from target to substrate (6.33 mm in this case) the film thickness is more drastically reduced. This is commonly reported in the literature and is reported to be due to a slowing down of the plume as it interacts with the gases present in the chamber^[142, 174, 181]. These interactions spread the cross-section of the plume and whilst producing a thinner

Background Gas	Pressure (mbar)	Fitted Thickness after 9,000 Pulses (nm)	Refractive Index at 633 nm
Vacuum	5×10^{-7}	374.34	3.11
Oxygen	1×10^{-5}	291.18	2.75
	1×10^{-4}	264.04	2.47
	5×10^{-4}	242.92	2.33
	1×10^{-3}	268.35	2.25
	1×10^{-2}	207.24	2.09
	5×10^{-2}	234.86	2.01
	1×10^{-1}	173.89	1.76
Argon	1×10^{-5}	221.97	3.09
	1×10^{-4}	179.04	2.85
	5×10^{-4}	159.82	2.89
	1×10^{-3}	159.72	2.76
	1×10^{-2}	101.16	2.68
	5×10^{-2}	100.81	2.61
	1×10^{-1}	98.42	2.54

Table 5-3. Physical thickness and refractive index of GLS thin films grown in vacuum and, for comparison, in different background pressures of oxygen and argon gases at constant fluence.

sample, it is more uniform and covers a larger area of the substrate. The larger the molecular weight of gas the greater the plume spread and consequently the thinner the film layer; this is also true for a lower MFP of the background gas. As with the previous table, the higher repetition rate causes an increased size and density of particulate matter, so reducing the optical quality of the layer.

Table 5-3 is presented to show how the oxygen background gas incorporates itself into the layer. The previous results showed that even very low pressures of oxygen in the chamber reduced the film thickness but only when the chamber is filled with other gasses does it become clear that oxygen is incorporated into the material. Argon, being an inert gas does not react with the atoms of GLS as they travel between target and substrate. So when comparing equivalent pressures of these two gases (the atomic mass of argon is 39.9 and O_2 has an equivalent value of 32.0, i.e. they have similar masses and momentum transfer), it can be seen that oxygen has a film thickening effect, i.e. incorporation. The more obvious proof was presented in Section 4-3-4 with the obvious presence of oxygen based absorption bands. This table is also shown graphically in Figure 5-6 to show the change of film thickness and the refractive index decrease when ablation takes place in the two gasses. It is worth mentioning at this point that the interaction between plume and background gas in the chamber can be seen visually during the interaction between the plasma and gas species

present. The emitted light is smallest in vacuum, slightly increased in Ar and N₂ and becomes quite spectacular in O₂. Examples of the pulsed laser ablation plume for each of the afore mentioned conditions are shown on the title page to this chapter.

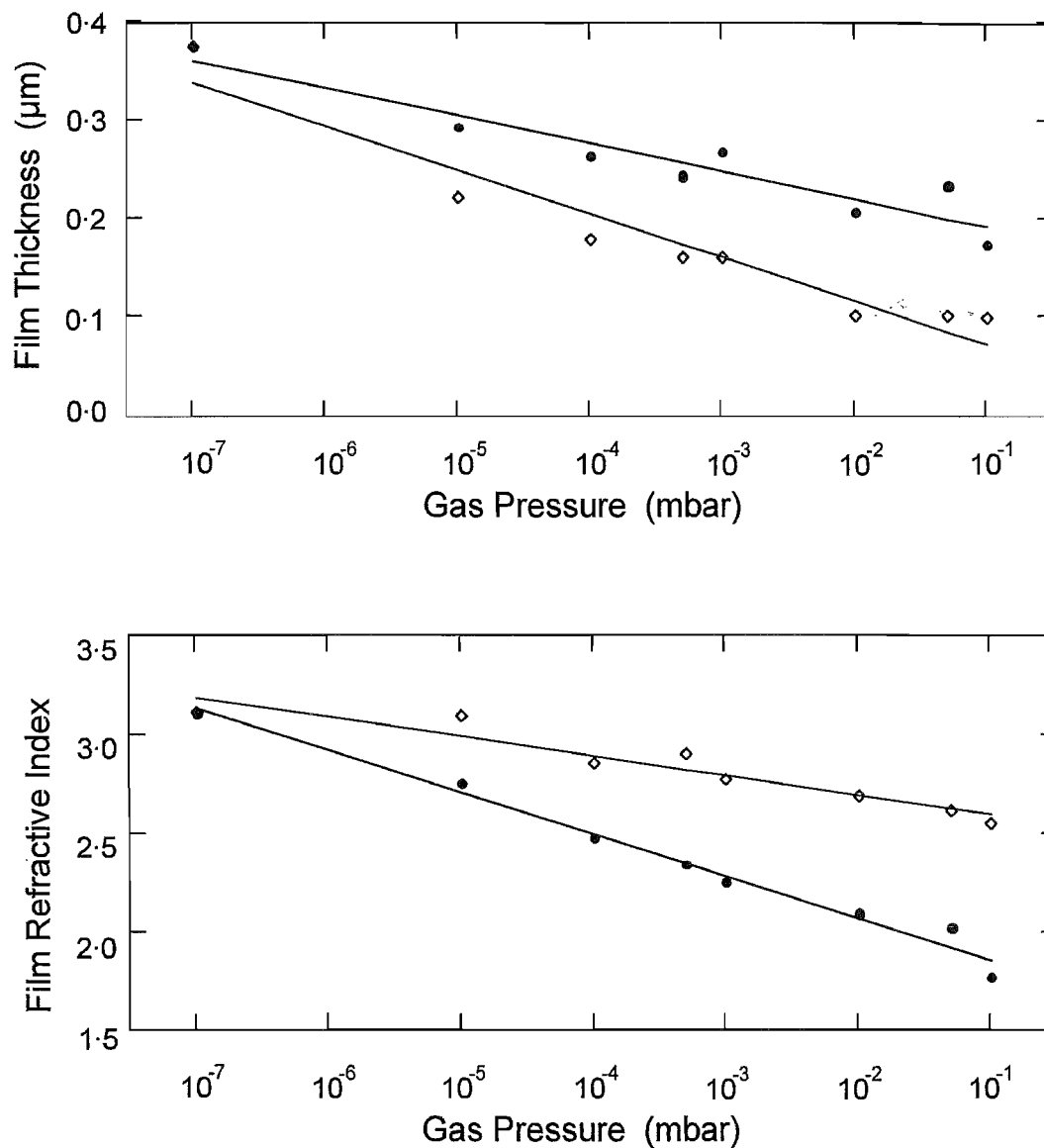


Figure 5.6. Graphical representation of the data in Table 5.3. (•) oxygen and (\diamond) argon gas data points with the respective coloured best fit line as a guide to the eye.

Finally, Figure 5.7 presents the data of a film set which was investigated by changing the angle of the substrate relative to the target (at a fluence of 3.5 J cm^{-2} and 9000 pulses). Zero degrees represents a substrate which is parallel to the target and 90° relates to a perpendicular substrate orientation. Whilst films grown in vacuum or inert gasses show a decreasing thickness with angle, oxygen incorporation has the ability to increase the thin film

thickness dramatically once the parallelism of the target and substrate holder is removed. This is likely to be a structural property, and it will be shown later that the increased thickness due to angle can be virtually removed when the thin film is photomodified.

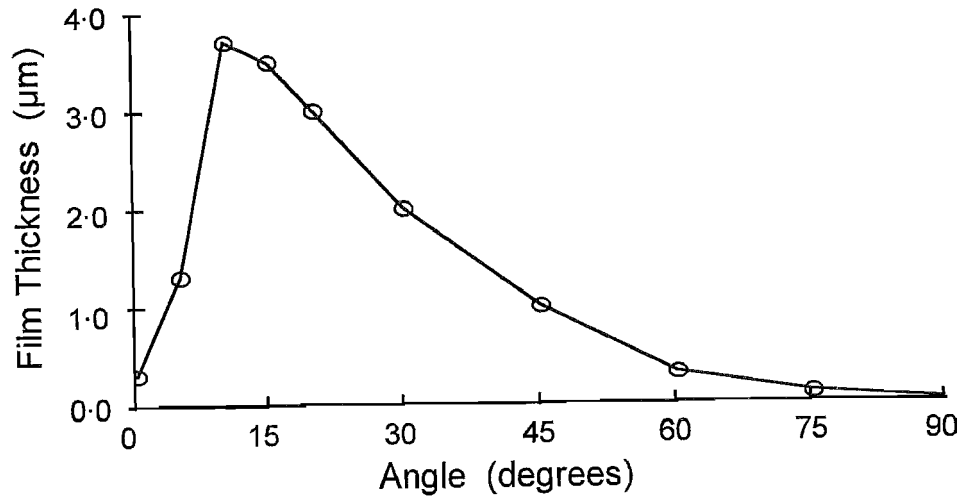


Figure 5.7. GLS film thickness changes rapidly as the parallelism of the target and substrate is removed and the angle between them becomes more obtuse. The films were grown in a background of 10^{-5} mbar of O_2 and 0° refers to a parallel target and substrate orientation. {Original in colour}

5.3.2 Absorption Coefficient of GLS

The optical absorption coefficient, α , was determined from measurements of transmittance T and reflectance R , for wavelengths ranging from 0.4 to 2.5 μm . In the low-absorption region ($\alpha < 10^4 \text{ cm}^{-1}$), the absorption coefficient of a film with thickness d was determined from the expression^[280].

$$T = \frac{(1-R_1)(1-R_2)(1-R_3)\exp(-\alpha d)}{1-R_2R_3} \times \{1 - [R_1R_2 + R_1R_3(1-R_2)^2]\exp(-2\alpha d)\} \quad (5.13)$$

where R_1 , R_2 , R_3 are the reflectivities of the air-film, film-substrate and substrate-air interface. When α is very small the imaginary part of the refractive index is negligible and

$$R_1 = \left(\frac{n-1}{n+1}\right)^2 \quad (5.14)$$

$$R_2 = \left(\frac{n-n_s}{n+n_s}\right)^2 \quad (5.15)$$

$$R_3 = \left(\frac{n_s-n_a}{n_s+n_a}\right)^2 \quad (5.16)$$

Since α is small in this region, the coherent multiple reflections become extremely important and the appearance of the interference fringes makes it difficult to estimate α . The maxima and minima of the interference fringes were then averaged for transmission spectra.

For the high absorption region ($\alpha \geq 10^4 \text{ cm}^{-1}$), when the fringes in transmittance and reflectance disappear (a typical example is shown in Figure 5-8(a)), the following approximate relation was used^[281]

$$T = (1 - R) \exp(-\alpha d) \quad \dots\dots\dots (5.17)$$

where T is the transmittance and R is the measured reflectance. This relation gives good results for absorption coefficient as long as $T + R$ remain significantly less than unity. The absorption coefficient as a function of energy for the low- and high-absorption regions overlapped and matched well using the two expressions.

Representative absorption edges for several films of different deposition energy density obtained from the above calculations are shown in Figure 5-8(b). The absorption edge shifts gradually to lower energy with rising energy density. Apart from the shift, the spectra broaden but remain essentially similar in shape at all energy densities.

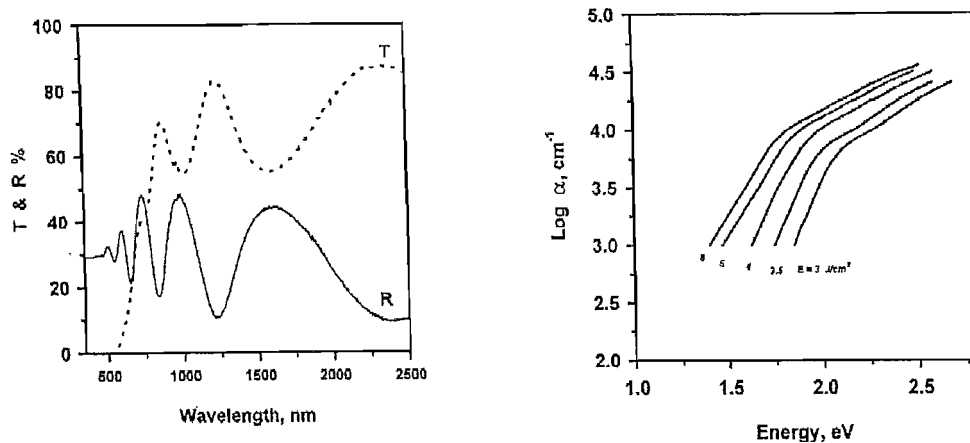


Figure 5-8(a). Transmission and reflectivity with wavelength for GLS thin film sample. (b) Absorption coefficient spectra deduced from T and R for GLS films prepared at different energy density.

Analysis of optical absorption spectra is one of the most productive tools for understanding and determining the band structure and energy gap of both crystalline and amorphous non-metallic materials. The absorption coefficients $\alpha(\omega)$, of the optical absorption near the band edge in many amorphous materials show an exponential dependence on photon energy, $\hbar\omega$, and obey Urbach's empirical reaction^[238,282]

$$\alpha(\omega) = \alpha_0 \exp \hbar\omega/E_e \quad \dots\dots\dots (5.18)$$

where α_0 is a constant, ω is the angular frequency of the incident photon, $\hbar = h/2\pi$ where h is Planck's constant and E_e is the width of the band tails of the localised states in the band gap.

In the high absorption region (where absorption is associated with interband transitions), the form of $\alpha(\omega)$ with photon energy was given in quadratic form by Tauc *et al.* [239,283], and discussed in more general terms by Davis and Mott [284], whose equation was of the form

$$\alpha\hbar\omega = \beta(\hbar\omega - E_{opt})^s \quad \dots\dots\dots (5.19)$$

where β is a constant, n is the refractive index, E_{opt} is the optical gap and s is an exponent that characterises the transition process and may take values 1, 2 or 3 as found for various amorphous semiconductors. The best fitting of equation 5.19 for the studied samples is obtained with $s=2$. The functional dependence of the optical absorption $(\alpha\hbar\omega)^{1/2}$ versus $\hbar\omega$ for the mean that the values of E_{opt} can be obtained from extrapolation of the linear regions and β^{-1} calculated from the slopes of the curves and are given in Table 5.4. Comparison of the data reveals that as the energy density reduces, both the optical gap and β^{-1} parameter increases. The results infer that the band tails increase continuously as the deposition energy density increases.

Energy Density (J cm ⁻¹)	Optical Gap (eV)
3.0	1.92
3.5	1.76
4.0	1.62
5.0	1.50
6.0	1.39

Table 5.4. The optical band gap for the thin films grown by pulsed laser ablation at different energy densities.

It is clear from these optical and the EXAFS results in the previous chapter that the deteriorating properties of the films deposited at high energy density are a result of Ga-Ga and S-S "wrong" bonds. For device applications optimum quality films are deposited at energy densities close to the ablation threshold. Although the degree of near infrared absorption caused by gap narrowing and tail absorption remains inconveniently high for

devices requiring very near infrared pumping (e.g. 810 nm pumped Nd^{3+} based devices) it is more promising for longer wavelength based systems (e.g. 980 nm pumped Er^{3+} based devices).

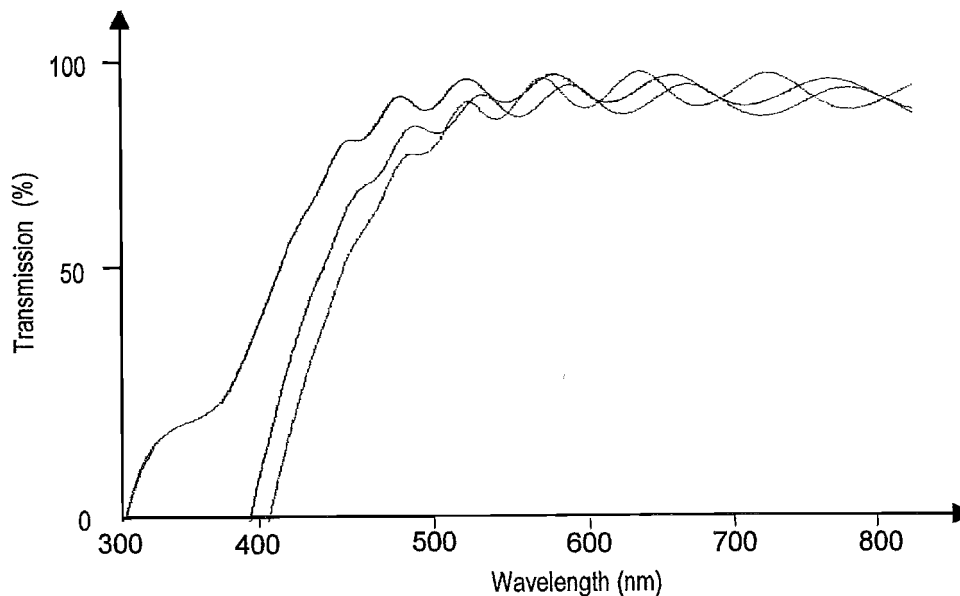


Figure 5-9. A typical transmission spectra through a thin GLS film (—), after saturated photomodification (---) and after annealing at 400 °C for three hours (···). {Original in colour}

In order to improve the quality of the GLS thin films, we annealed samples for a duration of three hours at a temperature of 400 °C in a nitrogen environment. The effect of the annealing is that the optical gap increases (from 1.9 to 2.1 eV) and the absorption edge shifts to higher energy. A typical example of film transmission is shown in Figure 5-9 for reference and will be discussed in more detail in Section 6-3. This may be due to the breakage of the "wrong" bond and the formation of heteropolar bonds in GLS film samples. Street *et al.* [285] suggested that the major contribution to the blue shift of the gap in chalcogenide (GeSe) thin films was from the reduction in the density of homopolar bonds.

5.4 Thin Film Uniformity

5.4.1 Thickness Profiling

The optical characterisation of amorphous films from only the transmission and reflection spectra at normal incidence should take into consideration the possible lack of film thickness uniformity. Thus, the assumption of considering a film as a layer of parallel faces leads inevitably to potential errors. In practice, thin film thickness is not constant but varies across the substrate. A plume of material, be it from laser ablation or a boat in an evaporator, will form a more even coating on a parallel substrate with greater separation. Plume expansion means that increasing this distance results in a lower area density of material coming into

contact with the substrate, hence causing increased growth times. The angular distribution of ablated material was initially regarded as a disadvantage of PLD because uniform thickness films were obtained only in a small region in the forward direction.

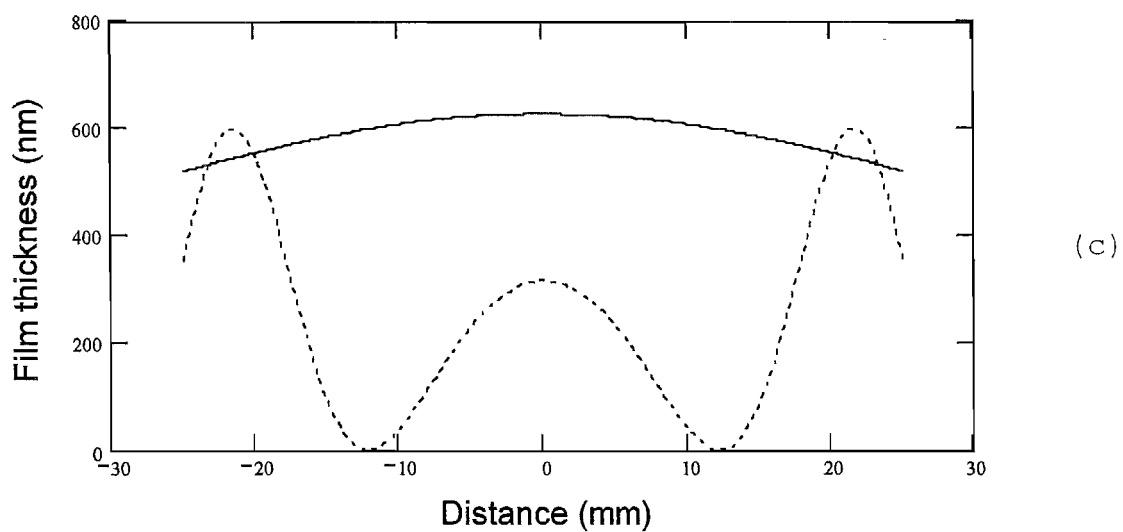
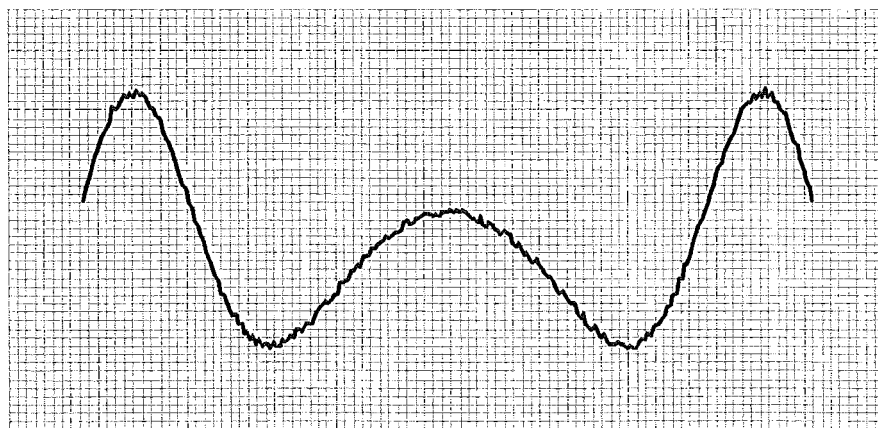
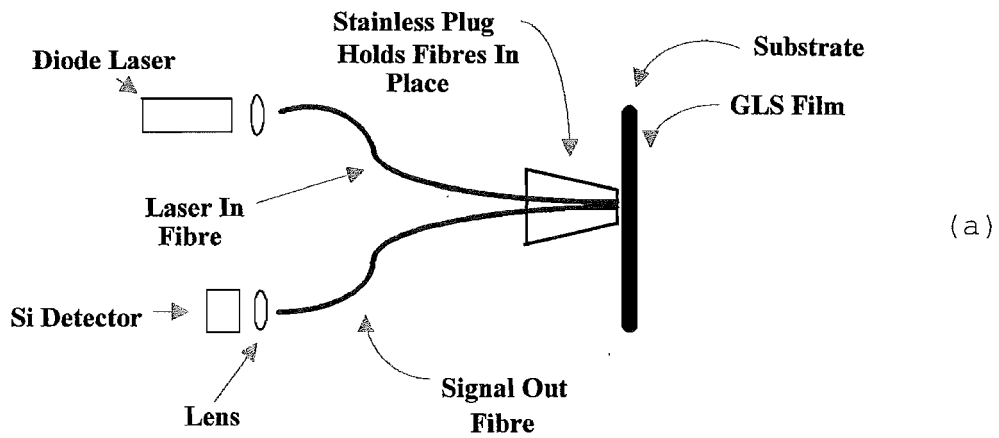


Figure 5-10. (a) The experimental arrangement used to produce the thickness profile of a thin film layer, (b) a plot of the interference fringes and (c) the averaged data (.....) and the film thickness change (—) {Original in colour}

Figure 5-10(a) shows the experimental arrangement used to plot the film thickness as it changes from the plume centre zone, the so-called 'bull's eye' region due to the apparent concentric circles which appear on the film surface (caused by the interference pattern in incident white light). Two multimode fibres, one to deliver laser light at 635 nm, normal incidence (polarisation state is irrelevant) and one to collect the reflected light, are used to monitor the intensity changes as the pair are translated across the varying thickness of the thin film layer. The thickness at the centre of the film is found by fitting the data to the multiple surface transmission Fresnel equation 5-12. The thickness variation can be characterised as a deviation from the centre thickness, Figure 5-10(b) with (c) show the averaged data and the thickness profile, for the same film, shown in the first spectrum of Figure 5-3.

Because the substrate holder was oscillated in the vertical plane to improve film uniformity it was not noted for some time that the three dimensional shape of the ablation plume is not actually conical. Horizontally, the thickness profile matches that of a traditional point source evaporation crucible, which typically has a $\cos^m \theta$ distribution profile where $m \simeq 4$ [286]. In the vertical (un-oscillated films) thickness distribution fits to $m \simeq 7$. To produce highly uniform films requires that methods need to be found to create a more evenly distributed area density and reduce the 7:4 ratio of thickness profile in the respective perpendicular directions.

5-4-2 Improved Film Uniformity

The laser pulse yields a highly forward angular distribution of the ejected mass and this fact has limited most laboratories to producing ablated thin films over relatively small substrates (1 or 2 cm in size). The profiles are highly non-uniform with thickness variations from substrate centre to edge and furthermore, there are significant differences between the distributions obtained from the same substrate in the two perpendicular directions. The maximum in the profile obtained in the "parallel" direction is located close to the centre. This peak of the ablated flux is actually tilted back toward the direction of the incident laser beam by about 5°. Results clearly indicate that a plume generated by a small rectangular laser spot yields an asymmetric and non-uniform flux distribution which can lead to non-uniform film properties.

Numerous techniques have been developed to improve thin film uniformity. These usually involve scanning the incident laser beam across the surface of the target and moving the plume centre location or, for example, using a half cylindrical target and a scanning mirror for the laser, to "paint" a plume across the substrate at different tangential angles which in turn moves the plume in both perpendicular directions [102, 214]. One expensive extreme has been developed which paints a long narrow rectangular, homogenised beam across a large

target and an equally sized parallel substrate^[287]. The only limitation of substrate size in this example is the quality of the homogeniser and the energy of the laser pulse. Larger target-to-substrates distances also increase thin film uniformity, but the results have shown this reduces the film quality which creates ultimately a trade-off.

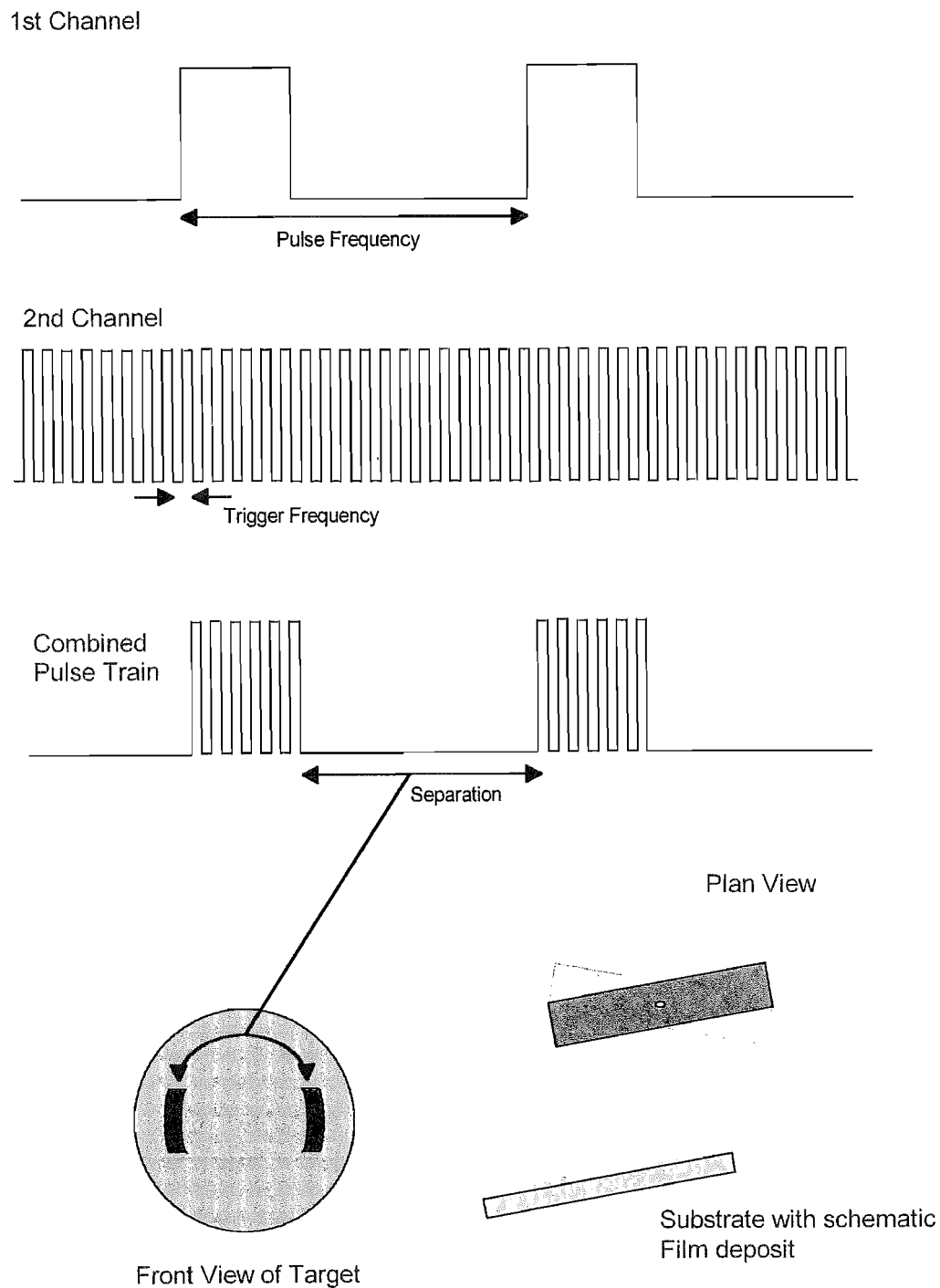


Figure 5.11. The electronic waveforms required to drive the laser pulses which work with the 'wobble' target holder to paint the plume and ultimately produce more uniform films across the substrate surface. {Original in colour}

A method was developed which is inexpensive and when calibrated can produce extremely uniform films. The technique is based on two simultaneous oscillations in perpendicular directions, one aims the plume and the second translates the substrate relative to the plume position. Figure 3-5 showed a schematic of the mounting arrangement and plume expansion direction based on the 'wobble device'. Remembering that the plume is ejected perpendicular to the target surface irrespective of the incident angle of the excimer laser beam (assuming a recently polished target surface, otherwise as previously stated, the plume axis tends slightly towards the incident angle of the pulsed laser), the plume direction can be adjusted.

With the ejected plume not being symmetrical, the two oscillation modes had to be combined to produce the best thin film uniformity. The substrate oscillation speed controlled the vertical uniformity and was used from the beginning of the project. The wobble device has to restrict its plume "painting" to horizontal sweeps. However with the spinning target being 'wobbled' a continuously changing plume direction results which, without additional control, provides a circular trace of deposited material on the substrate surface.

To remove this circular profile, a more elaborate laser triggering control circuit was produced. A pulse generator was set to match the current range of trigger speeds which were available from the lasers own internal trigger unit. Using the Boolean logic AND to combine this and a much slower pulsed signal, the resultant output (which acted as the laser trigger) was short bursts of higher frequency pulses. It is now possible to produce plumes which are 'painted' to the left or right of the substrate and omit pulses when the plume would be aimed up or down in the substrate plane. Figure 5-11 represents the trigger waveforms and the resultant ablation positions on the target which were achieved to 'paint' the plume.

Parameter (units)	Range of variance		
	minimum	intermediate	maximu
mark-space ratio	1:5	1:10	1:20
trigger speed (Hz)	5.0	10.0	20.0
target spin rate (Hz)	$\frac{1}{12}$	$\frac{8}{12}$	$\frac{16}{12}$
target-substrate separation (cm)	6.0	-	9.0
target mounting angle (°)	5.5	-	8.5

Table 5-5. Parameters which are believed to effect the thin film grown uniformity, showing the respective change in values which can be easily achieved, to experimentally find the optimum set of conditions for thin film production.

With this control unit an extensive investigation began to find the best combination of mark-space ratio, laser trigger speed, target spin frequency, target to substrate separation

and target mounting angle, which could produce the most uniform film profile over the largest area. Growth speeds were reduced by a factor of 3 or 4 as the laser was effectively turned on and off, producing pulses for a fraction of the original time. This also caused target wear in 2 sectors rather than a complete uniform removal in the more traditional ring pattern. This could be improved somewhat by turning the target by 90° every ten ablation runs. Table 5-5 lists these parameters, their easily achievable extreme values and the number of possible steps chosen for the experiment.

The range of variables were chosen and given values which would be easy to set as deposition conditions. The corresponding thin film which was produced using this set of parameters for a duration of sixty minutes, had its thickness profiles measured using the previously described back surface reflection technique (Figure 5-10). The centre thickness is recorded and the maximum deviation from this, recorded as a percentage of this value. The two important values which can be found from this are the thickness variation as well as the width of the uniform profile. The width of the thin film was determined as the distance between the two edge roll-off points with the same value as that recorded at the centre. This produced a fair comparison, since the centre value always exhibited a slight dip in thickness which the pulse control box induced. Table 5-6 shows the experimental data and the variables used. It can be seen from the data that relatively large area uniform films can be produced when using the electronic control for thin films growth in these conditions to achieve an optimum value.

Optimum growth conditions are obtained from the largest of the ratio - width of uniformity to percent deviation, which is shown in the final column of Table 5-6. All of the films had a characteristic dip in their thickness profile, shown schematically in Figure 5-11. The thickness of the film was measured at this point and then the difference between this and the point of maximum thickness recorded as a percentage. As previously stated the width of the uniformity is defined from the roll-off edge points where the film thickness falls below the centre thickness. The larger the width - deviation ratio, the better the film uniformity. In all three parts of the table, the two highest values are achieved with the largest target to substrate separation and the largest angle of sweep as would be expected. However these also exhibit slowest growth rates. The optimum trade-off between speed of growth and uniformity uses a width : deviation ratio above the average 6.55. The thickest film is formed from the shortest plume travel distance, the smallest sweep angle, and the higher repetition rate, as expected. The results show that the most uniform films are produced at longer target to substrate distances, higher target spin rate with slow trigger speeds to pulse the excimer laser, i.e. a small mark-to-space ratio. Figure 5-12 shows the improvement in thin film uniformity with only 10% (central) thickness when compared with the previous film shown by the data in Figure 5-10 (c). The difference was due to the lower growth rates with controlled growth, but still acts as a good comparison.

Mark-space ratio	Trigger speed (Hz)	Target spin rate (Hz)	Target to substrate separation (cm)	Target mounting angle, (°)	Centre thickness (nm)	Width of uniformity (mm)	Width % Deviation	
1:5	5.0	$1/_{12}$	6.0	5.5	262.97	3.39	0.46	
				8.5	195.86	3.37	0.40	
			9.0	5.5	132.50	5.81	0.47	
				8.5	100.81	6.17	0.55	
			6.0	5.5	32.17	10.86	11.09	
				8.5	24.96	11.66	13.06	
		$2/_{3}$	9.0	5.5	16.65	20.74	13.53	
				8.5	12.95	23.79	17.42	
			6.0	5.5	17.99	15.93	22.43	
				8.5	12.42	17.95	21.72	
			9.0	5.5	8.48	31.86	27.32	
				8.5	6.59	35.61	34.26	
		$1^{1}/_{4}$	6.0	5.5	524.74	2.60	0.17	
				8.5	396.15	3.27	0.18	
			9.0	5.5	295.39	5.49	0.22	
				8.5	197.01	6.16	0.26	
			6.0	5.5	65.79	10.82	4.01	
				8.5	52.59	11.50	3.55	
	10.0	$2/_{3}$	9.0	5.5	35.96	20.82	4.53	
				8.5	25.27	23.17	5.62	
			6.0	5.5	33.95	15.51	10.49	
				8.5	24.84	17.30	11.95	
			9.0	5.5	16.75	30.96	14.76	
				8.5	12.87	35.08	17.38	
		$1^{1}/_{4}$	6.0	5.5	1048.66	2.61	0.09	
				8.5	776.95	3.00	0.10	
			9.0	5.5	530.59	5.52	0.13	
				8.5	392.48	5.81	0.14	
			6.0	5.5	130.56	10.36	1.82	
				8.5	98.37	11.61	1.94	
		20.0	$2/_{3}$	9.0	5.5	65.81	20.79	2.41
					8.5	49.27	23.23	2.77
				6.0	5.5	65.73	15.34	5.48
					8.5	49.94	17.55	5.27
				9.0	5.5	34.57	31.55	7.01
					8.5	24.39	34.94	8.73

Table 5.6(a). GLS thin films grown with the various deposition parameters shown in Table 5.5 and rearrangement for providing improved uniformity presented schematically in Figure 5.II.

Mark-space ratio	Trigger speed (Hz)	Target spin rate (Hz)	Target to substrate separation (cm)	Target mounting angle, (°)	Centre thickness (nm)	Width of uniformity (mm)	Width % Deviation
1:10	5.0	$1/12$	6.0	5.5	136.93	5.91	0.49
				8.5	101.34	5.88	0.43
			9.0	5.5	68.81	10.11	0.54
				8.5	51.89	10.74	0.65
		$2/3$	6.0	5.5	16.73	18.90	13.23
				8.5	12.24	20.30	12.58
			9.0	5.5	8.75	36.08	14.03
				8.5	6.55	41.41	19.17
		$1 1/4$	6.0	5.5	9.31	27.71	26.66
				8.5	6.98	31.23	24.75
			9.0	5.5	4.12	55.43	30.79
				8.5	3.98	55.89	27.25
	10.0	$1/12$	6.0	5.5	271.06	4.54	0.21
				8.5	205.35	5.22	0.18
			9.0	5.5	137.91	9.60	0.26
				8.5	102.69	10.11	0.28
		$2/3$	6.0	5.5	33.51	18.03	4.07
				8.5	26.71	20.20	4.51
			9.0	5.5	18.24	36.18	5.23
				8.5	13.63	40.57	6.36
		$1 1/4$	6.0	5.5	17.05	26.72	12.57
				8.5	12.96	30.54	12.62
			9.0	5.5	8.75	54.69	15.15
				8.5	6.03	60.80	18.93
	20.0	$1/12$	6.0	5.5	543.54	4.53	0.11
				8.5	402.55	5.69	0.11
			9.0	5.5	274.71	9.55	0.13
				8.5	203.12	10.71	0.16
		$2/3$	6.0	5.5	67.64	18.83	2.20
				8.5	50.53	20.01	1.98
			9.0	5.5	33.89	36.22	2.50
				8.5	25.63	40.31	3.09
		$1 1/4$	6.0	5.5	33.37	21.98	5.09
				8.5	25.86	30.11	5.95
			9.0	5.5	17.33	53.87	7.50
				8.5	12.91	61.04	9.41

Value used in Figure 5.12

Table 5.6(b). GLS thin films grown with the various deposition parameters shown in Table 5.5 and rearrangement for providing improved uniformity presented schematically in Figure 5.11.

Mark-space ratio	Trigger speed (Hz)	Target spin rate (Hz)	Target to substrate separation (cm)	Target mounting angle, (°)	Centre thickness (nm)	Width of uniformity (mm)	Width % Deviation
1:20	5.0	$1/_{12}$	6.0	5.5	75.30	2.51	0.26
				8.5	56.14	2.88	0.26
			9.0	5.5	38.01	5.30	0.33
				8.5	28.69	5.59	0.39
		$2/_{3}$	6.0	5.5	9.33	10.44	8.70
				8.5	7.04	11.22	8.01
			9.0	5.5	4.85	19.93	9.97
				8.5	3.55	22.88	12.71
		$1^{1}/_{4}$	6.0	5.5	5.10	2.50	2.78
				8.5	3.58	3.14	2.99
			9.0	5.5	2.52	5.28	3.52
				8.5	1.91	5.92	4.39
	10.0	$1/_{12}$	6.0	5.5	150.26	3.27	0.17
				8.5	113.50	3.25	0.15
			9.0	5.5	76.11	5.59	0.17
				8.5	56.49	5.93	0.21
		$2/_{3}$	6.0	5.5	18.71	14.91	4.14
				8.5	14.91	16.64	3.96
			9.0	5.5	10.04	29.76	4.96
				8.5	7.23	33.72	6.24
		$1^{1}/_{4}$	6.0	5.5	9.55	9.96	5.53
				8.5	7.16	15.31	7.29
			9.0	5.5	4.75	30.22	10.07
				8.5	3.63	33.59	12.44
	20.0	$1/_{12}$	6.0	5.5	300.34	10.40	0.27
				8.5	222.55	17.25	0.39
			9.0	5.5	151.91	19.99	0.31
				8.5	112.52	22.27	0.38
		$2/_{3}$	6.0	5.5	37.44	10.55	1.47
				8.5	28.13	11.06	1.32
			9.0	5.5	18.69	30.62	2.55
				8.5	14.23	34.24	3.17
		$1^{1}/_{4}$	6.0	5.5	18.77	11.41	3.17
				8.5	14.06	16.87	4.01
			9.0	5.5	9.93	22.41	3.74
				8.5	7.11	33.47	6.20

Table 5-6(c). GLS thin films grown with the various deposition parameters shown in Table 5.5 and rearrangement for providing improved uniformity presented schematically in Figure 5.11.

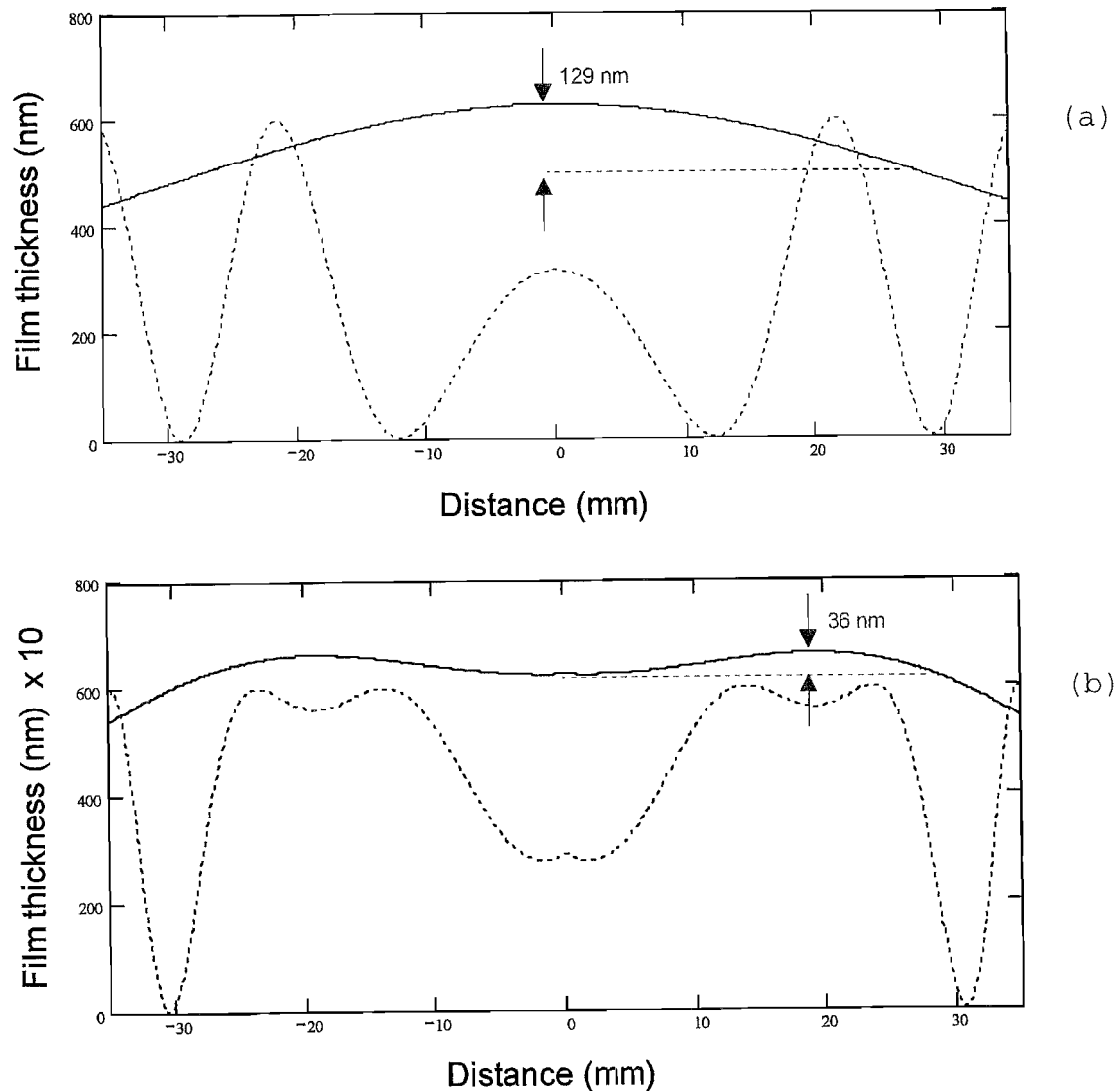


Figure 5-12. (a) Data from Figure 5-10(c) with the averaged data (.....) and the film thickness change (—) repeated for comparison with, (b) the thin film, only 10% thickness, but with optimum width:deviation ratio of 37.25 (see highlight in Table 5-6(b)). The respective thickness changes are indicated for the 55.89 mm uniformity width detailed in the Table. {Original in colour}

5.5 Conclusion

A variety of different expressions maybe used to describe material properties to characterise glassy materials through the determination of their optical constants. For GLS thin films, refractive indexes based on the Sellmeier formula produced the closest match between the modelled transmission equations and the actual experimental data.

The GLS films were grown with variations in one or more of the deposition parameters. Two examples were the fixed number of pulses and at the same pulse repetition rate with a

variation from 2.0 to 6.0 J cm⁻² energy density range. The thin films optical properties changed when the various deposition parameters were changed. It has been shown that energy density on the target surface affects the optical bandgap of the subsequent thin film layer and hence its region of transparency.

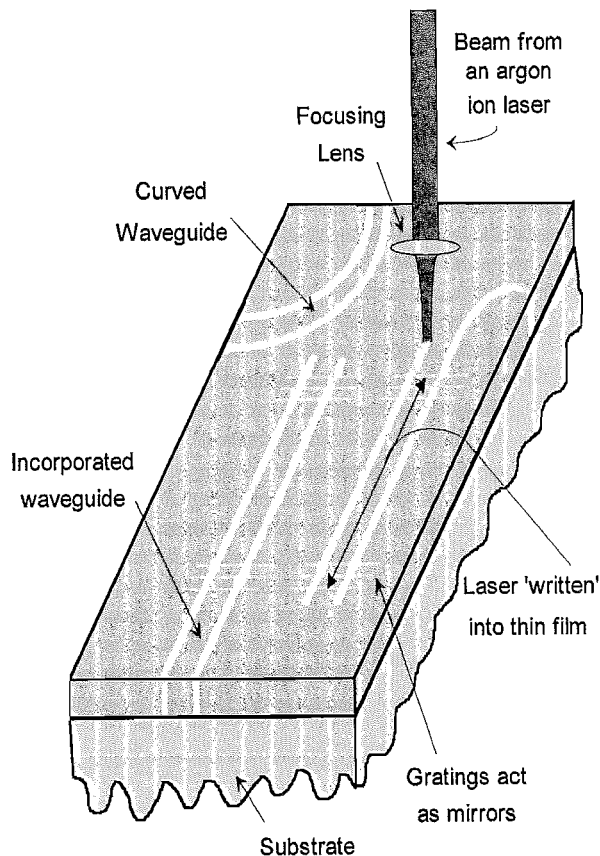
When thin films are grown in a background gas it has been shown that the larger the molecular weight of gas the greater the plume spread and consequently the thinner the film layer. Interaction between plume and background gas lowers its range and is emphasised by the visible emission during the interaction between the plasma and atoms present. However, results have shown that oxygen at low pressure in the vacuum chamber still affects the optical properties of the thin film significantly. This is probably due to surface reaction during the deposition process rather than a plume interaction. As Table 5-3 shows the film grown in higher pressures of oxygen (0.1 mbar) appears to be becoming an oxide with the much reduced refractive index.

A phenomenon which became apparent during a specific experimental data set, whilst trying to establish if a non-parallel orientation of target and substrate would make more uniform thin film coatings, was that the thin film thickness increases dramatically once the emerging plume and substrate holder are not perpendicular. This is believed to be a result of structural changes of the material. The results show there is an optimum orientation angle for thin film thickness before the effective surface area of the substrate reduces significantly and hence the rate of deposition drops.

The three dimensional shape of the ablation plume is not conical due to the rectangular shape of the excimer laser beam profile. Throughout the course of this work the ablating spot size was a 1 x 3 mm horizontal rectangle which defines the energy density for a fixed fluence. Horizontally, the thickness profile matches that of a traditional point source evaporation crucible. Extensive investigative work showed that by periodic re-deposition of material leads to improved uniformity of the plume, thin film uniformity can be optimised. This can be used in addition to translating the substrate relative to the plume position, but this reduces growth speeds by a factor of 3 or 4 as the laser was effectively turned on and off causing target wear in two sectors rather than a complete uniform removal in the traditional ring pattern.

6

Measurements of Photomodification



A Potential for thin films of chalcogenide based materials is the ability to change the refractive index via illumination with a focused laser beam and so removing the need for conventional masking.

6.1 Introduction

6.2 Differential Reflectance Technique

6.3 Photomodification of Thin Films

6.4 Fast Photomodification Effect

6.5 Bulk Photomodification

6.6 Photoinduced Gratings

6.7 Conclusions

6.1 Introduction

By way of a reminder, photomodification in chalcogenide materials occurs when the material is illuminated with above bandgap radiation causing a change in the refractive index and a shift of the absorption edge. It falls into two categories: those that photodarken (a red shift) and those that photobleach i.e. produce a blue shift in the absorption edge. In most chalcogenides this is achieved with the blue and green lines of the argon ion laser or UV lasers. Although the mechanism by which this process occurs is not yet fully understood it is thought to arise from a structural change caused by the breaking of atomic bonds^[288]. The majority of current non-chalcogenide waveguide devices presently use thermal diffusion, ion exchange or ion implantation to increase the refractive index of a channel in a thin film or bulk substrate of the waveguide material. Since chalcogenide materials can be directly 'written' into, tracks and gratings for example can easily be introduced without the need for masks and etching.

In any waveguide device an accurate knowledge of the optical characteristics (e.g. refractive index profile, mode profile, cut-off wavelength, propagation losses) is necessary for device design and specification. We routinely produce thin films of chalcogenide glasses on a variety of substrate materials^[289]. It is necessary to characterise, amongst other parameters, the refractive index of the material and its ability to photomodify as a function of deposition conditions. A novel technique has been developed which allows both the mapping of refractive index changes across a surface and measurement of the rate of photomodification in a given region of a GLS thin film. The technique is based on intensity measurements of reflected signals from two adjacent points on the surface of a material. A galvanometer mirror 'dithers' a polarised laser beam onto a sample surface and a phase sensitive detector (PSD) produces a differential reflectance signal which is converted to a refractive index change from the data by using the appropriate Fresnel equations. However, angle variations in the 'dither' itself affect surface reflection and these errors have to be minimised to achieve accurate results. The method then allows refractive index changes with a sensitivity $\sim 8.5 \times 10^{-5}$ to be monitored. Measurements can be made at any wavelength and since it is a non contact technique. The material can be treated whilst being analysed, for example film/substrate temperature changes.

For the majority of applications requiring index modification, accurate knowledge of the absolute refractive index is rarely required but a measurement of the difference between two adjacent regions is essential. This technique developed here addresses this second demand. Other methods for index profiling include the 'Propagation mode near field' method^[290] which requires propagating a beam for some distance along the guide and measuring its output intensity profile. In turn this means that the technique becomes subject

to material losses, coupling losses and is restricted to discrete wavelengths for the given material. It is also in general not applicable to the measurement of the time dependence of the photomodified refractive index, another strength of our technique. Similar problems occur for slab waveguide techniques such as WKB^[291, 292] and inverse WKB^[293, 294] (Wentzel, Kramers, Brillouin and Jeffreys, also called the phase integral method). Our method requires no guiding and can map large areas of sample surface where multiple waveguides can exist, at any wavelength. It has the additional advantage of measuring both increases and decreases in refractive index where waveguides are not easily formed. Our technique was developed to measure the magnitude and sign of the refractive index change in the thin films that we produced. This method of measurement is used extensively throughout this chapter.

6.2 Differential Reflectance Technique

6.2.1 Theory

6.2.1.1 Bulk Materials

We measure the reflectivity of a bulk or multilayer surface as a function of angle of incidence at two different positions using plane polarised, monochromatic light at any desired wavelength. If the incident angle is measured and the thickness of any thin film layers known, the difference in the refractive indices at the two points can be determined from the variation in the reflected intensity. Since dithering a laser beam introduces small angle differences in the two incident beams, the resultant reflection differences have to be addressed to prevent errors arising.

An incident light ray is represented by two orthogonal, usually equal amplitude, polarisation components. The individual components of reflectance are given by the well known Fresnel formulae^[271] which are given by equations 5.6 and 5.8 and using Figure 5.1 for reference. It can be seen that at incident angles less than θ_B (the Brewster angle) the partial differentials $\frac{\partial \mathfrak{R}_s}{\partial \theta_1}$ and $\frac{\partial \mathfrak{R}_p}{\partial \theta_1}$ are of opposite sign, see Figure 6.1. Hence for a specific polarisation angle the first differential of the total reflectivity with respect to incidence angle can be forced to zero. The required polarisation angle is dependent on the incident angle of the beam and refractive indices of the media, hence on the wavelength of the incident light ray. Figure 6.2 shows the required polarisation angles to force the gradient of $\mathfrak{R}_s \cos^2 \phi$ and $\mathfrak{R}_p \sin^2 \phi$ to have equal and opposite magnitudes, thus $\frac{d\mathfrak{R}}{d\theta_1} = 0$, for five materials with refractive indices of 1.5, 2.5, 3.0, 3.5 and 4.0 in air, over a range of incidence angles.

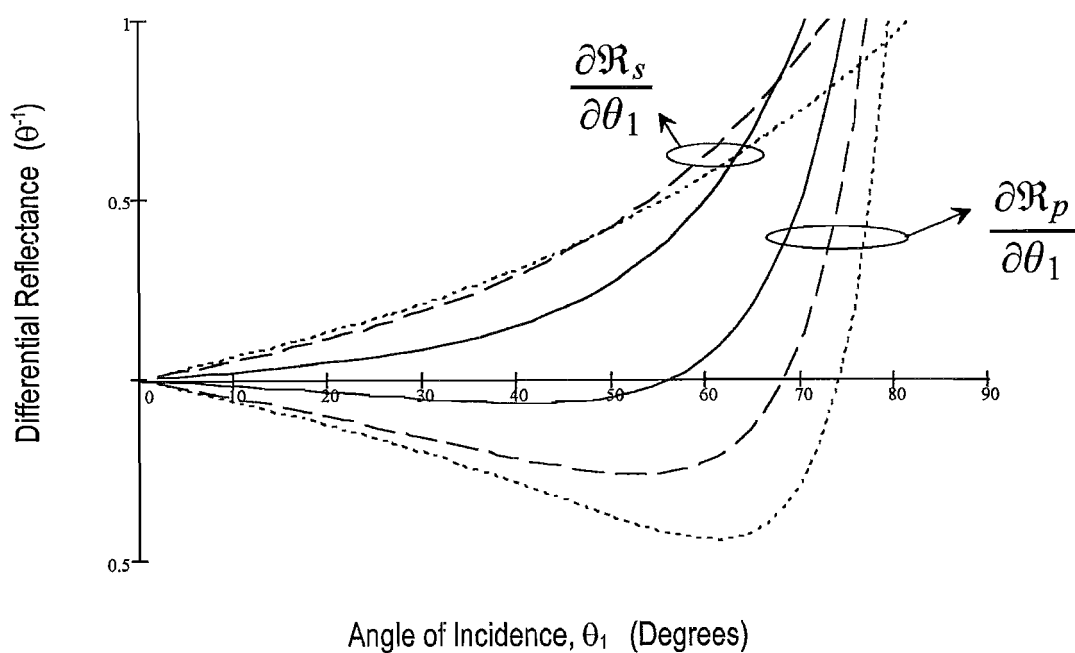


Figure 6.1. The differentials of $\frac{\partial \mathcal{R}_s}{\partial \theta_1}$ and $\frac{\partial \mathcal{R}_p}{\partial \theta_1}$ when n_2 is 1.5 (—), 2.5 (---) and 3.5 (····). {Original in colour}

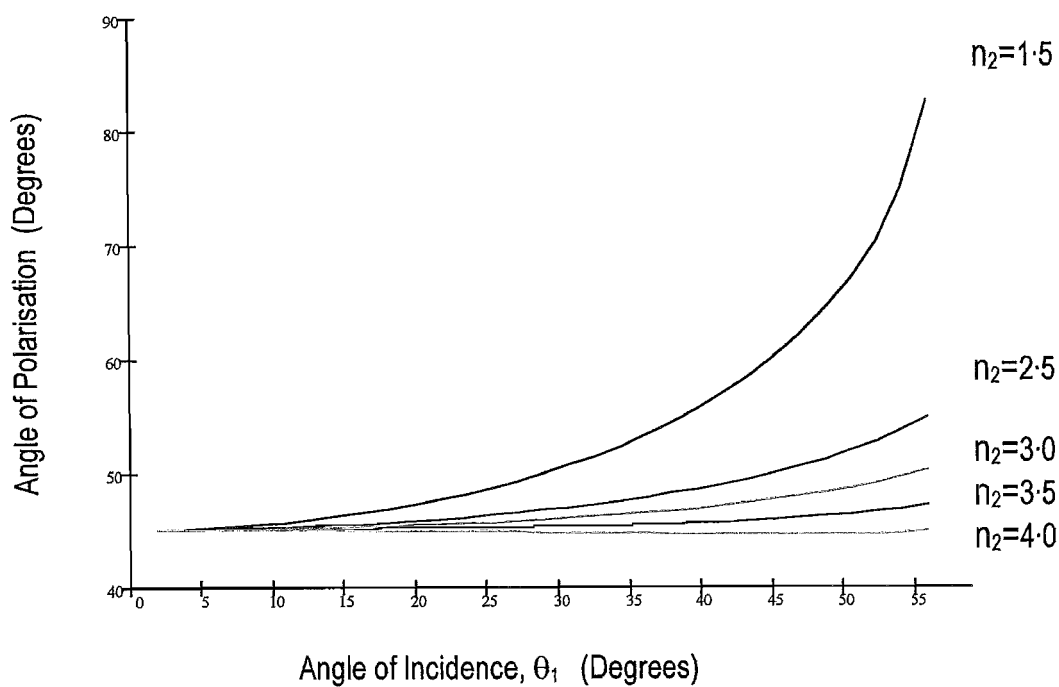


Figure 6.2. 'Optimum' polarisation angle as a function of angle of incidence with respect to p plane. The graph is plotted for media of refractive index, n_2 ; 1.5, 2.5, 3.0, 3.5 and 4.0 in air. {Original in colour}

Whilst the introduction of an incident polarised beam at the required angle reduces the rate of change of total reflectivity (with respect to incident angle) to zero there is a consequential reduction in the derivative of the reflected beam intensity with respect to the index of the thin film layer, n_2 . If we are to map small changes in the refractive index of a material based on these reflections, $\frac{\partial R}{\partial n_2}$ needs to be as large as possible to increase sensitivity. Figure 6.3 shows the ratio of the reflected beam intensity from unpolarised and plane polarised incident laser radiation, at the angle required to reduce $\frac{\partial R}{\partial \theta_1}$ to zero, χ , by showing the difference ratio for the partial differentials $\frac{\partial R_P}{\partial n_2}$ for the two cases ($\frac{\partial R_P}{\partial n_2}$ UNPOLARISED : $\frac{\partial R_P}{\partial n_2}$ POLARISED). It can be seen that after polarisation ($\frac{\partial R}{\partial \theta_1} \rightarrow 0$) approximately 50% of the reflected signal is lost at small incidence angles with less degradation for lower refractive indices and higher incidence angles. Up to a factor of ~ 2 loss in the signal is the consequence of forcing $\frac{\partial R}{\partial \theta_1}$ to zero.

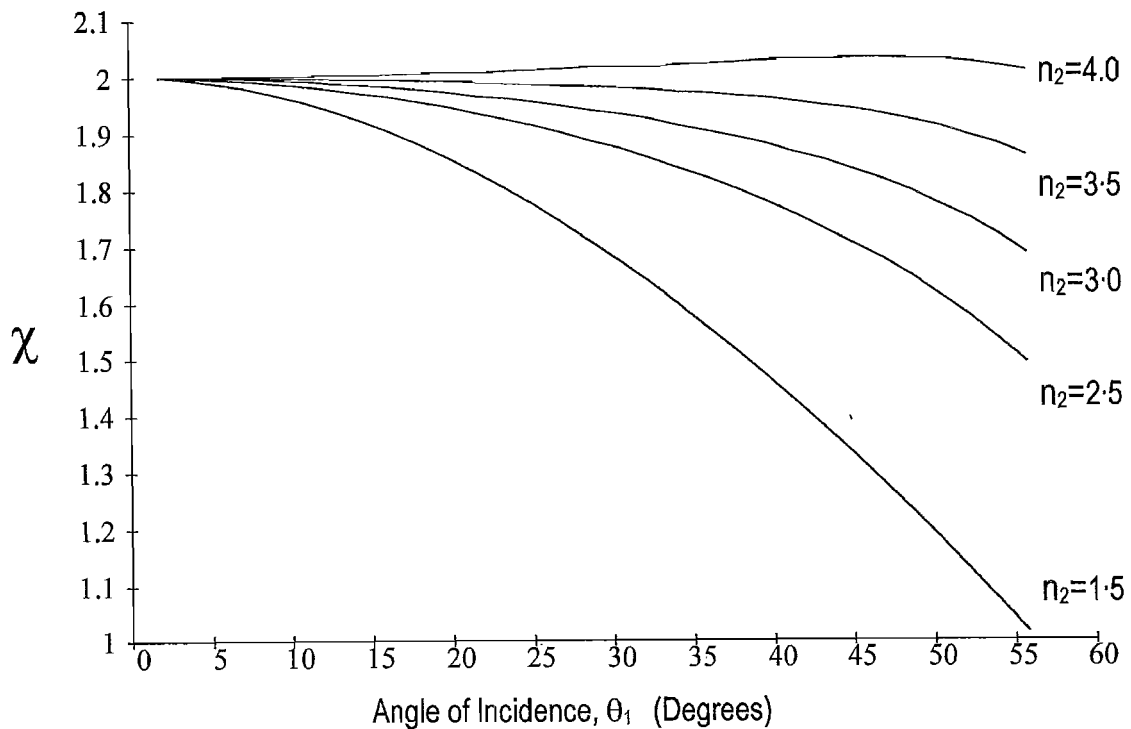


Figure 6.3. The ratio of the partial differential $\frac{\partial R_P}{\partial n_2}$ before and after orientation at the angles calculated for Figure 6.2, with values for n_2 at 1.5, 2.5, 3.0, 3.5 and 4.0.

6.2.1.2 Thin Films

Whilst the principles detailed above remain valid for multilayer materials made of many thin film layers on a substrate, the two equations for the polarised reflectivity become more complex. In this section the samples used are thin films of GLS (initially 70% Ga_2S_3 and 30% La_2S_3) on BK7 glass substrates. However the method is extremely flexible and applicable to a very wide range of bulk or thin film multilayer materials. For a single thin film

layer, equations 5.6 and 5.8 need to be modified to take account of the additional interface, with the substrate and media behind being defined by n_3 , n_4 , θ_3 and θ_4 (in our example media 4 is the same as media one, air). A thin film of refractive index n_2 , with thickness t on a substrate material n_3 , requires that the original equations for the intensity of the two polarisation state reflectances from the single surface, combine the Fresnel formulae as a geometrical progression to sum the total multiple reflections and transmissions which take place at each boundary. To simplify the presentation of these equations the individual interface reflectances and transmissions are generalised with the subscript x representing the media through which the light beam is incident prior to reaching the interface. R, T, S and P in the following equations refer to reflection, transmission, s and p polarisation respectively with equations 6.1 and 6.2 being the resultant surface reflectivity for a thin film on a bulk substrate material and α is the phase shift of the light as it passes through the thin film layer.

$$\mathcal{R}_s = \left| \frac{RS_1 + RS_2 \cdot a}{1 + RS_1 \cdot RS_2 \cdot a} \right|^2 + \frac{\left| \frac{TS_1 \cdot TS_2 \cdot a}{1 + RS_1 \cdot RS_2 \cdot a} \cdot RS_3 \right|^2 \cdot \frac{n_3 \cdot \cos \theta_3}{n_1 \cdot \cos \theta_1}}{1 - \left| \frac{RS_1 + RS_2 \cdot a}{1 + RS_1 \cdot RS_2 \cdot a} \cdot RS_3 \right|^2} \dots \dots (6.1)$$

$$\mathcal{R}_p = \left| \frac{RP_1 + RP_2 \cdot a}{1 + RP_1 \cdot RP_2 \cdot a} \right|^2 + \frac{\left| \frac{TP_1 \cdot TP_2 \cdot a}{1 + RP_1 \cdot RP_2 \cdot a} \cdot RP_3 \right|^2 \cdot \frac{n_1 \cdot \cos \theta_3}{n_3 \cdot \cos \theta_1}}{1 - \left| \frac{RP_1 + RP_2 \cdot a}{1 + RP_1 \cdot RP_2 \cdot a} \cdot RP_3 \right|^2} \dots \dots (6.2)$$

Where: $a = \exp[i \cdot \frac{4\pi t}{\lambda} \cdot n_2 \cdot \cos \theta_2]$, $TS_x = \frac{2 \cdot n_x \cdot \cos \theta_x}{n_x \cdot \cos \theta_x + n_{x+1} \cdot \cos \theta_{x+1}}$, $TP_x = \frac{2 \cdot n_{x+1} \cdot \cos \theta_x}{n_{x+1} \cdot \cos \theta_x + n_x \cdot \cos \theta_x}$, $RS_x = \frac{n_x \cdot \cos \theta_x - n_{x+1} \cdot \cos \theta_{x+1}}{n_x \cdot \cos \theta_x + n_{x+1} \cdot \cos \theta_{x+1}}$ and $RP_x = \frac{n_{x+1} \cdot \cos \theta_x - n_x \cdot \cos \theta_{x+1}}{n_{x+1} \cdot \cos \theta_x + n_x \cdot \cos \theta_{x+1}}$.

As the index of the film increases the multilayer combination has no Brewster angle, the characteristic dip in \mathcal{R}_p begins to disappear and at the same time moves towards higher angles and increasing reflectivity. As an example Figure 6.4 shows results for a sample grown by laser ablation and using a 633 nm laser beam which is not absorbed by the GLS thin film ($n_2=2.76$) or the probed glass substrate. The thickness of the film and a Sellmeier equation for the refractive index were determined by fitting the optical thickness to the transmission intensity over a range of wavelengths producing the quoted value for n_2 and a thickness of 0.151 μm . The example in Figure 6.4 shows the calculated parallel polarised reflectance, \mathcal{R}_p , of 0.151 μm thick film as its refractive index is varied. The figure also shows the effect of increasing the angle of incidence on the reflectivity profile. Good accuracy requires $\frac{d\mathcal{R}}{dn_2}$ to be large. The smallest practical, mean angle of incidence is 15° (See section 6.2.2). This also produces the greatest value of $\frac{d\mathcal{R}}{dn_2}$ for our thin film sample.

Increasing the thickness of the film layer increases the number of periods (See Figure 5.3), hence it is possible to maximise $\frac{\partial R_p}{\partial n_2}$ by selecting the optimal angle of incidence for each thin film thickness. At 15° incidence a polarised, dithered laser beam needs to be used because the two polarisation orientations do not have equal reflection intensities. As demonstrated earlier this will degrade the overall differential signal by up to a factor of 2.

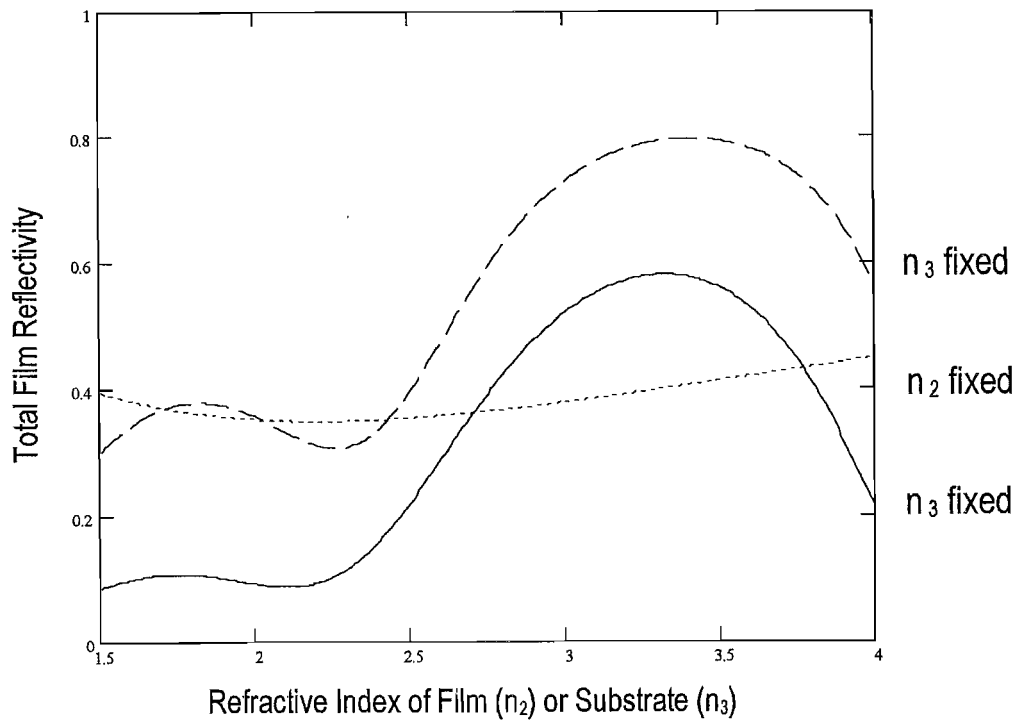


Figure 6.4. Reflectivity of a 0.151 μm thin film over a range of refractive indices on a BK7 glass substrate ($n_3=1.51$) at incidence angle: (a) 15° (—), (b) 60° (---) and (c) a GLS film ($n_2=2.76$) on an imaginary theoretical substrate (····) for p polarised light. {Original in colour}

The refractive index of GLS is slightly higher than most materials used in similar waveguide devices and optical arrangements. Growing thin films of different thickness can position the maximum of $\frac{\partial R_p}{\partial n_2}$ for the more common film indices of 1.7 to 2.2, for the first order peaks, with larger incidence angles producing higher reflectances. As well as maximising $\frac{\partial R_p}{\partial n_2}$ by changing the angle of incidence, it is also possible to move along the abscissa by changing the wavelength of the incident radiation as this produces a different effective n_2 for the film layer; this technique uses any convenient laser wavelength as a measuring source. Finally it can also be seen from Figure 6.4, that even large refractive index changes of the substrate for a fixed index, n_2 , produce only small variations in the overall surface reflection.

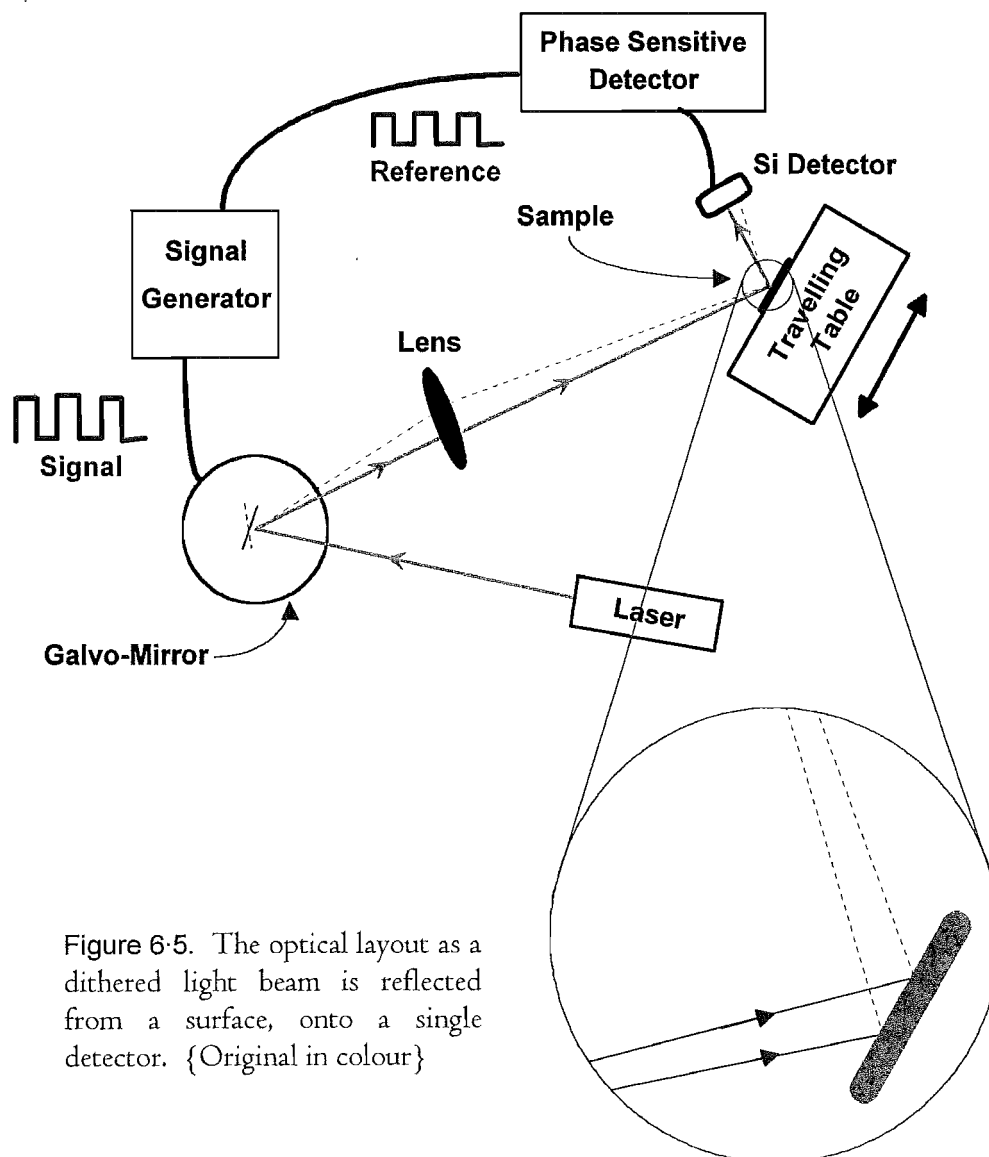


Figure 6-5. The optical layout as a dithered light beam is reflected from a surface, onto a single detector. {Original in colour}

6.2.2 Experimental Arrangement

Figure 6-5 shows the main components of the apparatus and the path taken by the laser beam. Three milliwatts of polarised 633 nm laser light are reflected from a mirror mounted on a galvanometer, through a cylindrical lens and onto the multilayer sample at an oscillation rate of 67 Hz. The galvo-mirror is driven by a square wave input signal whose amplitude determines the spot separation at the surface of the thin film layer, which is at the focal point of the lens. A 25 mm focal length, standard plano-convex lens produced focused spots which resulted in noisy signals due to the high sensitivity of the arrangement to tiny imperfections and particulate matter ^[291] in the deposited film. Channel waveguides are produced from relatively long, narrow areas of photomodified film, so a cylindrical lens is chosen to produce a thin stripe, allowing the reflections from the sample surface to be the average of a small linear surface area. On leaving the sample the intensity of the reflected dithered beam is measured by a single large area silicon photodiode. This signal is input to a phase sensitive detector using the galvanometer driving signal as a reference. As it can

be difficult to locate a photomodified region (by eye) the sample is mounted on a motorised travelling table with a transducer able to record positions to within $\pm 0.5 \mu\text{m}$ accuracy. The spot separation at the focal point is $f \cdot \Delta\theta_i$ (\gg laser divergence) where $\Delta\theta_i$ refers to the small change in the scan angle due to the dithering and f is the focal length of the lens. This is the separation between the spot centres and care should be taken to ensure that the spots do not overlap. The dithered beam should also be symmetrical about the centre of the lens to reduce errors caused by astigmatism and coma.

6.2.3 Calibration

Figure 6-6 shows, diagrammatically, the dithered beam as it travels across a photobleached, index reduced, area of a surface and the differential reflectance signal against the respective sample positions. The GLS sample used was prepared in our chamber by 9000 laser pulses (delivered at 10 Hz) at 3.5 J cm^{-2} with a target-to-substrate separation of 80 mm. Starting in region/position A, both parts of the dithered beam are reflected from outside the photomodified area (the region of increased/decreased refractive index) which on a uniform film produces no difference in reflectivity, hence an almost zero differential output. As the sample is translated, one spot (the first location of the dithered beam) begins to enter the modified region of the film which in turn changes its reflectivity. When one spot is fully inside the modified region the increased differential reflectivity is marked area B in the figure. As the second spot begins to enter the photomodified zone, the differential signal decreases, reaching zero again as both spots are of equal reflectance (C in the figure). The sequence reverses as the first spot leaves the modified region (position D) and finally enters region E, the same as A, as the sample translates further the equal reflectances from the surface produce zero signal. The difference in signal amplitude between A and E is due to the film being slightly non-uniform.

The spot separation and width of the photobleached area can be found directly from the differential reflectance signal, Figure 6-6. The reflectivity change between regions A and B is due to one of the dithered spots transferring between two areas of differing reflectance. Assuming, initially, that the spot separation is less than the stripe width, then at the half maximum point of the trace the spot is equally divided between the two areas, hence the Full Width Half Maximum (FWHM) distance is the separation between the dual beam centres and in the example shown is 0.47 mm. Region B and D represent the same half of the dithered beams two components entering and leaving the modified region respectively, hence it follows that the separation of the centre of these two regions defines the width of the photobleached stripe, 1.95 mm for this sample. However, if the spot separation is greater

than the stripe width then the relative measurements are interchanged. If neither value is known the two can be distinguished by adjusting the spot separation slightly and rerunning the same scan. The measurement which remains unchanged is that of the stripe width. On knowing the spot separation the apparatus can be used to map multiple, varying width, modulated regions across a single surface. Sharp edges of the photomodified areas and tightly focused laser beam spots allow mapping of thinner areas and produce more rapidly changing differential reflectivity results, but were unnecessary in our application.

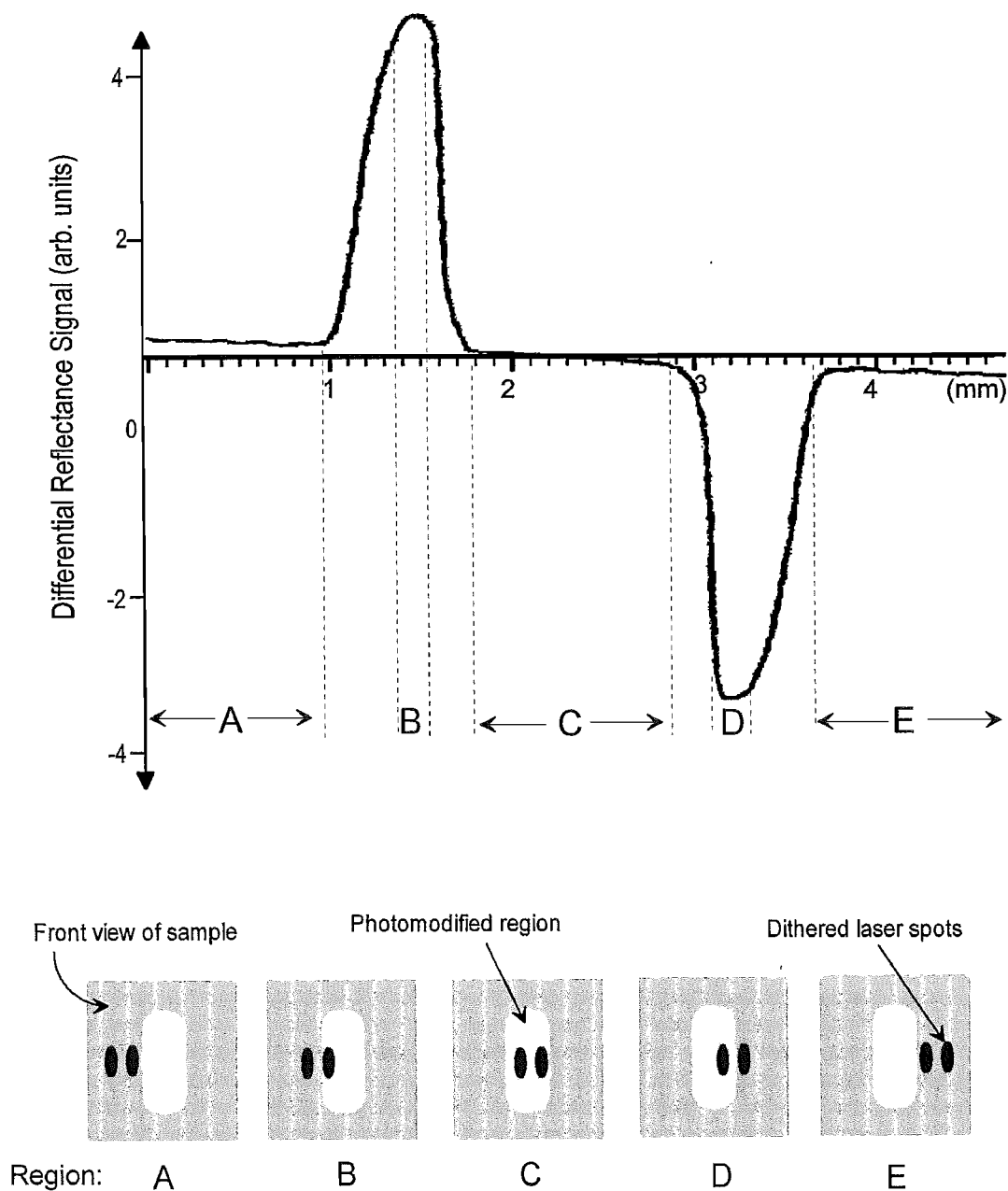


Figure 6-6. Differential reflectance signal as a photomodified sample of GLS travels through the path of a dithered, polarised laser beam for each respective region of translation. {Original in colour}.

In the experimental arrangement a cylindrical lens was used which created the thin laser lines shown schematically in Figure 6-6, rather than focused spots. The lines were 1.35 mm in height, this being the collimated beam diameter of the HeNe laser at 633 nm. The spot width can be deduced from Gaussian beam focusing theory ^[295] which gives the approximation:

$$\omega_o \times \omega(f) \approx \frac{f\lambda}{\pi} \dots\dots\dots (6.3)$$

where ω_o is the radius of the beam waist located at the focal length of the lens f (25 mm), λ is the laser wavelength and $\omega(f)$ is the radius of the laser beam at the lens. For the 633 nm reflectance measuring beam, the spot widths were $\approx 15 \mu\text{m}$.

A direct and simple measurement of the sign of Δn_2 is in contrast to the difficulty of measuring the sign of the induced change by grating techniques. It can be determined in several ways, for example a matt black line has a lower reflectance (simulating a lower refractive index). If this is scanned the differential reflectance signal will have the same sign as the experimental data if the index of the photomodified region is lower than the surrounding film and vice versa. Alternatively the sample can be translated until the first dithered spot is no longer reflected from the surface (i.e. missing the sample altogether). The signal then directly relates to the same spot arriving at the photomodified area, hence if this is in the same direction as before then the refractive index due to modification has decreased. This is true for the GLS thin film example shown: Δn_2 is negative.

Finally, it is necessary to calibrate the signal intensity in order that we find the magnitude of Δn_2 . Based on equations 5.6 and 5.8, Table 6.1 shows the polarisation angles required to force $\frac{\partial R}{\partial \theta_2}$ to zero for CaF_2 ^[272] and ZnSe ^[274] at room temperature and the relative refractive indices at three temperatures including air ^[296]. Calibration is achieved by mounting two halves of a single substrate on to two Peltier effect heat pumps, connected to operate with opposite current flow. This causes one half to be heated to up to 70 °C and the other to be cooled to a minimum of 1 °C changing the refractive index of the materials. It is assumed that the air at the sample surface is at the same temperature as the sample itself, a good approximation for both indices at the boundary layer. Since the refractive index of air is not exactly 1 and is temperature dependent, its value differs at the two positions of the dithered beam during a $\frac{\partial R}{\partial n_2}$ experimental investigation. An error of 1° in the polarisation angle (in this case at 15° incidence) would result in an error of 0.049% for Δn_2 in CaF_2 , based on the values calculated in Table 6.1.

Using ZnSe , with its increasing refractive index with temperature, as the calibration sample, CaF_2 (having a negative temperature differential) can then be used to test the apparatus.

For CaF_2 (from Table 6.1), Δn_2 has a theoretical value of -7.47×10^{-4} for a temperature increase of 69°C . Table 6.2 shows the differential reflectance results for the arrangement shown in Figure 6.5. Starting with the ZnSe results, a difference of $128.6 \mu\text{V}$ for a 3.39×10^{-4} reflectivity difference produces a reflectivity gradient of 2.64 V^{-1} . Combine this with the experimental differential reflectance signal for CaF_2 to find the actual reflectivity difference of the material as: $-13.9 \times 10^{-6} \times 2.64$, giving -3.7×10^{-5} . Using this figure and utilising the Fresnel equations it is possible to convert this to an experimental Δn_2 of -7.02×10^{-4} for CaF_2 . Given the very small changes involved, the difference from the calculated value (4.8×10^{-5}) is considered satisfactory.

Material	Refractive Index at 3 Temperatures	Initial polarisation angle required at 20°C (degrees)	Calculated Total Reflected Signal in air (%)
Calcium Fluoride (CaF_2)	$1^\circ\text{C} = 1.43251$	46.3	1.57461
	$20^\circ\text{C} = 1.43230$		1.57355
	$70^\circ\text{C} = 1.43176$		1.57064
Zinc Selenide (ZnSe)	$1^\circ\text{C} = 2.5921$	45.4	9.79647
	$20^\circ\text{C} = 2.5934$		9.80572
	$70^\circ\text{C} = 2.5969$		9.83041
Air (at 1 atmosphere)	$1^\circ\text{C} = 1.0002907$	N/A	N/A
	$20^\circ\text{C} = 1.0002718$		
	$70^\circ\text{C} = 1.0002321$		

Table 6.1. The characteristics of the materials used for calibration.

Interface	Calc. Δn_2	Calc. ΔR	Signal (μV)	Measured Δn_2
ZnSe, 20°C	0	0	1.4 - offset	-
ZnSe, 69°C diff.	4.8×10^{-3}	$+3.39 \times 10^{-4}$	128.6	Calibration
CaF_2 , 20°C	0	0	1.7 - offset	-
CaF_2 , 69°C diff.	-7.5×10^{-4}	-3.97×10^{-5}	-13.9	-7.02×10^{-4}

Table 6.2. PSD output signals for the calibration and test sample interfaces.

The electronics of the experimental arrangement produces the fundamental limitation of the technique. This would be mainly evident in the silicon detector where the dominant noise in such a p-n junction is shot noise¹. Equation 6.4 shows the noise current as a function of the bandwidth, B , and the current flow through the device, I ; e is the charge on an electron.

¹ Semiconductor devices display a type of noise which is temperature independent and is due to the fact that the current carrying mechanism involves randomly distributed doping impurities creating either excess electrons or positive charge carrying holes. The random way in which the carriers are swept across the p-n junction and then recombine, creates a variance in the operation of the junctions which is called Shot noise.

$$i_n = \sqrt{2eBI_t} \dots\dots\dots (6.4)$$

I_t is calculated from the product of the diodes responsivity and the laser power incident upon it. It is found from the square root of the sum of squares of the signal current and the constant 'dark' or leakage current present. With a diode responsivity of 390 mA W⁻¹ at 633 nm a dark current of 0.9 µA (negligible in this application), an incident laser power of 4.7x10⁻⁴ W using a bandwidth of 1 Hz, results in a signal noise of 7.7x10⁻¹² A. For this detector the signal-to-noise ratio is 2.4x10⁷. Hence when the reflectivity signal is 1 V the noise signal is 4.2x10⁻⁸ V, which in the case of the CaF₂ example would correspond to a minimum measurable Δn_2 of 8.5x10⁻⁵. The observed noise signal was ± 4.0 µV which relates to a Δn_2 change of 9x10⁻⁵, in excellent agreement. In this case the overall signal to noise ratio, S:N, is proportional to the square root of the incident laser power.

Different experimental arrangements and wavelengths would employ different types of detector. For example for a pyroelectric device, whose noise level is not dependent on the incident signal, the S:N is directly proportional to laser power. Johnson noise is dominant in photo conductive detectors and because this is a thermal effect it remains constant for a specific detector unless the laser power incident on the detector is large enough to cause heating.

The arrangement does not measure the refractive index of a material but the difference in two adjacent areas on a surface. This technique has successfully been used to resolve small negative changes in the refractive index of thin GLS films to one part in 10⁶ whilst only knowing the actual refractive index of one area to three significant figures.

This experimental arrangement can also monitor the photomodification process *in-situ*, which is not generally possible with other techniques. For these measurements the sample remains stationary and the signal is recorded as a function of time. The dithered beam is initially on a fresh sample, hence the signal is zero. If an argon ion laser beam covers only one of the two dithering spots (a few tens of milliwatts is used to photobleach GLS films), the area at this intersection will be photomodified. As the process progresses, the refractive index of the film changes and is monitored by the differential reflectivity measurement. Figure 6.7 shows a plot of this type. Initially the signal is zero (O→A) and at A photomodification begins producing an instantaneous increase in the refractive index of the thin film material (A→B) which then over the ¾ hour period completely photomodifies the sample to saturation (B→C). This initial rise is considered in more detail in Section 6.4. When the Ar⁺ laser is turned off, the refractive index decreases further (C→D). At any stage in the modification the light can be interrupted and the signal will show the same magnitude

of change ($A \rightarrow B$ or $C \rightarrow D$), returning to almost the same point if allowed to continue. Colour filters and non-photomodifiable samples were used to ensure that this step in the signal change is not merely Ar^+ light falling onto the detector. Thin film samples with a few tens of degrees centigrade differential across them have also been studied to assess the magnitude of temperature change on the reflectivity, which in itself shows diverse applications of the experimental technique. This showed that neither is responsible for the rapid, reversal of index change which is believed to be an effect in GLS itself. However this example does show how a film of known thickness can be photomodified to reduce the refractive index by an exact amount, *in-situ* which makes the arrangement unique. The experimental arrangement and principles of operation were published elsewhere^[297].

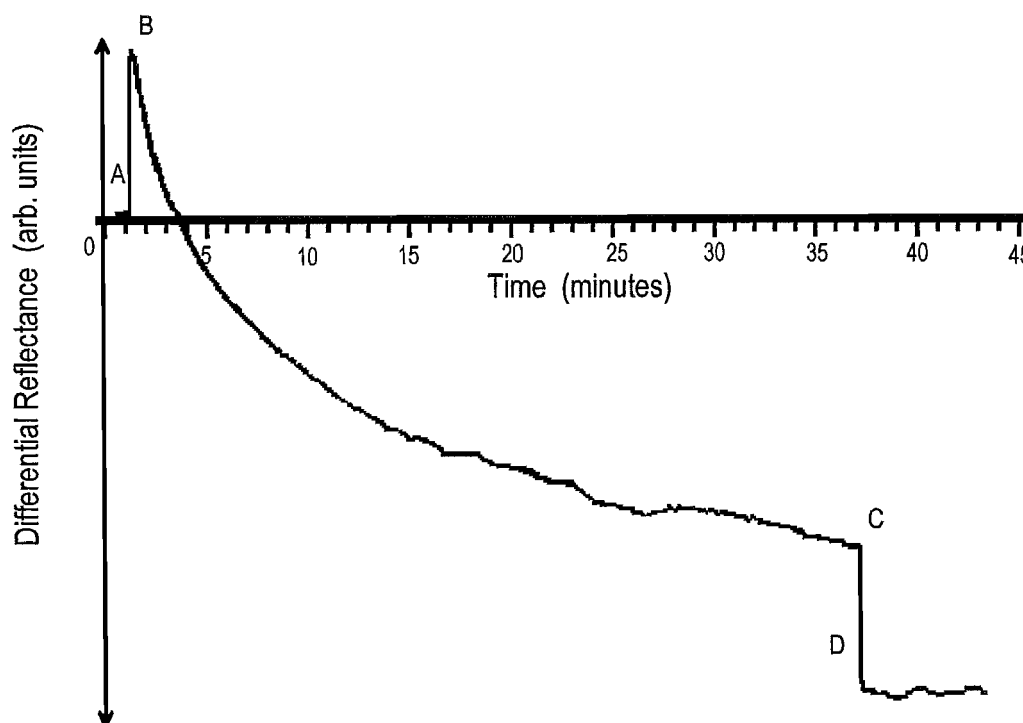


Figure 6.7. Differential reflectance signal from a GLS thin film being photomodified *in-situ*. One of the dithered spots is positioned in the area being modified whilst the other is in an adjacent area. As the refractive index changes the plot shows both the magnitude and direction of this change.

6.2.4 Summary

We have developed, and demonstrated, a highly accurate way of measuring very small changes in the refractive index of a material. The apparatus has the advantage over other techniques of being able to make *in-situ* measurements of, and map, index changes across an entire surface to an accuracy of 8.5×10^{-5} in the arrangement presented here. This would of course vary for different laser powers and detectors etc. The detailed, dimensional, mapping of changes in refractive index is limited only by the focused spot diameter and the

need for a separation between them when dithered, the surface quality and the noise associated with the combined detector and PSD electrical noise and can readily be implemented at any laser wavelength.

One of the important properties of Gallium Lanthanum Sulphide (GLS) that is utilised, is its ability to photomodify. The apparatus was designed to determine the refractive index change, found to be $\sim 1\%$ for these thin films, to an accuracy of $3 \times 10^{-4} \%$. The technique presented provides an accurate value for the difference between two adjacent surface areas, with both the magnitude and sign of Δn being determined.

Once calibrated, it has been shown that a dithered laser beam at almost any desired wavelength, can be employed to measure the dimensions and magnitude of index changes for regions on film surface which have been modified in some way. The simple experimental arrangement allows for rapid changes in optics and detector to suit the wavelength chosen. The apparatus is best suited to bulk samples or thin film layers with a thickness below $\sim 20 \mu\text{m}$.

When using a polarised incident beam, errors due to the slight angle difference in the dither process itself are shown to be minimised with an optimum choice of polarisation angle for small spot separations. The ability to record reflectance changes *in-situ* is also unique. Samples can be heated, illuminated or processed in other ways, with a constant record made of the refractive index changes which occur. The remainder of this chapter will utilise this experimental arrangement to its fullest potential, showing that this simple technique is extremely versatile. The technique could for example be applied in vacuum during ion implantation, or in a furnace during diffusion.

6.3 Photomodification of Thin Films

6.3.1 Measurements of Refractive Index Changes

With the fully calibrated arrangement it was possible to measure the magnitude of the refractive index change, due to photomodification. Using the set of films previously detailed in Section 5.3 (Table 5.1 and Table 5.3), it is necessary to locate a common point in the reflection verses wavelength plot for each material to keep the sensitivity of the Δn measurement at a maximum for all samples. The maximum reflectivity change due to a change in refractive index occurs at the maximum or minimum of the $\frac{dR}{dn}$ plot. For ease of data processing the maximum reflectivity is calculated for each thin film sample based on the refractive index and thickness data which is obtained using the fitting technique

Energy Density (J cm ⁻²)	Thickness after 9,000	Refractive Index at 633 nm	Maximum Reflectivity Achievable with this Thin Film		N° of pulses to produce required thickness	Measured		Deviation from Mean (%)	Δn (%)
			is (%)	at (nm)		Reflectivity (%)	Thickness (nm)		
2.0	no film	N/A	-	-	-	-	-	-	-
2.5	122.41	3.31	58.18	239	17,572	59.11	225	3.58	0.63
3.0	347.43	3.17	55.44	250	6,476	54.37	261	3.54	1.45
3.5	626.27	2.91	49.74	598	8,594	49.71	607	4.18	1.60
4.0	734.36	3.02	52.17	788	9,657	50.62	773	4.98	1.61
4.5	868.07	3.05	52.91	778	8,066	49.75	788	5.13	1.63
5.0	940.46	2.83	47.81	727	6,957	48.63	742	5.92	1.65
5.5	970.84	2.72	45.02	756	7,008	42.42	769	7.19	1.69
6.0	992.56	2.54	40.10	686	6,220	39.64	677	12.23	1.74

Table 6-3. GLS thin films grown at increasing energy density, increase in physical thickness with a complementary decrease in refractive index.

B'ground Gas	Pressure (mbar)	Thickness after 9,000	Refractive Index at 633 nm	Maximum Reflectivity Achievable with this Thin Film		N° of pulses to produce required thickness	Measured		Deviation from Mean (%)	Δn (%)
				is (%)	at (nm)		Reflectivity (%)	Thickness (nm)		
Vacuum	5×10^{-7}	374.34	3.11	54.20	356	8,559	55.25	345	3.55	1.41
Oxygen	1×10^{-5}	271.18	2.75	45.77	289	9,591	46.79	325	3.59	0.28
	1×10^{-4}	244.04	2.47	38.08	320	11,801	42.62	311	3.62	0.23
	5×10^{-4}	192.92	2.33	33.83	339	15,815	34.89	335	4.59	0.21
	1×10^{-3}	248.35	2.25	31.31	351	12,720	23.06	297	5.26	0.21
	1×10^{-2}	167.24	2.01	23.39	236	12,700	25.38	291	5.18	0.21
	5×10^{-2}	314.86	2.19	29.37	361	10,319	20.99	333	6.39	0.21
	1×10^{-1}	123.89	1.66	11.99	287	20,849	13.52	277	7.72	0.20
Argon	1×10^{-5}	221.97	3.19	55.85	347	14,069	53.77	358	3.87	0.80
	1×10^{-4}	179.04	2.65	43.16	299	15,030	45.50	293	3.80	0.77
	5×10^{-4}	159.82	3.12	54.41	355	19,991	42.35	302	4.25	0.76
	1×10^{-3}	159.72	2.96	50.90	267	15,045	43.43	297	5.23	0.75
	1×10^{-2}	101.16	2.68	43.97	295	26,246	40.68	335	5.98	0.75
	5×10^{-2}	100.81	2.91	49.74	272	24,283	34.77	335	6.07	0.74
	1×10^{-1}	98.42	2.14	27.73	222	20,300	29.68	217	6.78	0.44

Table 6.4. GLS thin films grown, some in vacuum and for comparison, some in different background pressures of both oxygen and argon gases. The results show changes in physical thickness and refractive index (samples grown at an energy density of 3.5 J cm^{-2}).

discussed in Section 5.3.1. The data from Tables 5.1 and 5.3 are reproduced in Table 6.3 and 6.4 respectively with additional columns, giving the calculated values for the maximum reflectivity achievable with the film and the required thickness needed to centre this maximum at 633 nm. Continuing this assessment, the number of pulses required from a laser ablation run, under the same original growth conditions which are required to achieve this. Each of the films were then produced and repeat measurements were made. The next 3 columns present the actual reflectivity and thickness of the film produced and its deviation from the theoretical target value.

Using a set of films previously detailed, the effects of background gases and Excimer laser energy density are derived. A multi-line Argon ion laser is tuned to each of its single lines and the ability of the same sample to photomodify with respect to wavelength are reported. Finally the effect of one single line from the argon laser at differing output powers and the speed of photomodification are presented.

These thin film structures can now be compared in photomodification experiments in order to assess how growth conditions during laser ablation, already known to change the structure and elemental bonding, affect the ability to photomodify. The final column in Tables 6.3 and 6.4 shows the decrease in refractive index which is produced using a multi-line argon ion laser with an output Gaussian beam of 0.8 mm diameter and a power of 300 mW (596.8 kW m⁻²) for a duration of thirty minutes. These data were obtained using the differential reflectance technique detailed in the previous section. It can now be seen that for films grown in a background gas of Argon the percentage decrease in refractive index of the material remains constant. Argon atoms are not easily incorporated during growth but merely act to slow the plume and change the refractive index.

For the films grown at differing energy density, there is a change in photomodification achievable. As the energy density increases, the quality of the material decreases and so does the ability to photomodify. These results show that as the GLS films lose stoichiometry they also reduce their ability to photobleach. These results are similar to those of the thin films which are grown in a background gas of oxygen. As the gas pressure increases the material becomes thinner and includes a higher percentage of oxygen atoms. Its ability to photomodify actually disappears under the experimental arrangements used here.

Using a film grown in vacuum (Va:1) photomodification effects were measured using five, single argon lines all at 46 mW (91.5 kW m⁻²). This power was chosen in the interests of consistency as it was the maximum achievable on the lowest power line. Figure 6.8 is a plot of the refractive index change, Δn , which is achieved using each wavelength from the argon ion laser. In summary the shorter the wavelength the greater the refractive index change which occurs. However, as Table 6.5 shows, if exposure time is sufficiently long for

saturation to be reached the value of Δn is not as large if saturation is eventually reached. Higher photon energy leads to greater absorption by the thin film layer and hence greater refractive index change in the same time period. The higher energy photons break bonds in the GLS structure more easily and so photomodify quicker.

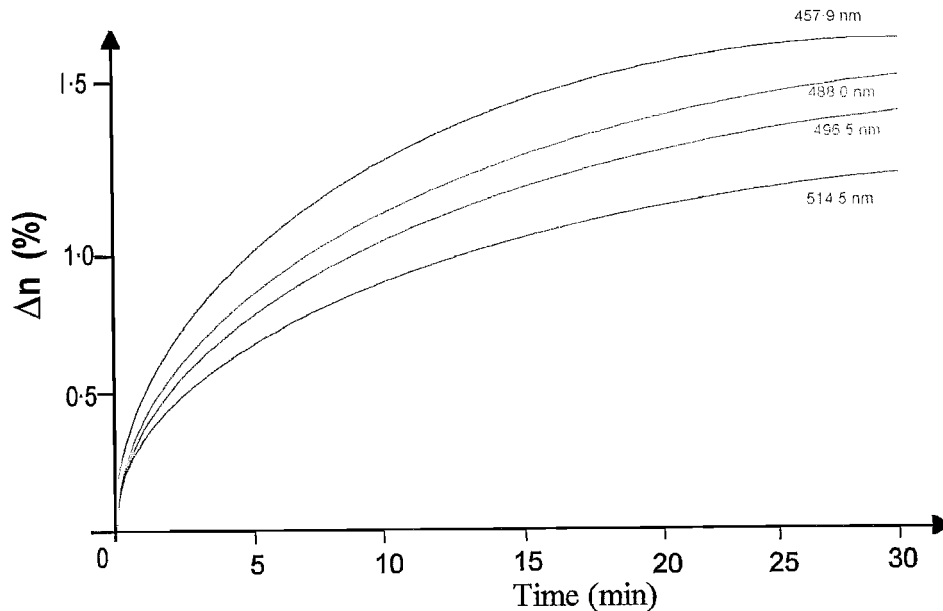


Figure 6-8. GLS photomodified with the various single lines of an Argon ion laser. Over a 30 minute period the same power of each line achieves a different magnitude of refractive index change. {Original in colour}

Wavelength	Δn reached (%)	Time taken (min)
514.5	1.40	56
496.5	1.44	49
488.0	1.47	40
476.5	1.49	30
457.9	1.49	15

Table 6-5. Decrease in refractive index and time taken to reach this saturation for a GLS thin film photomodified at various argon ion laser wavelengths (all at 46 mW).

Using a single wavelength from the argon ion laser at different powers and exposure times allows the same number of photons to be incident on the thin film layer. It was found that the time necessary for Δn saturation decreases with incident power. This means that

independent of power, the same quantity of photons creates the same change in refractive index. Figure 6-9 shows these results. It can be seen that the refractive index change results from photons changing the atomic structure of the chalcogenide glass and the higher this energy, the faster the process occurs.

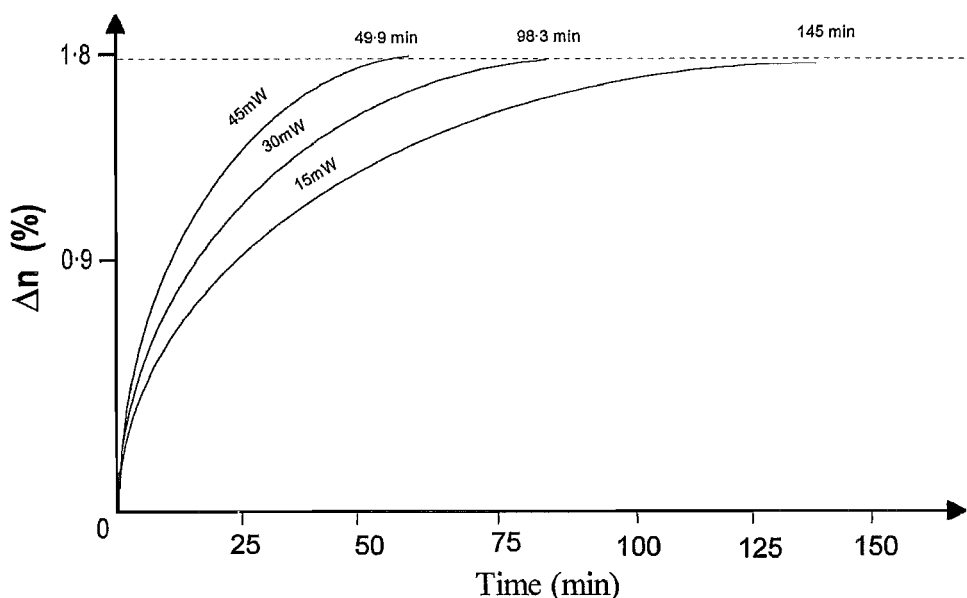


Figure 6-9. GLS photomodified with the 458 nm line of an Argon ion laser at differing output power and constant beam diameter, until saturation is reached. {Original in colour}

6.3.2 Ageing of Chalcogenide Thin Films

Due to the nature of laser ablation deposition, films are not thermally stable after ablation growth and relaxational structural changes start to take place ^[298]. Relaxational structural changes are inherent in all non-crystalline materials due to their thermodynamic instability. After deposition in vacuum a GLS thin film has stored some excess free energy because of the structural disorder and non-homogeneity. This excess energy decreases with time owing to relaxational structural changes. The driving forces behind this are the internal mechanical stresses arising during the film deposition and which diminish in the course of the relaxation ^[298]. This is facilitated by the non-rigidity of the film lattice. Only the short range order changes with time at room temperature. The main effect in sulphur based chalcogenide thin films is likely to be played by sulphur atoms themselves. Relaxational changes result in a decrease of absorption and an increase of refractive index ^[299]. The saturation values of the refractive index changes are smaller than in the case of photostructural changes ^[300].

Here the findings on the difference in photomodification between aged and fresh non-annealed GLS films shows that the age of the films should always be taken into

account. Five non-annealed thin films laser ablated onto optical glass substrates were studied over a two year period.

To show how the relaxational structural changes affect the as-ablated and photomodified thin film samples due to ageing, four of the films were used in a simple experiment to see how temperature and ambient light could relax both the unmodified GLS and a photomodified region, if left for an extended period of two years. Each film was attached to a copper block, one of the blocks was heated to 70 °C and the other cooled to 1 °C. One of the cooled films was covered in black cloth to reduce the light which reaches its surface and the other was illuminated with two white light emitting diodes (LED). The same illumination arrangement was also applied to the heated pair. Table 6.6 shows the measured refractive index, thickness and percentage of photomodification for the four films described above (the fifth film will be discussed later in this section). After the two year period, the refractive index and photomodified difference were again evaluated and recorded in the table. It can be seen that both heat and light assist in the relaxation process of the film, reducing the magnitude of the refractive index change. It should be noted that all samples were returned to room temperature before any measurements of reflectivity were made.

The fifth film sample was left in the laboratory and was then subjected to the light from the fluorescent tubes during the day and darkness over night. The room temperature was monitored to be within the range of 5 to 30 °C over the full period. This film was monitored for the full duration of the experiment with one data point taken each month to within a day. Figure 6.10 shows a plot of the refractive index difference with time as this sample relaxes over the period. Finally at the very end of the experiment, the fifth film was photomodified for a second time in a slightly different region (but close enough for the difference in film thickness to be negligible) to show that the structurally relaxed film is not as efficient as when it was first manufactured. The white LED's were intended to mimic the fluorescent room lights and they are an ideal source of light which has no infrared component and produce essentially no sample or environmental heating.

The results show that both light and heat affect the refractive index of the thin film layer. The experiment would have to be run for a time-scale beyond the scope of this work to conclusively show if the dark, cold sample would reach the same refractive index change as the illuminated, hot sample. However the results seem to show that light induced changes leave the GLS in a state from which thermally the structure can change further.

For samples to be of use in practical applications, the ageing process needs to be accelerated. It may not be possible to completely stop this process as it has already been shown that eventually the same number of incident photons will create the same saturated effect. One way to slow down the 'ageing' of the samples could be to control the

temperature of their environment (mainly substrate) and apply a capping layer to the thin film which would be capable of preventing light from reaching the underlying layer. In conclusion, due to the long relaxation time of the structural changes, the degree of photostructural change depends on the age of the as-ablated films.

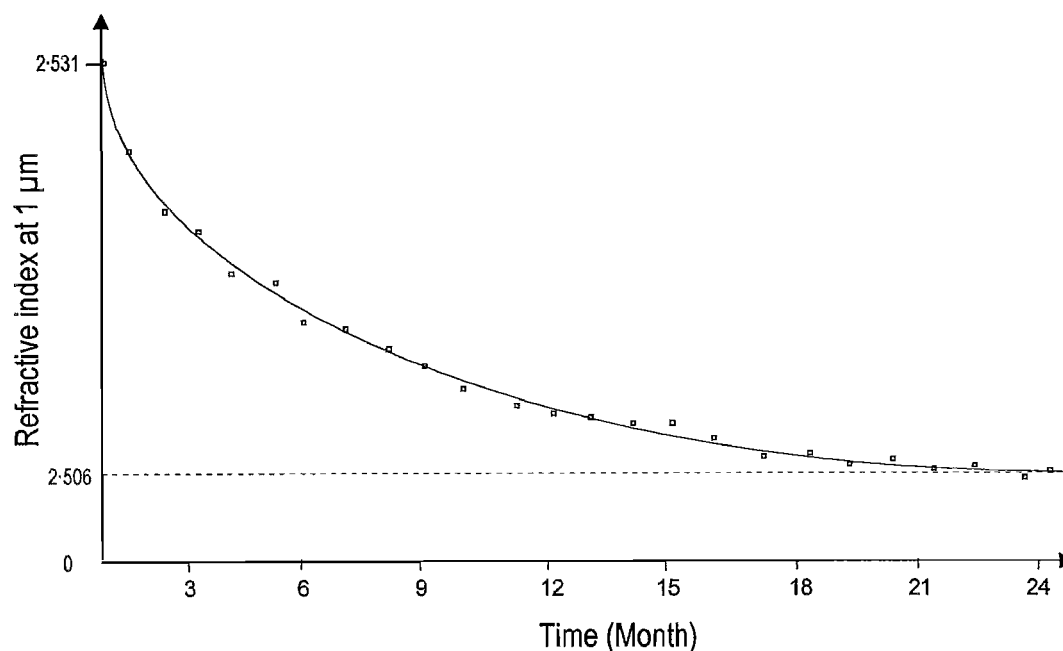


Figure 6-10. GLS refractive index as the structure self-relaxes over a two year period. The refractive index is measured on a monthly basis using the fitting technique detailed in Section 5.3.1, refractive index is quoted at one micron. {Original in colour}

Film Number	Control conditions	START			FINISH		
		Refractive index (at 633 nm)	Thickness (nm)	Δn (%)	Refractive index (at 633 nm)	Thickness (nm)	Δn (%)
1	● ●	3.121	372.21	1.61	3.109	372.12	1.51
2	● ○	3.063	369.87	1.63	3.042	369.89	1.14
3	● ●	3.104	370.01	1.59	3.082	369.92	1.16
4	● ○	3.081	369.93	1.61	3.052	370.03	0.97
5	N/A	3.087	371.75	1.62	3.064	371.65	1.22
Re-modified Data					3.066	372.57	1.40

Table 6-6. GLS thin films, refractive index (Δn) and thickness changes due to heating and room light over a two year period. ● cold, ● hot, ● dark and ○ light. {Original in colour}.

6.3.3 Monitoring the Photothermal Parameter, *in-situ*

Using the heater-cooler block which was initially designed for use in the calibration of the differential reflectance measurement arrangement, the optothermal parameter dn/dT was obtained for a GLS thin film grown in vacuum at $\sim 10^{-7}$ Torr.

The refractive index was originally measured at 1 °C, using the standard fitting technique based on the transmission spectra from the Perkin Elmer FTIR Spectrophotometer. This provides a value by which the differential reflectance technique can monitor the change in refractive index with respect to temperature. One half was held at 1 °C and the other heated to 70 °C. The measured sample resulted in a temperature coefficient of refractive index, dn/dT equal to $3.2 \times 10^{-5} \text{ K}^{-1}$ for a virgin film. For the second result the heated sample was first photomodified at room temperature, before being re-heated and its refractive index relative to the reference sample recorded. Finally if both halves of the sample are held at 1 °C, the refractive index difference with respect to temperature could be found. For the photomodified thin film the value reduced to $dn/dT = 2.4 \times 10^{-5} \text{ K}^{-1}$ showing that photoinduced changes strongly influence the optothermal coefficient. Similar values are found in the literature i.e. $2.1 \times 10^{-5} \text{ K}^{-1}$ and $1.8 \times 10^{-5} \text{ K}^{-1}$ respectively for As_2S_3 chalcogenide glass^[301].

6.3.4 Other Chalcogenide Thin Films

GLS is not unique in its ability to photomodify. Earlier chapters (mainly Section 2.4) have discussed extensively the various phenomena which have so far been found. One other chalcogenide glass; Gallium-sodium-sulphide (GNS) was briefly investigated during the course of this work.

In a similar way to the GLS samples, GNS was investigated using the same five single lines from an argon ion laser at increasing laser power and the results are presented in Figure 6.11. With 46 mW (91.5 kW m^{-2}) on each line, GNS will photomodify considerably in thirty seconds and the exposed film appears transparent to visible radiation when viewed by eye. Sodium sulphide safety data states that the starting material should be contained in a darkened environment due to reaction with visible light. Indeed the starting powders change from white to lilac if exposed to daylight for a few tens of minutes. This might explain why it is so efficient when exposed to laser light in the argon ion laser emission region. As with GLS, this material shows no signs of volumetric changes due to photomodification. However GNS is not stable in air and within a few months it was possible to see the thin film layer beginning to flake away from the substrate in various isolated patches at first, growing

larger over time. Time-scales did not allow as much investigation work with this material as would have been necessary to complete a more detailed comparative picture.

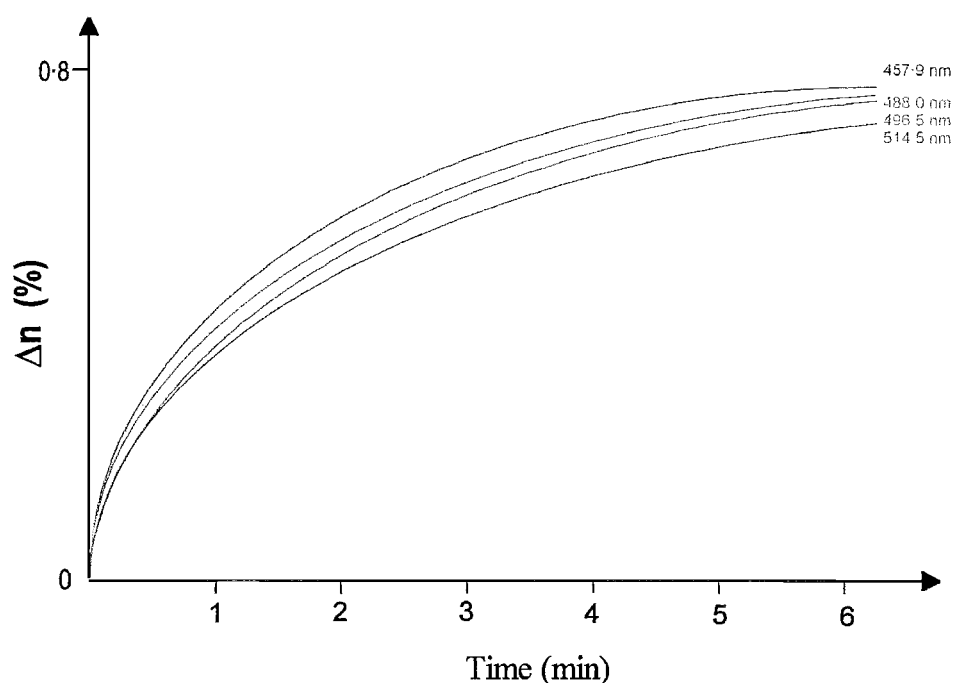


Figure 6-11. GNS photomodified with the various single lines of an Argon ion laser. Over a 6 minute period the same power of each line achieves a different magnitude of refractive index change. {Original in colour}

6.4 Fast Photomodification Effect

Figure 6-7 showed a typical in-situ monitoring of photomodification. Clearly visible, and not yet discussed, is the initial rise in refractive index of the material before the longer decreasing curve which follows indicating, a refractive index reduction. To investigate this further, the initial rapid change needs to be analysed on a much faster time scale. The rise time of the reflectance signal varies between a few hundred microseconds for very thin films to around ten seconds for thin films up to three microns in thickness. Figure 6-12 shows an example of a thin film, with thickness 3 μm showing the fast initial response of the surface reflectivity (blue line) due to the illumination by 300 mW (29.8 kW m^{-2}) of singlemode, multi-line radiation from the argon ion laser. The reflectance line does not appear to fall below zero even after 100 s in this figure, but it should be noted that Figure 6-7 shows that this point is not reached for around 4 minutes and so is not expected on the shorter time-scale. The second line (red) shows the intensity of the argon laser radiation which passes unabsorbed by the thin film layer through the substrate and onto a second detector during the photomodification process. The transmission initially dips before turning upwards, continuing through its original value as the photobleaching sets in and progresses even more positive. These observations are in keeping with the original in-situ photomodification

profile, where the reflectivity from the surface increases showing an increase in the refractive index which is attributed to photodarkening. As the photomodification turns into a bleaching effect (index decrease) the absorption of the thin film decreases. This interesting concept will be discussed in the next section which refers to bulk samples. These are photomodified and a similar effect of bi-directional photomodification is seen to occur with the naked eye.

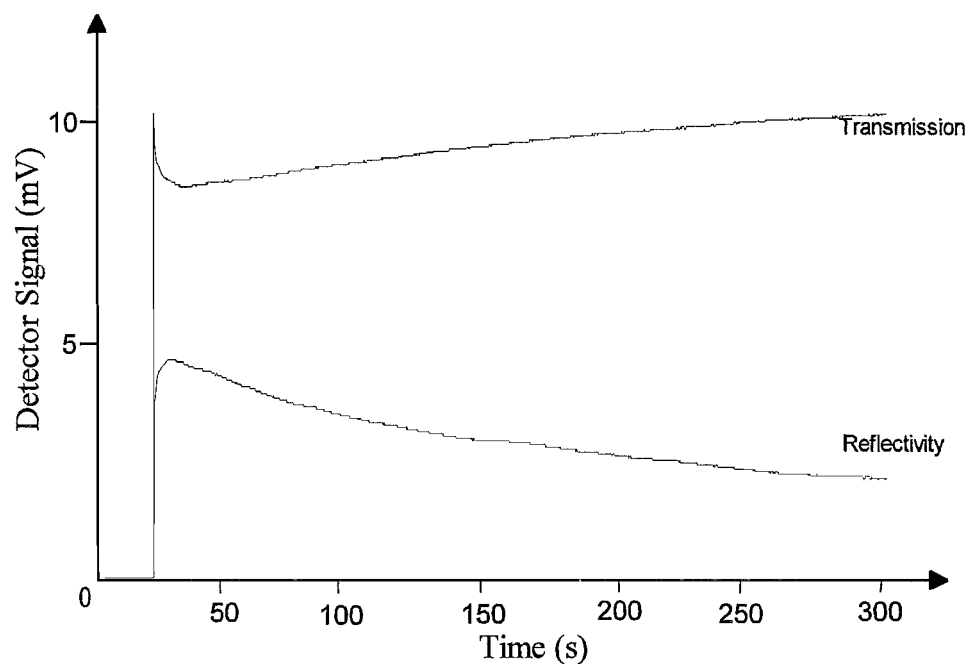


Figure 6.12. Comparison of the reflectivity change during in-situ photomodification and the intensity of the argon beam which passes through the GLS sample as it induces the structural change. Transmission can be seen to fall and rise again as the process progresses. {Original in colour}

The lack of this initial rise in the profile when the thin film layer is grown on high thermal conductivity substrates, such as copper, suggests that this is a thermal effect. To investigate this idea further, the end of a thermocouple was coated with a 3 μm layer of GLS. The tip was illuminated by the argon laser and the temperature change monitored. Over exactly the same time scale as the reflectivity profile changes, the thermocouple tip heated to 310 $^{\circ}\text{C}$ where it remains until the argon laser beam is removed. As a check, an uncoated thermocouple was held in the beam path and no temperature change was recorded. From this it can be deduced that the thin films are strongly heated due to absorption of above band gap radiation by the GLS thin film layer. The temperature of the coated thermocouple is dependent on both power and wavelength which are incident upon it. Any changes in thin film reflectivity which are observed due to heating are erased when the radiation is removed. This means that photothermal changes are erasable and the photo-optical changes are permanent. The heating process incurred on the substrate would be different as the thermal constants and geometry would not be the same as the thermocouple tip. Equation 6.5

represents the best fit to the thermal component of the thin film reflectivity^[302]. I represents the reflectivity intensity, t is the time taken to reach that value and t_s is the saturation time at which point the profile ceases to increase and k is a constant. The best fit to the data in this case shows saturation to occur at 1.67 s for this particular thin film. The same equation can be used to fit to the initial rise of the optical data from the reflectance signal, showing that they have equivalent forms.

$$I = k \left(1 - \frac{1}{1 + \frac{t}{t_s}} \right) \dots\dots\dots (6.5)$$

Figure 6-13 shows the peak increase in refractive index achievable from the multi-line argon emission at various optical powers. This profile can be seen to tend towards saturation and can also be fit to Equation 6-5, in this case the optical power would be substituted for t and t_s has a value, when fitted, of 274.4 mW (545.9 kW m⁻²) which indicates the power at which saturation of heating induced change occurs.

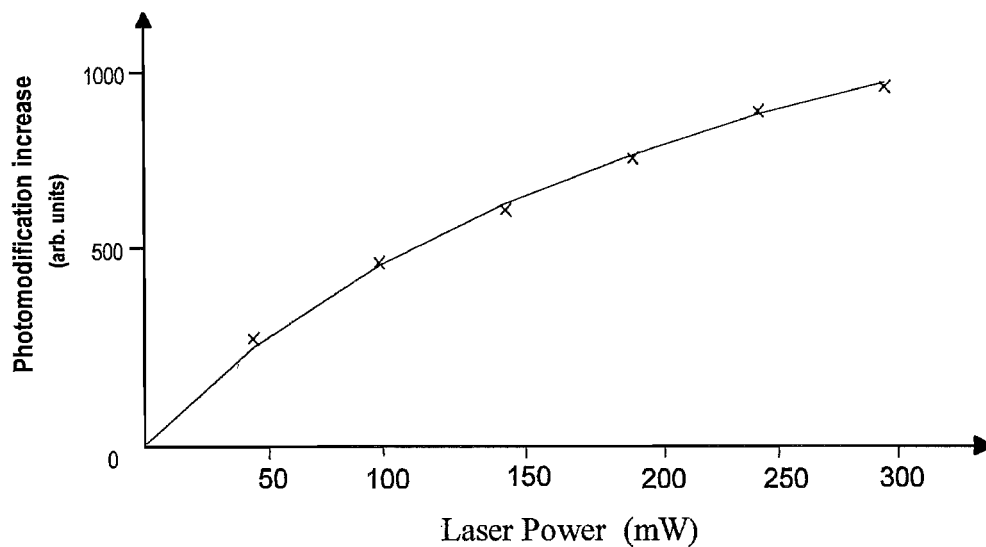


Figure 6-13. Comparison of the initial increase in GLS refractive index during in-situ photomodification and the required laser power. Also shown is the best fit line to these data points. {Original in colour}

In summary, there are two effects which occur when thin films of many chalcogenide materials are subjected to laser light whose wavelength lies above the optical band gap of the material. The first and initially most obvious is a heating effect which rapidly increases the refractive index of the material. For most materials the temperature coefficient of refractive index is negative at visible wavelengths and temperatures ranges of a few hundred degrees centigrade. As a material is heated it becomes less dense reducing the

refractive index. In some materials this can be offset by a much larger positive index change due to shift in the materials optical bandgap, for example ZnSe also has this positive coefficient. It is erasable and disappears when the light is removed. The second effect is typical photomodification in which the refractive index is permanently decreased (in the case of GLS).

6.5 Bulk Photomodification

6.5.1 Change in Refractive Index

Whilst the project was primarily to look at photomodification properties of thin films, no assessment would be complete without looking at how bulk samples respond to the photomodification process. Using the standard in-situ differential reflectance technique it has been found that the refractive index increases by up to 0.8%, usually with a 'red' shift in the absorption edge, known as photodarkening. This is contradictory to the photobleaching seen in the thin film samples.

A large bulk sample of GLS (20 mm² with a 5 mm thickness) was polished to an optical quality on all edges and used in this small scale investigation. As in the thin films of this material a photomodified region is visible by eye if viewed through a sample with a white light source behind. When modification is induced by a multi-line argon ion laser at 300 mW (596.8 kW m⁻²) an obvious dark brown spot appears on the surface after only a few minutes. Another key difference to the thin films is that this spot begins to fade. In under 10 minutes this photodarkened spot begins to disappear. Closer inspection of the photodarkened spot shows that before the region has a chance to fade, a pale ring appears to surround the darkened region. This is in keeping with the transmission intensity measurement which was observed in the previous section whilst considering the fast initial response.

To investigate this further, a slight modification was made to the differential reflectance technique to improve its ability to look at this effect. A digital gain amplifier² is combined with a pulse generator and a binary counter. The amplifier begins with a unity gain and the pulses from the square wave signal generator oscillate the galvo-mirror and act as a reference signal to the PSD. After 128 pulses are counted, the digital amplifier increases its gain slightly, which combined with the pulses results in a slightly increased amplitude and hence a shifted rest position for the galvo-mirror at one extreme. One rest position for the galvo-mirror is defined by zero volts in the drive signal and the other extreme of mirror swing is defined by the amplitude of the driving pulses. After a pre-set period the rest location of

² A digital gain amplifier is an operational amplifier configured as a closed loop gain device whose feedback resistor is a discrete semiconductor which has an equivalent resistance proportional to the number of square wave pulses which it receives. This allows the gain of the overall amplifier to be increased or decreased using clock pulses and counters.

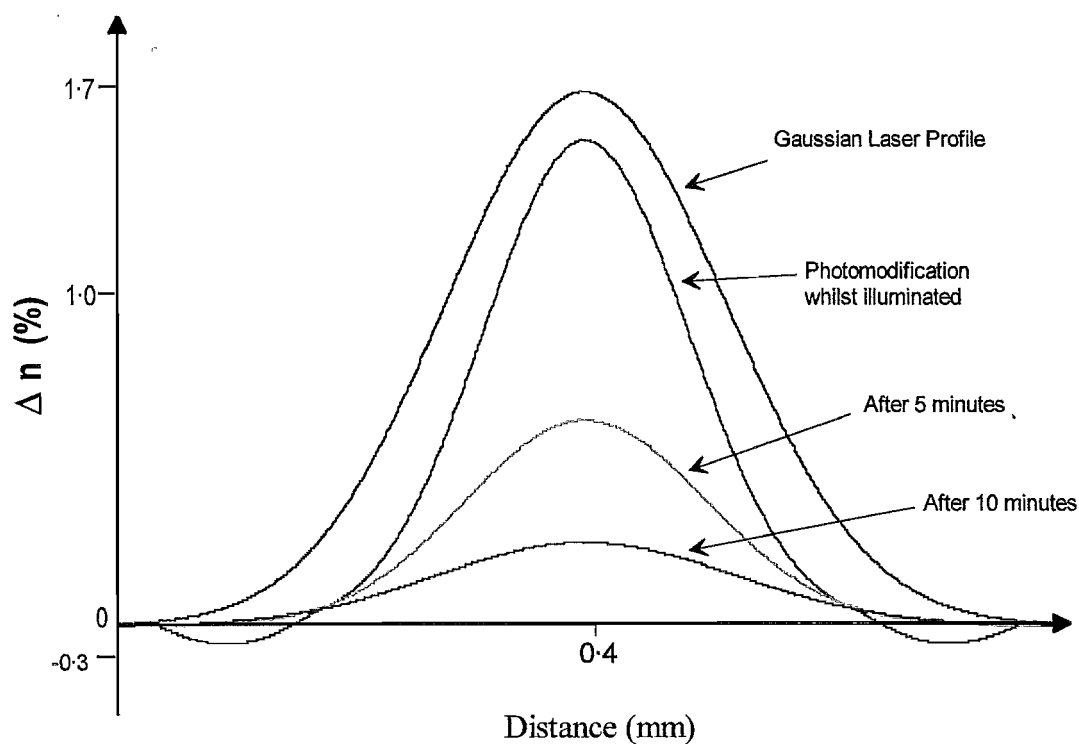


Figure 6.14. Comparison of the changes in refractive index from just before the laser is turned off, then 5 and 10 minutes after turn off. This is a bulk sample of GLS and hence has the characteristic increase in refractive index. {Original in colour}

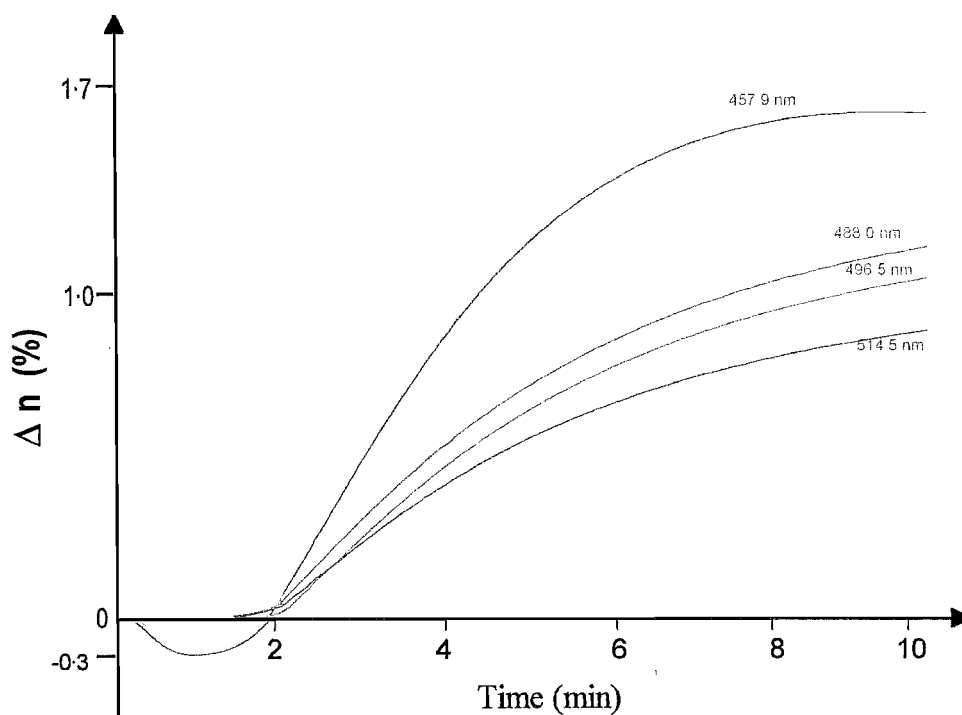


Figure 6.15. Change in refractive index during photomodification at various Argon Ion laser lines all at same power density on a bulk GLS sample. {Original in colour}

the second laser spot in the 'dither' experimental arrangement, moves across the sample surface as the gain of the amplifier increases the pulse amplitude. The quantised step size of this move is controlled by the gain step of the amplifier and the speed is set by the number of "dithers" between gain increments and is set by the binary counter.

With the argon laser in place to instigate photomodification, the dither spot is translated across the region using the above mapping technique. Figure 6.14 shows the resultant plot as such a scan is performed. The paler and darker, photo- bleached and darkened regions can now be better understood. The figure also shows two profiles taken five and ten minutes after turning the laser off. It is evident that the pale ring disappears more quickly than the centre region.

Two further investigations were now undertaken as a result of this observation. A combined graph (Figure 6.15) looks at how a bulk sample photomodifies with increasing argon power at five laser wavelengths. Again a maximum of 46 mW (91.5 kW m^{-2}) is used as this is the highest intensity from the weakest line of the argon ion laser. The graph shows how bulk samples of GLS photomodify over a range of laser powers and a range of wavelengths. It can be seen that whilst all of the wavelengths cause a decrease in the refractive index at low powers, the shorter the wavelength, the more effective the refractive index change. At longer wavelengths the beam begins to transmit further into the bulk sample and the photomodified region gains depth (when viewed from above). The depth profile can be seen by eye and it appears as a dark brown approximately Gaussian profile which matches that of the singlemode beam. In all cases, removing the source of energy allowed the bulk sample to return to its original condition and properties.

A novel reversible change in the optical transmission and refractive index, due to light irradiation has been found in the bulk GLS glass material. Illumination causes variation in the optical properties of the glass having two competing effects: thermal and purely optical. From this data it can be concluded that an optical effect, which appears upon illumination by low energy light, shifts the absorption edge to shorter wavelengths (photobleaching), causing an increase in the optical transmission of the film. The thermal effect, appears upon illumination with higher power density and shifts the absorption edge to longer wavelengths making the film less transparent.

6.5.2 Measurements at Longer Wavelengths

Whilst in principle the differential reflectance technique can measure reflectivity changes at any wavelength, variable reflectivity creates difficulty when measuring thin films. It is still possible to conduct multi-wavelength measurements in thin films, by fitting to the

transmission spectra and combining with the reflection technique to measure Δn under such conditions. Bulk sample measurements are very easy to make over a wide range of wavelengths. It has already been shown that the range of argon wavelengths photomodifies the material and hence these frequencies can not be used for data acquisition. The next wavelength that was available is 633 nm from the HeNe laser. There is no evidence that this wavelength changes the refractive index, tests carried out to measure the refractive index of GLS at 980 nm using a collimated diode having 25 mW output power at 641 nm for photomodification, results found no refractive index change (Δn) and so confirms this.

Figure 6-16 shows the refractive index for a bulk sample of GLS when being photomodified with the argon laser at 300 mW (596.8 kW m^{-2}) multi-line. The diodes (all set to 1 mW output power) used to make the differential reflectance measurements are shown on the abscissa and the respective index change at that wavelength shown. From these results it can be seen that the photoinduced index changes are too small to measure above 980 nm with our apparatus and given the sensitivity of the technique it is practical to deduce that they do not actually exist. Assuming that no change occurs at these wavelengths, structures made from GLS could be used to transmit longer wavelengths and interact with red and near infrared frequencies via photoinduced grating based structures etc. It would be important in such devices to maintain device stability which in a GLS sample means an element of temperature control would be necessary and the samples shielded from light in the visible region.

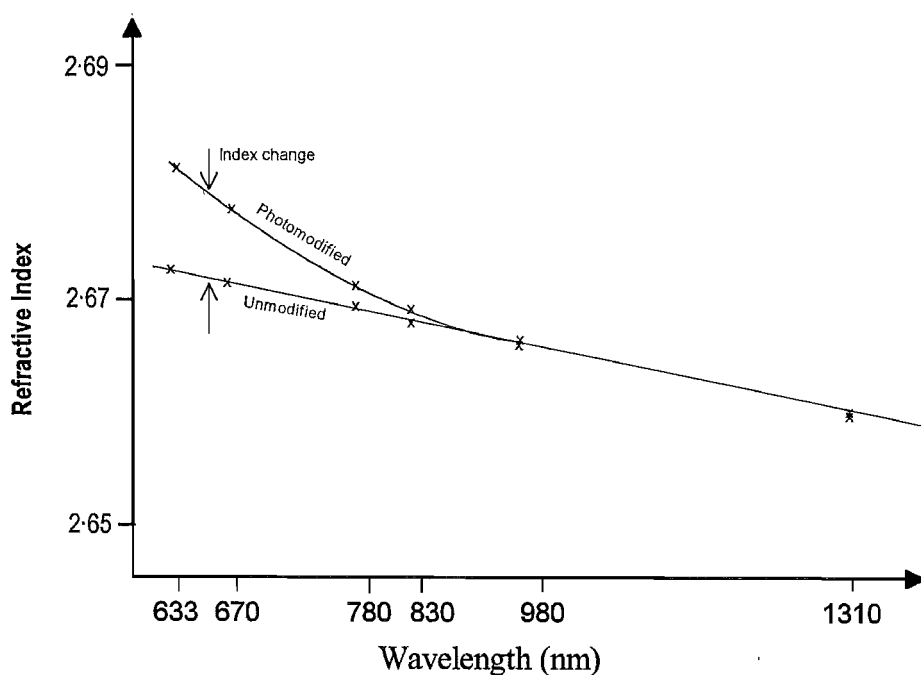


Figure 6-16. Change in refractive index at various wavelengths during photomodification by an Argon Ion laser in a bulk GLS sample. {Original in colour}

6.6 Photoinduced Gratings

6.6.1 Introduction to Gratings

When longitudinally pumping a laser, it is necessary to ensure that the pump radiation is coupled into the lasing medium with a high efficiency and the lasing radiation is coupled out from only one of the mirrors. One mirror must therefore be highly transparent at the pump wavelength and highly reflective at the lasing wavelength.

Most thin film slab or channel waveguides have their end surfaces perpendicular to the optical axis, cleaved or polished to produce flat, smooth faces. However, there are two problems which occur with polishing. Polishing gives truly flat surfaces if the polish rates of the film and substrate material are the same. The friction that results between the thin film surface and the polishing pad causes localised heating and softening of the glass. Particles of the fine-grained polishing powder may also become embedded in the last few micrometers of the thin film layer giving rise to a small loss by scattering and absorption.

When light is incident on an end surface, Fresnel reflection takes place. In the majority of situations, reflection can be an unwanted source of feedback. One solution is to immerse the end faces in refractive index matching oil. However, index matching fluids do not exist for the higher index chalcogenide glasses. The end surfaces and the mirrors must be mounted so that they are at an angle that is as close as possible to 90° to the ends of the waveguide structure. This necessitates the use of micropositioners, which offer both translational and rotational movements. Another difficulty that can arise in practice is bending of surface mirrors, which occurs when excessive force is applied in an effort to avoid separation from the end of the guide.

Another solution for cavity reflectors is to use directly coated ends^[303] in which one or more layers, usually a dielectric stack, are evaporated onto the waveguides end surfaces. The benefits of such a strategy are that many samples can be simultaneously mounted in an evaporation plant and thus the cost is lower. Similarly, it is not necessary to devise a means of mounting a separate mirror against the end. However, there are two serious disadvantages associated with directly coated lasers: End-coated mirrors are more sensitive to imperfections because they are usually multilayer dielectric coatings, cleaving must be performed to a higher standard^[304]. Second, if damage to the coating is caused by using excessively high power focused pump light, the whole laser is destroyed. In contrast, pump laser damage to bulk mirrors is usually restricted to a small area and the waveguide can be moved relative to the mirror surface to reinitiate lasing.

Photosensitive gratings can be written into our thin films by transversely exposing the surface to intense interfering wavefronts from a visible or ultraviolet laser. Optically induced

defect sites are thus created, causing a periodic perturbation in the refractive index. The variation of the pattern depends on the intensity of the exposing beams and the length of exposure. The reflectivity and the bandwidth that can be achieved by the photosensitive gratings in waveguides are determined by both the refractive index change and the grating length. Photosensitive gratings offer the potential of comparative ease of preparation.

An induced refractive index change in chalcogenide materials permits the fabrication of high spatial resolution grating structures using either laser^[305] or e-beam^[306] addressing, with applications such as Bragg reflectors, waveguide couplers and mode converters in integrated optical devices. To recall earlier results, photomodification is maximised after illumination for around forty five minutes at our power densities. In order that gratings be written into GLS thin films over this duration would require active stabilisation of the interferometric equipment.

6.6.2 Stabilised Interferometer

6.6.2.1 Introduction

Over the past twenty years gratings 'written' into fibres and thin films have been used as reflectors and in wavelength multiplexing applications^[289]. Usually these are written into a material by means of a refractive index change resulting in a permanent grating. For GLS thin films the argon ion laser interferometer produces an interference pattern to manufacture a grating taking at least 20 minutes depending on the thickness of the target material. In these circumstances, there is a need for the stabilisation of the interferometer.

During these long exposure experiments, the fringe pattern is very susceptible to temperature variation and vibration from the surrounding environment causing a smearing of the interference pattern^[307]. The fringe drift associated with vibration can be largely removed with the use of a good optical table; however, removal fringe drift due to temperature change requires active stabilisation^[308]. Most unwanted path changes associated with mechanical vibrations and thermal changes lie in the frequency range from 0 up to approximately 200 Hz. Therefore, to achieve practical stabilisation, a technique is required which is capable of producing optical path length changes and is able to operate over this frequency range. One solution is to alter the wavelength of the light by laser tuning^[309]. This approach is expensive, complicated and possible at only a small selection of wavelengths. An alternative solution is to alter the path length in the reference arm by physically moving the mirror. In its simplest form a mirror is mounted on a piece of piezoelectric material^[310]. A third technique involves the use of optical fibres and producing path length changes by straining the fibre^[311]. Stabilisation is achieved by employing some active element, in this case a piezoelectric multimorph™ crystal, together with a driving and detection system. The detection and driving system is controlled by a negative feedback

loop. Herbst and Beckwith^[312] stabilise the cavity spacing of a Fabry-Perot interferometer for the use as a tuneable filter during astronomical observations.

6.6.2.2 The Interference of Two Beams of Light

An important consideration, vital to designing an effective system to detect fringe drift, is the shape of the interference pattern. Several methods can be used to calculate the resultant intensity profile of two interfering waves of equal wavelength and amplitude. The resultant distribution, I , is a function of amplitude, a , and the phase difference, θ , in the form:

$$I = 4a^2 \cos^2\left(\frac{\theta}{2}\right) \dots\dots\dots (6.6)$$

The greater the difference between the fringe maximum and minimum the larger the change in intensity when the fringes drift. Drift of the interference pattern occurs when the optical path length of either arm of the laser beam varies. The reduction in fringe intensity due to the lack of constructive interference gives the impression of the pattern moving to either left or right and hence the term drift. The fringe period, is defined as the distance from one point to the same position on the next cycle.

6.6.2.3 Active Stabilisation

Whilst there are several alternatives that can be used to stabilise the fringe pattern, the most readily achievable in the laboratory and the most inexpensive method is to change the path length of the reference laser beam. This is achieved by altering the position of the mirror within the interferometer, which effects the path length and moves the fringe pattern to counteract the drift (demonstrated in Figure 6.17)

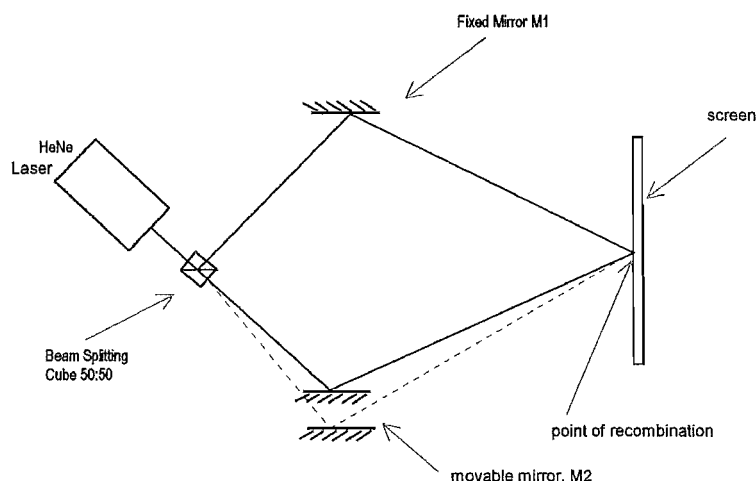


Figure 6.17. Basic principle of an interferometer used to write gratings into samples of GLS. {Original in colour}

The drift of the fringes is slow; approximately several fringes per minute. This as an advantage, as a slow control loop could be used and therefore the reaction time of the mirror could also be relatively slow. A fast reaction time would be hindered as the weight of the mirror on the mount would increase the momentum of the system. The following methods to mount the mirror were considered: piezoelectric ceramic, bimorph[™] strip, metal expansion and a loudspeaker.

Using the latter, a 7 mm² mirror was mounted in the centre of the speaker using epoxy resin. The speaker has a frequency operating range of 300 Hz to 20 kHz but this is severely reduced by the additional momentum of the mirror. It was necessary to carry out an experiment to see how much dc voltage would be required to drive the speaker. To achieve this, the speaker was held by an optical clamp in the interferometer configuration illustrated Figure 6-17. The experiment required the interference pattern to be magnified as describe in the following section. The results of the experiment are shown in Figure 6-18 where it is seen that there is a linear relationship between fringe shift and driver voltage. The 470 Ω resistor allows for more sensitive adjustment of the fringes and, most importantly, that the speaker system was capable of counteracting a drift of at least 10 fringes.

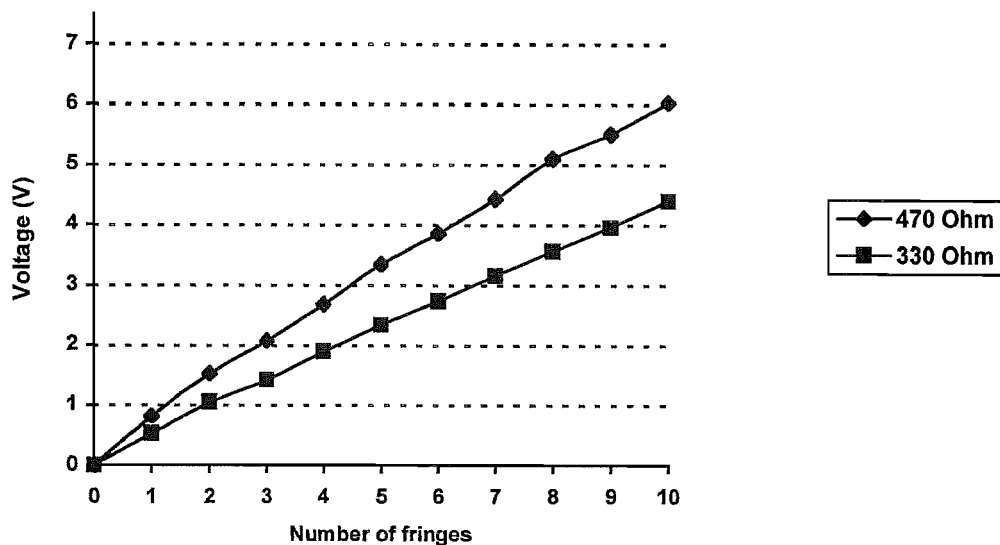


Figure 6-18. The correct choice of resistor shows how the control signal can move one arm of the interferometer is sensitive to fringe translation.
{Original in colour}

6.6.2.4 Magnification of the Fringe Pattern

In the overlapping region of the two laser beams the width of the fringe period is related to angular separation of the laser beams^[313, 314]. Simple geometric considerations show that the relationship between grating periodicity Λ and the beam angle α is given by:

$$\Lambda = \frac{\lambda_o}{2 \sin \alpha} \dots\dots\dots (6.7)$$

From this it is obvious that Λ is limited to values greater than $\lambda_o/2$. For the 458 nm line from an Argon ion laser the fringe period can vary from 5.24 μm for $\alpha = 5^\circ$ separation to 0.32 μm for $\alpha = 90^\circ$. At these periods it was very difficult to lock the fringes with conventional components due to size and hence detectable area available for one fringe. This meant it was necessary to expand the fringe pattern.

The amount of magnification required depends on the size of the original fringe pattern. At 35° , the interference pattern at the intersection of the laser beams would require approximately 150 times magnification to obtain a fringe width of at least 0.1 mm. This is an arbitrary minimum value and can be achieved with a microscope objective and another lens. This proved very successful, fringes of 2 mm being obtainable at a distance of 850 mm from the intersection of the laser beams. The optimum separation of the objective and lens was a compromise between light intensity and magnification. The fact that the fringe size could be varied from a fraction to several millimetres made the limitations of the detection system less critical. The microscope objective selected was a Melles Griot with a magnification factor of 63, a working distance of 0.14 mm and a focal length of 3.1 mm. The laser beams were recombined on the aperture of the microscope objective meaning the objective was focused on a virtual object at infinite distance as shown in Figure 6.19. Matching the focal points of the microscope objective with that of a second lens creates magnification on the detector surface. This method allows the laser beams to have an initial wide angular separation and therefore the corresponding interference pattern to have small fringe period with which to write on a photosensitive material.

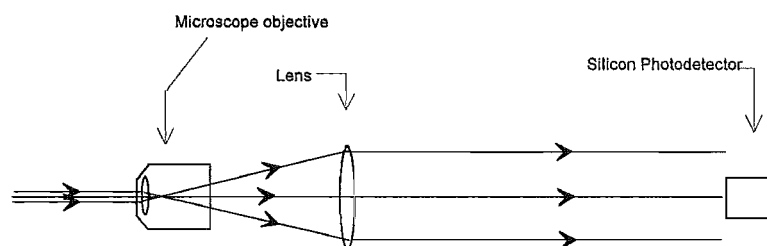


Figure 6.19. The principle of fringe magnification used in our interferometer.
{Original in colour}

6.6.2.5 Method of Detecting Magnified Fringes

With the enlarged fringe pattern, it is possible to select a narrow area of the illumination (half a fringe) by using a mask to select a particular fringe. The preferred option is based on a feedback loop in combination with an oscillating input to 'dither' the fringe pattern. This

'dither' was achieved by summing a square wave onto the speaker, forcing the fringes to artificially drift. Using this ac signal as a reference signal allows the use of a phase sensitive detector (PSD). The PSD compares the phase of the signal from the fringe detection system to the reference from the signal generator. Any drift of the fringe pattern will create a phase change and therefore a positive or negative output from the PSD dependent on the direction of drift. This detection method can be refined to allow rejection of various kinds of unwanted response^[315], for example noise can be electronically induced to simulate environmental changes. The use of a dither signal also negates the effect of errors induced by small vibrations of the optical table.

To maximise the amount of light intensity on the single detector means increasing the number of half fringes incident, the best option is to use a grating as this provides a maximum number of evenly spaced slits. 50:50 transmissive gratings are used in meteorology and are therefore easily available from commercial sources. The period of the transmissive gratings available, varying from 100 lines per mm up to 1 line per mm. We utilised a grating with a period of 2 lines per millimetre. This is a compromise between maximum magnification and maximum light intensity. An additional advantage of using a transmissive grating is that it gives an indication of the quality of the interference pattern and not, in the case of a single slit, one half fringe. The positioning of the grating over the fringe pattern is still vital. To match the period of the grating to the fringe width the grating is rotated in the vertical plane so that its period with respect to the plane of the fringe pattern decreases. The experimental arrangement is shown in Figure 6-20. Rotating the orientation of the grating means that instead of altering the size of the interference pattern to match the grating size, effectively the period of the grating is altered to match that of the interference pattern. The fringe pattern and the transmitted light through the grating produce Moiré fringes. When the periods of both the grating and fringe period match, the Moiré fringes disappear.

The signal from the photodiode is amplified by two stages of inverting amplifiers. Changes in temperature are slow, so there is little requirement for fast correction to counteract the drift of the interference pattern. This is an important factor as it affects the sensitivity and stability of the feedback loop.

6.6.2.6 Feedback electronics

To convert the photo-current from the silicon detector into a relative voltage requires a low noise transimpedance amplifier. Inverting amplifiers were constructed from operational amplifiers (Op-amps) employing negative feedback. The number of inversions must be such that the feedback of the loop remained negative i.e. an odd number of inverting amplifiers. Several stages of amplification were required to increase the output of the photodiode, by a factor of around 5000 V A^{-1} . Figure 6-20 shows the relative locations of the amplifiers used.

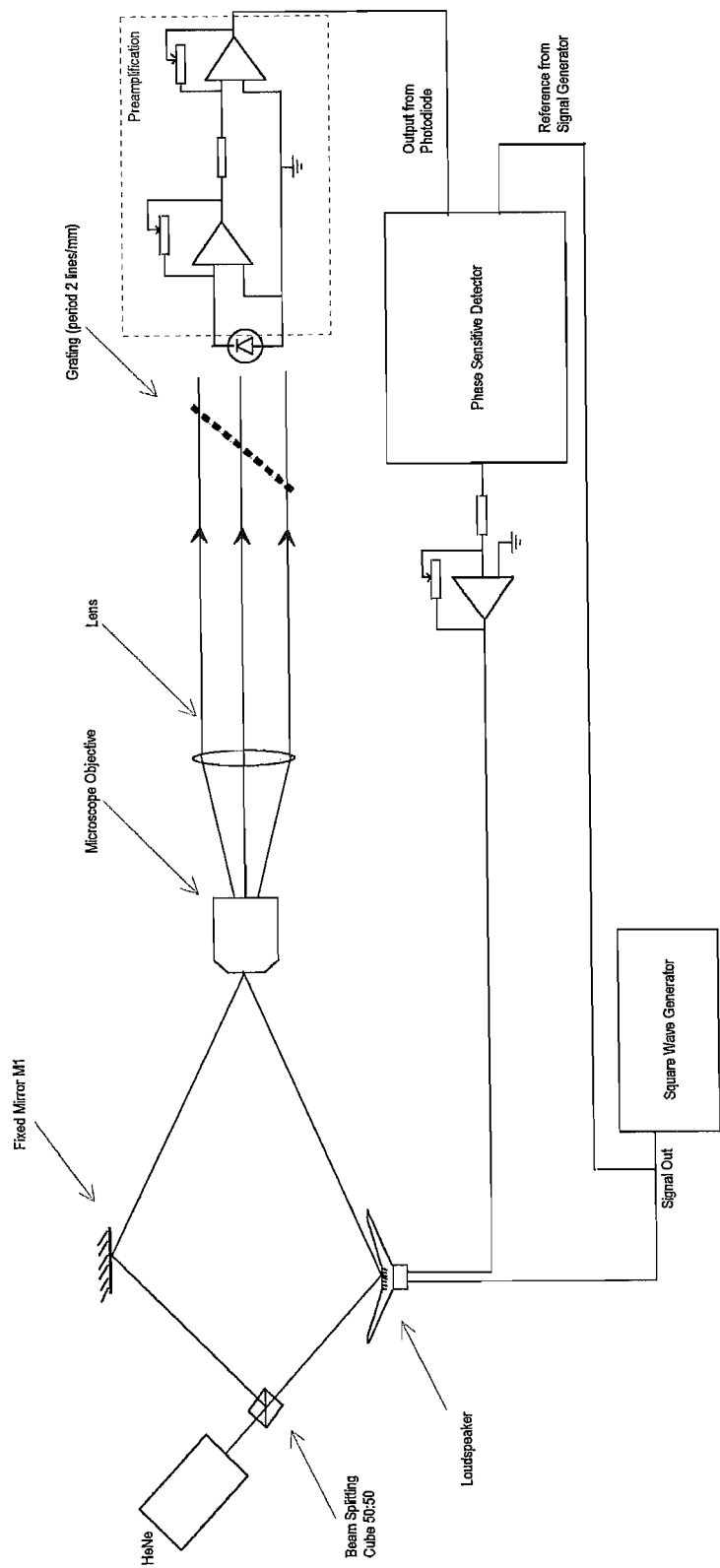


Figure 6-20. The experimental arrangement to stabilise the interference fringes used in our interferometer for the potential production of diffraction gratings. {Original in colour}

This circuit is connected to the PSD which has the input from the signal generator as a phase reference for the amplified detection signal. Since one arm of the interferometer is being oscillated at this frequency, any mismatch in the phase of the amplified photodiode signal is caused by the drifting of the interference pattern. The output of the PSD is a dc voltage whose magnitude is directly proportional to the phase difference between the reference signal and the photodiode detected signal. The direction (sign) relates to the phase of the drift indicating the need to increase or decrease the path length of one arm of the interferometer.

The amount of amplification required depends on the operating environment, i.e. the amount of noise in the room induced by lighting. Separately, the loudspeaker has a 'fringes moved per volt' transfer function and the photodetection system has a voltage dependent on the intensity function. The amount of gain is critical in all feedback loops as it affects the reaction speed of the complete system. More gain means a faster reaction; however the gain also effects the stability of the system, so if the correction is too quick, the system over corrects and has then to respond to its own over reaction. As with most control systems a small over shoot is acceptable, i.e. under damping, but if the gain is increased above this level the system tends to oscillate and cause instability.

6.6.2.7 Test Results

Initially simulations were required to prove that the interference pattern has actually stabilised. As stated in the previous section the PSD indicates when the fringe drifting begins to occur and the path difference required to return the interference to its original state. The signal intensity from the photodetection system (Figure 6-21) increases to a maximum by rotating the grating to the correct angle.

The square wave also shown in Figure 6-21 is that which is produced by the signal generator, providing the 'dither' to the loudspeaker. The signal from the photodetection system is exactly in phase with the reference signal. The photodiode signal is low pass filtered by the movement of the speaker cone, whereas the driving signal is a square wave, this is due to the delayed response caused by the extra momentum of the mirror and glue on the front. This effect could be counteracted if a lighter high quality mirror had been readily available instead of the aluminium coated microscope slide used in these experiments.

Drift can be simulated by summing a dc component into the dither signal. Figure 6-22 and Figure 6-23 continue on from Figure 6-21 to illustrate the simulated fringe drift over half a period i.e. from a maxima to a minima. More specifically, Figure 6-22 shows the fringe drift profile at 90° out of phase with the dither signal; the mismatch of phase is indicated by the PSD output being zero. Figure 6-23 illustrates the modulation waveform 180° out of phase

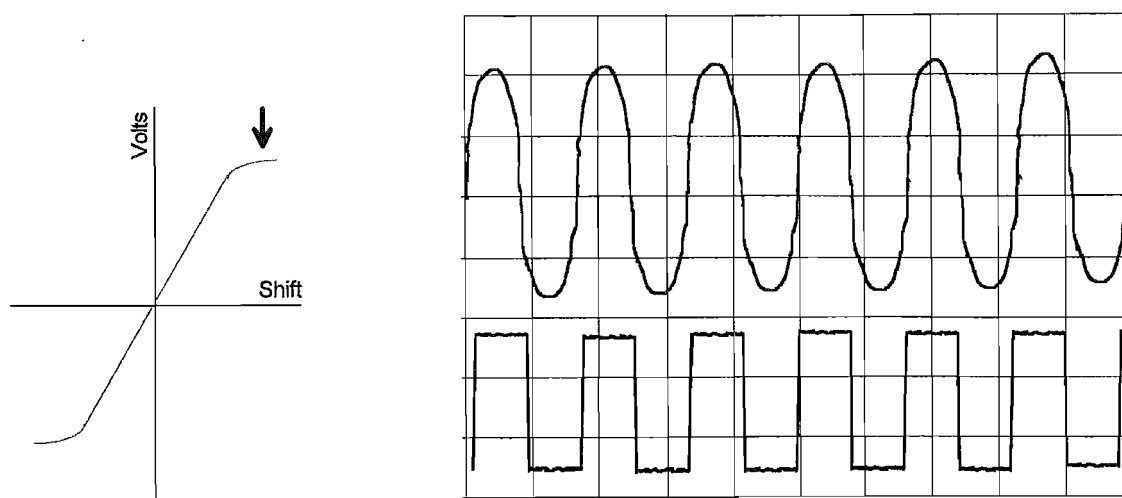


Figure 6-21. Fringe detection signal (—) is in phase with the reference mirror driver signal (—). {Original in colour}

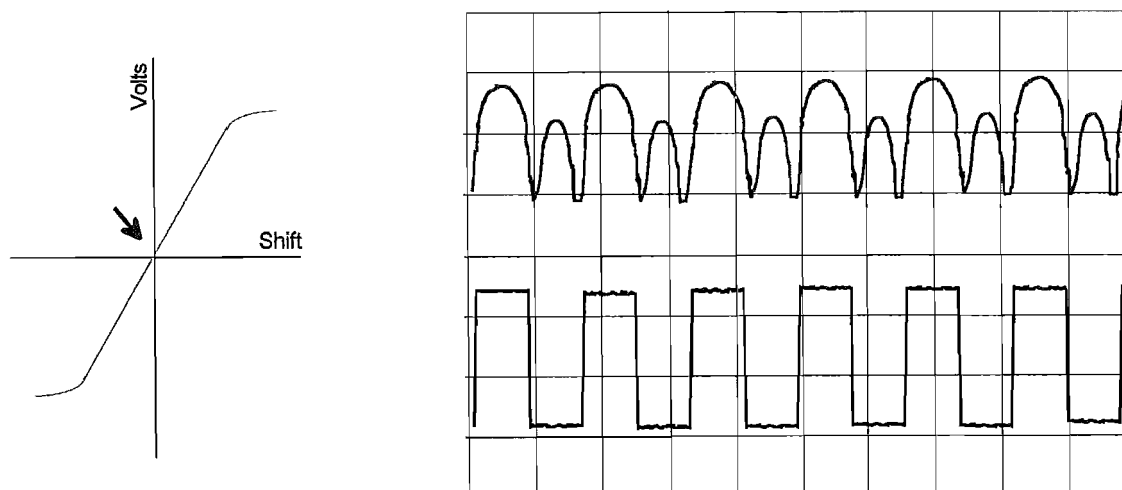


Figure 6-22. Fringes drift approximately 90° out of phase with the reference mirror driver signal (—). {Original in colour}

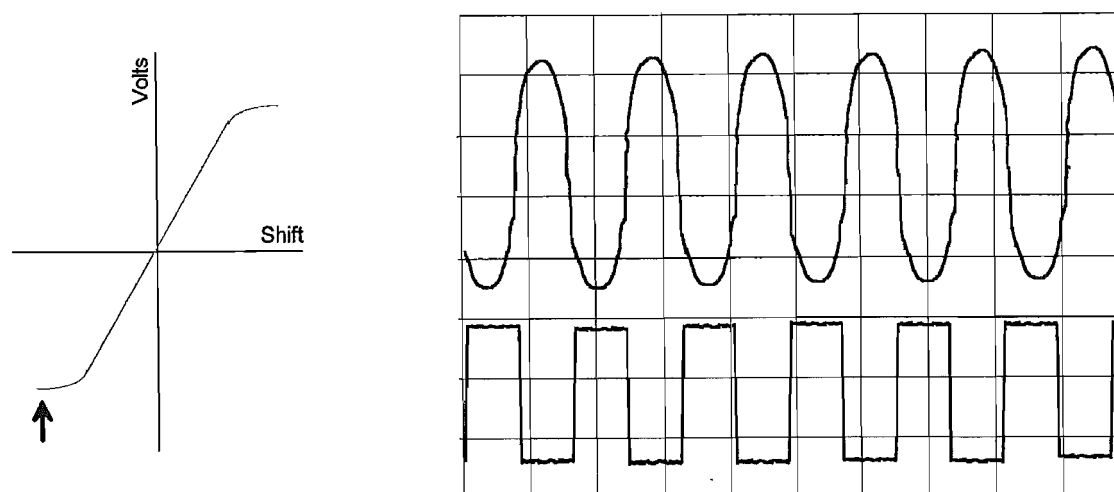


Figure 6-23. Fringes drift 180° out of phase with the reference mirror driver signal (—). {Original in colour}

with the dither signal and so the PSD output provides a feedback signal for the speaker cone to adjust and correct it. If the fringe pattern is made to drift more than one period the system locks on to the new fringe. To make the fringes drift more than one fringe period requires a fast change, which would not happen in a realistic situation i.e. with an increase in temperature or small physical vibrations. The output from the PSD is monitored via a voltmeter clearly showing the PSD detecting the change in phase.

Without the mirror the manufacturers quoted, effective frequency range of the speaker is 300 Hz to 20 kHz. Experimentation showed that the working frequency range for the loaded loudspeaker was between 400 Hz and 1.5 kHz. These are the 3 dB roll-off points of the relationship between driving signal and physical movement of the cone. The degradation in performance is due to the mass of the mirror causing increased momentum, returning to its initial position more slowly. The dither frequency used in this apparatus was set to 627 Hz, at this level there were no distinguishable effects or interference from mains electricity, room lighting or harmonics of them.

6.6.2.8 Final System

As a simple proof of principle the open loop drift, X and the closed loop drift, Y were measured. The 90° out of phase profile similar to that shown in Figure 6-22 was taken as the start/stop profile when all peaks were of equal amplitudes. Hence as the next tests were performed, the profile starts as above, has some random shape for a time period during which recovery takes place and finally when the profile returns to its original state the timing is stopped and recorded.

The first test was to time how long it took for the fringes to drift as the room temperature was reduced from 24 °C using the air-conditioning unit in the laboratory. For the open loop case the fringe drifted one whole period within the first 1 °C, in total moving 16 periods in 5 °C. With feedback activated no drift could be seen over the fifteen minutes needed to reduce the room temperature by 5 °C.

The second test used a hot air stream (from a decorators hot air gun) to heat the mirror mount of the fixed path length arm of the interferometer. For both open and closed loop drift the fringes drifted badly whilst the air stream was in place. However the time taken to return to a stable steady state when the air flow was removed was 41 seconds and 4 seconds respectively: An order of magnitude improvement.

Use of the system to write stabilised gratings in photosensitive materials requires an additional component, a beamsplitter positioned as shown in Figure 6-24. This transmits

90% of the light and reflects the remaining proportion. The photosensitive sample is placed in the combined transmitted beam and the stabilisation system described here, is placed in front of the reflected component. The results in the following section are produced using this stabilised interferometer and an argon ion laser on photosensitive thin film layers.

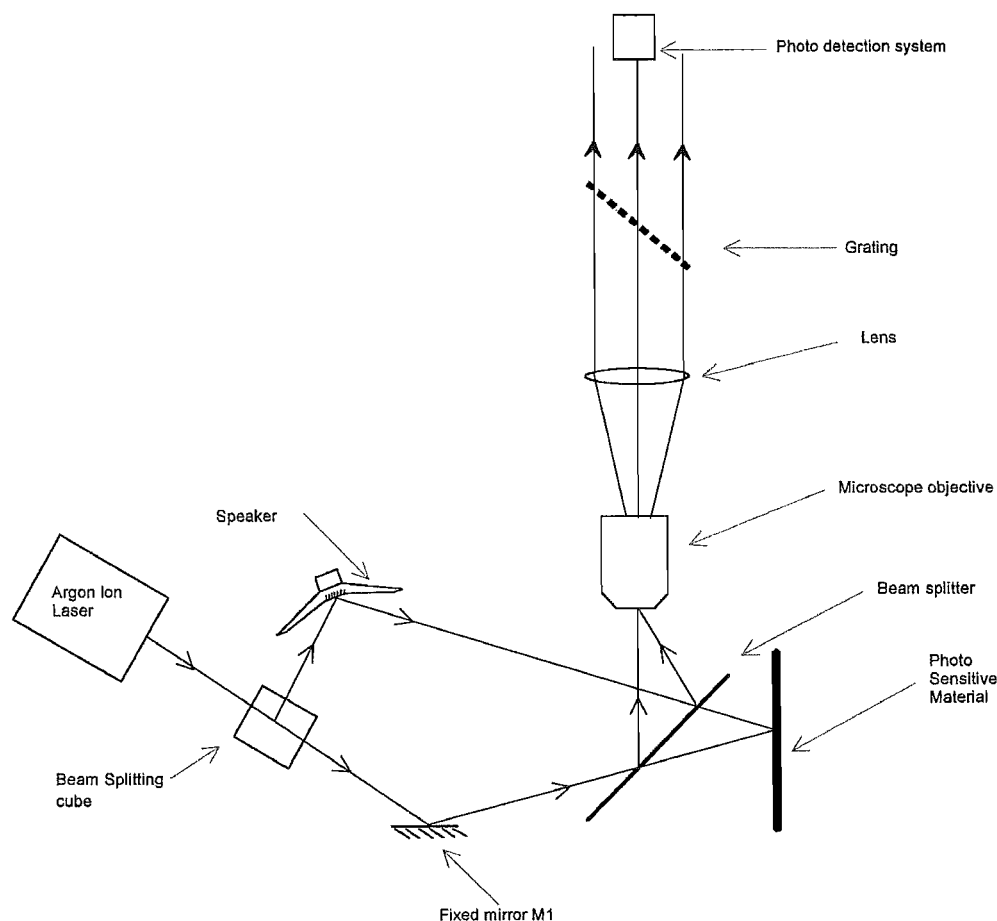


Figure 6.24. The full system layout combining sample holder and active stabilisation, showing schematic layout of components. {Original in colour}

6.6.3 Mapping Photomodified Gratings

To recap; full photomodification of the GLS thin films takes in the region of forty five minutes at our experimental intensities, meaning that active stabilisation is obviously necessary to achieve maximum diffraction efficiency of the grating structure. An optimum grating structure requires that the difference in refractive index between the periodic structures be as large as possible, with the steepest rise or fall possible at the edges. The technique of so called amplitude mapping, detailed in Section 6.5.1, is particularly useful in this application to measure both magnitude of the index change and the width of the individual grating features. The plan with this technique was two fold, primarily to look at the difference in the

gratings produced with the active stabilisation on or off and secondly to measure the physical dimensions of the grating period and structure. It is important to point out at this stage that the refractive index change measurements are less accurate using amplitude mapping than the original dither technique. This is due to slight angle changes between the beams as the spots separate, the spot size increases slightly and the surface reflectivity changes with the angle of incidence.

The versatility of this differential reflectance technique is further demonstrated in the following examples. The amplitude mapping technique is used whilst the active stabilisation arrangement is in place and operational. This allows constant scanning of the interference region on the thin film surface and continuous mapping of this area whilst the grating is produced. Figure 6·25 shows the map of scans after various time periods showing the refractive index change as the grating is produced, stabilised. The physical depth of these structural changes which produce the gratings is unknown as this measurement technique, can only monitor surface changes. Any differences in the map profile between the two halves of the figure is solely due to active stabilisation. It can be seen from Figure 6·26 that the active stabilisation has the effect of increasing the difference between maximum and minimum refractive index values. The stabilisation does however appear to square the profile of the peak index change, which could be due to the forced vibration which is used to drive the speaker cone via the phase sensitive detector.

Figure 6·27 is a theoretical plot of light intensity for the two recombined halves of the laser beam from the interferometer (red line). If the fringes drift, unstabilised by $\pm\frac{1}{6}$ fringe period (locations shown diagrammatically by blue dotted lines at their extreme locations) the refractive index difference will be reduced by the smudging of the grating structure. If the intensity required to photomodify is shown by the horizontal dashed line, it can be seen that a stabilised interferometer will produce regions of unmodified GLS, whereas the theoretical drift shows that the whole of the surface region will be subjected to some photomodification.

Before leaving this section, it is worth pointing out how the grating structure begins to fade as the refractive index contrast decreases over a period of time due to the ageing effects seen in Section 6·3·2. The film in the earlier figure (Figure 6·25) which had a stabilised grating written into it was re-scanned nearly two years after the initial photomodification had taken place. Figure 6·28 shows the original scan after forty minutes and the relaxed structure for comparison. Over the intermediate period the whole thin film structure had been stored at room temperature in an opaque container, so light reaching the GLS thin film would have been lower than that of the room. It can be seen that the ageing process relaxes the structure to a point where the refractive index difference has reduced, but more importantly the maximum value of the derivative of the index with respect to distance is decreased. This follows on from the previous discussions of aged films and their photomodification

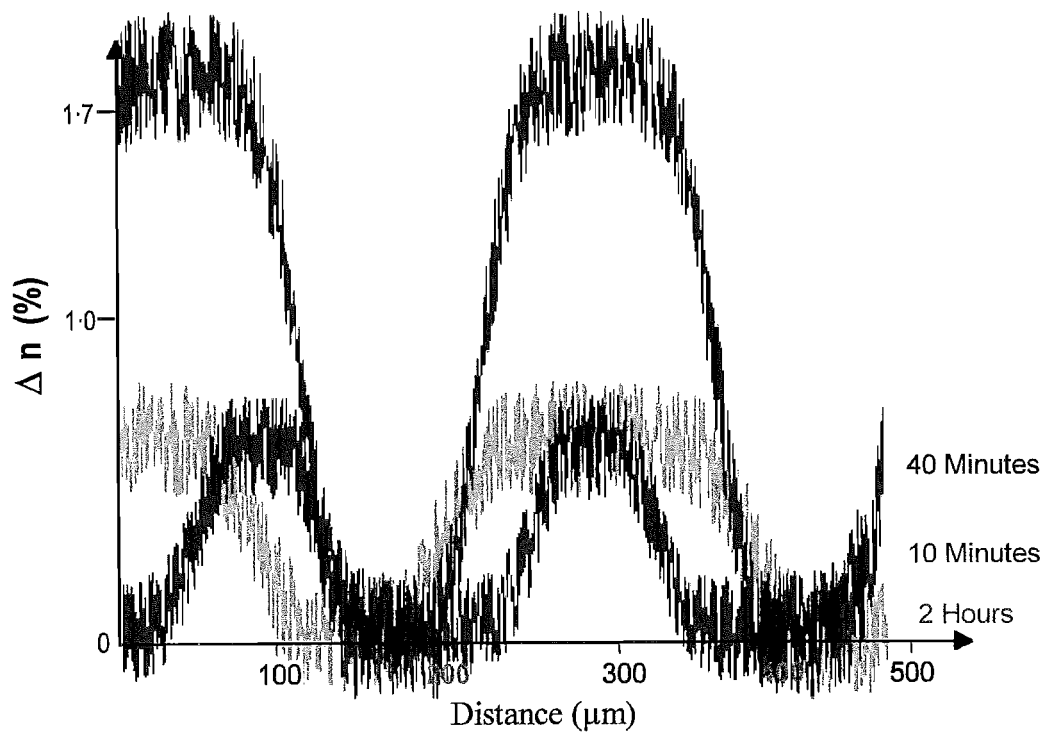


Figure 6-25. Grating profile written on the surface of a GLS thin film after different photomodification time periods. The measurement technique can only measure the difference in refractive index so all traces appear to start at 0% and must be viewed relative to each other rather than absolute. {Original in colour}

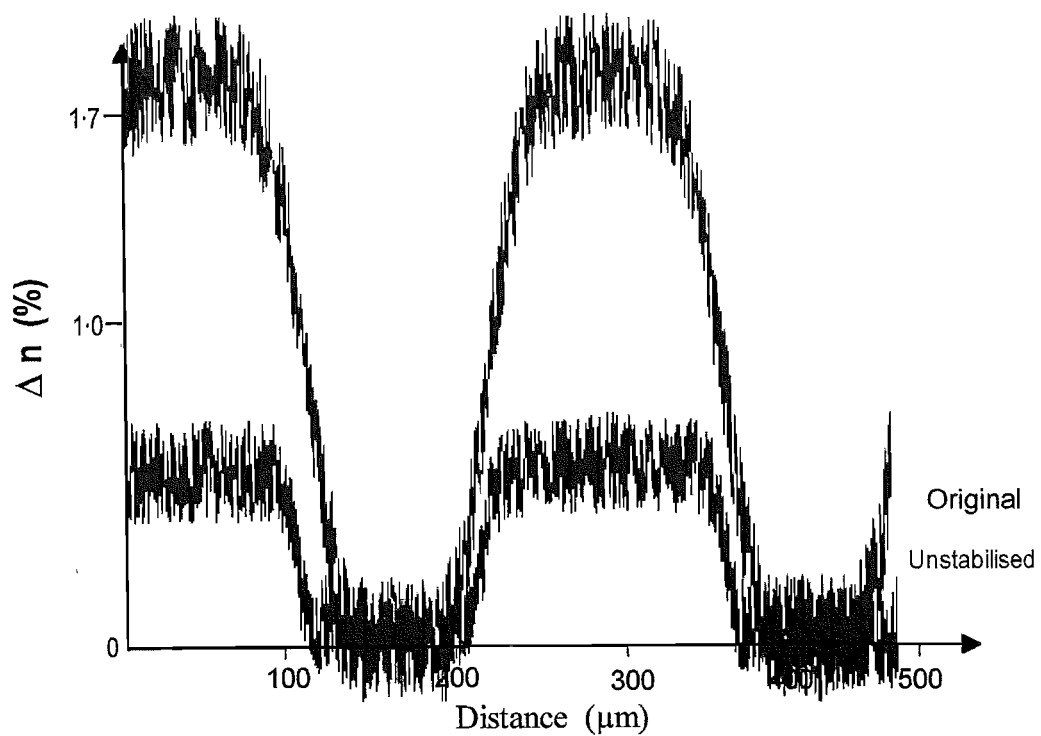


Figure 6-26. Grating profile written on the surface of a GLS thin film whilst being stabilised using the technique detailed in this section, and with stabilisation turned off for comparison. {Original in colour}

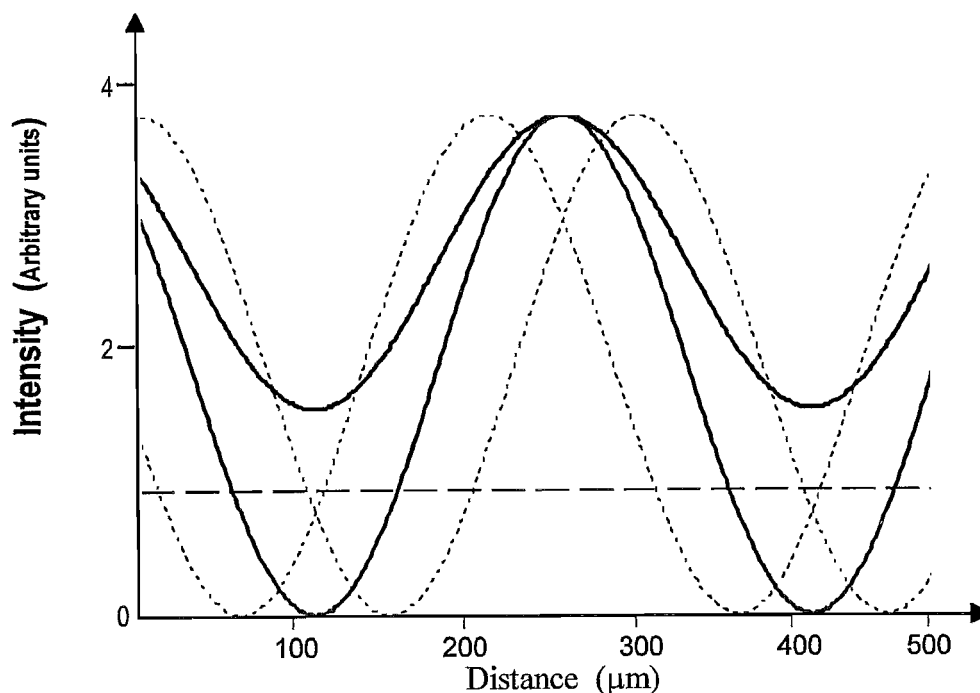


Figure 6.27. Intensity profile of a recombined laser beam (—) which if moved across the surface of a photomodifiable thin film by an amount shown (\cdots) as two extreme positions, will cause a resultant photomodified profile normalised and shown here (—). Theoretical intensity for the onset of photomodification is shown to stress this point ($- - -$). {Original in colour}

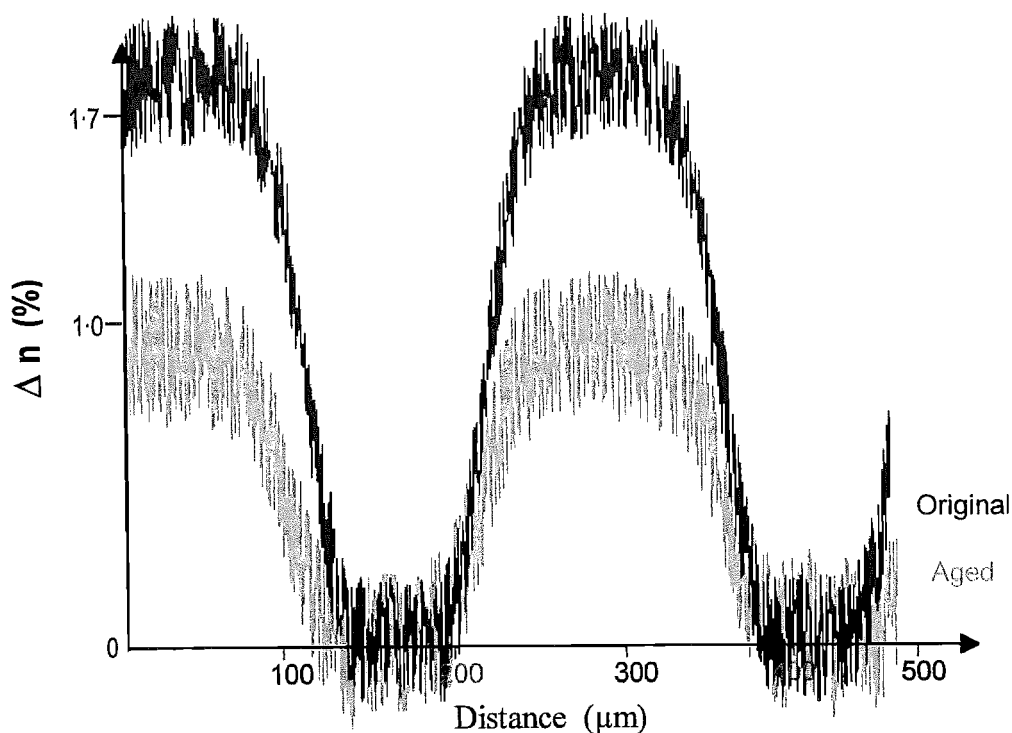


Figure 6.28. Grating profile written on the surface of a GLS thin film after photomodification and after being left for 21 months. The measurement technique can only measure the difference in refractive index so traces appear to start at 0% and must be viewed relative to each other rather than absolute. {Original in colour}

properties of the earlier section. It would be expected that further exposure to room light would reduce the refractive index difference even further.

6.7 Conclusions

A technique was developed to measure the magnitude and sign of the refractive index change on the surface of the thin films that we produced. This can map changes as they occur or the permanent changes induced. The apparatus was used throughout this Chapter to look at photomodification effects associated with films produced in different pressures of background gases and growth with various Excimer laser energies. A multi-line Argon ion laser was tuned to individual single lines and the ability of the sample to photomodify with respect to wavelength were investigated. The time necessary for Δn saturation, is inversely proportional to the pumping power. This means that independent of power, the same quantity of photons creates the same change in refractive index. Also represented is the effect of one single line from the argon laser at differing output powers and the relative speed of photomodification. It was shown that when photons change the refractive index, the higher their energy the faster the process occurs.

For films grown in a background gas of argon, the percentage decrease in refractive index of the material remains constant when illuminated at equal power densities. However for samples grown by laser ablation at differing energy density the degree of photomodification achievable varies. As the power density increases the ability to photomodify decreases. However oxygen shows the biggest effect in terms of photomodification, for as the gas pressure increases the material not only becomes thinner, but includes a higher percentage of incorporate oxygen atoms. The ability to photomodify actually disappears with the experimental argon ion laser power densities available to us. It was seen in the previous chapter that oxygen addition to the deposition chamber incorporates into the GLS thin films. Results in this chapter have shown that the oxygen also reduces the ability to photomodify, so the improved optical transmission losses of the material will not have the same ability to write waveguides and make changes in the refractive index of the material.

There are two effects which occur when thin films of many chalcogenide materials are subjected to laser light whose wavelength lies above the optical band gap of the material. First and initially most obvious is a heating effect which rapidly increases the refractive index of the material. If a thin film layer is grown on high thermal conductivity substrates photomodification is not achievable which suggests that there is a thermal effect present in thin GLS films. Normally this would be seen as an initial rapid refractive index increase. The temperature achieved is dependent on both power and wavelength of the incident

radiation. A second effect is typical photomodification in which the refractive index is permanently decreased. It has been shown that the photothermal changes are erasable while photo-optical changes are permanent. These two competing effects: thermal and purely optical are also found in bulk samples of GLS, but both appear reversible

Structures made from GLS could be used to transmit longer wavelengths and interact with red and near infrared frequencies. An induced refractive index change in chalcogenide materials permits the fabrication of high spatial resolution grating structures using a laser. In order to achieve this requires practical stabilisation, which is done by altering the path length in the reference arm via feedback electronics to close a feedback loop which incorporates a Phase Sensitive Detector. The PSD senses when drifting occurs and adjusts the path difference so as to return the interference to its original state.

Constant scanning of the interference region on the thin film surface whilst the grating is produced showed in-situ how the grating evolved. However the grating structure begins to fade over a period of time due to ageing effects. The ageing process relaxes the structure and the refractive index difference is slightly changed and the vertical walls of the grating bars are less well defined. The ageing process needs to be accelerated shortly after growth of the thin film layer; however it may not be possible to completely saturate this process and null the effects.

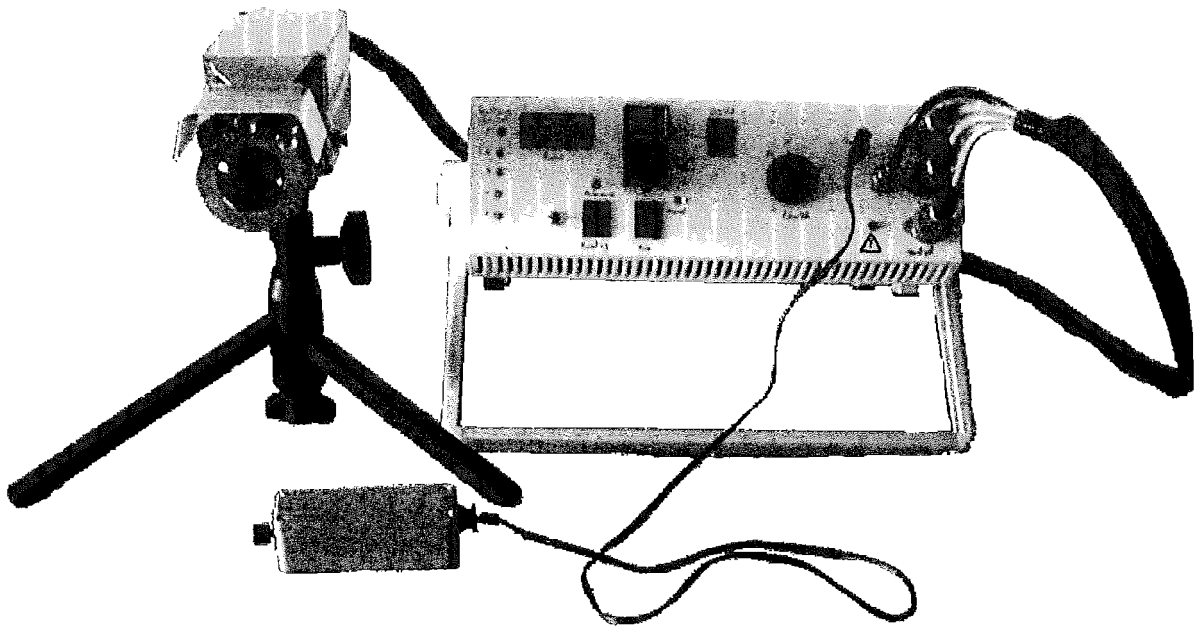
Whilst many processes affect the ability of the chalcogenide films to photomodify, for practical devices to take advantage of mask-less lithography, both optical transmission loss and the long term ageing effects need to be considered. It has not been possible in the time scales of this work to determine if the structure does eventually settle and stabilise enough to become a useful commercial product. Refractive index changes which are seen in the thin film samples are only seen at lower wavelengths. Beyond around nine hundred nanometres the functional dependence of refractive index does not change. This means that with the ultimate goal being to find if rare earth doped GLS could become a suitable thin film waveguide laser, index changes will not be effective in the two to five micron emission region. For photoinduced gratings to be suitable for waveguide devices at these wavelengths, a refractive index change at both the pump and emission laser wavelength is required.

Despite some attractive properties, GLS glasses are of limited interest as materials for bulk glass lasers too, because of the poor thermal properties of the glass. Interest centres on fibre optic and planar waveguide devices. Such devices offer a possible means of incorporating sources and amplifiers into integrated optical circuits. The interest in these devices is to exploit the advantages offered by the planar geometry and the optical properties of rare-earth ions. For example, wavelength division multiplexers, distributed

Bragg mirror or distributed feedback structures may be monolithically integrated to allow pumping and tuning of the lasers, complex multiple-cavity devices may be readily printed photolithographically, and gain regions may be selectively defined in the substrate. In addition, the devices are small, stable and easy to handle.

Part 2

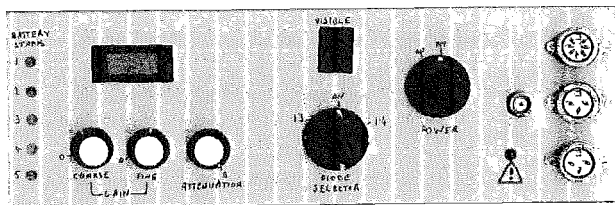
Practical Example of Sensing Using Infrared Lasers



The electronic control box for the laser surface moisture content indication system (digital latest version).

7

Remote Surface Moisture Detection



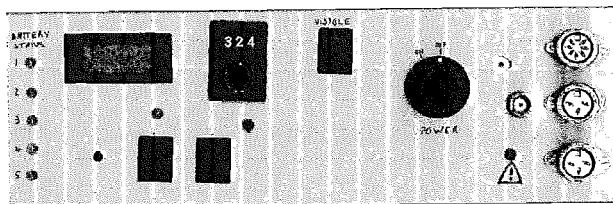
Front panel of the electronic control box for the analogue laser moisture measurement system.

7.1 Design Brief

7.2 Schematic Design

7.3 The Next Generation System

7.4 Results and Conclusion



Front panel of the electronic control box for the digital laser moisture measurement system.

7.1 The Design Brief

GLS appeared to have potential for waveguide devices to be produced in them. With the potential of producing laser devices able to operate in the 2 to 5 μm region, there was a possibility of using this material in sensor applications for detecting absorption bands due to overtones of various gases and liquids whose overtones lie in this region. As the detailed properties of GLS expanded throughout the course of this work, it became more obvious that a lasing device was not a viable possibility.

Table 1.2 presented a selection of absorption bands in various gases and hence potential wavelengths which could be monitored to detect the presence of such a gas. In exactly the same way the presence of water in a damp material could be detected to distinguish a particular sample from one which is dry or dryer. Figure 7.1 shows the absorption bands between 1 and 5 microns of standard tap water. The peaks at around 1.5 μm and 1.9 μm are the most dramatic and could be used to monitor the amount of water which appears at the surface of a sample if the light at these wavelengths was monitored. This requires a laser in this wavelength region whose intensity can be monitored as it is reflected from the sample for which rare earth doped GLS would have been a candidate.

Approached by a sponsor wishing to invest a small sum of money to assess the feasibility of a hand held instrument able to monitor water content of various materials, mainly those used in the construction industry, proof of principle investigations began. However for this to be

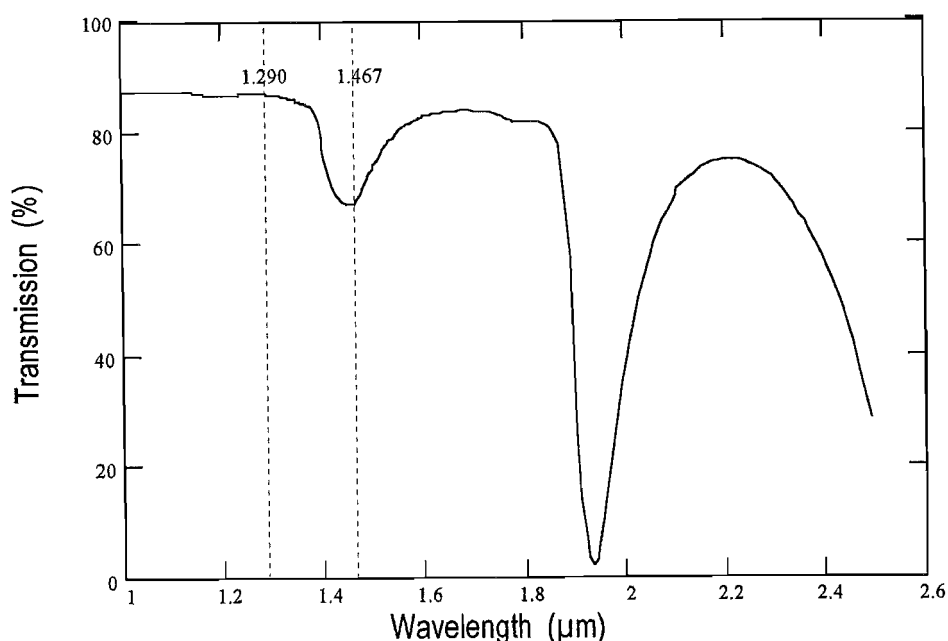


Figure 7.1. The absorption spectra of water used to identify the characteristic fingerprint of the molecules ^[316]. The dotted markers are at 1.29 μm and 1.47 μm wavelength, referred to in the text. {Original in colour}

practical, commercially available products need to be used and currently diode lasers are the cheapest option.

Two wavelengths are required to form reflectivity measurements at different wavelengths. One has to be chosen to show absolute surface reflectivity independent of water content, the other wavelength has to directly relate to one of the absorption bands and from the two results the water content could possibly be deduced.

The design requirement was initially split into two stages, the first to look at the reflection spectra of a sample of building materials to see if two such diode wavelengths could be found. If so, could a portable system be constructed which a surveyor could use to test for 'dampness' of a building up to 10 m from their standing point? Six materials were chosen as being representative of typical materials used in the building of a house: Plasterboard, plywood, brick, paving slab, chipboard and carpet tile. The reflection spectra of all of these samples are presented in Figures 7-5 (a) through 7-10 (a) when each are completely dry¹, wet and various levels between these extremes. The two dotted marker lines on Figure 7-1 show the selected diode wavelengths chosen to investigate the feasibility of a portable measuring device. Because one of these markers is within one of the water absorption bands it can be used to measure the strength of the absorption dependent on the intensity of the reflected signal. A second wavelength is needed as a reference to the general reflectivity of the investigated material independent of water content.

7.2 Schematic Design

7.2.1 Basic Components

The two laser wavelengths were selected from commercially available devices, 1.290 μm and 1.467 μm to be outside of, and within one of the absorption bands of water respectively. The 'wetness' of a sample can be measured from the ratio of the intensity of the reflected signal at these two wavelengths. The key requirement though is the need for this ratio to be known for a dry sample before it is possible to make 'damp' measurements.

The basics of such a system require a diode driver circuit, a phase sensitive detector, a photodiode and transimpedance amplifier, an adjustable gain amplifier and the output display. These are the basics of both systems detailed below. The (nicknamed) "analogue" system is a more basic signal measuring system which requires the manual calculation of the two diode reflected signal ratios. It was only the success of this system which lead to the

¹ Completely dry in this context means that the samples had been stored at room temperature in an indoor cupboard for at least 2 months prior to the beginning of any tests.

second 'digital' version able to produce ratios internally and display a value of 'wetness' without manual calculation.

The diode lasers have to be set to a maximum of 1 mW to prevent issues of eye safety. To improve signal to noise, the lasers are modulated. The frequency of modulation has to be chosen to avoid overtones of mains frequency at either 50 or 60 Hz and since room lighting is usually modulated at twice this frequency, 100 and 120 Hz need to be avoided. In the first system 135 Hz was chosen (15 Hz from both the 150 and 120 Hz overtones). An amplifier able to amplify between 0.1 and 500 times was required to accommodate the difference in reflectivity of the six materials and a 1 to 10 m required sampling range. A liquid crystal display and potentiometer able to measure potentials of 0 to 2 V are used to display the output ratios. The emission unit needs to hold three collimated laser diode units, which are on axis with the field of viewing area of a short focal length lens. A silicon filter is used to remove visible light from reaching the detector. The divergence of the diode lasers is such that at 10 m the spot size is of the order 10 cm and the field of view of the detector lens combination is 2 m. The 1 mm² InGaAs detector is connected to a transimpedance amplifier and has its own power supply in the 'head unit'. The third diode laser, previously mentioned, is at 670 nm and is used if necessary as a position locator so that at longer distances the region that is being illuminated and 'looked at' by the detector can be seen.

7.2.2 First Analogue System

The first version of the system, designed to produce a fully portable system, was made using the components and sub-units listed above. With the variable gain amplifiers set to 1, a dry sample of the material to be investigated is used as a reference. The reference ratio is obtained by turning on the 1.29 μm laser diode and increasing the gain of the amplifier until the signal is in the mid-range (1 V). For short ranges the gain in some cases could be less than unity. The reference ratio is now defined by firstly turning on the 1.47 μm diode without changing the gain of the amplifier. This value is divided by the first (from the 1.29 μm diode and usually 1 V as set and stated above) and forms the dry reference ratio.

With this recorded, it is now possible to move to a wet (also dryer if necessary) area (at a distance which does not have to be equal to that at which the reference was made). Now repeat the above stages with the two diodes to achieve a ratio for the test area. The ratio of these two ratio's shows the "wetness" of the test area as more damp than that of the reference area. The smaller this value the more wet the sample region. The implications of 'how wet' and defining this are considered in more detail in Section 7.4.

7.2.3 Progression to Digital Measurement System

Proving that in principle a system could be made portable and provide signals over the required 1 to 10 m range, sparked further interest from an industrial sponsor. However a commercial prototype would have to be demonstrated to prove that a more 'user friendly' system could be made. An improved system would eliminate the need to record two ratios manually and then divide these to produce a "dampness" reading. Ideally a reference sample would not be needed. This could be a possibility for future consideration by having a store of ratios for the various building materials. This could be extensive but as will be shown in the results in Section 7.4, a range of 3 or 4 settings could be used to group the materials into woods, bricks and plaster, concrete and plastic/oil based materials. The manual calculation of the ratio itself is cumbersome, time consuming and not ideal for field measurement. Finally, the handset needs to record both ratios by having both diodes measure their signals from exactly the same area. This is not easy with the various stages involved in switching and recording values in the first system. If both diodes are modulated at the same time then they could measure the same physical area. There are three possible methods able to achieve this:

Rapid Sequential Sample Hold. The two diodes could be pulsed sequentially swapping rapidly between the two and having a sample and hold circuit to measure the intensity of the signal at the two wavelengths. The ratio from the dry sample can be held for a period of 20 to 30 minutes (based on currently available devices, to the accuracy that we would need) allowing various regions of a similar material to be 'damp tested' in that time. The unit would need some method of indicating if the next reading is to be a new reference signal or an actual reading.

In Quadrature Modulation. Both lasers can be modulated simultaneously at the same frequency but in phase quadrature. This now requires two PSD's that are given quadrature reference inputs, however if the quadrature reference is not exact there will be cross talk and it is important to ensure that any phase shift is stable with time and temperature. This technique would be a good choice for low frequency modulation, say 25 Hz (half way between 50 Hz and DC).

Two Frequency Modulation. Both diodes can be modulated simultaneously at different frequencies, having two PSD's and diode drivers. Consideration of the choice of modulation frequency depends to some extent on the assumptions made about the amplitude spectrum of the interfering light. If we make the pessimistic assumption that both odd and even harmonics are important and wish to avoid both the 50 and 60 Hz 'problems', two pairs of frequencies are particularly good choices. The first is near 300 Hz, the sixth harmonic of 50 Hz and the fifth harmonic of 60 Hz. So we operate at 275 Hz and 325 Hz then the two

measuring frequencies are 50 Hz apart, the maximum possible from the 50 Hz harmonics and 25 Hz from the 60 Hz fifth, odd harmonic and 35 Hz from the adjacent even harmonics.

7.3 The Next Generation System

7.3.1 Principles of Operation

The two frequency modulation method referred to above was chosen for the digital version of the system using the 275 Hz and 325 Hz modulation frequencies. A switch on the control panel indicates if the reading required is a reference value or a reading. To reduce cost as much as possible during this development stage, the laser headset remained unmodified. In its simplest form the system has two automatic amplifiers, two diode drivers and two PSD's. During a reference reading (dry sample), both diodes are pulsed and both PSD's have the respective output potentials. With the output of the 1.29 μm PSD being monitored, clock pulses are being provided (by a 3rd clock pulse generator) to a digital amplifier (see footnote on page 160) to increase or decrease the gain of the incoming multi-pulse signal. When the potential achieved at the output of the 1.3 PSD reaches 1.25 V the amplifier locks its gain value. A second amplifier monitors the output of the 1.4 PSD and in turn alters the gain of this amplifier so as to match the 1.25 V target voltage. The PSD signals are always positive as the reflected signal is always in phase with the reference signal in this particular system. Throughout this section the 1.3 and 1.4 prefix PSD, amplifier and diode driver to distinguish the control of the signal to and from the 1.29 μm and 1.46 μm laser diodes respectively.

To take a sample reading the system behaves in a similar way, the whole signal is subjected to the first amplifier with the gain level being set by monitoring the 1.3 PSD output signal. However on this occasion the second amplifier, that which increases or decreases the 1.4 signal alone is not allowed to change. If the sample is wetter than the reference (as in most cases), the 1.4 signal will be lower than before and the output reading is a direct measure of 'wetness'. Figure 7.2 shows a schematic of the initial logic circuit and selector switches which control the amplifiers.

A monostable is included in the control circuit to force the system to make its reference signal measurements for at least 3 seconds. This was found by experiment to be the time required for the amplifiers to swing at least half of their full scale, assuming that the amplifiers would not often need to change over the whole range between readings.

The dotted lines in Figure 7.3 show what the various outputs of the logic section control on the amplifiers. The first shaded box in this figure highlights the two stage amplifier that increases the gain of the incoming signal which is the reflected pulsed combination of both

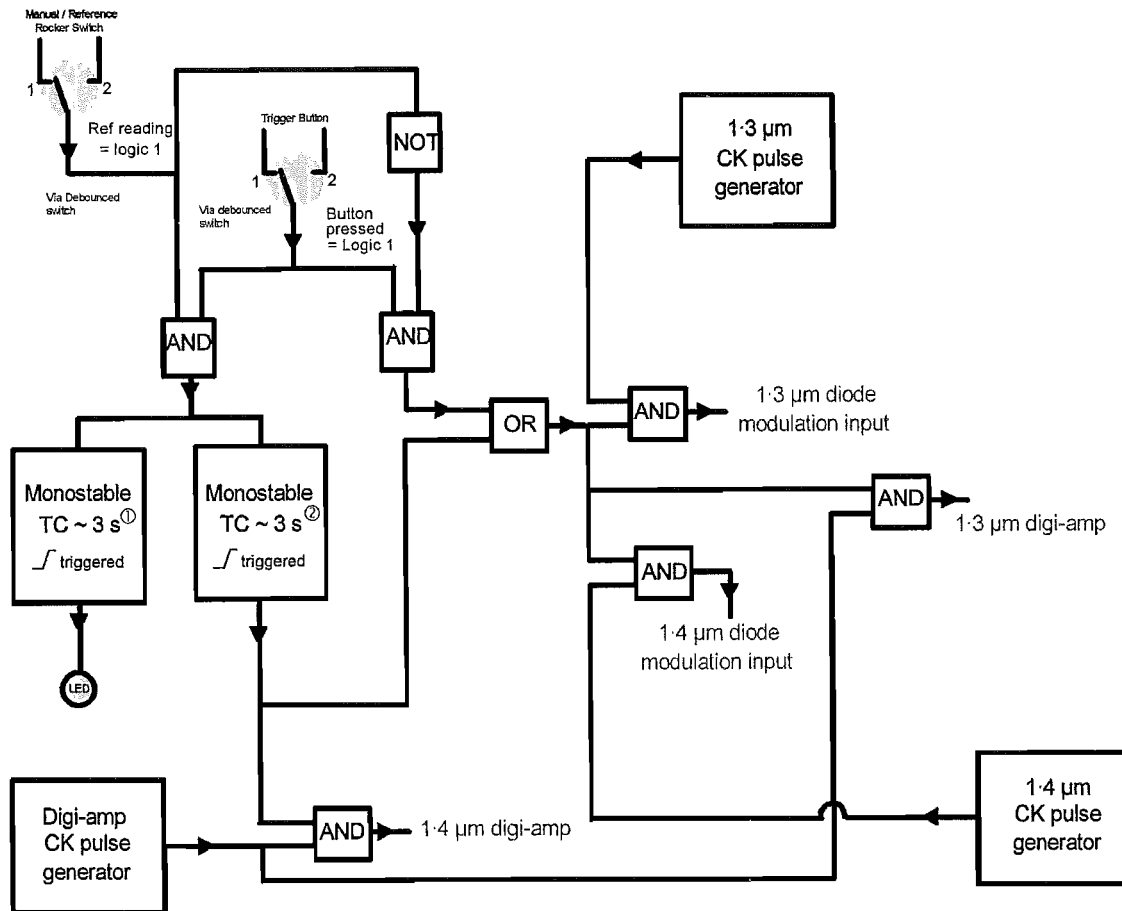


Figure 7.2. A schematic of the logic circuit and respective switch locations to select the amplifier operation of the digital moisture measurement system. {Original in colour}

diodes. The first amplifier has large gain steps and is required to bring the detector signal to within a “window” region, in this case between 0.60 and 1.24 V, the amplifier increases or decreases its gain (count up or down) using the clock pulses to “digital” resistors. The gain range can be 0.5 to 100 times in 100 possible steps rapidly increasing the signal to within a small range of potentials. This window is intentionally set just below the target voltage, so that a “fine” amplifier does not need to have a gain of less than unity or a large gain range. The gain of this amplifier is from 1 to 4 times in 500 steps. This amplifier aims to increase the whole signal, so that the 1.3 PSD output signal is exactly 1.25 V. In practice this is never achieved, the actual value is up to ± 0.005 V away and the resting value purely depends on the state when the reading trigger is released and the clock pulses in turn are stopped. Potentiometers are also shown in the figure (7.3) but these are still in place from testing where many manual overrides are often required during construction.

As previously detailed, if the current reading is to provide a reference for future readings the 1.4 amplifier (follows on from the 1.4 PSD in the figure) has to change the gain applied to the signal from the 1.4 PSD to also match the 1.25 V target. The amplifier has to have a

Note: All resistances shown are in K
All potentials shown in volts

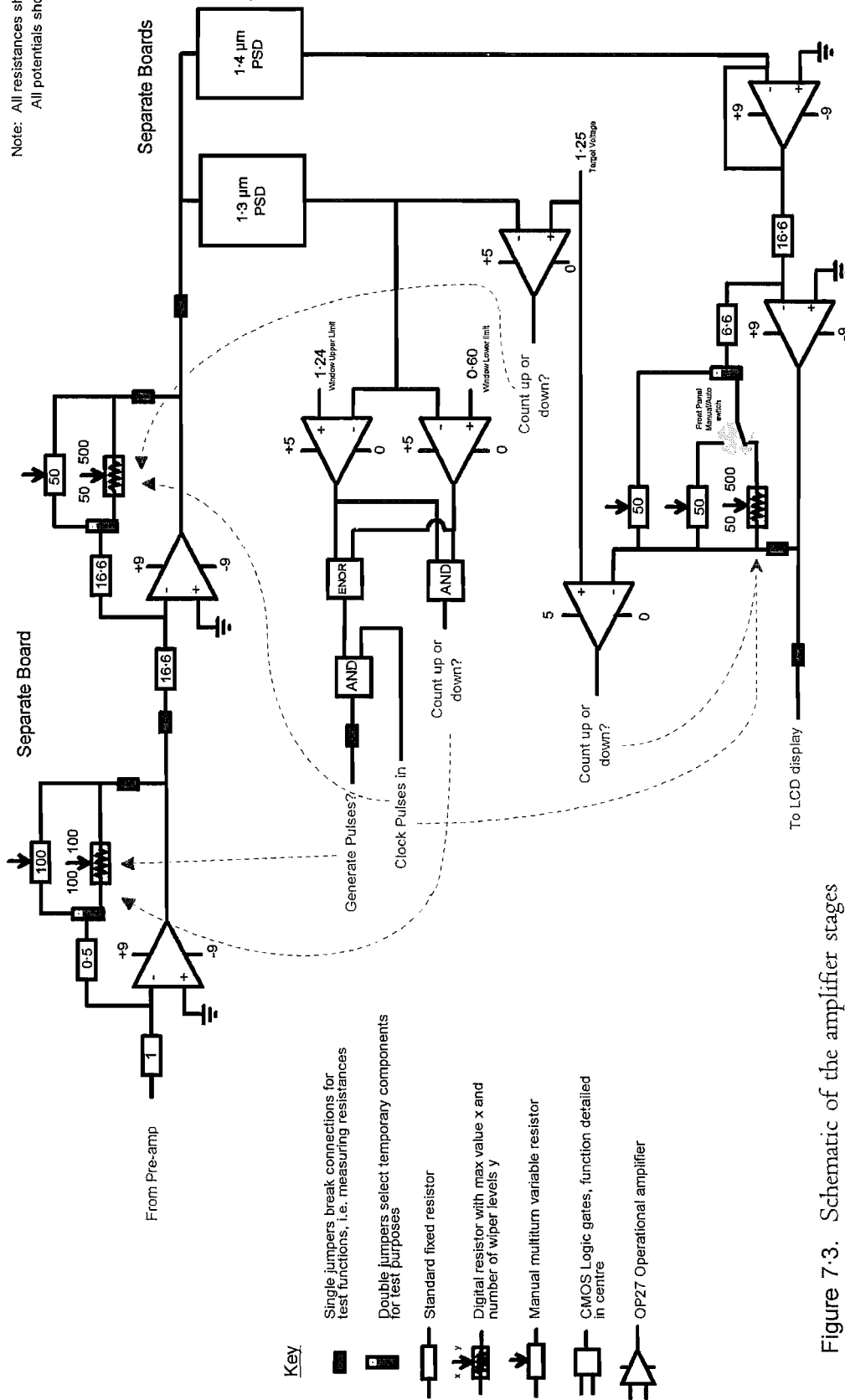


Figure 7-3. Schematic of the amplifier stages showing the logic link between them on the digital moisture measurement system. {Original in colour}

gain range which starts at less than 1 as the value currently being measured might be dryer, so the range is 0.4 to 3.4 in 500 steps. This potential actually registers as 1.000 on the LCD display to show a ratio of 1. For further versatility a manual switch is added to this amplifier which allows the gain of this amplifier to be set via a potentiometer on the control panel. This potentiometer has a mechanical counter which records ten thousand possible referenceable positions directly setting the gain for the ratio of 1.3:1.4 signal intensity. This function allows a range of dry samples to be measured and the gain ratio recorded for each. In the 'field' this means that a reference sample that is dry is not needed. This function was needed during the results presented here as the gain had to be continually changed as all the samples were measured every few hours sequentially. For multiple materials to be measured in this way the automatic reference is not suitable as it only "remembers" the last referenced material.

7.3.2 Model of System Response

The speed by which the whole system can respond is determined by two settings. The amplifiers have to be able to select up to 600 levels of amplification, stepping one unit for each clock pulse. For this to be done quickly, an ideal clock frequency would be in the region of 600 Hz and so allowing full scale movement in only one second. However, each gain step will change the size of the incoming signal and so change the output from the PSD's. The low pass filter of the PSD's restricts the output reaction speed, otherwise by the time the PSD has indicated the new signal level, the clocked amplifier has over shot its target gain value. The slower the PSD time constant the less noisy the output. A trade off then exists between rapid amplifier changes with a low noise usable signal. The system response can be modelled to see how the amplifier clocking frequency effects the overall system performance.

If, fairly arbitrarily, we require the reading to "settle" in one second we require a CR time constant of less than 0.2 seconds (settles to 0.76% in one second). This gives the low pass filter of the of the PSD a 0.8 Hz bandwidth; the effective bandwidth (3 dB) is twice this, or 1.6 Hz. Any potential interfering frequencies, either background light or the other modulated laser, must be kept sufficiently far enough away that they are adequately rejected. For a simple first order filter a decade, or 8 Hz will give 20 dB (a factor of ten in voltage) and 80 Hz would give 40 dB.

The system response was computer modelled to find the resulting amplified output voltage and measure the time needed to reach the desired target value of 1 volt. The basis for modelling this output is shown in Figure 7.4. If the amplifiers clock their gain too fast then the output potential is unstable because the gain changed faster than the PSD's can monitor

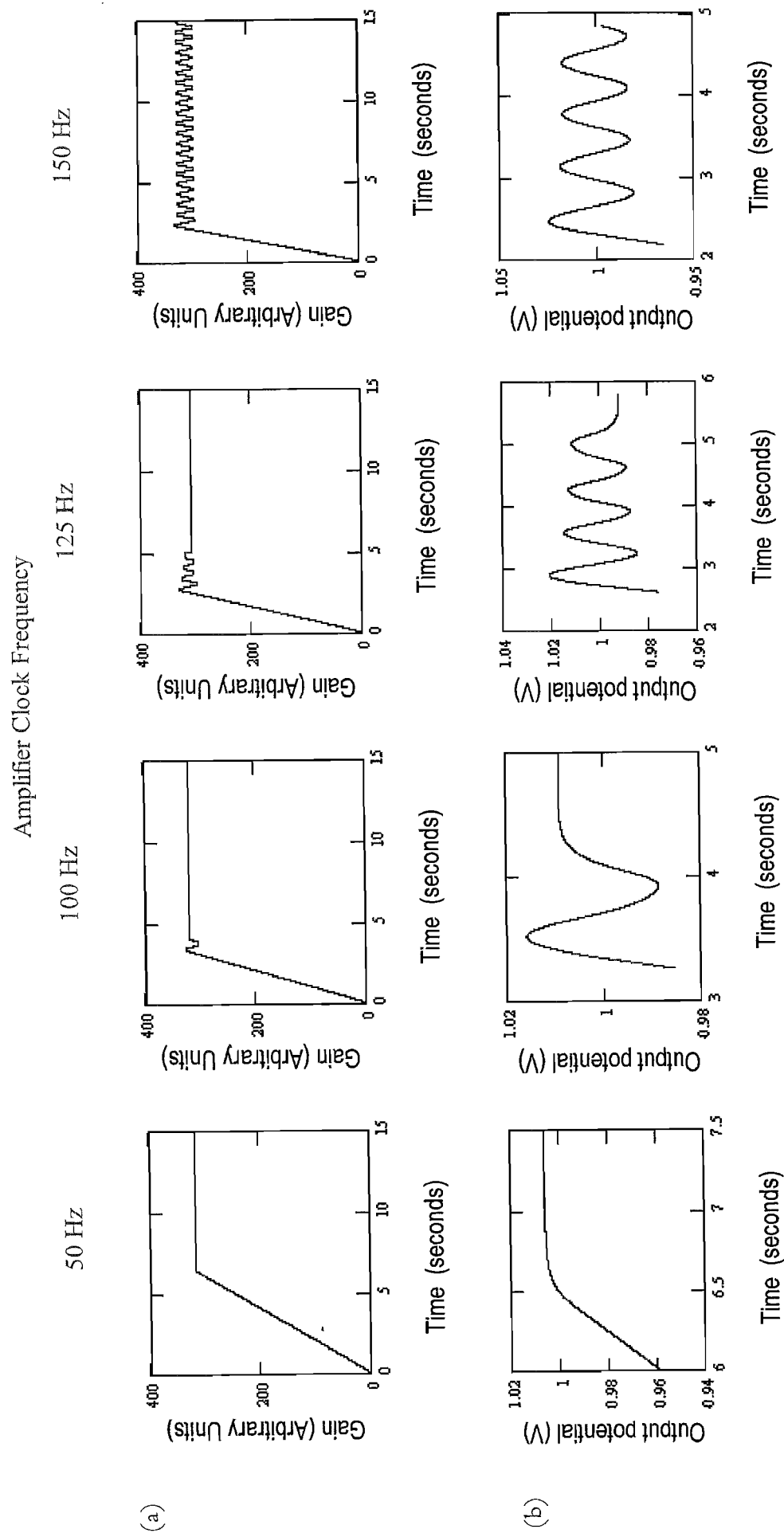


Figure 7-4. (a) The theoretical gain required to reach the target voltage for various amplifier gain clocking speeds, (b) the output voltage after amplification. Four speeds are chosen to show how the output is affected by the amplifier clock rate. {Original in colour}

the new result. Too slow and the instrument takes a long time to settle, increasing the time needed to make dampness measurements and the amount of time that the lasers need to be held in the same position, pointing to the same sample region. The results show how if the amplifiers are clocked at 50 Hz for example, the system response is slow, taking 7 seconds to settle at 1 V, if clocked at 150 Hz and above the output never reaches a stable value. The peak to peak value in amplitude of this oscillation increases with greater amplifier clock rates. In the final system the amplifier clock runs at 100 Hz which in turn could mean that because there are 500 levels it is possible to take 5 seconds to make a reading. However, statistically it is unlikely to have to swing full gain between readings so the time to take a reading will be much reduced. In practice 3 seconds was ample time for the results to be achieved.

7.4 Results and Conclusion

7.4.1 The Experimental Materials

The Table 7.1 below shows the six materials chosen for the comparative analysis of the Protimeter device. The actual materials were placed directly onto a flatbed scanner and in the enlarged 1 cm² surface picture reproduced here, the computer image is recorded as a red, green and blue component for each of the 1000 pixels shown, on a scale of 0 to 255.

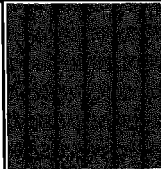
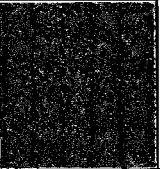
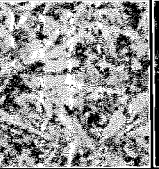
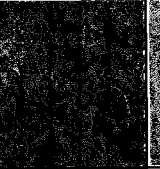
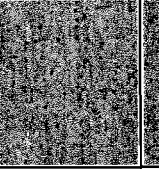
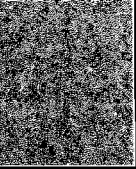


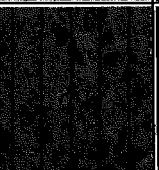
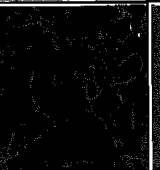
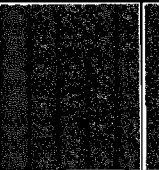

	Brick	Paving Slab	Chipboard	Carpet Tile	Plywood	Plasterboard
Dry						
Average	123, 071, 055	107, 089, 064	176, 152, 137	070, 065, 065	181, 134, 094	146, 128, 108
Wet						
Average	105, 058, 045	079, 064, 044	087, 061, 046	048, 044, 044	148, 091, 053	119, 096, 075
Weight (g)	2414	1648	170	95	53	132
Dimensions H x W x T (mm)	210 x 65 x 89	145 x 124 x 29	150 x 121 x 12	150 x 120 x 8	148 x 120 x 6	151 x 121 x 10
Laser device manual gain setting	25	5	88	15	54	25

Table 7.1. Characteristics of the six materials used to evaluate the feasibility of damp measurement using infrared surface reflections. {Original in colour}

The average value for each colour is indicated in a thin section of the resulting colour below each surface scan. This represents the average colour code for each of the dry starting materials and can be used as a guide to indicate a dry surface. Similarly the “completely wet”² values are also shown for visual comparative purposes only, both the actual scan and the average values of the red, green and blue components.

The dry weights are given in grams and refer to the weight of each sample at the start of the experiment. All of the materials had been stored indoors at room temperature for at least two years prior to this research and hence it is accurate to say that they are “completely dry”, in the sense that they were equilibrated with air at typical indoor UK humidity and had had no exposure to liquid water in that period.

The dimensions of each sample are also given in their dry state with only the plywood and chipboard showing any volume increase once wet, which was more than 50% in the latter case with the original values never being recovered.

7.4.2 Methodology and Results

Figures 7.5 to 7.10 are split into seven subsections (a) to (g). The processes required for the production of each graph is detailed below. In all cases, ‘wet’ means straight from the water bath, ‘dry’ being the starting values before submersion. The times shown on the abscissa represent hours since the removal from the water bath and so represent drying time (the temperature of the laboratory during the 24 hour measurement period was within the range of 16.3 to 20.1 °C):

(a) These are reflection spectra produced with a Perkin Elmer PE2000 FTIR Spectrophotometer. The 6 coloured lines represent spectra from ‘dry’, completely ‘wet’, after 2 hours, after 5½ hours, after 13½ hours and 24 hours. The values of reflection on the ordinate are all normalised to 100% reflection, the absolute figure is thus of little significance. In wavenumbers (cm^{-1}) the laser diodes used in the actual device are at 7752 cm^{-1} ($1.290 \mu\text{m}$) and 6817 cm^{-1} ($1.467 \mu\text{m}$) which represent the peak output of the devices when measured. The important information to extract from this graph is represented by graph (b), i.e. the relative reflectivity values at the two laser wavelengths.

(b) The reflection value for the nominal $1.3 \mu\text{m}$ diode is shown in red, the nominal $1.4 \mu\text{m}$ diode is shown in green and the difference between them shown in blue. This blue line shows the difference in reflection from the sample surface at the two wavelengths as the sample dries. The dotted lines in the respective colour represent the “dry” value which in some cases was never actually reached within the 24 hour period.

² The samples were submerged in a bath of water for 3 days. This ensured that all six were “completely wet”.

(c) This is a copy of the 'wet' and 'dry' surface scans, shown in Table 7·1, reproduced here as a quick aid as to the material whose results are being displayed in the figure and as a reminder as to how the values in graph (g) are produced.

(d) A "Draper Tools" damp tester was used to measure the surface moisture of each sample. It has two prongs which are 29 mm apart and the device produces an audio output proportional to the surface water between these two. In reality the instrument presumably monitors conductivity. A frequency meter is connected to the loud speaker terminals to record the audio frequency being emitted. 0 Hz represents 'dry' and pure water produces a signal of 4·45 kHz although this figure will depend on the conductivity (purity) of the water. This represents the current, traditional method of measuring dampness of building materials. The 'dry' values for all materials tested is 0 Hz.

(e) The laser based digital moisture detector output for the material: In this case, a value of 1 represents a 'dry' sample and a smaller value 'wet'. The wetter the sample surface the smaller the number. The readings were taken in a closed laboratory whose windows are blackened, but with the fluorescent tubes on (room lighting). The lines shown here should be very similar to the blue line in the respective section (b).

(f) These are the weights of the sample as it dries out during the 24 hour period. Once again the dotted line represents the value for the completely 'dry' sample.

(g) Using (c) as the visual representation, this graph represents the average red, green and blue component from the 1000 pixels recorded by placing the samples directly onto a flatbed scanner and recording the image. This was primarily done to attempt to represent when the samples looked visibly dry and see if water could still be detected. This is a practical, quantitative way to describe the samples appearance.

Figures 7·11 through to 7·15 are a display of the same type of experiment with all six materials. This has been done to aid comparison and better assess the performance of the instrument. The figure captions show the data set being displayed. Finally Figure 7·16 has been produced as a combination of all the results for all 6 materials. All data points are graphed after being subtracted from 1. This inverts the results providing a signal for "dry" as 0 and the wetter the sample the closer to 1 the lines become. Figure 7·17 displays the same information in 3 parts, splitting the materials into three major groups, the clay based building materials, the wood type materials (plasterboard fits in here due to the cardboard outer surface) and synthetic materials which in this case is the carpet tile. The ordinate in this figure has 20 grid lines to provide a simple visual guide as to the practicality of having a display consisting of an array of 20 light emitting diodes (LED's) from green, through amber to red, to indicate a level of wetness respectively.

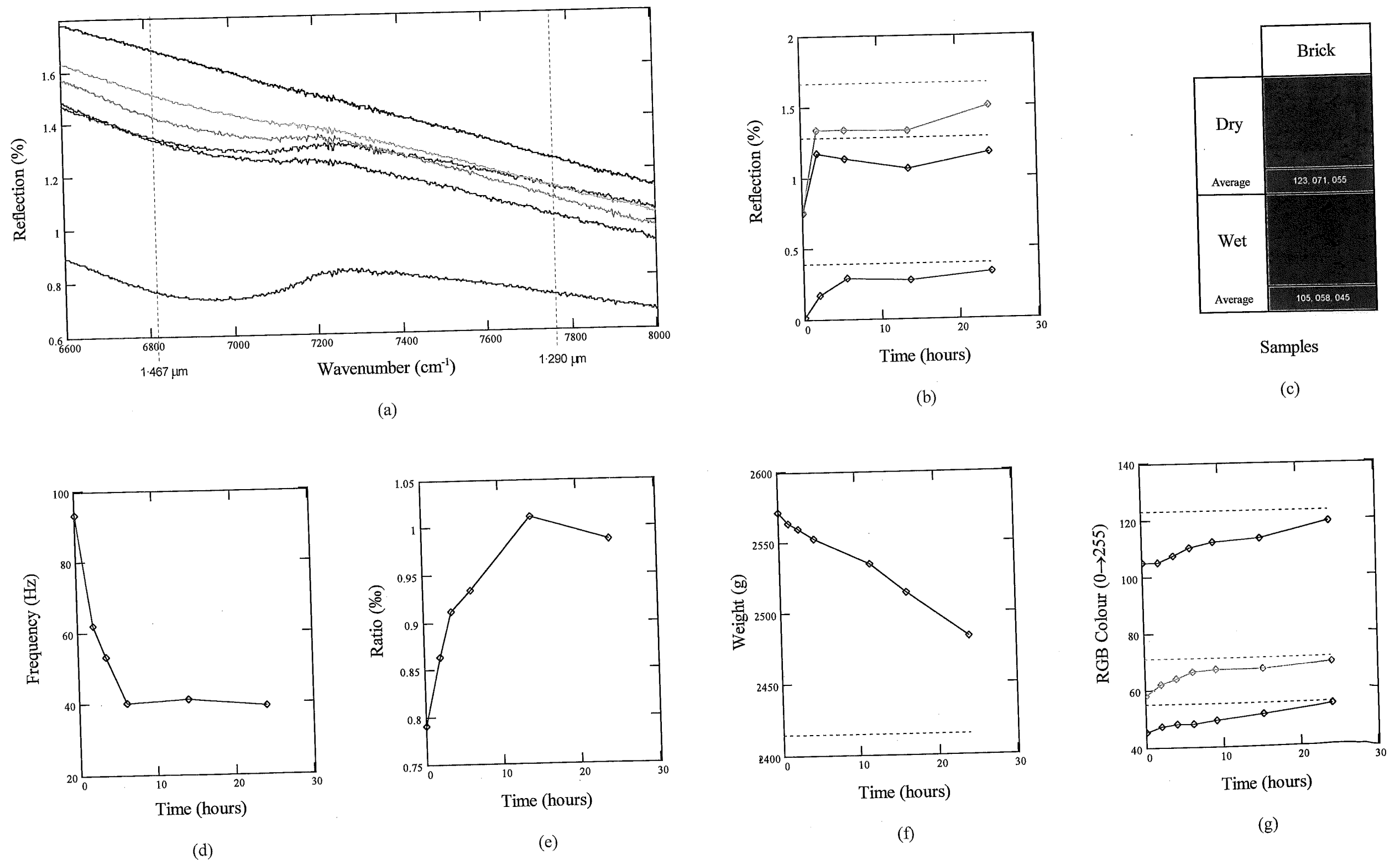


Figure 7.5 The results of moisture measurements for a full size red house brick. (a) FTIR reflection spectra after: (—) 'wet', (—) after 2 hours, (—) after 5½ hours, (—) after 13½ hours, (—) after 24 hours, (—) 'dry', (b) The reflection spectra values at 1.3 μm wet (—) and dry (---), at 1.4 μm wet (—) and dry (---), and the difference between them when wet (—) and completely dry, after 24 hours, (—) 'dry', (c) A small scanned area of sample, 'wet' and 'dry' including the average colour for the region in terms of its Red, Green and Blue constituents, (d) frequency of sound emitted as a measure of 'dampness' from a 2 probe "Draper" damp detector, (e) 'dampness' ratio from prototype laser damp detector, (f) Weight of sample as it dries with time (—) and completely dry, original as new, weight (---), (g) The Red, Green and Blue colour values for all sample scans over test period, see (c) above {Original in colour}.

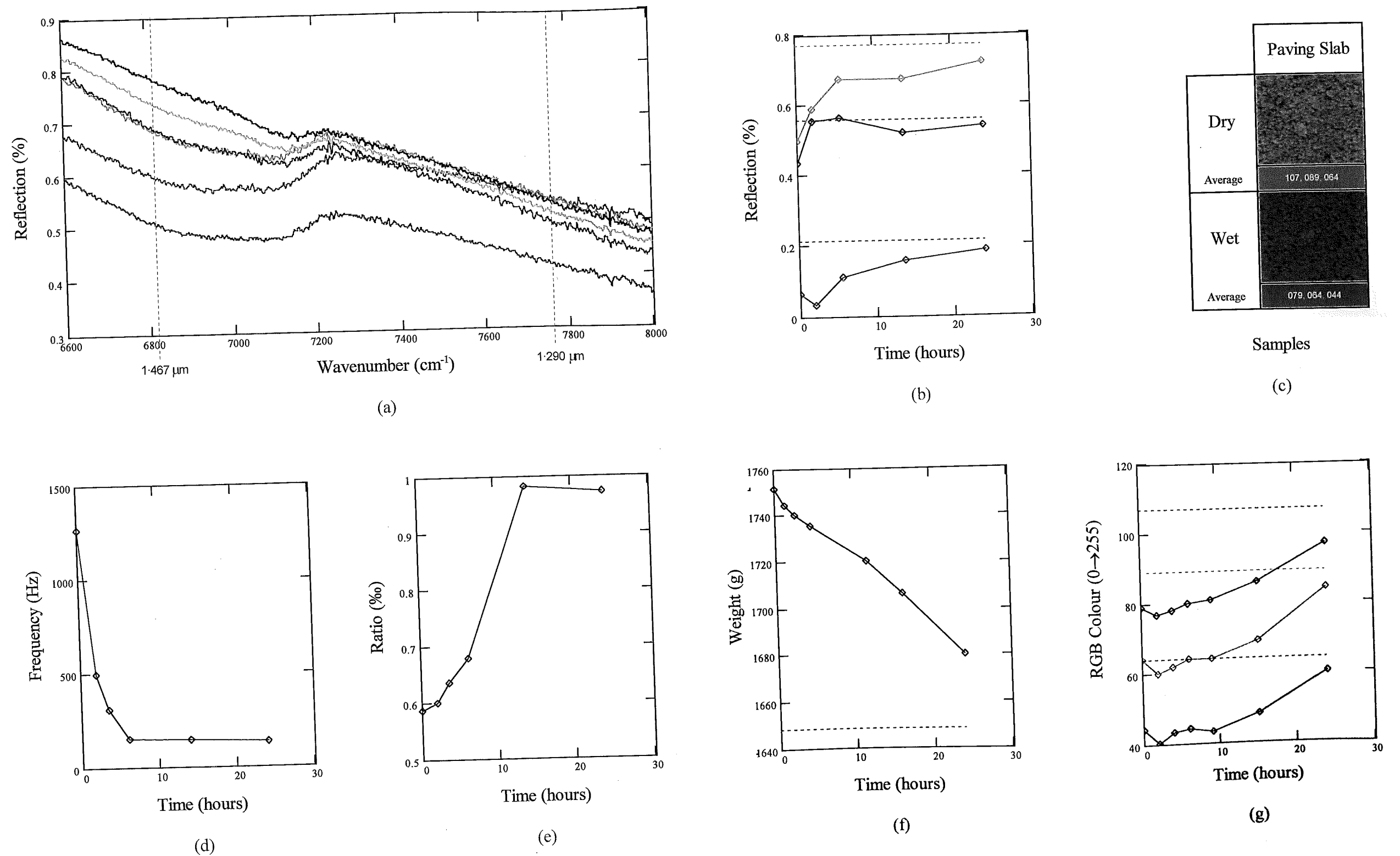


Figure 7.6 The results of moisture measurements for square yellow paving slab. (a) FTIR reflection spectra after: (—) 'wet', (—) after 2 hours, (—) after 5½ hours, (—) after 13½ hours, (—) after 24 hours, (—) 'dry', (b) The reflection spectra values at 1.3 μm wet (—) and dry (---), at 1.4 μm wet (—) and dry (---), and the difference between them when wet (—) and completely dry, after 24 hours, (—) 'dry', (c) A small scanned area of sample, 'wet' and 'dry' including the average colour for the region in terms of its Red, Green and Blue constituents, (d) frequency of sound original as new, weight (---), (e) 'dampness' ratio from prototype laser damp detector, (f) Weight of sample as it dries with time (—) and completely dry, original as new, weight (---), (g) The Red, Green and Blue colour values for all sample scans over test period, see (c) above {Original in colour}.

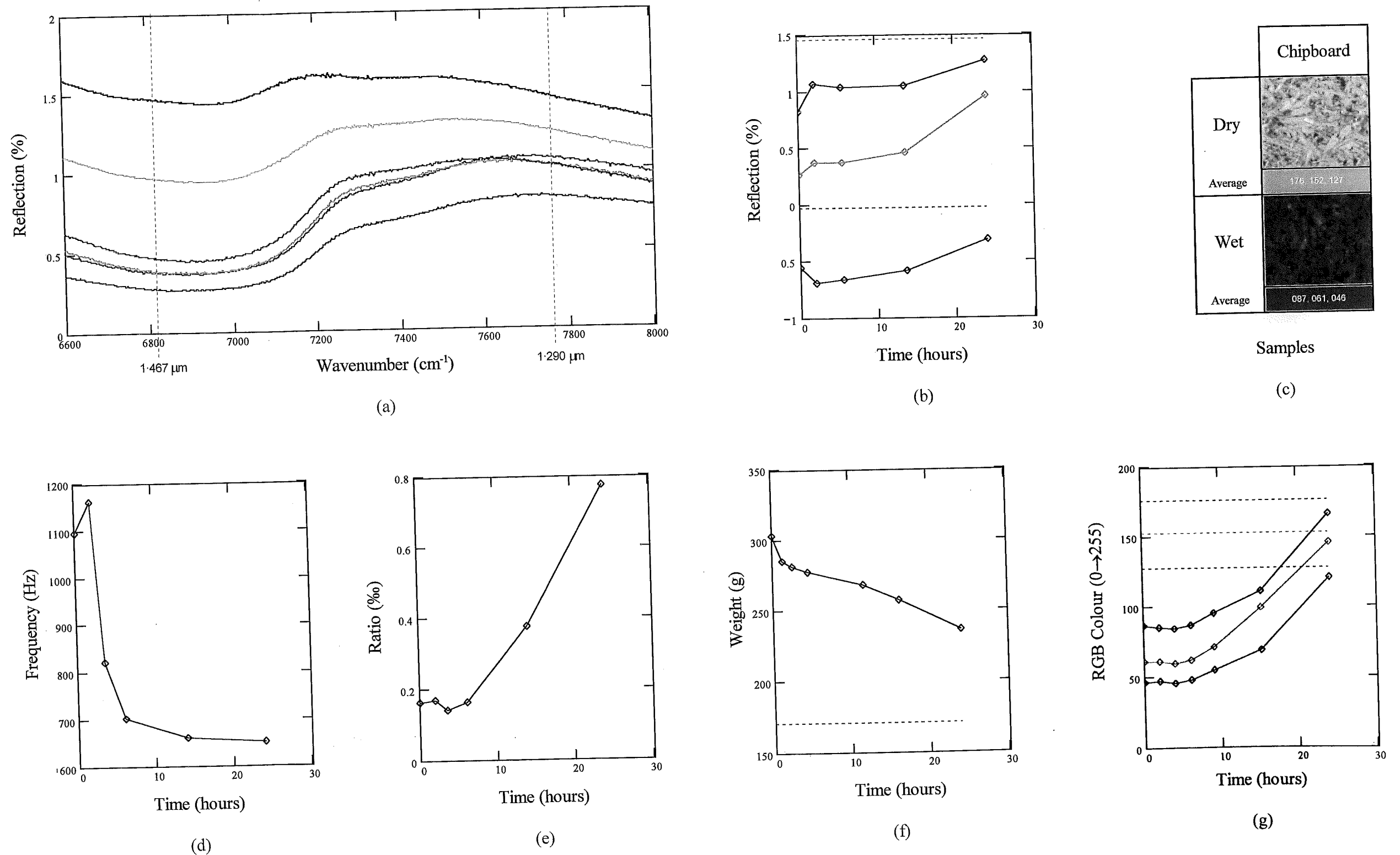


Figure 7-7 The results of moisture measurements for 10 mm thick medium density chipboard. (a) FTIR reflection spectra after: (—) 'wet', (—) after 2 hours, (—) after 5½ hours, (—) after 13½ hours, (—) after 24 hours, (—) 'dry', (b) The reflection spectra values at 1.3 μm wet (—) and dry (---), at 1.4 μm wet (—) and dry (---), and the difference between them when wet (—) and dry (---), (c) A small scanned area of sample, 'wet' and 'dry' including the average colour for the region in terms of its Red, Green and Blue constituents, (d) completely dry, original as new, weight (---), (e) 'dampness' ratio from prototype laser damp detector, (f) Weight of sample as it dries with time (—) and completely dry, original as new, weight (---), (g) The Red, Green and Blue colour values for all sample scans over test period, see (c) above {Original in colour}.

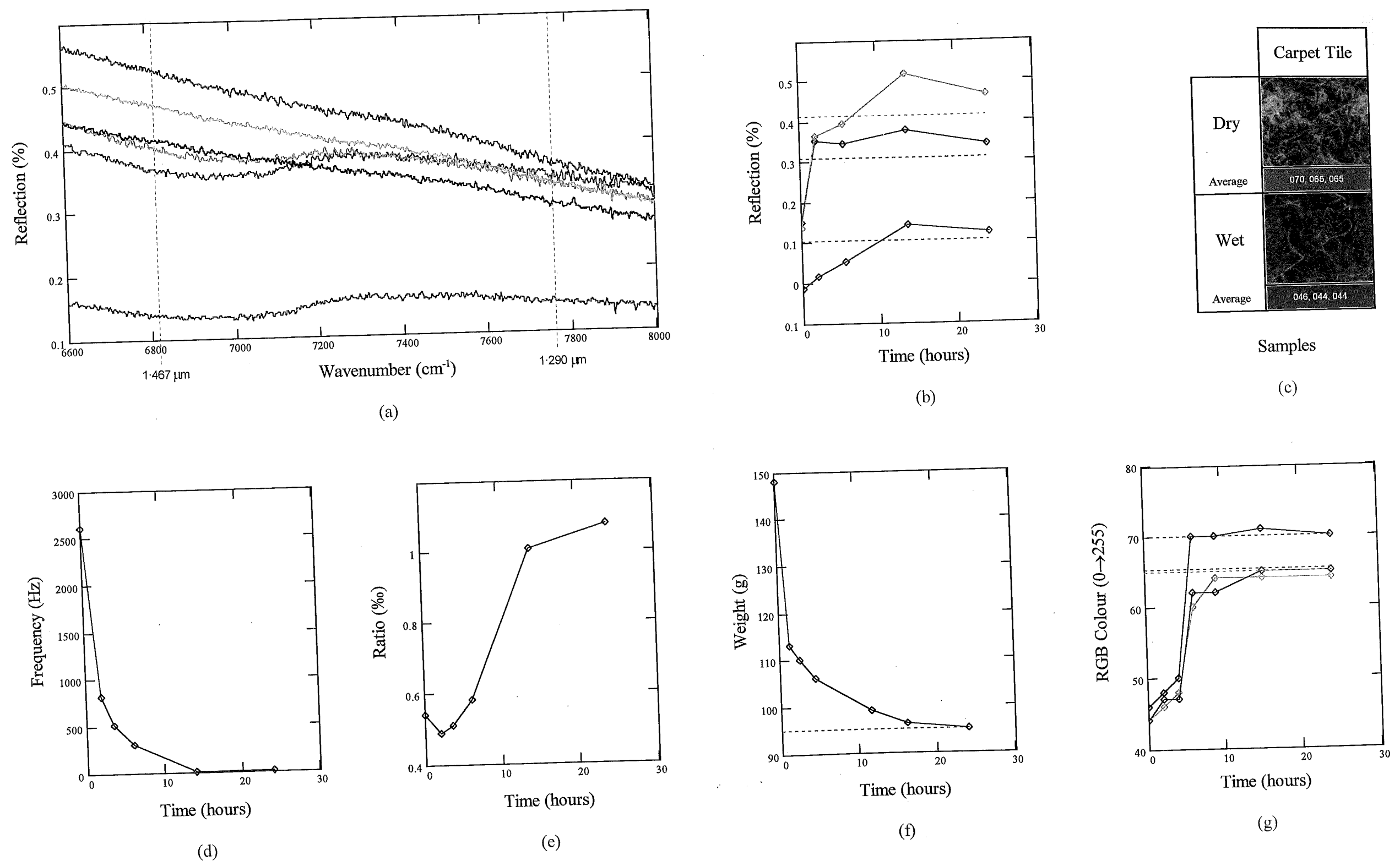
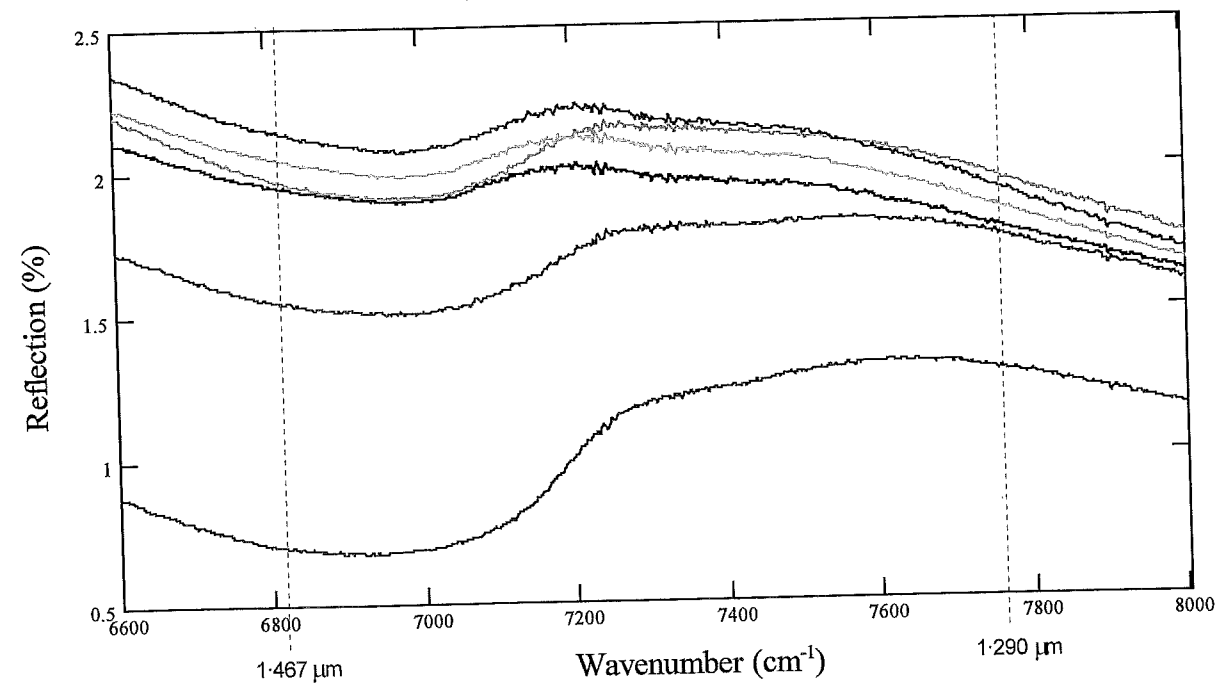
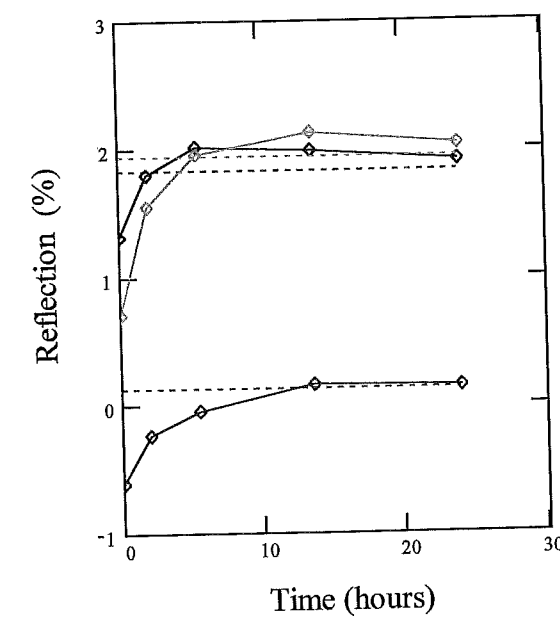


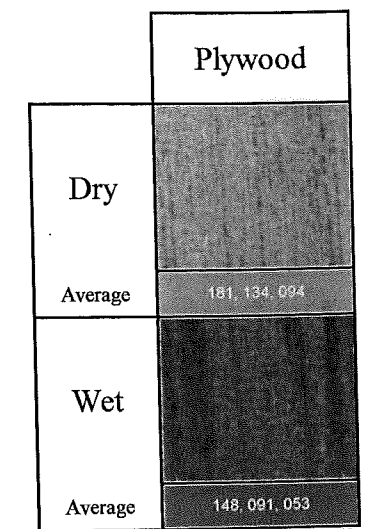
Figure 7.8 The results of moisture measurements for an interior dark grey carpet tile. (a) FTIR reflection spectra after: (—) 'wet', (—) after 2 hours, (—) after 5½ hours, (—) after 13½ hours, (—) after 24 hours, (—) 'dry', (b) The reflection spectra values at 1.3 μm wet (—) and dry (---), at 1.4 μm wet (—) and dry (---), and the difference between them when wet (—) and completely dry, original as new, weight (---), (c) A small scanned area of sample, 'wet' and 'dry' including the average colour for the region in terms of its Red, Green and Blue constituents, (d) frequency of sound emitted as a measure of 'dampness' from a 2 probe "Draper" damp detector, (e) 'dampness' ratio from prototype laser damp detector, (f) Weight of sample as it dries with time (—) and completely dry, original as new, weight (---), (g) The Red, Green and Blue colour values for all sample scans over test period, see (c) above. {Original in colour}.



(a)

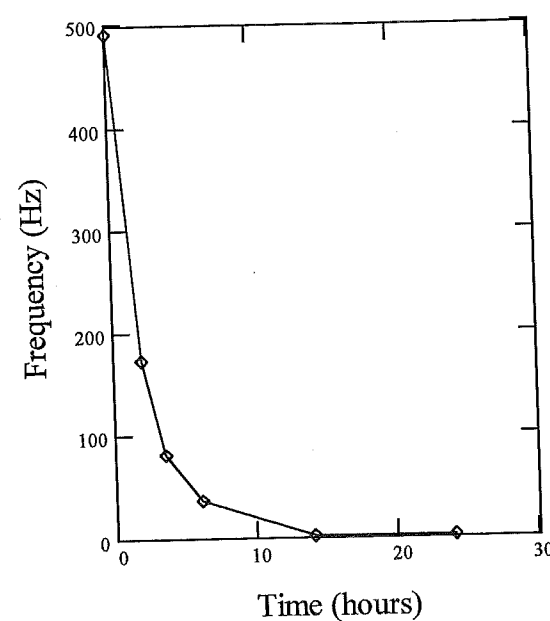


(b)

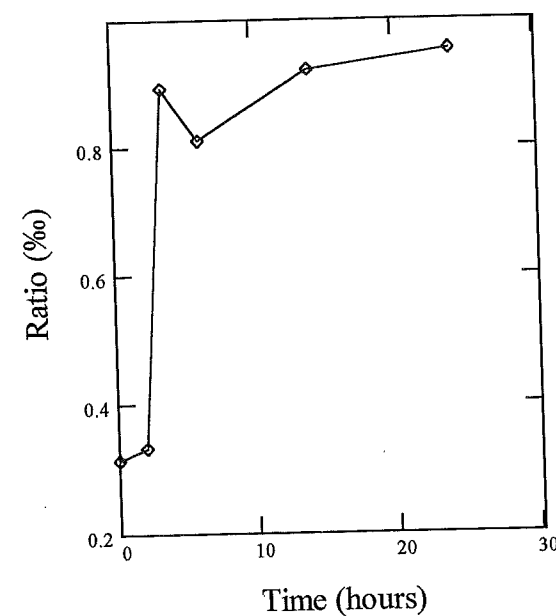


Samples

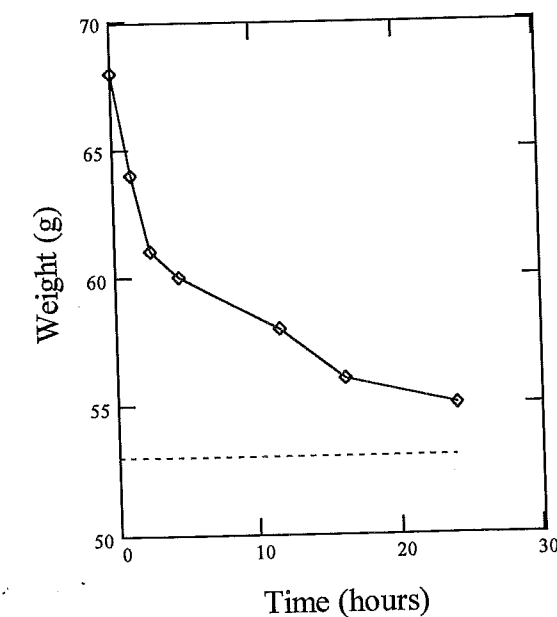
(c)



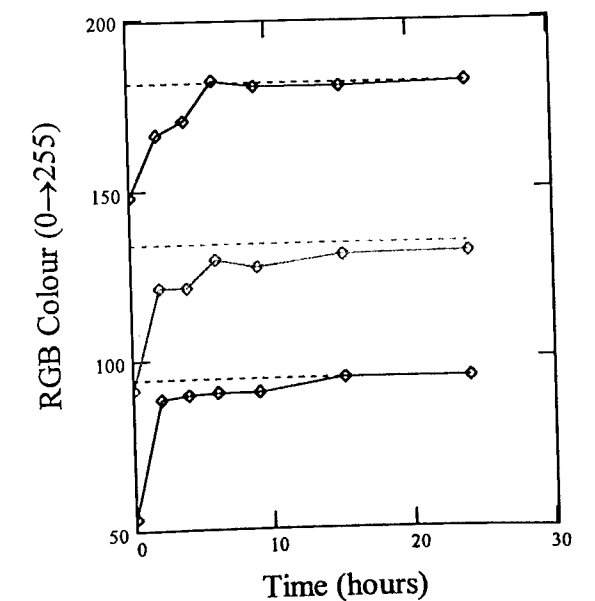
(d)



(e)



(f)



(g)

Figure 7.9 The results of moisture measurements for 6 mm thick plywood. (a) FTIR reflection spectra after: (—) 'wet', (—) after 2 hours, (—) after 5½ hours, (—) after 13½ hours, (---) after 24 hours, (—) 'dry', (b) The reflection spectra values at 1.3 μm wet (—) and dry (---), at 1.4 μm wet (—) and dry (---), and the difference between them when wet (—) and completely dry, 24 hours, (c) A small scanned area of sample, 'wet' and 'dry' including the average colour for the region in terms of its Red, Green and Blue constituents, (d) frequency of sound original as new, weight (---), (e) 'dampness' ratio from prototype laser damp detector, (f) Weight of sample as it dries with time (—) and completely dry, original as new, weight (---), (g) The Red, Green and Blue colour values for all sample scans over test period, see (c) above {Original in colour}.

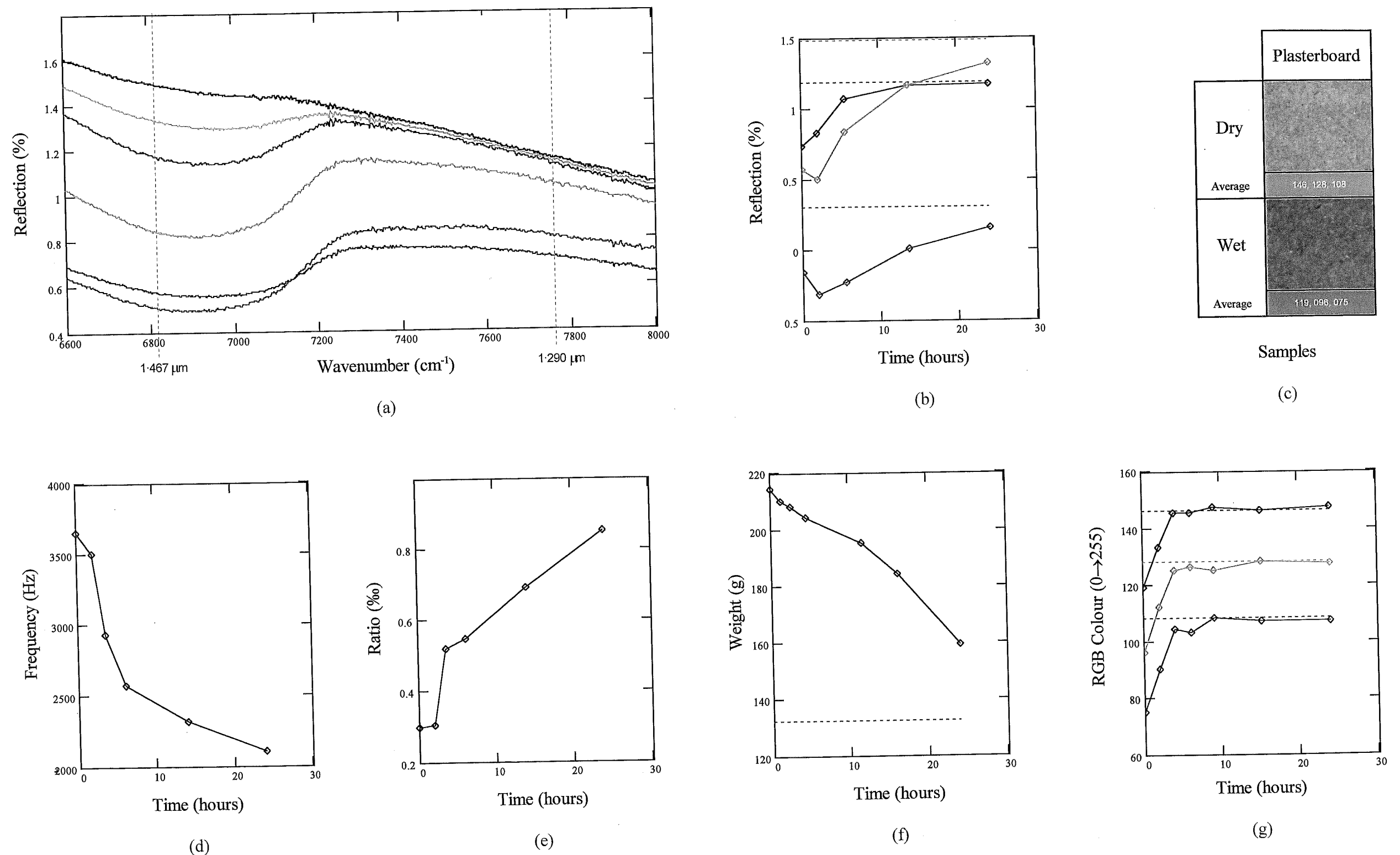


Figure 7.10 The results of moisture measurements for 10 mm thick plasterboard. (a) FTIR reflection spectra after: (—) 'wet', (—) after 2 hours, (—) after 5½ hours, (—) after 13½ hours, (—) after 24 hours, (—) 'dry', (b) The reflection spectra values at 1.3 μm wet (—) and dry (---), at 1.4 μm wet (—) and dry (---), and the difference between them when wet (—) and completely dry (---) after 24 hours, (c) A small scanned area of sample, 'wet' and 'dry' including the average colour for the region in terms of its Red, Green and Blue constituents, (d) frequency of dry, original as new, weight (---), (e) 'dampness' ratio from prototype laser damp detector, (f) Weight of sample as it dries with time (—) and completely dry, original as new, weight (---), (g) The Red, Green and Blue colour values for all sample scans over test period, see (c) above {Original in colour}.

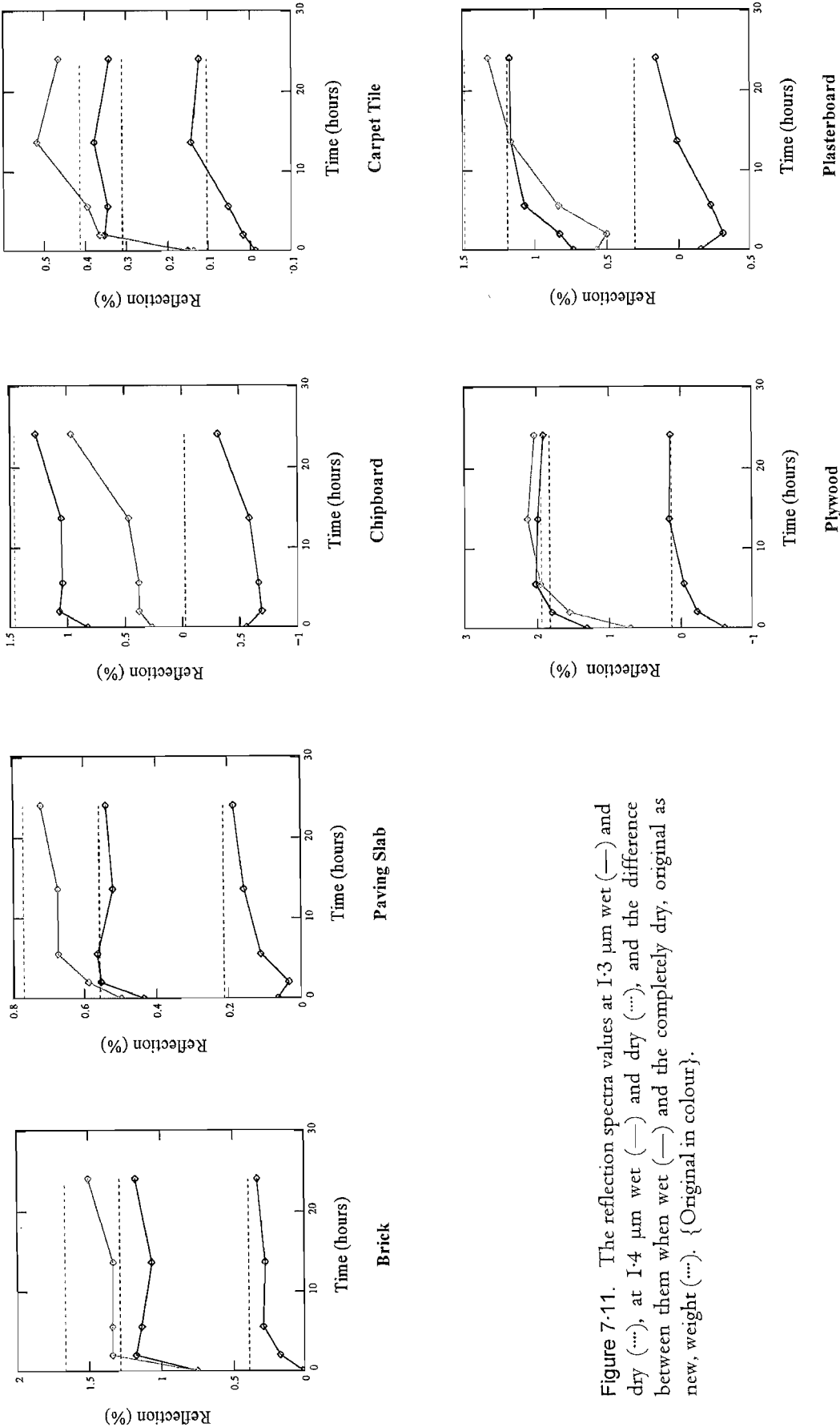


Figure 7.11. The reflection spectra values at 1.3 μm wet (—) and dry (---), at 1.4 μm wet (—) and dry (---), and the difference between them when wet (—) and the completely dry, original as new, wet (---). {Original in colour}.

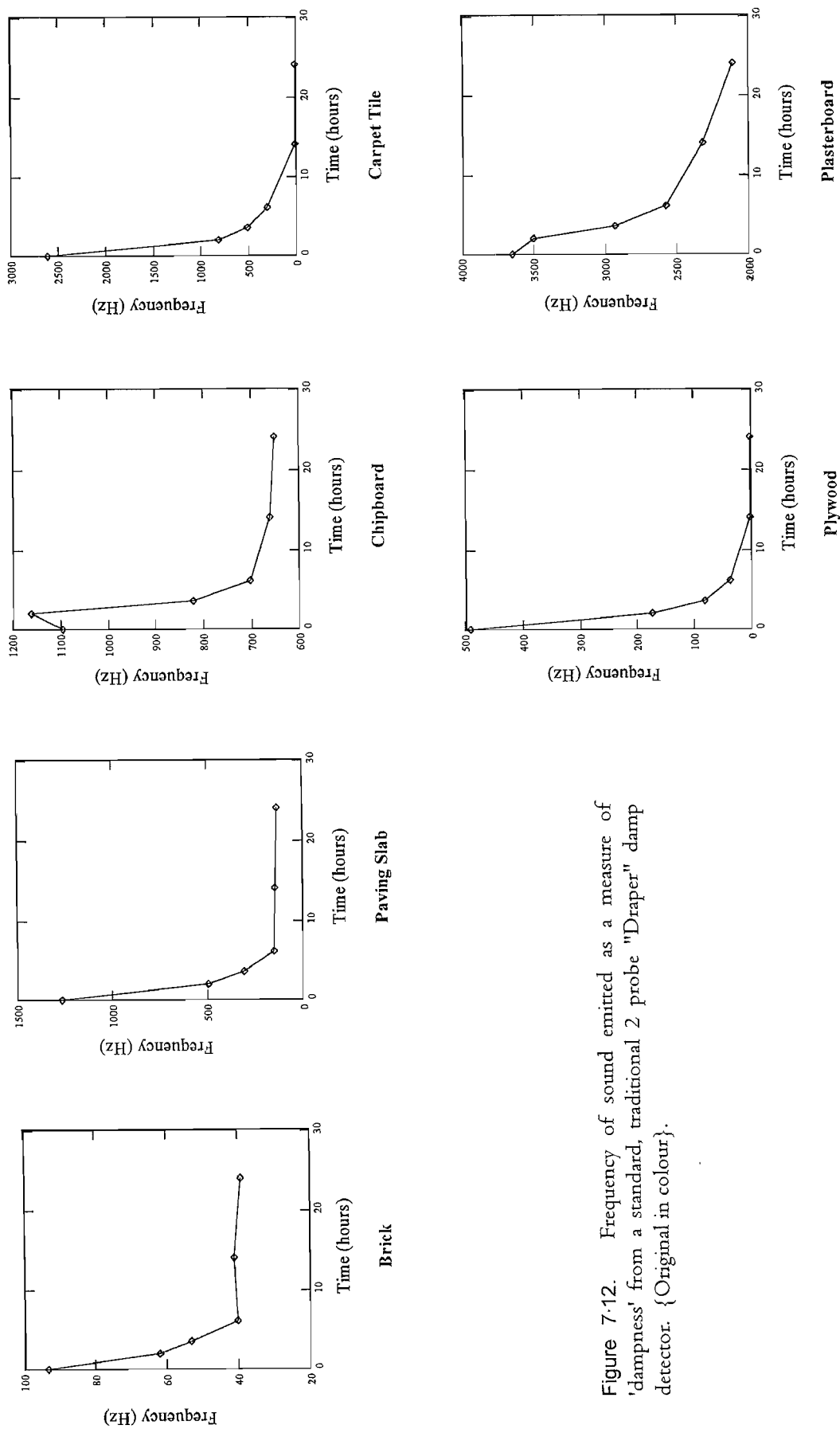


Figure 7-12. Frequency of sound emitted as a measure of 'dampness' from a standard, traditional 2 probe "Draper" damp detector. {Original in colour}.

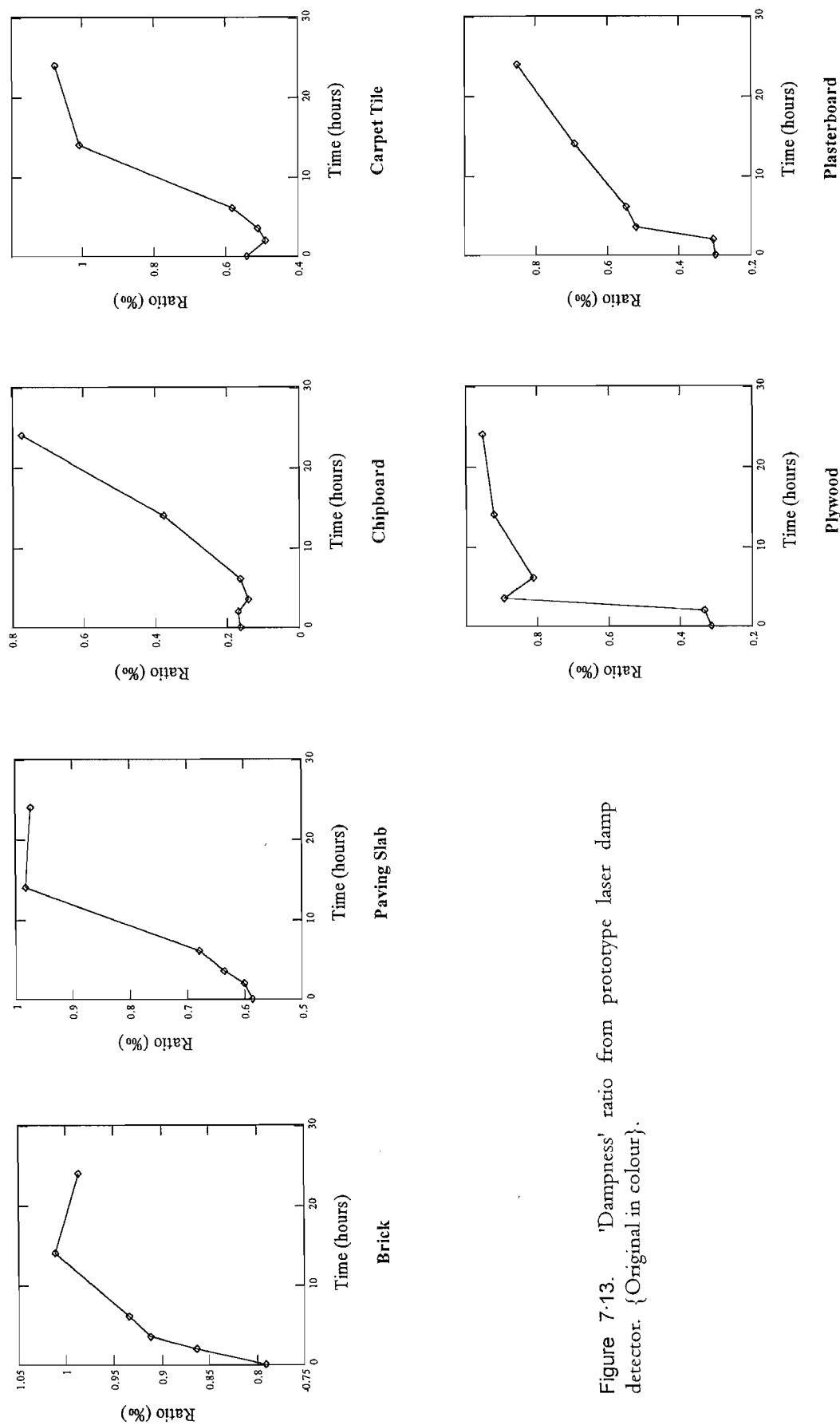


Figure 7.13. 'Dampness' ratio from prototype laser damp detector. {Original in colour}.

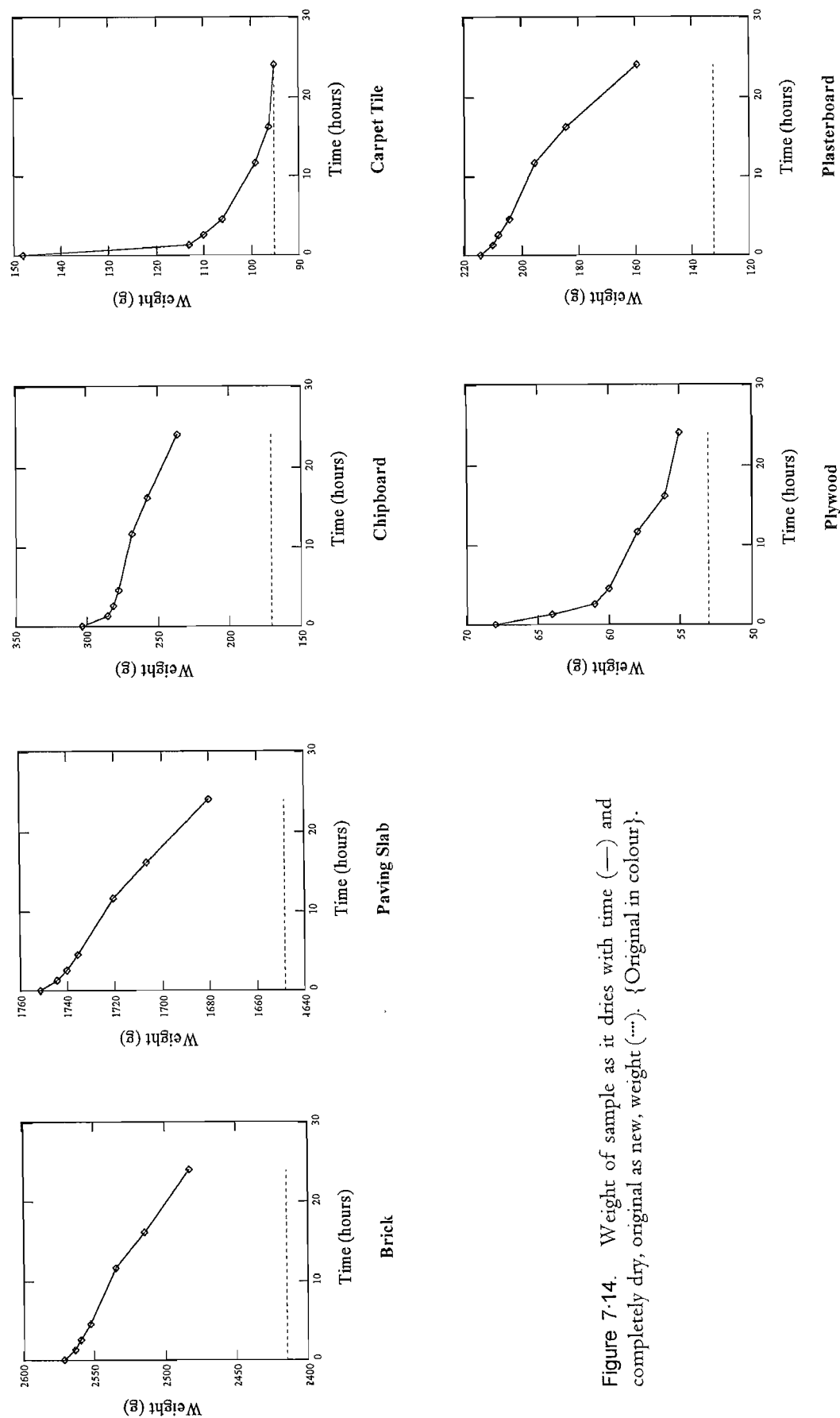


Figure 7-14. Weight of sample as it dries with time (—) and completely dry, original as new, weight (---). {Original in colour}.

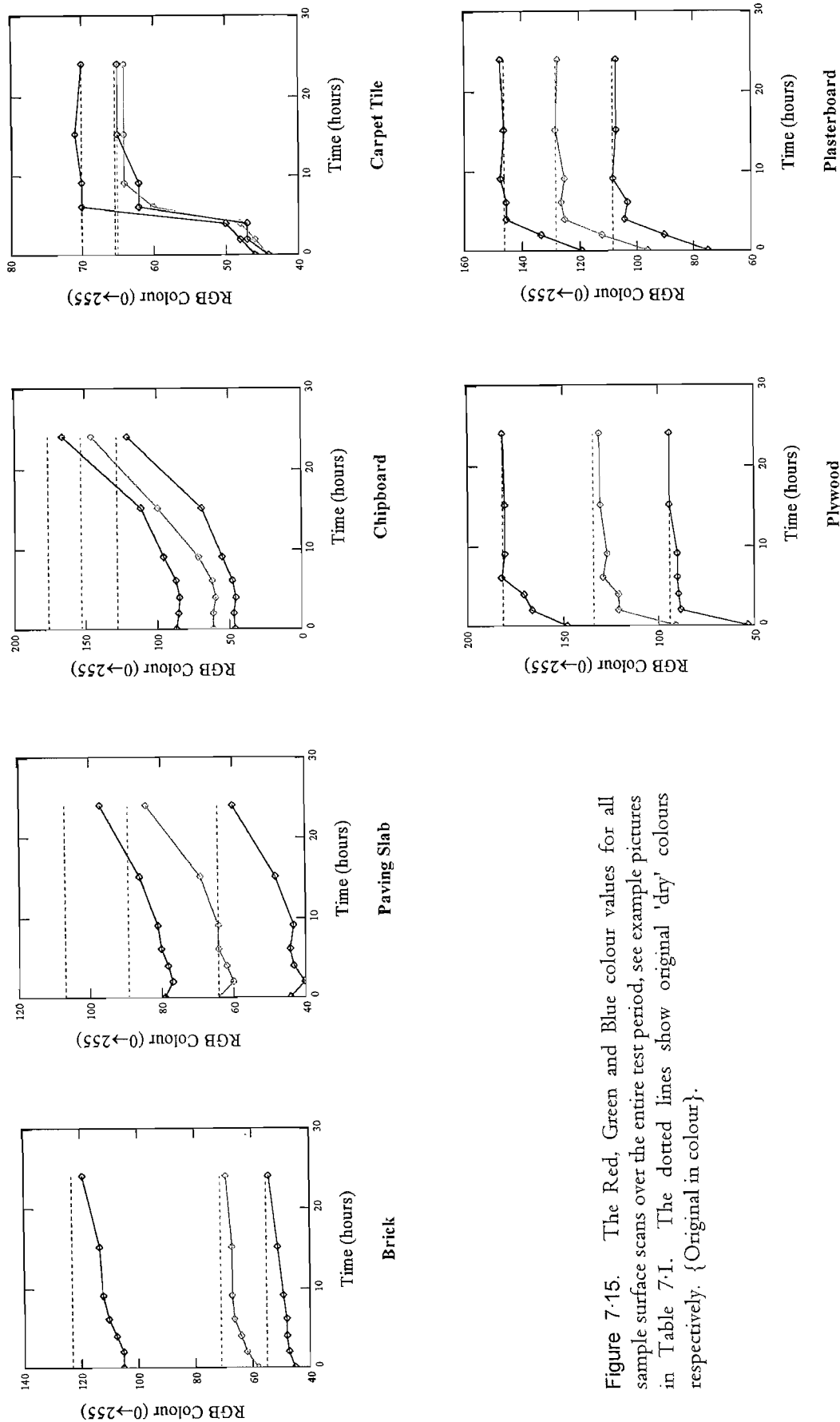


Figure 7.15. The Red, Green and Blue colour values for all sample surface scans over the entire test period, see example pictures in Table 7.1. The dotted lines show original 'dry' colours respectively. {Original in colour}.

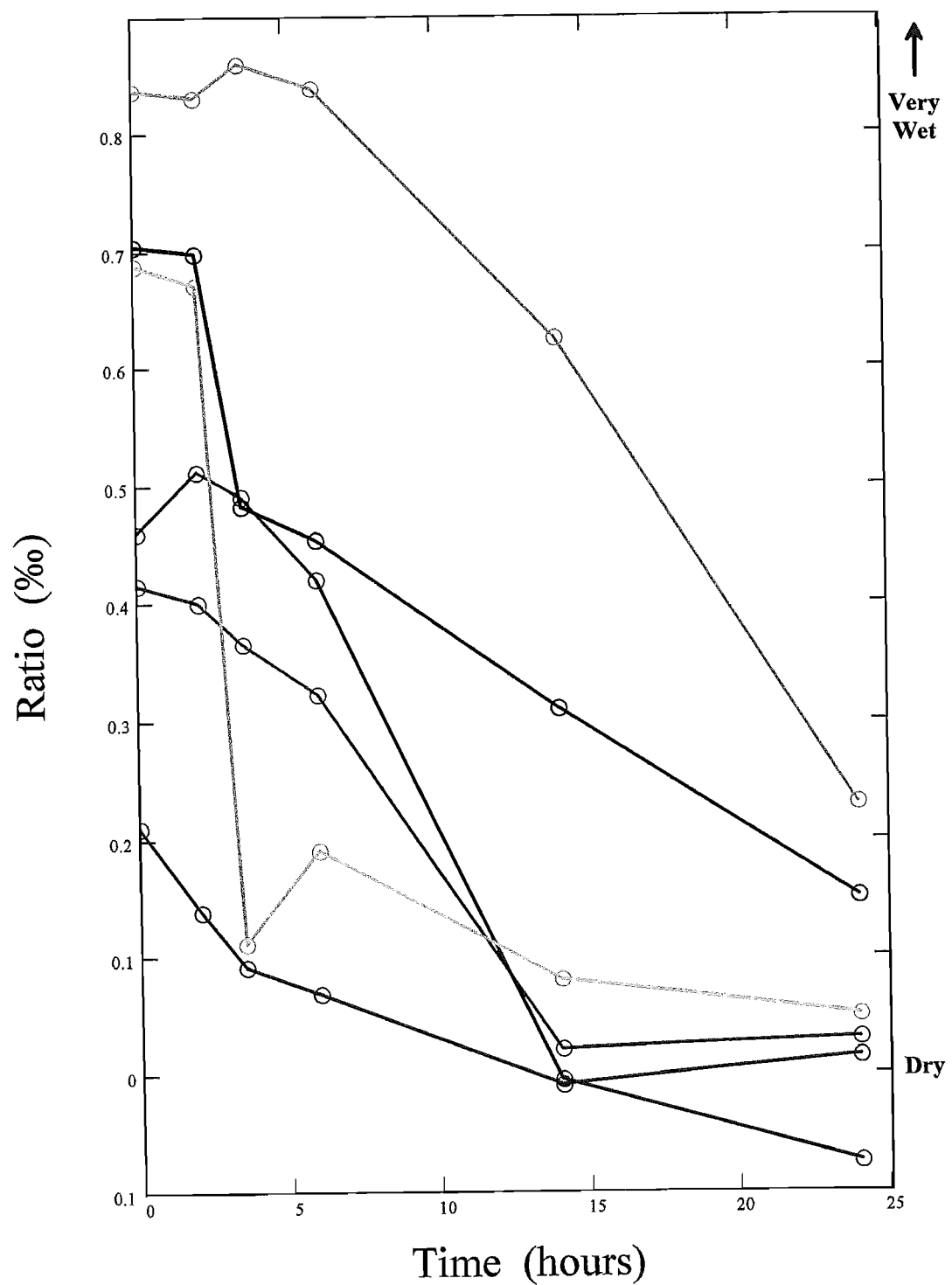


Figure 7-16. 'Dampness' ratio from "Protimeter" prototype laser damp detector, (—) brick, (—) paving slab, (—) chipboard, (—) carpet tile, (—) Plywood and (—) plasterboard.

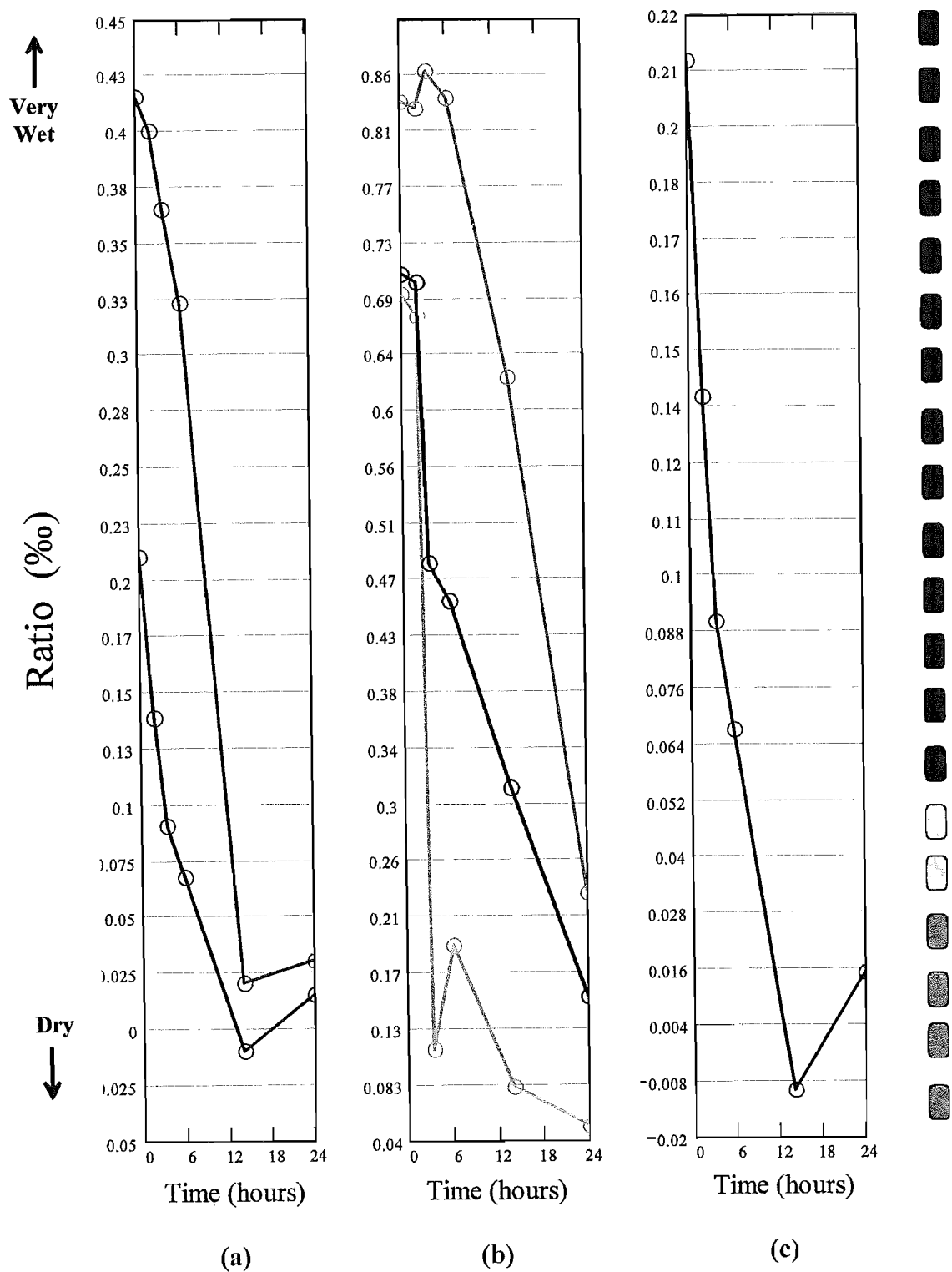


Figure 7-17. 'Dampness' ratio from "Protimeter" prototype laser damp detector; (—) brick, (—) paving slab, (—) chipboard, (—) carpet tile, (—) Plywood and (—) plasterboard. 20 divisions have been marked along ordinate to show accuracy of a 20 bar light emitting diode array as output signal. (a) clay based, (b) woods and (c) synthetic materials.

All of the samples were tested in the order of their appearance in Table 7.1, i.e. Brick was always measured first and plywood last in all experiments. For the infrared spectra results it took up to twenty minutes to take a set of data points for the six materials, meaning that brick values are being measured ten minutes before the time on the graph and plywood up to ten minutes later. All other experiments were completed within five minutes per data point set.

7.4.3 Analysis of Data

For all materials the difference in the reflection spectra at the respective diode wavelengths, the blue lines of Figures 7.5 to 7.10 (b), should be an identical shape to the laser device results, (e) in the same figures. Other than the occasional anomaly, this is the case for all 6 materials. Where the first point appears slightly higher than expected, it is most probably due to surface water being present after the initial removal from the water bath.

For the weight data, Figure 7.5 to 7.10 (f), it can be seen that the loss of water from all but one sample is linear. Only the carpet tile actually lost all of its acquired water within the 24 hour period. This is more likely due to it being a synthetic material which would not absorb water but merely trap it at the surface until it all evaporated. The plywood, being the thinnest of the materials almost became dry.

It should be noted that relative weight changes are affected by the 'storage' of internal water which the laser device will not detect. A relatively small change in weight may reflect the loss of surface water which will produce a disproportionately large decrease in apparent 'dampness'. The qualitative measurement of surface colour gives an indication of these more rapid, superficial changes. The electrical meter is probably intermediate - its reading will tend to be dominated by the conductivity near the probe tips, but some what affected by deeper moisture in the current path between the probes.

The frequency measurement provided by the two probe damp meter, Figure 7.5 to 7.10 (d), shows a very similar, but inverted, profile to that of the laser device results (Figure 7.5 to 7.10 (e)). As above, it is the thinnest material and the non-absorbing synthetic material which are the only two to show complete dryness. Comparing the two sets of data, (d) and (e), across the whole range the frequency measurements seem to be more sensitive for the first few hours with the laser device results grouped together indicating "wet", as the drying process continues; it gives a more accurate midrange set of values, before they both settle again towards the end. This is an advantage for this device as its maximum sensitivity falls in the region where real results, from a true building environment, are most likely to be. Few building materials are going to be as wet as the samples were at the beginning of the experimental runs.

7.4.4 Future Requirements and Considerations

There are number of issues connected with the practical realisation of the remote wet/dry indicator. Improvement of its performance under high background light conditions is of particular concern. A further optical filter is one addition which could improve this. The objective of the filter is to pass the 1.29 μm and 1.46 μm signals with minimum loss, whilst blocking as much stray light as possible. Since the InGaAs detector does not respond beyond 1.7 μm stray light at longer wavelengths is of no concern.

Stray light has two effects. If it overloads the input pre-amplifier, the device ceases to work at all. If we reduce the pre-amplifier gain to reduce the chance of overload its dynamic range and signal to noise ratio all suffer. However even if there is no overload the continuous background current caused by the sunlight etc. induces shot noise in the detector again worsening the signal to noise ratio. This effect is fundamental and can only be reduced by preventing stray light hitting the detector.

Stray light overload can be improved with the reduction in the stray light level, but the shot noise only reduces as the square root of the stray light level. Note that whilst the desired signals are modulated, which distinguishes them from the continuous (sunlight) or 50 Hz modulated and overtones of this in the (most artificial sources) background. This fact does not eliminate the saturation and shot noise problems. Optical filtering reduces all stray light problems, and is the best solution, if it is practical.

Filters can be categorised into four designs, listed here in order of increasing complexity: Long pass filter closer to 1.29 μm than the existing silicon filter; a short pass cutting off just past 1.47 μm ; "bracket both wavelengths" i.e. high and low pass filters transmitting in the range 1.25 to 1.50 μm ; a double narrow pass filter which is similar to the previous "bracket" with an additional "notch" in the spectrum between 1.29 and 1.47 μm . The single range cut-off filters would give modest reductions in stray light, hardly worth while on their own, but could be part of a multilayer design. If the "bracketing" filter is a high and low pass just above and below the two laser wavelengths, as close as tolerances and filter cut-off slopes permit. It can be accomplished with a substrate and multilayer combination. The "notch" filter is the best possible option, but if we make it too narrow, the diode laser tolerances and temperature drifts become a concern.

Electronic techniques can be considered as a method for reducing background light effects. There are four problems associated with background light: shot noise from its DC component is unavoidable electronically, only optical filtering can help; saturation from mains harmonic AC components; saturation from its DC component and interference to the

required signal from harmonics of mains frequencies 'breaking through' the PSD. These can all be considered for improved performance of a production device

The issue of lens and detector choice are tightly coupled. At first sight only the lens aperture would appear to matter, since that is what collects the returned scattered light; however the spot size scales with the focal length and smaller spots means smaller and less noisy (also cheaper but harder to align) detectors. However it is important to realise that these assumptions only apply in the absence of significant aberrations. Provided the situation remains dominated by pre-amplifier noise and not by detector noise, then making the detector smaller no longer reduces the noise. Smaller detectors have higher shunt resistance and eventually the transimpedance amplifier becomes the limiting factor and not the detector.

The alignment tolerances of the lasers and the detector are set by the need to keep the target area illuminated by the 1.3 and 1.4 μm lasers within the field of view of the detector and the need to keep the two differing wavelength spots close enough together that they measure essentially the same region. Additionally the red aiming laser needs to give a meaningful indication of where the measurement is being made. The lasers are initially about 4 cm apart and a reasonable alignment specification would be that the spots do not move more than 4 cm over a 10 m range. This implies bore sighting the lasers to each other to within 4 mRad or $0.23^\circ 14'$ of arc. This is an easy machining tolerance for alignment by V grooves for example.

A related issue is that of lateral offset. If the lasers are accurately bore sighted and collimated, the measurement spot is off-axis by the axial offset of the lasers to the detector axis which we denote O . With focal length f and range R the image is offset to a good approximation by a distance,

$$\text{offset} = \frac{f \cdot O}{R} \dots\dots\dots (7.1)$$

The problem is worse at close ranges; if we take $f = 50$ mm, $O = 30$ mm and $R = 1$ m, the offset is 1.5 mm and at 10 m is 0.15 mm. With a 1 mm detector, the image would miss altogether at the 1 metre range, yet in practice the device worked well. The apparent contradiction is caused by the deliberately large aberrated spot and by defocus. The detector is overlapping the edge of the offset spot and a lot of signal is wasted, but at close range the signal is very intense and the loss 'affordable'. In fact the progressively improving centration at longer ranges helps to offset the reducing signal and reduces the dynamic range. It would be better to offset the detector by the calculated offset at the longest range envisaged, especially if small detectors are used, but this does add some mechanical

complexity in that centration is easy (e.g. in turned parts), with a controlled de-centration perhaps more difficult, but certainly achievable. Aside from the size of the aberrated spot, defocus helps. If we focus the lens on infinity, the image from one metre away is significantly defocused.

The lens F number, the ratio of focal length to the diameter, determines how much light it collects (as in a camera). It also strongly affects the lens aberrations and cost. The lens focal length determines the length of the optical part of the measuring device, since the detector is located at the focus and also determines the effective spot size and hence detector size. Strictly speaking optical calculations need to include all the components (filters, detector window etc.) since they all effect aberrations.

The aperture actually used was about 32 mm, so the lens was operating at an F number of 1.56 and aberrations obviously severe. Calculation showed that the 1 mm diameter detector captured around 90% of the energy for a source at infinity, hence the use of a 1 mm detector. A further reason for using this size, was the offset argument above. It was clear that for a small detector and good lens system the spot could walk off the detector at short ranges and in this respect the aberration is helpful, as is the defocus .

7.4.5 Conclusions

There are a considerable number of design trade-offs, especially in a cost benefit sense. In other cases decisions depend on factors which are rather badly characterised, such as the likely background light levels and sources in real usage. In these conclusions suggestions are made regarding the best way to build a practical commercial instrument, based on the arguments set out above.

If using a bandpass, 'bracketing' multilayer filter on a silicon substrate in sunlight we get considerable benefit from the reduced solar spectrum near 1.45 μm . If in practice this proves inadequate when combined with electronic measures, the double notch filter approach must be used but the cost may be excessive. The optimum electronics use two PSD's, at 275/325 Hz, with a two pole output filter at about 0.8 Hz. It should be possible to a single compromise feedback resistor in the transimpedance amplifier and see if the stray light performance is adequate under real conditions. The range versus stray light performance compromise can be made with this single component. There is a significant chance that to retain performance under brightly sunlit conditions (but at short range), electrical switching will be needed. This is most easily done by switching the detector between two pre-amplifiers, not by switching the feedback resistor itself. Only two values will be needed.

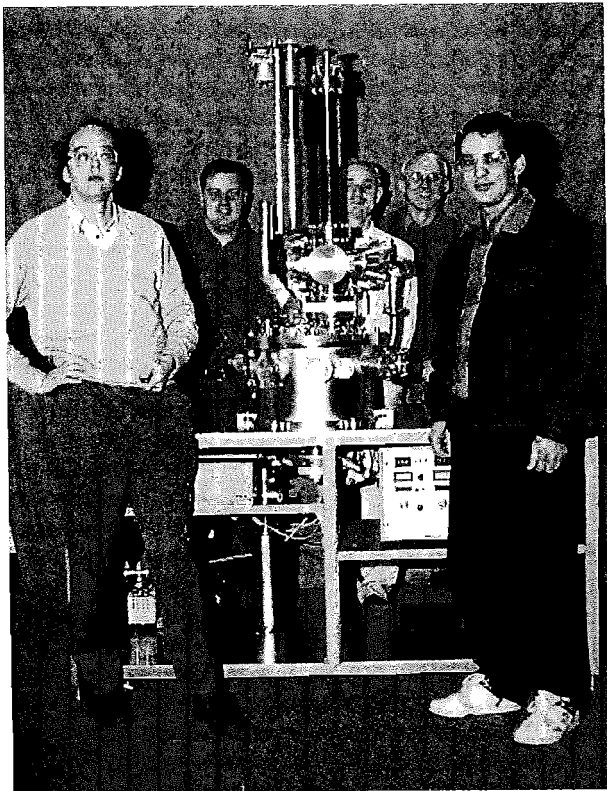
There are arguments in favour of nine volt (more would be better) battery operation to improve PSD dynamic range and background light saturation effects. Low voltages (three volts) would make good performance much more difficult. Lens and detector size are tightly coupled issues. The prototype is somewhat non optimum for long range; a 0.5 mm detector and 25 mm aperture would be smaller, cheaper and perform slightly better, with a re-optimised pre-amplifier. However the short range performance, currently better than needed, will be compromised. If this is excessive, a small static detector offset would help, but some form of range adjustment moving the detector sideways by around 1.5 mm might become essential. If the reduction in short range performance does not prove excessive, then use of a high index glass lens would be worth considering with very minor extra cost.

Finally the target effects. Performance will undoubtedly be best in a 'local reference' mode, where the instrument indicates other regions as wetter or dryer than a given reference spot. In a pre-set mode, where the instrument is "told" this is a brick wall etc., by setting the manual dial or selecting from a pre-printed list, only an extensive trial with a variety of brick walls for example can show how accurate the instrument will be. There are a considerable number of other possibilities and "fall back" options identified in this chapter if various types of difficulty are encountered. The above represents my view of the likely format of a device which should be very close to final form, but might require some final optimisation before production engineering is done.

In principle the results show that it is possible to measure the "dampness" of a surface in a given region from a distance of up to 20 m. This opens up possibilities for use as a commercial product in more than water detection for the construction industry. By changing the wavelength of the lasers themselves (and maybe the detector if necessary) other chemical or compounds could be monitored, including gases. One single unit could be designed which has different detector "heads" which if changed would allow the instrument to "look" for another material.

8

Conclusion and Future Work



8.1 Conclusions

8.2 Future Considerations

The people that made the GLS team included (left to right) Harvey, myself, Ken, Andy and Rasool. We are all gathered round the pulsed laser deposition chamber prior to its first use.

8.1 Conclusions

Despite some attractive properties, GLS glasses are of limited interest as materials for bulk glass lasers because of the poor thermal properties of the glass. This means that research has centred on fibre optic and planar waveguide devices. Thin chalcogenide films offer a possible means of incorporating sources and amplifiers into integrated optical circuits. The interest in these devices is to exploit the advantages offered by the planar geometry and the optical properties of rare-earth ions which may be monolithically integrated to allow pumping and tuning of the lasers. Complex multiple-cavity devices may be readily printed photolithographically, and gain regions may be selectively defined in the substrate. This requires that the bulk material be transferred congruently from glass target into thin film form.

Using laser ablation our results show that the most uniform films are achieved at longer target to substrate distances, higher target spin rate with slow trigger speeds to pulse the excimer laser. Laser ablation is usually conducted with the target and substrate in parallel. A phenomenon which became apparent during a specific experimental data set is an ability to increase the thin film thickness dramatically once the emerging plume and substrate holder are not perpendicular. This is believed to be related to a specific structural organisation of the material with results showing that there is an optimum angle for thin film thickness. EXAFS analysis of these films should reveal how the structure differs with deposition angle.

For waveguide structures to be produced in thin film layers, a detailed knowledge of the optical parameters is needed. A variety of different equations may be used to characterise the glassy materials through the determination of their optical constants. For GLS thin films, refractive indexes modelled using the Sellmeier formula produced the closest match with the actual experimental data. Using a fitting technique, it has been shown for example that energy density on the target surface will affect the optical bandgap of the subsequent thin film layer and hence its region of transparency.

Chalcogenide glasses must have all traces of oxygen and hydrogen removed from the glass melt, to reduce intrinsic absorption bands. Brief work here at Southampton showed that laser ablation warranted further investigation after initial tests with a simple laser ablation rig showed that thin films of GLS could be grown on substrates. The vacuum pressure was three orders of magnitude greater than the unique chamber which we manufactured and used throughout this work. When the new chamber produced its first films, the optical absorption was found to be very high in the visible transmission region and the original chamber conditions were simulated by back filling the new chamber with a background gas

mix of oxygen and nitrogen to approximate atmospheric percentages. When oxygen gas is introduced to the chamber it becomes incorporated into the thin films. For comparison a gallium-lanthanum-oxysulphide thin film was grown in vacuum. Results showed that there is no detectable difference in the absorption of the thin films of Ga or La sulphides and oxides, if the initial material contains the oxygen or if the chamber is back-filled with O₂. This is believed to be due to the bond energy of oxygen being higher than sulphur and hence favoured in reactions in the plume or on the film surface.

Argon and nitrogen have also been used as background gases when thin films are grown. It has been shown that the larger the molecular weight of gas the greater the plume spread and consequently the thinner and more uniform the film layer. Interaction between plume and background gas is emphasised by the photons which are emitted during the interaction between the plasma and atoms/molecules present. Results have shown that oxygen at low pressure in the vacuum chamber still affects the optical properties of the thin film significantly. This is probably due to an on-surface reaction during the deposition process rather than a plume interaction. Films grown in higher oxygen pressures appear to be becoming an oxide with a much reduced refractive index. Oxygen also shows the biggest effect in terms of photomodification; as the gas pressure increases the material not only becomes thinner, but includes a higher percentage of incorporated oxygen atoms. Its ability to photomodify actually disappears with the experimental argon ion laser power densities available to us. Results have shown that the oxygen reduces the ability to photomodify, so that although the visible optical transmission improves it becomes more difficult to write waveguides and make changes in the refractive index of the material.

Atomic scale structure changes in GLS bulk glass and PLD thin films were studied by EXAFS. Spectra have been recorded at the S and Ga K-edges and the La L_{III}-edge for thin films grown at different energy density. The lanthanum environment was found to be constant, into which other rare earths could be substituted, suggesting low inhomogeneous broadening. The high "wrong bonding" which has been shown demonstrates the structural origin of the absorption problems which were found in the shift of the Urbach tail. The photomodification results show that the films grown at higher energy density have a larger refractive index change when photomodified. Since photomodification is believed to involve bond breaking and small scale restructuring, films grown at a higher energy density are less structurally relaxed, which indicates why photomodification is more easily seen in these samples. Visual evidence and the EXAFS results show that there is a very high possibility that the undetectable La-La bonds create high optical absorption.

Using a multi-line Argon ion laser tuned to individual single lines the ability of the sample to photomodify with respect to wavelength were studied. The time necessary for Δn saturation, is inversely proportional to the pumping power. This means that independent of power, the

same quantity of photons creates the same change in refractive index. Also investigated was the effect of one single line from the argon laser at differing output powers and the relative speed of photomodification. It was shown that when photons change the refractive index, the higher their energy the faster the process occurs.

There are two effects which occur when thin films of chalcogenide materials are subjected to laser light whose wavelength lies above the optical band gap of the material. First and initially most obvious is a heating effect which rapidly increases the refractive index of the material. The temperature achieved is dependent on both power and wavelength of the incident radiation. A second effect is typical photomodification in which the refractive index is permanently decreased. It has been shown that the photothermal changes are reversible yet photo-optical changes are permanent. These two competing effects: thermal and purely optical are also found in bulk samples of GLS, but there both appear reversible. Because the refractive index does not change across the whole transmission range, structures made from GLS could be used to transmit longer wavelengths and interact with red and near infrared frequencies. Beyond around nine hundred nanometres the functional dependence of refractive index does not change. This means that with the ultimate goal being to find if rare earth GLS could become a suitable thin film waveguide laser, index changes will not be effective in the two to five micron emission region. For photoinduced gratings to be suitable for waveguide devices at these wavelengths a refractive index change through photomodification is required at both the pump and emission laser wavelength.

Whilst many processes affect the ability of the chalcogenide films to photomodify, for practical devices to take advantage of mask-less lithography, both optical transmission loss and the long term ageing effects need to be considered. It has not been possible in the time scales of this work to find if over time the structure does eventually settle and stabilise enough to become a useful commercial product. However results gathered over a two year period have shown that some relaxational effects do occur.

In the beginning, GLS appeared to have many attractive properties which would make it suitable for use as waveguide based structures which can be written into thin films. When a target of pure sulphur was ablated and no thin film layer was produced on the substrate, this confirmed our suspicion that sulphur based films were more difficult to produce using this growth technique. This suggests why the majority of films grown by PLD in the current facilities are oxygen based. Oxides can be grown successfully by this techniques, but very little literature exists to show laser ablation being successfully used for anything other than these materials. Background gasses such as hydrogen sulphide produced virtually no change in thin film optical properties when tested. Sulphur does not appear to interact with the substrate surface in the same way that oxygen does and again this is likely to have something to do with the bond energy differences.

The problems of particulates was never properly addresses as they did not appear to deteriorate the film quality. However proper analysis of the macro structure of the surface will become more important if further research into sulphide materials proves to be more promising. This is the largest reported difficulty with this growth technique in the literature and often limits the expansion of the system to other materials including oxides.

With the ultimate desire to produce a small solid state laser to use in the 2 to 5 μm region obviously beyond the reach of this project, diode lasers were purchased to assist in a demonstration device for the kind of sensing application that GLS thin films were intended candidates for. With a proof of principle system built, results showed that it is possible to use infrared reflection to measure the "dampness" of a surface in a given region from a distance of up to 20 m. This opens up possibilities for use as a commercial product in more than water detection for the construction industry. By changing the wavelength of the lasers themselves (and maybe the detector if necessary) other chemicals or compounds could be monitored, including gases. One single unit could be designed which has different detector "heads" which if changed would allow the instrument to "look" for another chemical.

8.2 Future Considerations

It is unlikely that GLS is going to fulfil its potential as a mask-less lithographic thin film structure into which various systems could be 'written'. However there are many parameters of laser ablation which were not investigated in depth in the present work. For example the influence of substrate temperature during growth of the thin film was studied analysed even though temperatures as low as $-100\text{ }^{\circ}\text{C}$ were achievable. At lower temperatures the film composition might change as it does when the substrate is heated in comparable crystal growth techniques.

The chamber was equipped with the ability to install two targets. This would allow pulses to be directed to either target which could alter the composition of the final thin film layer, dependent on how many pulses hit each respective target. This would also allow for capping and under layers to be added to the structure without the need to raise the pressure of the chamber to atmospheric and increase the risk of airborne contaminants reaching both the substrate and target surface. Capping layers would allow thin films to be grown which are, for example, sensitive to atmospheric moisture and protect the whole structure after deposition. They could also be used to change the refractive index difference at the boundary and so increasing or decreasing the thin film thickness required to produce a waveguide device.

Other materials could also be tried. Aluminium sulphide and iodine sulphide are two examples which when mixed with gallium sulphide might be grown more successfully by PLD than the materials presented in this thesis; however these materials are hygroscopic and so would need to employ a capping layer as referred to above. More EXAFS analysis of the materials would be useful to look in detail at how the bonding changes during the photomodification process. This 'beam time' is hard to obtain as the synchrotron radiation sources is a precious resource in most parts of the world.

The moisture measuring instrument has a lot of potential as a commercial product and could be developed further. More effort needs to go into the problem of reference materials whose characteristics are known well enough to prevent the need for an actual 'on-site' dry area. Microprocessor control should speed up the process of taking readings with the instrument and neglecting the need for the two signals having to aim for a specific target value. Full software control would allow the system to 'remember' the various figures and mathematically calculate the ratio's.

List of Publications and Conferences

Asal R, Rivers PE and Rutt HN, "*Laser ablation deposition of Ga₂S₃-La₂S₃ glass films* ", Materials Research Society Symposium Proceedings, Vol. 397, Ch.98, pp.253-258, 1996.

Rutt HN, Asal R and Rivers PE, "*Gallium Lanthanum Sulphide films for waveguide devices* ", Conference on Lasers and Electro-Optics (CLEO), Anaheim, CA, USA., June 2 - 7, Paper CWG6, 1996.

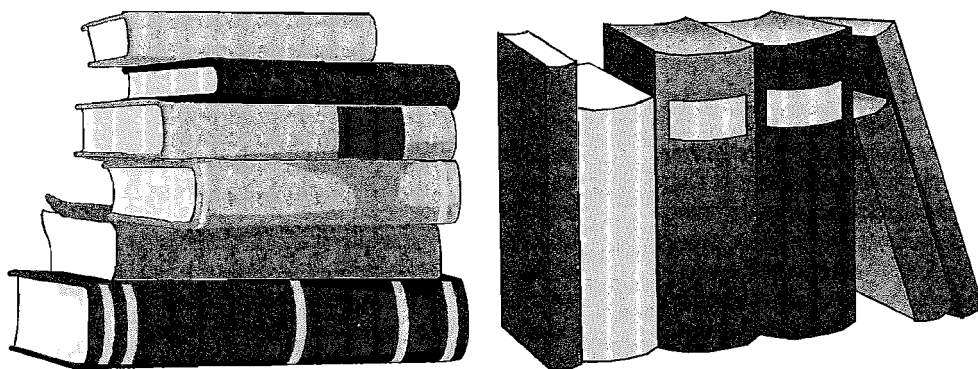
Rutt HN, Asal R and Rivers PE, "*Gallium Lanthanum Sulphide films for infrared waveguide devices* ", Guided Waves Propagation & Devices Conference, Canberra, Au, July 1996.

Asal R, Rivers PE and Rutt HN, "*A structural study of gallium lanthanum sulphide glass bulk and thin films by x-ray absorption fine structure spectroscopy* ", Journal of Physics C: Condensed Matter, Vol. 9, pp. 6217-6230, 1997.

Asal R, Rivers PE and Rutt HN, "*Optical properties and local structure of gallium lanthanum sulphide/oxide thin films for waveguide lasers* ", Poster presented at QE13 conference, Cardiff, UK, 1997.

Rivers PE, Rutt HN and Asal R, "*High-sensitivity mapping of refractive index across a surface using a dual-beam differential reflectance technique* ", Measurement Science & Technology, Vol. 9, pp. 86-94, 1998.

References



-
- [1] Townes CH, Journal of the Institute of Electrical Commun. Eng. (Jpn), Vol. 36, pp. 650-654, 1953.
 - [2] Gordon JP, Zeiger HJ and Townes CH, "Molecular microwave oscillator and new hyperfine structure in the microwave spectrum of NH_3 ", Physical Review, Vol. 95, pp. 282-284, 1954.
 - [3] Maiman TH, "Stimulated optical radiation in ruby", Nature, Vol. 187, 4736, pp. 493-494, 1960.
 - [4] Maiman TH, "Optical maser action in ruby", British Communications and Electronics, Vol. 7, pp. 674-675, 1960.
 - [5] Franken PA, Hill AE, Peters CW and Weinreich G, "Generation of optical harmonics", Physical Review Letters, Vol. 7, pp. 118-119, 1961.
 - [6] Snitzer E, "Optical maser action of Nd^{3+} in a barium crown glass", Physical Review Letters, Vol. 7, pp. 444-446, 1961.
 - [7] Newman R, "Excitation of the Nd^{3+} Fluorescence in CaWO_4 by recombination in GaAs", Journal of Applied Physics, Vol. 34, pp. 437-437, 1963.
 - [8] Keyes RJ and Quist TM, "Injection luminescent pumping of $\text{CaF}_2:\text{U}^{3+}$ with GaAs diode lasers", Applied Physics Letters, Vol. 4, pp. 50-52, 1964.
 - [9] Ostermayer FW, Jr., " $\text{GaAs}_{(1-x)}\text{P}_x$ diode pumper YAG:Nd lasers", Applied Physics Letters, Vol. 18, pp. 93-96, 1971.
 - [10] Scifres DR, Burnham RD and Streifer W, "Phase-locked semiconductor laser array", Applied Physics Letters, Vol. 33, pp. 1015-1017, 1978.
 - [11] Lumpp JK and Allen SD, "Excimer laser machining and metallization of vias in aluminum nitride", IEEE Transactions on Components Packaging and Manufacturing Technology Part B: Advanced Packaging, Vol. 20, pp. 241-246, 1997.
 - [12] Borgia I, Fantoni R, Flamini C, Di Palma TM, Guidoni AG and Mele A, "Luminescence from pigments and resins for oil paintings induced by laser excitation", Applied Surface Science, Vol. 129, pp. 95-100, 1998.
 - [13] Reisfeld R, "Spectra and energy transfer of rare earths in inorganic glasses", Structure and Bonding, Vol. 13, pp. 53-98, 1973.
 - [14] Reisfeld R, "Radiative and non-radiative transitions of rare-earth ions in glasses", Structure and Bonding, Vol. 22, pp. 123-175, 1975.
 - [15] Shinn MD, Krupke WF, Solarz RW and Kirchoff TA, "Spectroscopic and laser properties of Pm^{3+} ", IEEE Journal of Quantum Electronics, Vol. 24, pp. 1100-1108, 1988.
 - [16] Chang NC, "Fluorescence and stimulated emission from trivalent europium in yttrium oxide", Journal of Applied Physics, Vol. 34, pp. 3500-3504, 1963.
 - [17] Etzel HW, Gandy and Ginther RJ, "Stimulated emission of infrared radiation from Ytterbium activated silicate glass", Applied Optics, Vol. 1, pp. 534-536, 1962.
 - [18] Johnson LF, "Optical maser characteristics of rare earth ions in crystals", Journal of Applied Physics, Vol. 34, pp. 897-909, 1963.

- [19] Adam JL, Docq AD and Lucas J, "Optical transitions of Dy^{3+} ions in fluorozirconate Glass", Journal of Solid State Chemistry, Vol. 75, pp. 403-412, 1988.
- [20] Canalejo M, Cases R and Alcala R, "Optical transitions of Sm^{3+} ions in fluorozirconate Glass", Physics and Chemistry of Glasses, Vol. 29, pp. 187-191, 1988.
- [21] Piksis AH, Dieke GH and Crosswhite HM, "Energy levels and crystal fields of $LaCl_3:Gd^{3+}$ ", Journal of Chemical Physics, Vol. 47, pp. 5083-5089, 1967.
- [22] Blasse G and Bril A, "A new phosphor for flying-spot cathode-ray tubes for colour television: yellow emitting $Y_3Al_5O_{12}:Ce^{3+}$ ", Applied Physics Letters, Vol. 11, pp. 53-55, 1967.
- [23] Robbins DJ, Cockayne B, Lent B and Casper JL, "The mechanism of 5D_3 - 5D_4 cross relaxation in $Y_3Al_5O_{12}:Tb^{3+}$ ", Solid State Communications, Vol. 20, pp. 673-676, 1976.
- [24] Iqbal T, Shahriari MR, Hajcak P, Sigel Jr. GH, Copeland LR and Reed WA, "Optical properties of AlF_3 -based glasses doped with Pr^{3+} , Yb^{3+} and Lu^{3+} ", Applied Optics, Vol. 33, pp. 965-968, 1994.
- [25] Nachimuthu P, Jagannathan R, Nirmal Kumar V and Narayana Rao D, "Absorption and emission spectral studies of Sm^{3+} and Dy^{3+} ions in PbO - PbF_2 glasses", Journal of Non-Crystalline Solids, Vol. 217, pp. 215-223, 1997.
- [26] Srinivasan R, "Ablation of polymers and biological tissue by ultraviolet lasers", Science, Vol. 234, pp. 559-565, 1986.
- [27] Savage JA, "Optical properties of chalcogenide glasses", Journal of Non-Crystalline Solids, Vol. 47, pp. 101-116, 1982.
- [28] Miniscalco WJ, "Rare earth doped fiber lasers and amplifiers", (Marcel Dekker Inc., New York), Ch. 2, pp. 19-133, 1993.
- [29] Layne CB, Lowdermilk WH and Weber MJ, "Multiphonon relaxation of rare-earth ions in oxide glasses", Physical Review B: Condensed Matter, Vol. 16, pp. 10-20, 1977.
- [30] Reisfeld R, Bornstein A, Flahaut J and Loireau-Lozac'h A-M, "The rare earths in modern science and technology", (Plenum Press, New York, USA), Vol. Ed. 2, pp. 463-468, 1979.
- [31] Schultz-Sellack C, "Diathermansie einer reihe von stoffen für wärme sehr geringer Brechbarkeit", Annalen de Physik Chem., Vol. 139, pp. 182-187, 1870.
- [32] Frerichs R, "New optical glasses transparent in the Infra-red up to $12\ \mu$ ", Physical Review, Vol. 78, pp. 643-643, 1950.
- [33] Frerichs R, "New optical glasses with good transparency in the infrared", Journal of the Optical Society of America, Vol. 43, pp. 1153-1157, 1953.
- [34] Fraser WA, "A new triaxial system of infrared glasses", Journal of the Optical Society of America, Vol. 43, pp. 823-832, 1953.
- [35] Dewulf G, "Glasses transparent in the infrared", Revue d'Optique Theorique et Instrumentale, Vol. 33, pp. 513-518, 1954.
- [36] Glaze FW, Blackburn DH, Osmalov JS, Hubbard D and Black MH, "Properties of Arsenic Sulfide glass", Journal of Research of the National Bureau of Standards, Vol. 59, pp. 83-92, 1957.

- [37] **Sveshnikova EB, Sokolov VV and Stroganov AA**, "Nonradiative deactivation of rare-earth ions in chalcogenide glasses", *Optical Spectroscopy (USSR)*, Vol. 63, pp. 83-86, 1987.
- [38] **Dumbaugh WH**, "Infrared transmitting glasses", *Optical Engineering*, Vol. 24, pp. 257-262, 1985.
- [39] **Ohmachi V and Ishida N**, "Vitreous As_2Se_3 ; Investigation of acousto-optical properties and application to infrared modulator", *Journal of Applied Physics*, Vol. 43, pp. 1709-1712, 1972.
- [40] **Krause JT, Kurkjian CR, Pinnow DA and Sigety EA**, "Low acoustic loss chalcogenide glasses- A new category of materials for acoustic and acousto-optic applications", *Applied Physics Letters*, Vol. 17, pp. 367-368, 1970.
- [41] **Abu-Zeid ME, Rakhshani AE, Al-Jassar AA and Youssef YA**, "Determination of the thickness and refractive index of Cu_2O thin film using thermal and optical interferometry", *Physica Status Solidi A: Applied Research*, Vol. 93, pp. 613-620, 1986.
- [42] **Goryunova NA and Kolomiets BT**, "New vitreous semiconductors", *Izvestiya Akademii Nauk SSSR Seriya Fizicheskaya*, Vol. 20, pp. 1496-1500, 1956.
- [43] **Tichý L, Tichá H, Beneš L and Málek J**, "The glass-forming region and electrical conductivity of Ge-Bi-S glasses", *Journal of Non-Crystalline Solids*, Vol. 116, pp. 206-218, 1990.
- [44] **Sedeeq K and Fadel M**, "Electrical and optical studies in some Bi doped amorphous chalcogenide thin films", *Thin Solid Films*, Vol. 229, pp. 223-226, 1993.
- [45] **Sokolov VV, Kamarzin AA, Trushnikova LN and Savelyeva MV**, "Optical materials containing rare earth Ln_2S_3 sulphides", *Journal of Alloys and Compounds*, Vol. 225, pp. 567-570, 1995.
- [46] **Korkinova TsN and Andreichin RE**, "Chalcogenide glass polarization and the type of contacts", *Journal of Non-Crystalline Solids*, Vol. 194, pp. 256-259, 1996.
- [47] **Wilson J, Stegeman GI and Wright EM**, "Soliton switching in an erbium-doped nonlinear fiber coupler", *Optics Letters*, Vol. 16, pp. 1653-1655, 1991.
- [48] **Fadel M**, "Switching phenomenon in evaporated Se-Ge-As thin films of amorphous chalcogenide glass", *Vacuum*, Vol. 44, pp. 851-855, 1993.
- [49] **Ewen PJS, Slinger CW, Zakery A, Zekak A and Owen AE**, "The fabrication and properties of chalcogenide IR diffractive elements", *Proceedings of SPIE: Infrared and Optoelectronic Materials and Devices*, Vol. 1512, pp. 101-111, 1991.
- [50] **Lucazeau G, Barnier S and Loireau-Ozac'h A-M**, "Spectres vibrationnels, transitions électroniques et structures a courtes distances dans les verres: sulfures de terres rares- sulfure de gallium", *Materials Research Bulletin*, Vol. 12, pp. 437-448, 1977.
- [51] **Flahaut J, Guittard M and Loireau-Lozac'h A-M**, "Rare earth sulphide and oxysulphide glasses", *Glass Technology*, Vol. 24, pp. 149-156, 1983.
- [52] **Loireau-Lozac'h A-M, Guittard M and Flahaut J**, "Verres formes par les sulfures Ln_2S_3 des terres rares avec le sulfure de gallium Ga_2S_3 ", *Materials Research Bulletin*, Vol. 11, pp. 1489-1496, 1976.

- [53] **Loireau-Lozac'h A-M, Guittard M and Flahaut J**, "Systèmes L_2S_3 - Ga_2S_3 ($L = La, Ce, Dy, Er$ et Y) diagrammes de phases", *Materials Research Bulletin*, Vol. 12, pp. 881-886, 1977.
- [54] **Walker PJ and Ward RCC**, "The preparation of some ternary sulphides MR_2S_4 ($M=Ca, Cd$; $R=La, Sm, Er$) and the melt growth of $CaLa_2S_4$ ", *Materials Research Bulletin*, Vol. 19, pp. 717-725, 1984.
- [55] **Mamontova TN, Mukanov K, Vinogradova GZ, Maisashvili NG and Babievskaya IZ**, "A study of the optical properties and photoluminescence of glasses in the Ge - P - S system", *Physica Status Solidi A: Applied Research*, Vol. 93, pp. 635-644, 1986.
- [56] **Fuxi G, Xilai M, Hao W and Peihong Y**, "Study on devitrification and properties of Ge - As - S glass system", *Journal of Non-Crystalline Solids*, Vol. 56, pp. 309-314, 1983.
- [57] **Raptis C and Ivanova ZG**, "Raman investigation of reversible photoinduced effects in semiconducting Ge - S - Ga thin-film glasses", *Journal of Applied Physics*, Vol. 64, pp. 2617-2620, 1988.
- [58] **Cervinka L and Hruby A**, "Structure of amorphous and glassy Sb_2S_3 and its connection with the structure of As_2X_3 arsenic chalcogenide glasses", *Journal of Non-Crystalline Solids*, Vol. 48, pp. 231-264, 1982.
- [59] **Igo T and Toyoshima Y**, "A reversible optical change in the As - Se - Ge glass", *Journal of Non-Crystalline Solids*, Vol. 11, pp. 304-308, 1973.
- [60] **Hilton AR, Jones CE and Brau M**, "New high temperature infrared transmitting glasses", *Infrared Physics*, Vol. 4, pp. 213-221, 1964.
- [61] **Oe K, Toyoshima Y and Nagai H**, "A reversible optical transition in Se - Ge and P - Se - Ge glasses", *Journal of Non-Crystalline Solids*, Vol. 20, pp. 405-411, 1976.
- [62] **Balevia MI, Maksimov MH, Metev SM and Sendova MS**, "Laser-assisted sputtering of $Pb_{1-x}Cd_xSe$ films", *Journal of Materials Science Letters*, Vol. 5, pp. 533-536, 1986.
- [63] **Savage JA and Nielsen S**, "The infra-red transmission of telluride glasses", *Physics and Chemistry of Glasses*, Vol. 7, pp. 56-59, 1966.
- [64] **Cheung JT**, "Epitaxial growth of $Hg_{0.7}Cd_{0.3}Te$ by laser-assisted deposition", *Applied Physics Letters*, Vol. 43, pp. 255-257, 1983.
- [65] **Sedeek K, Mahmoud EA, Terra FS, Said A and El-din SM**, "Optical properties of amorphous chalcogenide thin films: the effect of Te isovalence substitution in the Ge - S - Se system", *Journal of Physics D: Applied Physics*, Vol. 27, pp. 156-159, 1994.
- [66] **Dubowski JJ, Williams DF, Sewell PB and Norman P**, "Epitaxial growth of (100) $CdTe$ on (100) $GaAs$ induced by pulsed laser evaporation", *Applied Physics Letters*, Vol. 46, pp. 1081-1083, 1985.
- [67] **Guittard M, Loireau-Lozac'h AM, Pardo MP, Flahaut J and Lucazeau G**, "Verres formes par les oxysulfures de terres rare Ln_2O_2S ", *Materials Research Bulletin*, Vol. 13, pp. 317-322, 1978.
- [68] **Flaschen SS, Pearson AD and Northover WR**, "Low melting sulphide-halogen inorganic glasses", *Journal of Applied Physics*, Vol. 31, p. 219, 1960.
- [69] **Lin FG and Ho SN**, "Chemical durability of arsenic-sulfur-iodine glasses", *Journal of the American Ceramic Society*, Vol. 46, p. 24, 1963.

- [70] **Eaton DL**, "Electrical conduction anomaly of semi-conducting glasses in the system As-Te-I", *Journal of the American Ceramic Society*, Vol. 47, p. 554, 1964.
- [71] **Seddon AB and Hemingway MA**, "Thermal characterisation of infrared-transmitting Ge-S-I glasses", *Journal of Non-Crystalline Solids*, Vol. 161, pp. 323-326, 1993.
- [72] **Hector JR, Wang J, Brady D, Kluth M, Hewak DW, Brocklesby WS and Payne DN**, "Spectroscopy and quantum efficiency of halide-modified gallium lanthanum sulfide glasses doped with praseodymium", *Journal of Non-Crystalline Solids*, Vol. 239, pp. 176-180, 1998.
- [73] **Smolorz S, Liu X, Qian L, Wise F, Wang J, Brady D, Hewak D and Payne DN**, "Reduction of optical nonlinearities of Ga-La-S glasses for active fibre applications through addition of CsCl", *Electronics Letters*, Vol. 34, pp. 2268-2269, 1998.
- [74] **Reisfeld R and Eckstein Y**, "Dependence of spontaneous emission and nonradiative relaxations of Tm^{3+} and Er^{3+} on glass host and temperature", *Journal of Chemical Physics*, Vol. 63, pp. 4001-4012, 1975.
- [75] **Bornstein A, Flahaut J, Guittard M, Jaulmes S and Loireau-Lozac'h AM**, "The rare earths in modern science and technology", (Plenum Press, New York, USA), pp. 599-606, 1978.
- [76] **Reisfeld R and Bornstein A**, "Absorption and emission spectra in chalcogenide glass of the composition $0.7Ga_2S_3 \cdot 0.27La_2S_3 \cdot 0.3Nd_2S_3$ ", *Chemical Physics Letters*, Vol. 47, pp. 194-196, 1977.
- [77] **Reisfeld R and Bornstein A**, "Fluorescence of Er^{3+} doped $La_2S_3 \cdot 3Ga_2S_3$ glasses", *Journal of Non-Crystalline Solids*, Vol. 27, pp. 143-145, 1978.
- [78] **Kumta PN and Risbud SH**, "Novel glasses in rare-earth sulphide systems", *American Ceramic Society Bulletin*, Vol. 69, pp. 1977-1984, 1990.
- [79] **Reisfeld R**, "Chalcogenide glasses doped by rare earths: structure and optical properties", *Annales de Chimie Science des Materiaux*, Vol. 7, 2-3, pp. 147-160, 1982.
- [80] **Feinleib J, deNeufville J, Moss SC and Ovshinsky SR**, "Rapid reversible light-induced crystallization of amorphous semiconductors", *Applied Physics Letters*, Vol. 18, pp. 254-257, 1971.
- [81] **Tanaka K**, "Light intensity dependence of photodarkening in amorphous As_2S_3 film", *Thin Solid Films*, Vol. 157, pp. 35-41, 1988.
- [82] **Elliott SR**, "A unified model for reversible photostructural effects in chalcogenide glasses", *Journal of Non-Crystalline Solids*, Vol. 81, pp. 71-98, 1986.
- [83] **Tanaka K and Odajima A**, "Configuration-coordinate model for photodarkening in amorphous As_2S_3 ", *Journal of Non-Crystalline Solids*, Vol. 46, pp. 259-268, 1981.
- [84] **Tanaka K**, "Configurational and structural models for photodarkening in glassy chalcogenides", *Japanese Journal of Applied Physics Part 1- Regular Papers & Short Notes*, Vol. 25, pp. 779-786, 1986.
- [85] **Tanaka K**, "Photoinduced structural changes in chalcogenide glasses", *Review of Solid State Science*, Vol. 4, pp. 641-659, 1990.
- [86] **Tanaka K**, "Photo-induced dynamical changes in amorphous As_2S_3 films", *Solid State Communications*, Vol. 34, pp. 201-204, 1980.

- [87] Piekara U, Langer JM and Krukowska-Fulde B, "Shallow versus deep In donors in CdF_2 crystals", Solid State Communications, Vol. 23, pp. 583-587, 1977.
- [88] Levanyuk AP and Osipov VV, "Optical distortion in crystals", Physica Status Solidi A: Applied Research, Vol. 35, pp. 605-614, 1976.
- [89] Mitchelotti F, Fazio E, Senesi F, Bertolotti M, Chumash V and Andriesh A, "Non-linearity and photostructural changes in glossy As_2S_3 thin films", Optics Communications, Vol. 101, pp. 74-78, 1993.
- [90] Petkov K and Dinev B, "Photo induced changes in the optical properties of amorphous As-Ge-S thin films", Journal of Materials Science, Vol. 29, pp. 468-472, 1994.
- [91] Utsugi Y and Mizushima Y, "Lattice-dynamical aspects in photoexcited chalcogenide glasses", Japanese Journal of Applied Physics, Vol. 31, pp. 3922-3933, 1992.
- [92] Elliott SR and Kolobov AV, "Athermal light-induced vitrification of $\text{As}_{50}\text{Se}_{50}$ films", Journal of Non-Crystalline Solids, Vol. 128, pp. 216-220, 1991.
- [93] Brezhkin VV, "Phenomenological model of crystal-amorphous phase change", Journal of Non-Crystalline Solids, Vol. 124, pp. 34-40, 1990.
- [94] Frumar M, Firth AP and Owen AE, "Optically induced crystal-to-amorphous-state transition in As_2S_3 ", Journal of Non-Crystalline Solids, Vol. 192-3, pp. 447-450, 1995.
- [95] Judd BR, "Optical Absorption Intensities of Rare-Earth Ions", Physical Review, Vol. 127, pp. 750-761, 1962.
- [96] Weiser K, Gambino RJ and Reinhold JA, "Laser-beam writing on amorphous chalcogenide films: crystallization kinetics and analysis of amorphizing energy", Applied Physics Letters, Vol. 22, pp. 48-49, 1973.
- [97] Salminen O, Nordman N, Riihola P and Ozols A, "Holographic recording and photocontraction of amorphous As_2S_3 films by 488.0 nm and 514.5 nm laser light illumination", Optics Communications, Vol. 116, pp. 310-315, 1995.
- [98] Singh B, Rajagopalan S, Bhat PK, Pandya DK and Chopra KL, "Giant photocontraction effect in amorphous chalcogenide thin films", Journal of Non-Crystalline Solids, Vol. 35-36, pp. 1053-1059, 1980.
- [99] Blatter A and Ortiz C, "Laser ablative hole formation in amorphous thin films", Journal of Applied Physics, Vol. 73, pp. 8552-8560, 1993.
- [100] Hisakuni H and Tanaka K, "Giant photoexpansion in As_2S_3 glass", Applied Physics Letters, Vol. 65, pp. 2925-2927, 1994.
- [101] Hisakuni H and Tanaka K, "Optical fabrication of microlenses in chalcogenide glasses", Optics Letters, Vol. 20, pp. 958-960, 1995.
- [102] Dubkov VM, "Analysis of the condition for obtaining homogeneous optical coatings by the pulsed laser evaporation method", Soviet Journal of Optical Technology, Vol. 49, p. 168, 1982.
- [103] Ewen PJS, Taylor W, Firth AP and Owen AE, "A Raman study of photochemical reactions in amorphous As_2S_3 on polycrystalline Ag_2S substrates", Philosophical Magazine B- Physics of Condensed Matter Structural Electronic Optical and Magnetic Properties, Vol. 48, pp. L15-L21, 1983.

- [104] **Hajtó J, Jánossy I and Forgács G**, "*Laser-induced optical anisotropy in self-supporting amorphous GeSe₂ films*", Journal of Physics C: Solid State Physics, Vol. 15, pp. 6293-6303, 1982.
- [105] **Janai M**, "*Photolithographic processes in amorphous semiconductors*", Journal of Physics (Paris), Vol. 42, pp. 1105-1114, 1981.
- [106] **Gacoin T, Malier L and Boilot JP**, "*New transparent chalcogenide materials using a sol-gel process*", Chemistry of Materials, Vol. 9, pp. 1502-1504, 1997.
- [107] **Marquez E, Bernal Olivia AM, Gonzalez Leal JM, Prieto Alcon R and Jimenez Garay R**, "*On the irreversible photo-bleaching phenomenon in obliquely-evaporated GeSe₂ glass films*", Journal of Non-Crystalline Solids, Vol. 222, pp. 250-257, 1997.
- [108] **Nordman O, Nordman N and Ozols A**, "*Influence of the age of amorphous nonannealed As₂S₃ thin films on holographic properties*", Optics communications, Vol. 145, 1-6, pp. 38-42, 1998.
- [109] **Corrales C, Ramirez-Malo JB, Fernandez Pena J, Villares, Swanepoel R and Marquez E**, "*Determining the refractive index and average thickness of AsSe semiconducting glass films from wavelength measurements only*", Applied Optics, Vol. 34, pp. 7907-7913, 1995.
- [110] **Jiang FS, Fach A, Maissen C, Masek J and Blunier S**, "*Film preparation and structure analysis of optical recording domains of amorphous Ge-Sb-Te*", Journal of Non-Crystalline Solids, Vol. 184, pp. 51-56, 1995.
- [111] **Schulz S, Gillan EG, Ross JL, Rogers LM, Rogers RD and Barron AR**, "*Synthesis of gallium cubanes and their use as CVD precursors for Ga₂E₃ (E=S, Se)*", Organometallics, Vol. 15, pp. 4880-4883, 1996.
- [112] **McCann PJ and Aanegola SK**, "*The role of graphite boat design in liquid-phase epitaxial-growth of PbSe_{0.78}Te_{0.22} on BaF₂*", Journal of Crystal Growth, Vol. 141, pp. 376-382, 1994.
- [113] **Jungbluth ED**, Laser Focus World, Vol. 30, 7, p. 15, 1994.
- [114] **Meneghini C, Viens JF, Villeneuve A, Knystautas EJ, Duguay MA and Richardson KA**, "*Luminescence from neodymium-ion-implanted As₂S₃ waveguides*", Journal of the Optical Society of America B: Optical Physics, Vol. 15, pp. 1305-1308, 1998.
- [115] **Bonar JR and Aitchison JS**, "*Co-doping effects in rare-earth-doped planar waveguides*", IEE proceedings J: Optoelectronics, Vol. 143, pp. 293-297, 1996.
- [116] **Brech F and Cross L**, "*Optical micromission stimulated by a ruby maser*", Applied Spectroscopy, Vol. 16, p. 59, 1962.
- [117] **Linlor WI**, "*Plasmas produced by laser bursts*", Bulletin of the American Physical Society, Vol. 7, pp. 440-441, 1962.
- [118] **Honig RE and Woolston JR**, "*Laser induced emission of electrons, ions and neutral atoms from solid surfaces*", Applied Physics Letters, Vol. 2, 7, pp. 138-139, 1963.
- [119] **Murray JJ**, "*Photoelectric effect induced by high intensity laser light beam from quartz and borosilicate glass*", Bulletin of the American Physical Society, Vol. 8, p. 77, 1963.
- [120] **Ready JF**, "*Development of plume of material vaporized by giant-pulse laser*", Applied Physics Letters, Vol. 3, pp. 11-13, 1963.

- [121] **Rosan RC, Healy MK and McNary Jr WF**, "Spectroscopic ultramicroanalysis with a laser", *Science*, Vol. 142, pp. 236-237, 1963.
- [122] **Howe JA**, "Observations on the maser induced graphite jet", *Journal of Chemical Physics*, Vol. 39, pp. 1362-1363, 1963.
- [123] **Berkowitz J and Chupka WA**, "Mass spectrometric study of vapor ejected from graphite and other solids by focused laser beams", *Journal of Chemical Physics*, Vol. 40, pp. 2735-2736, 1964.
- [124] **Basov NG and Krokhin ON**, "Conditions for heating up of a plasma by the radiation from an optical generator", *Soviet Physics- JETP*, Vol. 19, 1, pp. 123-125, 1964.
- [125] **Ehler AW and Weissler GL**, "Vacuum ultraviolet radiation from plasmas formed by a laser on metal surfaces", *Applied Physics Letters*, Vol. 8, pp. 89-91, 1966.
- [126] **Langer P, Tonon G, Floux F and Ducauze A**, "Laser induced emission of electrons, ions and X-rays from solid targets", *IEEE Journal of Quantum Electronics*, Vol. QE2, 9, pp. 499-506, 1966.
- [127] **Archbold E and Hughes TP**, "Electron temperature in a laser heated plasma", *Nature*, Vol. 204, p. 670, 1964.
- [128] **Sonnenberg H, Heffner H and Spicer W**, "Two photon photoelectric effect in Cs_3Sb ", *Applied Physics Letters*, Vol. 5, pp. 95-96, 1964.
- [129] **Logothetis EM and Hartman PL**, "Three-photon photoelectric effect in gold", *Physical Review Letters*, Vol. 18, 15, pp. 581-583, 1967.
- [130] **Smith HM and Turner AF**, "Vacuum deposited thin films using a ruby laser", *Applied Optics*, Vol. 4, pp. 147-148, 1965.
- [131] **Zaitsev SV, Martynyuk AN and Protasov EA**, "Superconductivity of $\text{BaPb}_{1-x}\text{Bi}_x\text{O}_3$ films prepared by laser evaporation method", *Soviet Physics- Solid State*, Vol. 25, pp. 100-103, 1983.
- [132] **Dijkkamp D, Venkaatesan T, Wu XD, Shaheen SA, Jisrawi N, Min-Lee YH, Mclean WL and Croft M**, "Preparation of Y-Ba-Cu oxide superconductor thin films using pulsed laser evaporation from high T_c bulk material", *Applied Physics Letters*, Vol. 51, pp. 619-621, 1987.
- [133] **Wu XD, Dijkkamp D, Ogale SB, Inam A, Chase EW, Miceli PF, Chang CC, Tarascon JM and Venkatesan T**, "Epitaxial ordering of oxide superconductor thin films on (100) SrTiO_3 prepared by pulsed laser evaporation", *Applied Physics Letters*, Vol. 51, pp. 861-863, 1987.
- [134] **Cheung JT and Magee T**, "Recent progress on LADA growth of HgCdTe and CdTe epitaxial layers", *Journal of Vacuum Science and Technology A: Vacuum, Surfaces and Films*, Vol. 1, 3, pp. 1604-1607, 1983.
- [135] **Cheung JT and Madden J**, "Growth of HgCdTe epilayers with any predesigned compositional profile by laser molecular beam epitaxy", *Journal of Vacuum Science and Technology B: Microelectronics Processing and Phenomena*, Vol. 5, 3, pp. 705-708, 1987.
- [136] **Bartholemew CS, Betz HT, Greiser JL, Spence RA and Murarta NP**, "Rugate filters by laser flash evaporation of Si_xO_y on room temperature polycarbonate", 31st Annual International Technical Symposium: Optical Optoelectronics Applied Science Engineering, San Diego, pp. 198-204, August 1987.

- [137] **Calí C, Daneu V, Orioli A and Riva-Sanseverino S**, "*Flash evaporation of compounds with pulsed-discharge CO₂ laser*", *Applied Optics*, Vol. 15, pp. 1327-1330, 1976.
- [138] **Dupendant H, Gavigan JP, Givord D, Lienard A, Rebouillat JP and Souche Y**, "*Velocity distribution of micron-size particles in thin film laser ablation deposition (LAD) of metals and oxide semiconductors*", *Applied Surface Science*, Vol. 43, pp. 369-376, 1989.
- [139] **Pompe W, Scheibe H-J, Richer A, Bauer H-D, Bewilogua K and Weissmantel C**, "*On the influence of residual stresses and density fluctuations on the crystallization of amorphous carbon films*", *Thin Solid Films*, Vol. 144, pp. 77-92, 1986.
- [140] **Durand H-A, Brimaud J-H, Hellman O, Shibata H, Sakuragi S, Makita Y, Gesbert D and Meyrueis P**, "*Excimer laser sputtering deposition of TiO₂ optical coating for solar cells*", *Applied Surface Science*, Vol. 86, pp. 122-127, 1995.
- [141] **Ortiz C and Blatter A**, "*Laser irradiation of amorphous thin films*", *Thin Solid Films*, Vol. 218, 1-2, pp. 209-218, 1992.
- [142] **Rouleau CM, Lowndes DH, Strauss MA, Cao S, Pedraza AJ, Geohegan DB, Puretzky AA and Allard LF**, "*Effect of ambient gas pressure on pulsed laser ablation plume dynamics and ZnTe film growth*", *Materials Research Society Symposium Proceedings*, Vol. 397, Ch. 98, pp. 119-124, 1996.
- [143] **Chen LC and Hall EL**, "*Nature and application of particulate matter produced by pulsed laser ablation*", *Materials Research Society Symposium Proceedings*, Vol. 285, pp. 519-526, 1993.
- [144] **Zaldo C, Gill DS and Eason RW**, "*Growth of KNbO₃ thin films on MgO by pulsed laser deposition*", *Applied Physics Letters*, Vol. 65, pp. 502-504, 1994.
- [145] **Greene JE, Edited by Auciello O and Engemann J**, "*Multicomponent and thin films for advanced microtechnologies: Techniques, fundamentals and devices*", (Kluwer Academic Publishers, Dordrecht, The Netherlands), pp. 39-85, 1993.
- [146] **Horwitz JS, Chrisey DB, Stroud RM, Carter AC, Kim J, Chang W, Pond JM, Kirchoefer SW, Osofsky MS and Koller D**, "*Pulsed laser deposition as a materials research tool*", *Applied Surface Science*, Vol. 129, pp. 507-513, 1998.
- [147] **Cheung JT and Sankur H**, "*Growth of thin films by laser induced evaporation*", *CRC Critical Reviews in Solid State Materials Science*, Vol. 15, pp. 63-109, 1988.
- [148] **Gaponov SV, Gusev SA, Luskin BM, Salashchenko NN and Gluskin ES**, "*Long-wave X-ray radiation mirrors*", *Optics Communications*, Vol. 38, pp. 7-9, 1981.
- [149] **Martin MJ, Alfonso JE, Mendiola J, Zaldo C, Gill DS, Eason RW and Chandler PJ**, "*Pulsed laser deposition of KNbO₃ thin films*", *Journal of Materials Research*, Vol. 12, 10, pp. 2699-2708, 1997.
- [150] **Fried D, Zuerlein M, Featherstone JDB, Seka W, Duhn C and McCormack SM**, "*IR ablation of dental enamel: mechanistic dependence on the primary absorber*", *Applied Surface Science*, Vol. 129, pp. 852-856, 1998.
- [151] **Schawlow AL**, "*Lasers*", *Science*, Vol. 149, pp. 13-22, 1965.
- [152] **Matthews DL**, "*Laser zaps graffiti onto powder*", *MRS Bulletin*, Vol. 21, 7, p. 9, 1996.
- [153] **Matthews DL**, "*Graffiti busters*", *Technology Review*, Vol. 99, 6, p. 16, 1996.

- [154] Fotakis C, "*Lasers for art's sake!*", Optics and Photonics News, Vol. 6, 5, pp. 30-35, 1995.
- [155] Tam AC, Park HK and Grigoropoulos CP, "*Laser cleaning of surface contaminants*", Applied Surface Science, Vol. 129, pp. 721-725, 1998.
- [156] Panzner M, Wiedemann G, Henneberg K, Fischer R, Wittke Th and Dietsch R, "*Experimental investigation of the laser ablation process on wood surfaces*", Applied Surface Science, Vol. 129, pp. 787-792, 1998.
- [157] Bonch-Bruevich AM and Imas YaA, "*Recoil momentum and ejection of metal particles under the action of a giant laser pulse*", Soviet Physics- Technical Physics, Vol. 12, 10, pp. 1407-1409, 1968.
- [158] Kelly R, Miotello A, Braren B, Gupta A and Casey K, "*Primary and secondary mechanisms in laser-pulse sputtering*", Nuclear Instruments & Methods in Physics Research Section B: Beam Interactions with Materials and Atoms, Vol. 65, 1-4, pp. 187-199, 1992.
- [159] Geohegan DB, Mashburn DN, Culbertson RJ, Pennycook SJ, Budai JD, Valiga RE, Sales BC, Lowndes DH, Boatner LA, Sonner E, Eres D, Christen DK and Christie WH, "*Pulsed laser deposition of thin superconducting films of $\text{Ho}_1\text{Ba}_2\text{Cu}_3\text{O}_{7-x}$* ", Journal of Materials Research, Vol. 3, pp. 1169-1179, 1988.
- [160] Dyer PE, Greenough RD, Issa A and Key PH, "*TEA CO_2 laser ablation studies of Y-Ba-Cu-O*", Applied Surface Science, Vol. 43, pp. 387-392, 1989.
- [161] Ban VS and Kramer DA, "*Thin films of semiconductors and dielectrics produced by laser evaporation*", Journal of Materials Science, Vol. 5, pp. 978-982, 1970.
- [162] Snakur H and Cheung JT, "*Highly oriented ZnO films grown by laser evaporation*", Journal of Vacuum Science and Technology A: Vacuum, Surfaces and Films, Vol. 1, pp. 1806-1809, 1983.
- [163] Miotello A and Kelly R, "*Critical assessment of thermal models for laser sputtering at high fluences*", Applied Physics Letters, Vol. 67, pp. 3535-3537, 1995.
- [164] Honig RE, "*Laser-induced emission of electrons and positive ions from metals and semiconductors*", Applied Physics Letters, Vol. 3, pp. 8-11, 1963.
- [165] Geohegan DB, "*Fast intensified CCD photography of $\text{YBa}_2\text{Cu}_3\text{O}_7$ laser ablation in vacuum and ambient oxygen*", Applied Physics Letters, Vol. 60, pp. 2732-2734, 1992.
- [166] Bhat PK, Dubowski JJ and Williams DF, "*Detection of optical emission from InSb induced by pulsed laser evaporation*", Applied Physics Letters, Vol. 47, pp. 1085-1087, 1985.
- [167] Dyer PE, Ramsden SA, Sayers JA and Skipper MA, "*The interaction of CO_2 laser radiation with various solid targets*", Journal of Physics D: Applied Physics, Vol. 9, pp. 373-382, 1976.
- [168] Smith GA, Chen LC and Chuang MC, "*Effects of processing parameters on KrF excimer laser ablation deposited ZrO_2 films*", Materials Research Society Symposium Proceedings, Vol. 235, pp. 843-848, 1992.
- [169] Dickinson JT, Langford SC, Jensen LC and Eschbach PA, "*Consequences of simultaneous exposure of inorganic solids to excimer laser light and an electron beam*", Journal of Applied Physics, Vol. 68, pp. 1831-1836, 1990.

- [170] Gill DS, Eason RW, Zaldo C, Rut HN and Vainos NA, "Characterisation of Ga-La-S chalcogenide glass thin film optical waveguides, fabricated by pulsed laser deposition", *Journal of Non-Crystalline Solids*, Vol. 191, pp. 321-326, 1995.
- [171] Tang SP, Wicke BG and Friichtenicht JF, "Studies of the chemiluminescent reaction $\text{Ho}^+\text{N}_2\text{O} \rightarrow \text{HoO}^*$ ", *Journal of Chemical Physics*, Vol. 68, 12, pp. 5471-5473, 1978.
- [172] He M, Wang H and Weiner BR, "Production and laser-induced fluorescence spectrum of aluminum sulphide", *Chemical Physics Letters*, Vol. 204, 5-6, pp. 563-566, 1993.
- [173] Serra P and Morenza JL, "Analysis of hydroxyapatite laser ablation plumes in a water atmosphere", *Applied Physics A: Materials science & Processing*, Vol. 67, 3, pp. 289-294, 1998.
- [174] Papakonstantinou P, O'Neill MC, Atkinson R, Alwazzan R, Morrow T and Salter IW, "Influence of oxygen pressure on the expansion dynamics of Ba-hexaferrite ablation plumes and on the properties of deposited thin films", *Journal of Magnetism and Magnetic Materials*, Vol. 189, 1, pp. 120-129, 1998.
- [175] Dyer PE, Issa A and Key PH, "Dynamics of excimer laser ablation of superconductors in an oxygen environment", *Applied Physics Letters*, Vol. 57, pp. 186-188, 1990.
- [176] Strikovski M and Miller JH, "Pulsed laser deposition of oxides: Why the optimum rate is about 1 Å per pulse", *Applied Physics Letters*, Vol. 73, pp. 1733-1735, 1998.
- [177] Bulgakov AV and Bulgakova NM, "Gas-dynamic effects of the interaction between a pulsed laser-ablation plume and the ambient gas: analogy with an under expanded jet", *Journal of Physics D: Applied Physics*, Vol. 31, pp. 693-703, 1998.
- [178] Kanamori T, Terunuma Y, Takahashi S and Miyashita T, "Transmission loss characteristics of $\text{As}_{40}\text{S}_{60}$ and $\text{As}_{38}\text{Ge}_5\text{Se}_{57}$ glass unclad fibers", *Journal of Non-Crystalline Solids*, Vol. 69, pp. 231-242, 1985.
- [179] Kanamori T, Terunuma Y, Takahashi S and Miyashita T, "Chalcogenide glass fibers for mid-infrared transmission", *Journal of Lightwave Technology*, Vol. LT-2, pp. 607-613, 1984.
- [180] Ching-Hsong W, Weber WH, Potter TJ and Tamor MA, "Laser reflective interferometry for in situ monitoring of diamond film growth by chemical vapor deposition", *Journal of Applied Physics*, Vol. 73, pp. 2977-2982, 1993.
- [181] Wood RF, Leboeuf JN, Chen KR, Geohegan DB and Puretzky AA, "Dynamics of plume propagation, splitting and nanoparticle formation during pulsed-laser ablation", *Applied Surface Science*, Vol. 129, pp. 151-158, 1998.
- [182] Lubben D, Barnett SA, Suzuki K, Gorbatskin S and Greene JE, "Laser-induced plasmas for primary ion deposition of epitaxial Ge and Si films", *Journal of Vacuum Science and Technology B: Microelectronics Processing and Phenomena*, Vol. 3, pp. 968-974, 1985.
- [183] Leuchtner RE, Chrisey DB and Horwitz JS, "Particulate ejection in pulsed laser deposition", *Proceedings of SPIE: Excimer Lasers*, Vol. 1835, pp. 31-41, 1992.
- [184] Holzapfel B, Roas B, Schultz L, Bauer P and Saemann-Ischenko G, "Off-axis laser deposition of $\text{YBa}_2\text{Cu}_3\text{O}_{7-g}$ thin films", *Applied Physics Letters*, Vol. 61, pp. 3178-3180, 1992.

- [185] **Watanabe Y**, "Reactive rapid sequential pulse laser deposition of $\text{YBa}_2\text{Cu}_3\text{O}_7$: A candidate to eliminate particulate formation", *Applied Physics Letters*, Vol. 64, pp. 1295-1297, 1994.
- [186] **Koren G, Gupta A, Baseman RJ, Lutwyche MI and Laibowitz RB**, "Laser wavelength dependent properties of $\text{YBa}_2\text{Cu}_3\text{O}_7$ thin films deposited by laser ablation", *Applied Physics Letters*, Vol. 55, pp. 2450-2452, 1989.
- [187] **Foltyn SR, Muenchausen RE, Dye RC, Wu XD, Luo L and Cooke DW**, "Large-area, two-sided superconducting $\text{YBa}_2\text{Cu}_3\text{O}_{7-x}$ films deposited by pulsed laser deposition", *Applied Physics Letters*, Vol. 59, pp. 1374-1376, 1991.
- [188] **German RM**, "Powder Metallurgy Science", (Metal Powder Industries Federation, New Jersey, USA), pp. 74-96, 1984.
- [189] **Lide DR**, "CRC Handbook of chemistry and physics, 79th Ed.", (CRC press, Boca Raton, Florida, USA), pp. 112-124, 1998.
- [190] **Li S and El-Shall S**, "Synthesis of nanoparticles by reactive laser vaporization: silicon nanocrystals in polymers and properties of gallium and tungsten oxides", *Applied Surface Science*, Vol. 129, pp. 330-338, 1998.
- [191] **Schwarz H and Tourtellotte HA**, "Vacuum deposition by high-energy laser with emphasis on barium titanate films", *Journal of Vacuum Science and Technology A: Vacuum, Surfaces and Films*, Vol. 6, pp. 373-378, 1969.
- [192] **Kautek W, Roas B and Schultz L**, "Formation of Y-Ba-Cu-Oxide thin films by pulsed laser deposition: A comparative study in the UV, visible and IR range", *Thin Solid Films*, Vol. 191, pp. 317-334, 1990.
- [193] **Sankur H and Cheung JT**, "Formation of dielectric and semiconductor thin films by laser assisted evaporation", *Applied Physics A: Solids and Surfaces*, Vol. 47, pp. 271-284, 1988.
- [194] **Watanabe Y, Tanamura M, Matsumoto S and Seki Y**, "Laser power dependence of particulate formation on pulse laser deposition films", *Journal of Applied Physics*, Vol. 78, pp. 2029-2036, 1995.
- [195] **Misra DS and Palmer SB**, "Laser ablated thin films of $\text{Y}_1\text{Ba}_2\text{Cu}_3\text{O}_7$ the nature and origin of the particulates", *Physica C*, Vol. 176, pp. 43-48, 1991.
- [196] **Gaponov SV, Gudkov AA and Fraerman AA**, "Processes occurring in an erosion plasma during laser vacuum deposition of films. III. Condensation in gas flows during laser vapourization of materials", *Soviet Physics- Technical Physics*, Vol. 27, 9, pp. 1130-1133, 1982.
- [197] **Gaponov SV, Gudkov AA, Luskin BM, Luchin VI and Salashchenko NN**, "Formation of semi-conductor films from a laser erosion plasma scattered by a heated screen", *Soviet Physics- Technical Physics*, Vol. 26, 5, pp. 598-600, 1981.
- [198] **Koren G, Baseman RJ, Gupta A, Lutwyche MI and Laibowitz RB**, "Particulates reduction in laser-ablated $\text{YBa}_2\text{Cu}_3\text{O}_7$ thin films by laser induced plume heating", *Applied Physics Letters*, Vol. 56, pp. 2144-2146, 1990.
- [199] **Matsunawa A, Katayamas S, Susuki A and Ariyasu T**, "Laser production of metallic ultra-fine particles", *Transactions of the Journal Welding Research Institute*, Vol. 15, pp. 61-72, 1986.

- [200] Haruna M, Ishizuki H, Tsutsumi J, Shimaoka Y and Nishihara H, "Characterization of LiNbO_3 optical waveguide film grown on sapphire by ArF excimer laser ablation", Japanese Journal of Applied Physics Part 1: Regular Papers Short Notes & Review Papers, Vol. 34, 11, pp. 6084-6091, 1995.
- [201] Koren G, "Observation of shock waves and cooling waves in laser ablation of Kapton films in air", Applied Physics Letters, Vol. 51, pp. 569-571, 1987.
- [202] Schenck PK, Vaudin MD, Bonnell DW, Hastie JW and Paul AJ, "Particulate reduction in the pulsed laser deposition of barium titanate thin films", Applied Surface Science, Vol. 129, pp. 655-661, 1998.
- [203] Sankur H, Gunning WJ, DeNatale J and Flintoff JF, "High-quality optical and epitaxial Ge films formed by laser evaporation", Journal of Applied Physics, Vol. 65, pp. 2475-2478, 1989.
- [204] Oyama T, Ishii T and Takeuchi K, "Synthesis of fullerenes by ablation using pulsed and cw-Nd:YAG lasers", Fullerene Science and Technology, Vol. 5, pp. 919-933, 1997.
- [205] Barr WP, "The production of low scattering dielectric mirrors using rotating vane particle filtration", Journal of Physics E: Scientific Instruments, Vol. 2, pp. 1112-1114, 1969.
- [206] Beavitt AR, "A wide-band particle eliminator", Thin Solid Films, Vol. 1, pp. 69-70, 1967.
- [207] DeLeon RL, Joshi MP, Rexer EF, Prasad PN and Garvey JF, "Progress in thin film formation by laser assisted molecular beam deposition (LAMBD)", Applied Surface Science, Vol. 129, pp. 321-329, 1998.
- [208] Singh RK, Bhattacharya D and Narayan J, "Control of surface particle density in pulsed laser deposition of superconducting $\text{YBa}_2\text{Cu}_3\text{O}_7$ and diamondlike carbon thin films", Applied Physics Letters, Vol. 61, pp. 483-485, 1992.
- [209] Van de Riet E, Nillesen CJCM and Dieleman J, "Reduction of droplet emission and target roughening in laser ablation and deposition of metals", Journal of Applied Physics, Vol. 74, pp. 2008-2012, 1993.
- [210] Venkatesan T, Wu XD, Muenchausen R and Pique A, "Pulsed laser deposition: Future Directions", MRS Bulletin, Vol. 17, pp. 54-58, 1992.
- [211] Greer JA and Tabat MD, "On- and off-axis large area pulsed laser deposition", Materials Research Symposium Proceedings, Vol. 388, pp. 151-161, 1996.
- [212] Greer JA and Tabat MD, "Large-area pulsed laser deposition: Techniques and applications", Journal of Vacuum Science and Technology A: Vacuum, Surfaces and Films, Vol. 13, 3, pp. 1175-1181, 1995.
- [213] Greer JA, "Comparison of large-area pulsed laser deposition approaches", Proceedings of SPIE: Excimer Lasers, Vol. 1835, pp. 21-30, 1992.
- [214] Greer JA, "High quality YBCO films grown over large areas by pulsed laser deposition", Journal of Vacuum Science and Technology A: Vacuum, Surfaces and Films, Vol. 10, 4, pp. 1821-1826, 1992.
- [215] Tittmann BR, Cohen-Tenoudji F, de Billy M, Jungman A and Quentin G, "A simple approach to estimate the size of small surface cracks with the use of acoustic surface waves", Applied Physics Letters, Vol. 33, pp. 6-8, 1978.

- [216] **Lozac'h A-M and Flahaut J**, "*Sur une nouvelle famille de combinaisons soufrees, de type 'melilite'*", Materials Research Bulletin, Vol. 8, pp. 75-86, 1973.
- [217] **Elder FR, Gurewitsch AM, Langmuir RV and Pollock HC**, "*Radiation from electrons in a synchrotron*", Physical Review, Vol. 71, pp. 829-830, 1947.
- [218] **Xenakis D, Faucher O, Charalambidis D and Fotakis C**, "*Observation of two-XUV-photon ionization using harmonic generation from short, intense laser pulse*", Journal of Physics B: Atomic Molecular and Optical Physics, Vol. 29, pp. L457-L463, 1996.
- [219] **Elam WT, Kirkland JP, Neiser RA and Wolf PD**, "*Depth dependence for extended x-ray absorption fine-structure spectroscopy detected via electron yield in He and in vacuum*", Physical Review B- Condensed Matter, Vol. 38, pp. 26-30, 1988.
- [220] **Binstead N, Campbell JW and Gurman SJ**, "*EXCURV92 (EXAFS analysis programs)*", (Daresbury Laboratory, UK), 1991.
- [221] **Gurman SJ, Binstead N and Ross I**, "*A rapid, exact, curved-wave theory for EXAFS calculations: II. The multiple-scattering contributions*", Journal of Physics C: Solid State Physics, Vol. 19, pp. 1845-1861, 1986.
- [222] **Gurman SJ, Binstead N and Ross I**, "*A rapid, exact, curved-wave theory for EXAFS calculations*", Journal of Physics C: Solid State Physics, Vol. 17, pp. 143-151, 1984.
- [223] **Lee PA and Pendry JB**, "*Theory of the extended x-ray absorption fine structure*", Physical Review B- Condensed Matter, Vol. 11, pp. 2795-2811, 1975.
- [224] **Benazeth S, Tuilier MH and Guittard M**, "*Structural and atomic effects in lanthanum L_{II} , L_{III} EXAFS spectra of chalcogenide materials*", Physica B, Vol. 158, pp. 39-40, 1989.
- [225] **Benazeth S, Tuilier MH, Loireau-Ozac'h A-M, Dexpert H, Lagarde P and Flahaut J**, "*An EXFAS structural approach of the lanthanum-gallium-sulfur glasses*", Journal of Non-Crystalline Solids, Vol. 110, pp. 89-100, 1989.
- [226] **Mott NF and Davis EA**, "*Electronic processes in non-crystalline materials*", (Oxford University Press, Oxford, UK), 1979.
- [227] **Theye M-L, Gheorghiu A and Launois H**, "*Investigation of disorder effects in amorphous GaAs and GaP by EXAFS*", Journal of Physics C: Solid State Physics, Vol. 13, pp. 6569-6584, 1980.
- [228] **Del Cueto JA and Shevchik NJ**, "*EXAFS of amorphous GaAs: Evidence for inequivalent environments of Ga and As*", Journal of Physics C: Solid State Physics, Vol. 11 pp. L829-L832, 1978.
- [229] **Ichikawa T**, "*Electron diffraction study of the local atomic arrangement in amorphous gallium films*", Physica Status Solidi A- Applied Research, Vol. 19, pp. 347-356, 1973.
- [230] **Sharma BD and Donohue J**, Zeitschrift Fur Kristallographie, Vol. 177, p. 293, 1962.
- [231] **Chrisey DB and Hubler GK**, "*Pulsed laser deposition of thin films*", (Wiley, New York, USA), 1994.
- [232] **Asal R, Rivers PE and Rutt HN**, "*A structural study of gallium lanthanum sulphide glass bulk and thin films by x-ray absorption fine structure spectroscopy*", Journal of Physics C: Condensed Matter, Vol. 9, pp. 6217-6230, 1997.

- [233] **Palazzi M**, "*Study of the system $Ga_2S_3-Na_2S$* ", Comptes Rendus Des Seances De L Academie Des Sciences Serie II (Paris), Vol. 299, 9, pp. 529-532, 1984.
- [234] **Barnier S, Palazzi M, Massot M and Julien C**, "*Vibrational spectra of the vitreous $Ga_2S_3-Na_2S_3$ system*", Solid State Ionics, Vol. 44, 1-2, pp. 81-86, 1990.
- [235] **Guittard M, Pardo MP and Chilouet A**, "*Action of some sulphides. Part of some impurities on Ga_2S_3* ". Preparation of a ' Ga_2S_3 ', Materials Research Bulletin, Vol. 25, 5, pp. 563-566, 1990.
- [236] **Viana B, Palazzi M and LeFol O**, "*Optical characterization of Nd^{3+} doped sulphide glasses*", Journal of Non-Crystalline Solids, Vol. 215, pp. 96-102, 1997.
- [237] **Jaulmes S, Palazzi M and Laruelle P**, "*Preparation and structure of $La_6(Ga, Na)Ga_2S_{14}$* ", Materials Research Bulletin, Vol. 23, pp. 831-835, 1988.
- [238] **Urbach F**, "*The long-wavelength edge of photographic sensitivity and of the electronic absorption of solids*", Physical Review, Vol. 92, pp. 1324-1324, 1953.
- [239] **Tauc J**, "*Amorphous and liquid semiconductors*", (Plenum Press, New York, USA), pp. 159-220, 1974.
- [240] **Webber PJ and Savage JA**, "*Some physical properties of Ge-As-Se infrared optical glasses*", Journal of Non-Crystalline Solids, Vol. 20, pp. 271-283, 1976.
- [241] **Moynihan CT, Macedo PB, Maklad MS, Mohr RK and Howard RE**, "*Intrinsic and impurity infrared absorption in As_2Se_3 glass*", Journal of Non-Crystalline Solids, Vol. 17, pp. 369-385, 1975.
- [242] **Savage JA, Webber PJ and Pitt AM**, "*The potential of Ge-As-Se-Te glasses as 3-5 μm and 8-12 μm infrared optical materials*", Infrared Physics, Vol. 20, pp. 313-320, 1980.
- [243] **Feltz A, Burckardt W, Voigt B and Linke D**, "*Optical glasses for IR transmittance*", Journal of Non-Crystalline Solids, Vol. 129, pp. 31-39, 1991.
- [244] **Ye CC, Hewak DW, Hempstead, Samson BN and Payne DN**, "*Spectral properties of Er^{3+} -doped gallium lanthanum sulphide glass*", Journal of Non-Crystalline Solids, Vol. 208, 1-2, pp. 56-63, 1996.
- [245] **Ye CC, Hempstead M, Hewak DW and Payne DN**, "*Proposal for an Er^{3+} doped chalcogenide glass fiber upconversion laser operating at 980 nm and pumped at 1480 nm*", IEEE Photonics Technology Letters, Vol. 9, pp. 1104-1106, 1997.
- [246] **Pruneri V, Kazansky PG, Hewak D, Wang J, Takebe H and Payne DN**, "*Frequency doubling in gallium-lanthanum-sulphide optical glass with microcrystals*", Applied Physics Letters, Vol. 70, pp. 155-157, 1997.
- [247] **Hector JR, Hewak DW, Wang J, Moore RC and Brocklesby WS**, "*Quantum-efficiency measurements in Oxygen-containing gallium lanthanum sulphide glasses and fibres doped with Pr^{3+}* ", IEEE Photonics Technology Letters, Vol. 9, pp. 443-445, 1997.
- [248] **Mattos Jnr L and Clare AG**, "*The crystallisation and optical properties of gallium cerium lanthanum sulphide glass*", Physics and Chemistry of Glasses, Vol. 34, pp. 244-250, 1993.

- [249] Takebe H, Murata T, Nishida H, Hewak DW and Morinaga K, "Compositional dependence of optical properties of Nd^{3+} in gallate glasses", *Journal of the Ceramic Society of Japan*, Vol. 104, 3, pp. 243-246, 1996.
- [250] Samson BN, Schweizer T, Hewak DW and Laming RI, "Properties of dysprosium doped gallium lanthanum sulfide fiber amplifiers operating at $1.3\ \mu\text{m}$ ", *Optics Letters*, Vol. 22, pp. 703-705, 1997.
- [251] Schweizer T, Brady DJ and Hewak DW, "Fabrication and Spectroscopy of erbium doped gallium lanthanum sulphide glass fibres for mid-infrared laser applications", *Optics Express*, Vol. 1, 4, pp. 102-107, 1997.
- [252] Schweizer T, Hewar DW, Payne DN, Jensen T and Huber G, "Rare-earth doped chalcogenide glass laser", *Electronics Letters*, Vol. 32, pp. 666-667, 1996.
- [253] Schweizer T, Samson BN, Moore RC, Hewark DW and Payne DN, "Rare-earth doped chalcogenide glass fibre laser", *Electronics Letters*, Vol. 33, pp. 414-416, 1997.
- [254] Stenin SI, "Molecular beam epitaxy of semiconductor, dielectric and metal films", *Vacuum*, Vol. 36, 7-9, pp. 419-426, 1986.
- [255] Demay Y, Arnoult D, Gailliard JP and Medina P, "In situ spectroscopic ellipsometry during molecular- beam epitaxy of cadmium mercury telluride", *Journal of Vacuum Science and Technology A: Vacuum, Surfaces and Films*, Vol. 5, pp. 3139-3142, 1987.
- [256] Aspnes DE, Kelso SM, Logan RA and Baht R, "Optical properties of $\text{Al}_x\text{Ga}_{1-x}\text{As}$ ", *Journal of Applied Physics*, Vol. 60, pp. 754-767, 1986.
- [257] Aspnes DE, Harbison JP, Studna AA and Floex LT, "Optical-reflectance and electron-deffraction studies of molecular-beam-epitaxy growth transients on $\text{GaAs}(001)$ ", *Physical Review Letters*, Vol. 59, pp. 1687-1690, 1987.
- [258] Kobayashi N and Horikoshi Y, "Optical investigation on the growth process of GaAs during migration-enhanced epitaxy", *Japanese Journal of Applied Physics Part 2- Letters*, Vol. 28, 11, pp. 1880-1882, 1989.
- [259] Donnelly VM and McCalley JA, "Infrared-laser interferometric thermometry: A nonintrusive technique for measuring semiconductor wafer temperatures", *Journal of Vacuum Science and Technology A: Vacuum, Surfaces and Films*, Vol. 8, pp. 84-92, 1989.
- [260] Farrell T, Armstrong JV and Kightley P, "Dynamic optical reflectivity to monitor the real time metalorganic molecular beam epitaxial growth of AlGaAs layers", *Applied Physics Letters*, Vol. 59, pp. 1203-1205, 1991.
- [261] Donnelly VM, "Real-time determination of the direction of wafer temperature change by spatially resolved infrared laser interferometric thermometry", *Journal of Vacuum Science and Technology A: Vacuum, Surfaces and Films*, Vol. 11, 5, pp. 2393-2397, 1993.
- [262] Donnelly VM, "Extension of infrared- laser interferometric thermometry to silicon wafers polished on only one side", *Applied Physics Letters*, Vol. 63, 10, pp. 1396-1398, 1993.
- [263] Reizman F and Van Gelder W, "Optical thickness measurement of $\text{SiO}_2\text{-Si}_3\text{N}_4$ films on silicone", *Solid State Electronics*, Vol. 10, pp. 625-632, 1967.

- [264] **Pliskin WA and Conrad EE**, "Nondestructive determination of thickness and refractive index of transparent films", IBM Journal of Research and Development, Vol. 8, pp. 43-51, 1964.
- [265] **Azzam RMA and Zaghloul A-RM**, "Polarization-independent reflectance matching (PIRM) a technique for the determination of the refractive index and thickness of transparent films", Journal of Optics (Paris), Vol. 8, 3, pp. 201-205, 1977.
- [266] **Nussenzveig HM**, "Causality and Dispersion Relations", (Academic Press, New York), Ch. 1, pp. 3-53, 1972.
- [267] **Iwadate Y, Kawamura K, Murakami K, Igarashi K and Mochinaga J**, "Electronic polarizabilities of Ti^{4+} , Ag^{+} , and Zn^{2+} ions estimated from refractive index measurements of $TiNO_3$, $AgNO_3$, and $ZnCl_2$ melts", Journal of Chemical Physics, Vol. 77, 12, pp. 6177-6183, 1982.
- [268] **Ditchburn RW**, "Light", (Blackie & Son Limited, London, UK) 2nd Ed., pp. 562-568, 1963.
- [269] **Herzberger M**, "Modern Geometrical Optics", (Interscience Publishers Inc., New York, USA), pp. 120-131, 1958.
- [270] **Herzberger M**, "Colour correction in optical systems and a new dispersion formula", Optica Acta, Vol. 6, pp. 197-215, 1959.
- [271] **Born M and Wolf E**, "Principles of Optics- Electromagnetic Theory of Propagation, Interference and Diffraction of Light", (Pergamon Press, Oxford, UK) 6th Ed., pp. 60-65, 1980.
- [272] **Malitson IH**, "A redetermination of some optical properties of calcium fluoride", Applied Optics, Vol. 2, pp. 1103-1107, 1936.
- [273] **Li HH**, "Refractive index of ZnS, ZnSe and ZnTe and its wavelength and temperature derivatives", Journal of Physical and Chemical Reference Data, Vol. 13, 1, pp. 103-150, 1984.
- [274] **Klocek P**, "Handbook of Infrared Optical Materials", (Dekker, New York, USA), pp. 401-405, 1991.
- [275] **Klocek P**, "Handbook of Infrared Optical Materials", (Dekker, New York, USA), pp. 409-419, 1991.
- [276] **Edwards DF and Ochoa E**, " ", Applied Optics, Vol. 19, p. 4130, 1980.
- [277] **Hazewinkel M**, "Encyclopedia of mathematics", (Kluwer Academic Publishers Group, Dordrecht, The Netherlands) Vol. 6, pp. 170-171, 1990.
- [278] **Marquardt DW**, "An algorithm for least-squares estimation of nonlinear parameters", Journal of the Society for Industrial and Applied Mathematics, Vol. 11, pp. 431-441, 1963.
- [279] **Levenberg K**, "A method for the solution of certain non-linear problems in least squares", Quarterly Applied Mathematics, Vol. 2, pp. 164-168, 1944.
- [280] **Brodsky MH, Title RS, Weiser K and Pettit GD**, "Structural, optical, and electrical properties of amorphous silicon films", Physical Review B: Solid State, Vol. 1, pp. 2632-2641, 1970.

- [281] **Asal R and Rutt HN**, "Optical properties of laser ablated gallium lanthanum sulphide chalcogenide glass thin films prepared at different deposition laser energy densities", *Optical Materials*, Vol. 8, pp. 259-268, 1997.
- [282] **Mott NF**, "Conduction in glasses containing transition metal ions", *Journal of Non-Crystalline Solids*, Vol. 1, pp. 1-17, 1968.
- [283] **Tauc J, Grigorovici R and Vancu A**, "Optical properties and electronic structure of amorphous germanium", *Physica Status Solidi*, Vol. 15, pp. 627-637, 1966.
- [284] **Davies EA and Mott NF**, "Conduction in non-crystalline systems V. conductivity, optical absorption and photoconductivity in amorphous semiconductors", *Philosophical Magazine*, Vol. 22, pp. 903-922, 1970.
- [285] **Nemanich RJ, Connell GAN, Hayes TM and Street RA**, "Thermally induced effects in evaporated chalcogenide films. I. Structure", *Physical Review B: Condensed Matter*, Vol. 18, pp. 6900-6914, 1978.
- [286] **Rancourt JD**, "Optical thin films- users' handbook", (Macmillan publishing Company, New York, USA), Ch. 2, 1987.
- [287] **Wagner FX, Scaggs M, Koch A, Endert H, Christen H-M, Knauss LA, Harshavardhan KS and Green SM**, "Epitaxial HTS thin films grown by PLD with a beam homogenizer", *Applied Surface Science*, Vol. 129, pp. 477-480, 1998.
- [288] **Owen AE, Firth AP and Ewen PJS**, "Photo-induced structural and physico-chemical changes in amorphous chalcogenide semiconductors", *Philosophical Magazine B-Physics of Condensed Matter Structural Electronic Optical and Magnetic Properties*, Vol. 52, pp. 347-362, 1985.
- [289] **Asal R, Rivers PE and Rutt HN**, "Laser ablation deposition of Ga₂S₃-La₂S₃ glass films", *Materials Research Society Symposium Proceedings*, Vol. 397, Ch.98, pp. 253-258, 1996.
- [290] **Morishita K**, "Index Profiling of Three-Dimensional Optical Waveguides by the Propagation-Mode Near-Field Method", *Journal of Lightwave Technology*, Vol. LT-4, 8, pp. 1120-1124, 1986.
- [291] **Gedeon A**, "Comparison between rigorous theory and WKB-analysis of modes in graded index waveguides", *Optics Communications*, Vol. 12, pp. 329-332, 1974.
- [292] **Tien PK, Riva-Sanseverino RJ, Martin RJ, Ballman AA and Brown H**, "Optical waveguide modes in single-crystalline LiNbO₃-LiTaO₃", *Applied Physics Letters*, Vol. 24, pp. 503-506, 1974.
- [293] **Chiang KS**, "Construction of refractive-index profiles of planar dielectric waveguides from the distribution of effective indexes", *Journal of Lightwave Technology*, Vol. LT-3, pp. 385-391, 1985.
- [294] **Ramaswamy V and Lagu RK**, "Numerical field solution for an arbitrary asymmetrical graded-index planar waveguide", *Journal of Lightwave Technology*, Vol. LT-1, pp. 408-417, 1983.
- [295] **Siegman AE**, "Lasers", (University Science Books, Sausalito CA USA), pp. 675-679, 1986.
- [296] **Kaye GWC and Laby TH**, "Tables of Physical and Chemical Constants", (Longman Scientific & Technical, New York, USA), 15th Ed., pp. 99-100, 1989.

- [297] **Rivers PE, Rutt HN and Asal R**, "*High-sensitivity mapping of refractive index across a surface using a dual-beam differential reflectance technique*", *Measurement Science & Technology*, Vol. 9, pp. 86-94, 1998.
- [298] **Ozols A, Salminen O and Reinfelde M**, "*Relaxational self-enhancement of holographic gratings in amorphous As₂S₃*", *Journal of Applied Physics*, Vol. 75, pp. 3326-3334, 1994.
- [299] **Kumar B and White K**, "*Thermal aging effects in vitreous As₂S₃ films*", *Thin Solid Films*, Vol. 135, pp. L13-L17, 1986.
- [300] **Ozols A, Nordman N and Nordman Olli**, "*Effect of structure relaxation on the holographic recording in amorphous As₂S₃ films*", *Optics Communications*, Vol. 136, pp. 365-369, 1997.
- [301] **Bertolotti M, Ferrari A, Livoti R, Sibilia C, Chumack V and Liackhou G**, "*Optothermal characterization of As₂S₃ chalcogenide glasses*", *Materials Science and Engineering B: Solid State Materials for Advanced Technology*, Vol. 9, 4, pp. 459-461, 1991.
- [302] **Siegman AE**, "*Lasers*", (University Science Books, Sausalito CA USA), Ch. 7, 1986.
- [303] **Shimizu M, Suda H and Horiguchi M**, "*High-efficiency Nd-doped fibre lasers using direct-coated dielectric mirrors*", *Electronics Letters*, Vol. 23, pp. 768-769, 1987.
- [304] **Marcuse D**, "*Coupling efficiency of front surface and multi layer mirrors as fibre-end reflectors*", *Journal of Lightwave Technology*, Vol. LT-4, pp. 377-381, 1986.
- [305] **Andriesh AM, Bykovskii YuA, Kolomeiko EP, Makovkin AV, Smirnov VL and Shmal'ko AV**, "*Wave guide structures and functional elements of integrated optics systems based on volume holographic gratings in thin As₂S₃ films*", *Soviet Journal of Quantum Electronics*, Vol. 7, 3, pp. 347-352, 1977.
- [306] **Litinskaya LI and Radygina NV**, "*Induced changes in the transmission spectra of optical recording media based on chalcogenide glasses*", *Telecommunication and Radio Engineering*, Vol. 47, pp. 99-100, 1992.
- [307] **Kudryashov AV and Seliverstov AV**, "*Adaptive stabilized interferometer with laser diode*", *Optics Communications*, Vol. 120, pp. 239-244, 1995.
- [308] **Yamaguchi I, Liu J, Nakajima T and Kato J**, "*Active stabilization and real time analysis of interference fringes*", *Proceedings of SPIE*, Vol. 2782, 89, pp. 354-362, 1996.
- [309] **Olsson A, Tang CL and Green EL**, "*Active stabilization of a Michelson interferometer by an electrooptically tuned laser*", *Applied Optics*, Vol. 19, pp. 1897-1899, 1980.
- [310] **Palmer CH and Green RE Jr.**, "*Materials evaluation by optical detection of acoustic emission signals*", *Materials Evaluation*, Vol. 35, pp. 107-112, 1977.
- [311] **White RG and Emmory DC**, "*Active feedback stabilization of a Michelson interferometer using a fixture element*", *Journal of Physics E: Scientific Instruments*, Vol. 18, pp. 658-663, 1985.
- [312] **Herbst TM and Beckwith SVW**, "*Active stabilization system for fabry-perot interferometers*", *Applied Optics*, Vol. 28, pp. 5275-5277, 1989.
- [313] **Ng WW, Hong C and Yariv A**, "*Holographic interference lithography for integrated optics*", *IEEE Transactions: Electronic Devices*, ED-25, 10, p. 1193, 1978.

-
- [314] **Schmahl G and Rudolph D**, "*Holographic diffraction gratings*", (Progress in Optics, Ed. E Wolfe, North-Holland, Amsterdam), p. 95, 1976.
- [315] **Wilmshurst TH**, "*Signal recovery from noise in electronic instrumentation*", (Adam Hilger, London, UK), Ed. 2, p. 37, 1990.
- [316] **Kou L, Labrie D and Chylek P**, "*Refractive indices of water and ice in the 0.65-2.5 μm spectral range*", Applied Optics, Vol. 32, pp. 3531-3540, 1993.